POLITECNICO DI TORINO

Department of Applied Science and Technology
Ph.D. in Chemical Engineering
XXV cycle (2010-2012)

MULTISCALE SIMULATION OF POLYMER NANOPARTICLES PRECIPITATION FOR PHARMACEUTICAL APPLICATIONS

PhD Student

Nicodemo Di Pasquale

Supervisors

Dott. Paola Carbone
Prof. Daniele L. Marchisio
Prof. Antonello A. Barresi

Second Referee:
Prof. Maurizio Fermeglia

Coordinator:
Prof. Vito Specchia

To my family, and Martina

Contents

Abstract

This work focuses on the development and use of a multiscale computational tool for the simulation of the process of precipitation of polymeric nanoparticles in micro-mixers. This process, as will be shown through the rest of the thesis, is not very easy to model with single scale model (i.e., Computational Fluid Dynamics, Population Balances, Molecular Dynamics). The main reason stands in the complex behaviour of the system investigated (the polymer); the behaviour at atomistic scale influences the macro-scale. With micro-scale (which is equivalent in our notation to the atomistic scale) we refer to all the phenomena occurring at length-scales of nanometres (1 nm = 10^{-9} m) and time-scales of picoseconds (1 ps = 10^{-12} s), whereas with macroscale we intend all the phenomena occurring at length-scale of meters and at time-scale of seconds. There are different models used to describes these (apparently) uncorrelated phenomena. Computational Fluid Dynamics (CFD) which describes at the macroscale the motion of a fluid in a given domain often coupled with Population Balance Model (PBM) to describe the presence of a dispersed colloidal phase, and Molecular Dynamics (MD) which describes the motion of a collection of atoms in an interval of time. The coupling of these methods in a unique description of the problem is called *multiscale modelling*, a research area which has raised much interests in the last few years. In this work, precipitation of nanoparticles occurs in a micromixer, is investigated trough CFD-PBM, whilst the precipitation process is described by extracting some information from MD simulations, hence, coupling these different models in one description. The thesis is structured as follows:

1. The First Chapter is an introduction to the investigated problem. A brief description of the use of polymer nanoparticles in the pharmaceutical industry is given, with the current state of the art. A brief overview of the

different production processes and devices used will be also given

2. The Second Chapter in intended to give all the theoretical background required for the understanding of the subsequent chapters. Starting from the very beginning, the governing equations for the generic N-body problem are derived together with the description of the theoretical tools for the molecular dynamics. By using the Boltzmann Equation we show how to move from a description of the problem a the micro-scale (here represented by the MD) to a description of the problem at the macro-scale (represented by the CFD). The introduction of the Boltzmann equation (and the mesoscale) is also useful since the PBM is a kinetic equation very similar to the Boltzmann equation

3. The Third Chapter involves the description of the CFD model of the micromixer used in this study. The polymeric nanoparticles precipitation model is presented along with its intrinsic limitations highlighting the need of a more fundamental approach

4. In the Fourth Chapter we discuss the improvement of the CFD model by developing a nucleation theory adequate to the description of the polymer particle formation. The parameters appearing in this theory are estimated by using the standard full atoms MD simulations. Eventually the nucleation theory is integrated into the CFD-PBM and used to simulate the entire process

5. The Fifth Chapter is devoted to the extension of the MD framework. In fact, in order to further investigate the polymer particle formation process, larger systems, involving many polymeric chains have to be described. This requires some form of partial coarse-graining, resulting in hybrid atomistic/coarse-grained model. The framework to do this is in this chapter described, showing how the model allows to speed up the simulation by neglecting some Degrees of Freedom of the original problem but maintaining the necessary details where needed

6. In the last Chapter some conclusions from the simulations presented are drawn.

Chapter 1

Introduction

The last few years have known an enormous increase in the research in nanotechnology applied to many fields, such as environmental technology, energy and medicine. In particular the application of nanotechnologies in medicine has proven to be a very promising research area, through the use of the so-called pharmaceutical nanocarriers. With nanocarriers we intend all the devices used in the field of controlled drug release as liposomes and polymer nanoparticles. The activity of certain drugs depends on their concentrations on the target site and the problem arises from the fact that the undesired side effects are related to the concentration of the drug inside the organism. The problem of the side effects is even more dangerous, if we consider that most of drugs used in chemotherapy, are extremely hazardous, even at low concentration. Moreover, some drugs can not have any affinity with the interested area of the body, because the distribution of the drug in the body depends from the physicochemical properties of the drug. A way to overcome these problems is to use nanocarriers designed appositely to carry the drug to a specified area and hence have the ability to accumulate in the diseased region of the body. In this framework, the dimension of the nanocarriers is of primary importance. First of all, the particle size distribution of the nanocarrier must guarantees that the particle can freely flow in capillaries, hence particle size can not exceed 1 μm. Moreover, even if the size of the carriers is below this threshold it is not sure that they will reach the targeted area. In the blood there exist a number of ways used by the human body to eliminate foreign bodies. One of these defense mechanisms is represented by the Reticuloendothelial System

which is very efficient for particles whose size is larger than 300 nm. In fact, it was observed that nanoparticles with size smaller than 300 nm and hydrophilic surface have longer circulation times, because of the reduced opsonization (in wich a foreign body is marked by binding on its surface an opsonin), the reduce phagocytosis by macrophages [Brannon-Peppas and Blanchette, 2004] and the clereance rate (the rate with which the kidney purifies the blood from external components). At the same time circulation time can be increased by binding to the surface hydrophilic molecules such as polyethylene glycol (PEG), because it creates an aqueous shell around the particles which avoids the adhesion of the opsonins on the particle surface. It was found that small size and enhanced circulation time lead to a spontaneous accumulation in various pathological sites of this kind of particles (and obviously of the entrapped drug) [Maeda, 2001; Maeda et al., 2001]. This effect, which allows a passive targeting of some specific areas in the body, is called *Enhanced Retention Permeability* effect. It is widely used in the treatment of cancer disease. In a cancer sites the vasculature changes also. The vascular permeability increases and the lymphatic drainage decreases leading to a net accumulation of nanoparticles in the diseased area higher than in a healthy part of the body [Maeda et al., 2001]. Because of the high toxicity of most of the drugs used in the treatment of cancer disease, this way seems to be a very promising route able to reduce these undesired side effects, due mainly to the high doses of drugs needed in a normal treatment to reach the desired accumulation in the cancer site. Pharmaceutical nanocarriers development is not only important for their ability to selectively target a specific region in the human body, but also because they are able to carry a number of water insoluble drugs that otherwise would face a number of serious problems in their use. The low-water insolubility is in fact responsible for the poor absorption and low biovaiability of the drugs [Lipinski et al., 2001] and the attitude of this kind of drugs to form aggregate which can be a serious hazard for human health, because they lead to embolism [Torchilin, 2007]. By using polymeric nanocarriers (e.g., nanoparticles, nanospheres, liposomes) in which the drug is entrapped, one can easily overcome these issues, hence obtaining a less hazardous and a more effective use of the drugs.

Therefore, in application as drug carriers the nanoparticles must have very specific characteristics. The polymer used in the production must be bio-compatible, or rather the polymer itself or its degradation products must be non-toxic

for human tissues. In this work the poly-ϵ-caprolactone (PCL) is considered. Its main biodegradation product is the 6-hydroxycaproic acid that can be removed by metabolism [Wu et al., 2000] and is one of the most studied polymer in the production of polymeric nanocarrier.

In this work we are interested in modelling the preparation/production process. We intend to develop a fully predictive model that predicts the final polymer particle characteristics, by defining the operating parameter of the process. This model, following the product engineering approach can be used to identify the best conditions under which particles with desired characteristics are obtained, avoiding expensive experimental campaigns.

Particles are produced with solvent displacement with the mixing of a solvent (containing the polymer and the drug) and the anti-solvent, inducing the formation of polymer particles entrapping drug molecules inside. Mixing of the two solutions is critical for controlling particle size, since particle formation is extremely rapid [Johnson and Prud'homme, 2003a]. Special continuous mixers must be employed in order to achieve the mixing efficiency needed for the production of ultra-fine (nano-)particles. During the last decade a variety of devices has been developed and tested which can be divided in two main different typologies. The first comprises the devices in which the high mixing efficiency is reached through the active mixing, that is, the complete and fast mixing obtained by an external energy input, such as high-gravity controlled precipitation, sono-precipitation or electrospraying (for a complete review of these techniques cf. Chan and Kwok [2011]). The second type is formed by the so-called *passive mixers* in which the flow energy, often generated by pump action, is used to restructure a flow in a way which results in faster mixing. This second type of mixers are the ones considered in this work. Among the passive mixers we can consider the vortex reactor (VR)[Marchisio et al., 2008, 2009], multi-inlet vortex reactor (MIVR) [Liu et al., 2008], T-mixer [Gradl et al., 2006], Y-mixer [Choi et al., 2005] and confined impinging jets reactor (CIJR) [Johnson and Prud'homme, 2003b]. CIJRs are analyzed in this study and have been used to produce not only PCL nanoparticles but also nano-spheres made of other polymers [Lince et al., 2008, 2011b,c; Valente et al., 2012a]. Moreover, lately the mixing performance of these different devices has been compared [Lince et al., 2011e] and the possibility of using adjustable CIJRs has been assessed [Lince et al., 2009]. CIJR consists of a small cylindrical chamber with two opposite inlets for the solvent

and anti-solvent respectively. The inlet streams collide in the centre of the chamber creating an impinging plane in which they are quickly mixed. Nanoparticles in CIJR are produced by using the solvent displacement process which will be described in Chap. 3. A sketch of the geometry of the CIJR is reported in Fig. 1.1

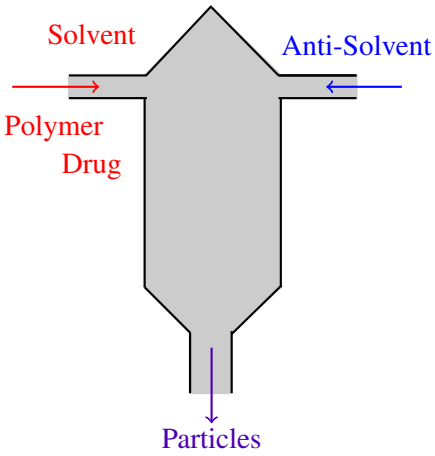

Figure 1.1: Sketch of the geometry of the CIJR. In solvent displacement process the drug and the polymer are dissolved in a solvent. The latter is fast mixed with an anti-solvent in which the solvent is soluble and the polymer not. This lead to formation of the particles

In Fig. 1.1 is possible to see how a CIJR works. The inlet streams, entering from the side of the mixer, collide in the center of the chamber. Afterwards, particles are immediately formed because of the mixing of the solvent stream and the anti-solvent stream. The model used in this work involves different scales. Turbulent mixing between solvent and anti-solvent is described by Computational Fluid Dynamics (CFD) by using the Reynolds-averaged Navier-Stokes equations (RANS) approach. Mixing at the molecular level is accounted for with the Direct Quadrature Methods of Moments coupled with Interaction and Exchange with the mean (DQMOM-IEM).

In this work the presence of the drug is neglected and the precipitation of PCL alone, for which many experiments are available, is modeled. Polymer particles formation is described through a Population Balance Model (PBM) solved with the Quadrature Method of Moments (QMOM). In a first part of the work

(Chap. 3) polymer particle nucleation is described with the Classical Nucleation Theory (CNT). Although the model results are in a decent agreement with experiments the presence of a number of fitting parameters, that have to change with the changing the operating conditions, highlights the inadequacy of the approach. Therefore an Augmented Nucleation Theory (ANT) is used in Chap. 4, whose parameters are derived by standard full-atom Molecular Dynamics (MD). In these simulations the interactions between simple PCL molecules with solvent and anti-solvent molecules is simulated. Eventually, the ANT is implemented with the CFD-PBM approach and results validated with experiments. However, in order to further study polymer particles nucleation a framework in which larger systems can be simulated is developed. This is based on an hybrid atomistic/coarse-grained model that is developed and tested on a simpler system (i.e., polymer melts) and results are reported in Chap. 5.

Chapter 2

Methodology

2.1 Statistical Introduction

Let us consider an event E, e.g. $E \equiv (U < V_a)$; the probability $p = P(E)$ associated with the event E is a real number ($0 \leq p \leq 1$) which measures the possibility that such an event occurs. In probability it is possible to define the cumulative distribution function (CDF) which describes the probability distribution of the random variable U:

$$V \rightarrow F_U(V) = P(U \leq V). \tag{2.1}$$

Each CDF is a monotonically increasing function with the following properties

$$\lim_{V \rightarrow -\infty} F(V) = 0, \qquad \lim_{V \rightarrow +\infty} F(V) = 1.$$

The derivative of the CDF with respect to variable V is equal to the Probability Density Function (PDF):

$$f(V) = \frac{dF(V)}{dV}. \tag{2.2}$$

From the proprieties of the CFD the proprieties of the PDF can be obtained. The PDF is non-negative ($f(V) \geq 0$), normalized

$$\left(\int_{-\infty}^{+\infty} f(V)\, dV = 1 \right)$$

and $f(-\infty) = f(+\infty) = 0$. The probability that the random variables U is contained in a given interval $V_a \leq U \leq V_b$ is equal to the integral of the PDF over the same interval:

$$P(V_a \leq U \leq V_b) = F(V_b) - F(V_a) = \int_{V_b}^{V_a} f(V)\, dV. \tag{2.3}$$

If we let the width of the interval to become infinitesimal Eq. (2.3) will results in:

$$P(V \leq U \leq V + dV) = F(V + dV) - F(V) = f(V)\, dV. \tag{2.4}$$

The PDF can be considered as the measure of the sample space of the variable V. We call expected value of a random variable U the weighted average of all possible values that U can take on:

$$\langle U \rangle = \int_{-\infty}^{+\infty} V f(V)\, dV, \tag{2.5}$$

it is important to highlight here that the expected value of a random variable is not a random variable. The fluctuation of a random variable is defined as the difference between the random variable and its average:

$$u = U - \langle U \rangle. \tag{2.6}$$

The variance of a random variable is defined as:

$$\langle u^2 \rangle \equiv \int_{+\infty}^{-\infty} (V - \langle U \rangle)^2 f(U)\, dV \tag{2.7}$$

and the standard deviation is the square root of the variance:

$$\sigma_U \equiv \sqrt{\langle u^2 \rangle}. \tag{2.8}$$

2.2 Molecular Dynamics

Usually the description of a physical system involves the knowledge of few variables which define the state of the system. In order to describe the motion of a particle in space, it is sufficient to know its position and velocity at some time t_0 which we call initial time. The coordinates which describe the configuration of

a system are called generalized coordinates, they are usually independent of one another and have the propriety to uniquely define all the possible configurations of the system considered. The minimum number of independent generalized coordinates that must be specified to completely define the configuration of the system is called the Degrees of Freedom (DOF) of the system. In the case of one single material particle one needs to know only the three coordinates of its position.

If we consider another system composed by a particle (A from now on) and another particle (B from now on) the coordinates of the particle A alone are no longer sufficient to describe the entire system. In fact, the movement of the system composed by the two particles can be decomposed in 6 different and independent movements. We can consider the translation of the position of the centre of mass of the body composed by the two particles, the rotation around the two axes perpendicular to the connection between the particles and the vibration of the particles along the connection, hence the total number of DOF will be six and we will need six different generalized coordinates to specify the position of our system. This can be extended to an arbitrary number of particles. If we consider a system composed by N particles we will need $3N$ coordinates to completely define their positions. Each generalized coordinate $\mathbf{q} = \{q_1, q_2, \ldots, q_{3N}\}$ can be associated to a generalized velocity $\dot{\mathbf{q}} = \{\dot{q}_1, \dot{q}_2, \ldots, \dot{q}_{3N}\}$ defined as follows:

$$\dot{\mathbf{q}} = \frac{\mathrm{d}\mathbf{q}}{\mathrm{d}t} \quad .$$

From the description of the force that acts on a system and from the Newton's laws it is possible to obtain a function which summarizes the dynamics of the system, the Lagrangian $\mathcal{L}(\mathbf{q}, \dot{\mathbf{q}}, t)$[1]. To obtain a complete and compact description it was found convenient to replace the velocities associated to the generalized coordinates with the so-called generalized momenta $\mathbf{p} = \{p_1, p_2, \ldots, p_{3N}\}$ and the Lagrangian function with another function called Hamiltonian, $\mathcal{H}(\mathbf{q}, \mathbf{p}, t)$ [2].

[1] The Lagrangian is defined as the difference between the potential energy of the system $V(\mathbf{q})$ which is always considered independent of time and the overall kinetic energy, defined as $T = \frac{1}{2}\dot{\mathbf{q}}\cdot\mathbf{p}$

[2] The expression "compact" does not imply "easy". Here it is intended that the Hamiltonian equations lead to an easier description than other approaches, and in most cases they can highlight some useful properties of the system without the need to explicitly solve the associated equations. For a complete discussion of the Hamiltonian equations cf. Arndold [1989].

These are defined as:

$$\mathbf{p} = \frac{\partial \mathcal{L}}{\partial \dot{\mathbf{q}}} \tag{2.9}$$

$$\mathcal{H}(\mathbf{q}, \mathbf{p}, t) = \dot{\mathbf{q}} \cdot \mathbf{p} - \mathcal{L}(\mathbf{q}, \dot{\mathbf{q}}, t). \tag{2.10}$$

where it is immediate to show that $\mathcal{H}$ represents the total (kinetic, $T(\mathbf{p})$, plus potential $V(\mathbf{q})$) energy of the system:

$$\mathcal{H}(\mathbf{q}, \mathbf{p}, t) = T(\mathbf{p}) + V(\mathbf{q})$$

and is constant in close conservative systems. Conservative systems are those in which the forces acting on the particles can be defined as the gradient of a potential:

$$\mathbf{F} = -\nabla V(\mathbf{q}) = -\frac{\partial V(\mathbf{q})}{\partial \mathbf{q}}.$$

It can be shown [Arndold, 1989] that the dynamics of the system can be completely described by a system of differential equations of first order of the generalized coordinates and momenta, by specifying an initial state of the system. This system of linear differential equations is called the Hamiltonian equations of motion:

$$\dot{\mathbf{p}} = -\frac{\partial \mathcal{H}}{\partial \mathbf{q}}, \tag{2.11}$$

$$\dot{\mathbf{q}} = \frac{\partial \mathcal{H}}{\partial \mathbf{p}}. \tag{2.12}$$

They represent a formalism very common in quantum mechanics and in molecular mechanics (especially in the absence of geometric constraints). A typical atomistic system contains a number of particles of the order of magnitude of the Avogadro number ($N_A = 6.023 \cdot 10^{23}$ mol^{-1}), hence the knowledge of the dynamic of such a system is dictated by the solution of a system of ordinary differential equations with $6N$ equations ($N \propto 10^{23}$) and with same number of initial conditions of the particles in the system.

The $6N$ set of Eq. (2.11) and Eq. (2.12) can be immediately solved once the potential energy of the system is defined. The potential energy is typically defined

as the summation of pair-wise interactions, resulting in the following expression:

$$V(\mathbf{q}) = \frac{1}{2}\sum_{i}\sum_{j\neq i} V_{ij}(\mathbf{q_i}, \mathbf{q_j}). \tag{2.13}$$

Typical pair-wise potential are the harmonic potential, the Morse potential, the Buckingam potential, the Lennard-Jones potential and the Coulomb potential. In the next section, details on how these potentials can be used to describe bonded and non-bonded interactions among atoms will be given.

Due to this intrinsic difficulty in solving this kind of problem, at the end of 19*th* century Boltzmann and Gibbs proposed to use the tool of statistical analysis to describe the systems with huge number of DOF. The first development of this theory introduced the concept of ensemble. An ensemble is a collection of realizations of the same system in different molecular configurations (e.g. different value of the positions and momenta of the atoms) to each of which corresponds the same value of a defined set of macroscopic thermodynamic variables (e.g., pressure, temperature, internal energy, volume) in the phase space[3]. In fact, it is assumed that the measure of a macroscopic quantity is the time averages of microscopic quantities. Let F a macroscopic quantity which depends from f, its microscopic counterpart. Then we can write:

$$\bar{F} = \lim_{T\to+\infty} \frac{1}{T}\int_{t_0}^{t_0+T} f(\mathbf{q}(t), \mathbf{p}(t))\mathrm{d}t. \tag{2.14}$$

The main problem arises from the fact that to integrate the previous equation one must know the evolution of the quantity f and hence it will be necessary to solve the equation of motion, a task impossible to perform [4]. However in the ergodic systems the following hypothesis holds: the average of some quantities performed on the ensemble are equal to the evolution of the reference system

[3]The phase space is a $6N$ dimensional Euclidean space in which the $6N$ orthogonal axes represent the generalized coordinates and the generalized momenta.

[4]This impossibility is not only due to the high number of the DOFs of the order of the Avogadro number, but even if an integration of the Hamiltonian system would be possible the resolution of the equations of motion require to perfectly know the configuration of the system at a certain time t_0. Therefore, one must to specify $6N$ initial conditions for the system considered. This configuration is generally unknown.

with time. By defining the ensemble average as

$$\langle F \rangle = \int_{\Gamma} \rho_d(\mathbf{q}, \mathbf{p}) f(\mathbf{q}, \mathbf{p}) \mathrm{d}\mathbf{q}\mathrm{d}\mathbf{p} \tag{2.15}$$

where $\rho_d(\mathbf{q}, \mathbf{p})$ is a probability density function in the phase space and Γ is a volume of the accessible states, or rather the regions in the phase space that represent the configurations of the system. The ergodic hypothesis states that:

$$\langle F \rangle = \bar{F}. \tag{2.16}$$

The ergodic hypothesis is the fundamental of statistical mechanics because allows to calculate all the thermodynamic quantities by solving a definite integral instead of the Hamiltonian equation of motion. The next step in the developing of the theory is then to specify $\rho_d(\mathbf{q}, \mathbf{p})$, the probability density function in the phase space. As it was already said, the distribution is based on the concept of ensemble, a big collection of replica of the same system in different configuration but with the characteristics that each replica leads to the same thermodynamic state. There are different ensembles considered in statistical mechanics:

- Microcanonical Ensemble (N, V, E) where the number of atoms (N), the volume of the container (V) and the energy E are kept fixed. This is a representation for isolated system, that is a system which does not exchange energy and matter with the external environment.

- Canonical Ensemble (N, V, T) where the number of atoms, the volume of the container (V) and the temperature T are kept fixed. It can be represented by a room isolated with a thermostat to regulate the temperature.

- Grand Canonical Ensemble (μ, V, T) where the chemical potential (μ), the volume of the container and the temperature T are kept fixed. In this system both exchange of matter and energy are allowed.

- Isothermal-Isobaric Ensemble (N, P, T) where the number of atoms, the pressure of the container (P) and the temperature T are kept fixed. This system has the number of atoms constant, but the volume is allowed to change to keep the pressure fixed.

Each distribution is characterized by a partition function specific for each ensemble. The partition functions are used to obtain the macroscopic thermodynamic quantities of the system, hence are of fundamental interests in statistical mechanics. The different distributions and the different partition functions obtained for the various ensembles are summarized in Table 2.1.

Ensemble	Distribution $\rho_d(\mathbf{q},\mathbf{p})$	Partition Function
N,V,E	$\frac{\delta(\mathcal{H}(\mathbf{q},\mathbf{p})-E)}{\Omega(N,V,E)}$	$\Omega(N,V,E) = \int_\Gamma \mathrm{d}\mathbf{q}\mathrm{d}\mathbf{p}$
N,V,T	$\frac{1}{h^{3N}N!}\frac{e^{-\frac{\mathcal{H}}{k_BT}}}{Z(N,V,T)}$	$Z(N,V,T) = \frac{1}{h^{3N}N!}\int_\Gamma e^{-\frac{\mathcal{H}}{k_BT}}\mathrm{d}\mathbf{q}\mathrm{d}\mathbf{p}$
μ,V,T	$\frac{1}{h^{3N}N!}\frac{e^{-\frac{(\mathcal{H}-N\mu)}{k_BT}}}{\Xi(\mu,V,T)}$	$\Xi(\mu,V,T) = \frac{1}{h^{3N}N!}\sum_{N=0}^{+\infty} e^{\frac{N\mu}{k_BT}}\int_\Gamma e^{-\frac{(\mathcal{H}-N\mu)}{k_BT}}\mathrm{d}\mathbf{q}\mathrm{d}\mathbf{p}$
N,P,T	$\frac{1}{h^{3N}N!}\frac{e^{-\frac{(\mathcal{H}-pV)}{k_BT}}}{Q(N,P,T)}$	$Q(\mu,V,T) = \frac{1}{h^{3N}N!}\int_0^{+\infty} e^{\frac{pV}{k_BT}}\mathrm{d}V\int_\Gamma e^{-\frac{(\mathcal{H}-pV)}{k_BT}}\mathrm{d}\mathbf{q}\mathrm{d}\mathbf{p}$

Table 2.1: Distribution and partition functions in the various ensembles. $\delta(\mathcal{H}(\mathbf{q},\mathbf{p})-E)$ is the Dirac function centered on E, h and k_B are the Planck and Boltzmann constant respectively

One important propriety of the various ensemble is based on the concept of thermodynamic limit. The thermodynamic limit can be expressed as

$$\lim_{N,V\to+\infty}\frac{N}{V} = l \tag{2.17}$$

with l some finite quantity. It represents the limit in which the dimension of the system approaches the macroscopic dimension. In the thermodynamic limit all the ensembles are equivalent, or rather all the thermodynamics observables predicted are equals. This limit is a consequences of the central limit theorem of statistics. In fact, in the thermodynamic limit all the fluctuations of the propriety are averaged out and the value of the observables tend to their average value which should of course be equal for all the ensembles to their measured value. In MD simulations we obtain a trajectory, or rather the motion of the N-atoms system over a certain period of time. The way to obtain this trajectory is to integrate the Newton's equation of motion for each atom by specifying the interactions which occur between atoms. Hence, MD simulation technique is based on the concept of force-field in a way that will be specified later.

2.2.1 Computer Simulation

Since the early developments of computer science a lot of attention was addressed to the solution of the N-body problem which led in the seventies of 20th century to the development of the molecular dynamics (MD). Molecular dynamics consists in solving numerically the equation of motion for a system composed by a certain number of atoms to obtain the so-called trajectory of the system. The results of MD is then a sample of the phase space from which the thermodynamics quantity can be calculated by using the Eq. (2.14). In a typical MD simulation the total linear momentum $\mathbf{p}$ and the energy E are constant of motion. Thus, a MD simulation considers an ensemble very similar to the microcanonical ensemble. As already discussed in the previous section, there is no difference from one ensemble to another in terms of results of the observables. Though, this condition is valid in the thermodynamic limit only. A typical MD simulation consider only tens of thousands or hundred of thousands atoms[5], hence is far away to the thermodynamic limit and the results for the observables, especially those strongly dependent from the fluctuation of the microscopic propriety of the system, can vary significantly from one ensemble to another. Thus the ensemble in which the simulation will be carried out must be chosen very carefully in dependence of the characteristics of the system

- (N, V, E) ensemble is the easiest to implement and it is often used to check the results of an algorithm. Anyway, a real experiments is carried out at atmospheric pressure (constant p) or controlled temperature (constant T) hence the isothermal isobaric ensemble is preferable
- (N, V, T) ensemble is the most used because has a good compromise between ease of implementation and similarity with real conditions of an experiment
- (N, P, T) ensemble is the closest to real systems
- (μ, V, T) ensemble has the propriety of variable number of atoms, thus is used to simulate phase transitions.

[5]The largest system simulated reaches $\approx 10^{10}$ atoms. However, this kind of simulations are very rare because they need the biggest existing cluster.

In order to perform simulation in an ensemble different from the microcanonical we must keep the characteristic parameters (volume, pressure, temperature) at the desired value. Hence a number of models were developed to maintain constant pressure and temperature of the system during the simulation and the most important will be revised in the next sections.

2.2.1.1 Force Field

Each atom in a molecule and each molecule in a system experiences a lot of interactions between the other atoms in the system. All these interaction are taken into account by using a force-field, which specify the potential field in which each atom is immersed and is responsible for the force that each atom experiences. Hence, force field is a mathematical function which returns the energy of the system as a function of its conformation. There are different kinds of interactions but they all can be divided in two big categories: bonded and non-bonded interactions. Bonded interaction are responsible for the interactions of atoms inside the same molecules and they can be divided in

- Bonds. Each atoms can be connected to other atoms. The atomic bonds is modelled by using an harmonic potential

$$V_b(\boldsymbol{r}) = \sum_{i=1}^{N_b} k_{r_i}(\boldsymbol{r}_i - \boldsymbol{r}_{0_i})^2 \tag{2.18}$$

  where $\boldsymbol{r}_{0_i}$ and k_{r_i} are the equilibrium distance and the energetic constant respectively for the generic couple of atoms (j, k) and N_b is the total number of bonds in the system. This situation is presented in Fig. 2.1.

- Angles. A group of three atoms connected by bonds form an angle which is responsible for the orientation of the molecule. The angle potential is modelled through an harmonic potential

$$V_a(\theta) = \sum_{i=1}^{N_a} k_{\theta_i}(\theta_i - \theta_{0_i})^2 \tag{2.19}$$

  where θ_{0_i} and k_{θ_i} are the equilibrium distance and the energetic constant respectively for the generic triplet of atoms (j, k, l) and N_a is the total number

of angles in the system. This situation is presented in Fig. 2.2.

- Dihedrals. A group of four atoms connected by bonds form an angle which is responsible for the orientation of the molecule. The functional form most used is the series of cosines

$$V_d(\phi) = \sum_{i=1}^{N_d} \sum_{h} V_{i_h} \cos(h\phi_i) \tag{2.20}$$

where ϕ_{0_i} is the equilibrium dihedral angle for the generic triplet of atoms (j, k, l, m) and N_d is the total number of dihedral angles in the system. This situation is presented in Fig. 2.3.

- Improper dihedrals. If a molecule must assume a definite shape (e.g. they are used to keep the ring of a benzene molecules planar), a dihedral (which is called "improper") is defined between four atoms. Their functional form is an harmonic potential

$$V_i(\kappa) = \sum_{i=1}^{N_i} k_{\kappa_i}(\kappa_i - \kappa_{0_i})^2 \tag{2.21}$$

where κ_{0_i} and k_{κ_i} are the equilibrium distance and the energetic constant respectively for the generic group of atoms (j, k, l, m) and N_i is the total number of angles in the system.

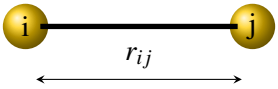

Figure 2.1: Representation of a bond between atom i and j

Non-bonded interactions are used to consider interactions between atoms which usually[6] do not belong to the same molecule. They can be divided into two categories:

- Dispersion forces interaction. These interactions are called short range interactions because they decade as r_{ij}^{-6} where r_{ij} is the distance between

[6] If the molecule is particularly long as a polymer chain the non-bonded interactions can be considered between atoms inside the same chain also.

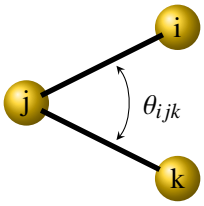

Figure 2.2: Representation of an angle between atom i, j, and k

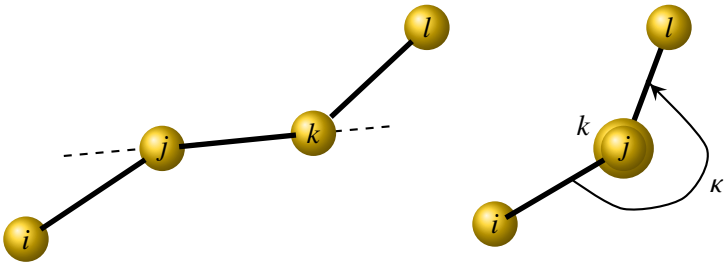

Figure 2.3: Representation of a torsion angle between atom i, j, k and l

the two atoms. Because of their fast decay with the distance they can be calculated explicitly by counting all the interaction pairs in the system. Actually, a number of algorithms (e.g. Neighbour List algorithm. A complete description can be found in Allen and Tildesley [1987]) were developed to avoid the waste of computational time by considering only the pairs which are close enough to experience an interaction due to the Van der Waals potential. One of the most used functional forms for the non-bonded interactions is the (LJ) Lennard-Jones potential

$$V^{LJ}_{nonbonded}(r) = \sum_{i=1}^{Np_{LJ}} 4\epsilon_{i_{LJ}} \left(\left(\frac{\sigma_i}{r_i} \right)^{12} - \left(\frac{\sigma_i}{r_i} \right)^{6} \right) \tag{2.22}$$

where r_i is the distance between a pair of atoms, Np_{LJ} is the number of pairs in the system, ϵ_{LJ} and σ are two constants defining this kind of potential

- Electrostatic interactions. These interactions are called long range interactions because in these case they decay as $\propto r_{ij}^{-1}$. To consider the electrostat-

ics interactions is much more difficult respect to the LJ potential because their long range nature. An explicit treatment is not feasible except for the smallest systems without periodic boundary conditions[7]. Thus, a number of models to consider these interactions without the need to perform the explicit sum were proposed [Steinhauser, 1982; Hockney and Eastwood, 1988; Smith and Van Gunsteren, 1995; Darden et al., 1995; Rokhlin, 1987]. In general these methods consider an explicit sum for atoms at distances equal to those used in the LJ potential, the result is then corrected to take into accounts for atoms at long distance

$$V^{El}_{nonbonded}(r) = \sum_{i=1}^{Np_{el}} \frac{1}{4\pi\epsilon_0\epsilon} \frac{q_{1_i} q_{2_i}}{r_i}, \tag{2.23}$$

where r_i is the distance between a pair of atoms, Np_{el} is the number of pairs in the system, ϵ and ϵ_0 are the dielectric constant in a medium and in the vacuum and q_{1_i} and q_{2_i} are the charge on the first and second atom respectively.

2.2.2 Ergodicity in MD simulations

In order to obtain the macroscopic properties of a system from a MD simulation we must make sure to sample the phase space sufficiently. As it was said in the first part of this chapter any measurable quantity F can be interpreted in term of some function $f(\mathbf{q}, \mathbf{p})$ that depends on the position of the phase point in the phase space. When a measure of some kind (e.g, pressure or temperature) is performed on a system, we do not obtain an instantaneous value of the property, since the measure take a certain interval T to be done, usually much greater than the characteristic time of motion of atoms. Therefore, what is obtained is an average value of the property:

$$F_m = \frac{1}{T} \int_{t_0}^{t_0+T} f(\mathbf{q}(\tau), \mathbf{p}(\tau)) \mathrm{d}\tau \tag{2.24}$$

But with F_m we can identify the average over the trajectory obtained with the MD also. In this case the equations of motion are integrated numerically over M time

[7] Cf. Allen and Tildesley [1987]; Haile [1992].

steps (in this case the time interval T will be $T = M\Delta t$ with Δt the single time step) and the integral is replaced by a summation over the time steps

$$F_m = \frac{1}{M} \sum_{k=1}^{M} f(\mathbf{q}(k\Delta t), \mathbf{p}(k\Delta t)) \tag{2.25}$$

For a system at the equilibrium we can consider the average independent from t_0 and that for a sufficiently small value of Δt and sufficiently large value of M the average F_m is equal to $\bar{F}$, the average over an infinite period of time (given in Eq. (2.14)). If we consider the system ergodic then Eq. (2.16) holds and the average over a small[8] Δt is equal to the ensemble average. The ergodic hypothesis is crucial in MD simulations because some important thermodynamic quantities can not be expressed (or can be expressed in a very difficult form) as time averages over the time trajectory in the phase space but are function of the phase-space volume. Thermodynamic properties of a system can be divided in three main categories depending on how they are computed. The difficulty in computing these quantityies increases by going from the first type to the third:

1. Function of the Hamiltonian (structural properties, simple thermodynamic function as internal energy or temperature)

2. Thermodynamic response functions (adiabatic compressibility, constant volume heat capacity)

3. Function on the phase-space volume (entropy and Gibbs, Helmholtz free energy)

The equality $F_m = \bar{F}$ is much more correct as the value of M increases. The latter equality represents the most crucial point, since all the calculations of the measurable macroscopic quantities are based on this one. The problem with this definition is that in principle we should consider a trajectory over an infinite time to have a correct sample, but it is not feasible in practice, hence results of simulations in terms of time averages are more accurate with the increase of the simulated time. In order to overcome the problem of having a sufficient sample of the phase space with the need to simulate systems as much closer to a real system as possible (e.g. a polymer of high molecular weight) a number of methods

[8] Small compared to an infinite time interval

which reduce the DOF of the system has been developed. These methods will be treated in detail in Chap. 5 but they can be divided essentially in methods which retain only a part of the fully atomistic system and eliminate the rest (as the implicit solvent method in which the solvent is not treated explicitly but additional interactions are added in the force field and united-atoms methods for organic molecules in which the lightest atoms as hydrogen are coupled with their bonded carbon), and coarse-grained methods. In these latter methods a certain number of atoms are grouped together into a super-atom called "bead". These methods allow a speed-up in the simulation at the cost of losing some information about the system.

2.2.2.1 Function of the Hamiltonian

The internal energy E for an isolated system is just the Hamiltonian

$$E = \mathcal{H}(\mathbf{q}, \mathbf{p}) = const. \tag{2.26}$$

and is constant in conservative systems. It can be divided into two contribution, a kinetic part E_k and a configurational part $\mathcal{U}$ as $E = E_k + \mathcal{U}$. The kinetic part of the energy can be used to compute the temperature of the system

$$\langle E_k \rangle = \frac{3}{2} N k_B \langle T \rangle = \frac{1}{M} \sum_{k=1}^{M} \sum_{i=1}^{N} \frac{1}{m_i} \mathbf{p}(k\Delta t) \cdot \mathbf{p}(k\Delta t) \tag{2.27}$$

where m_i is the mass of the $i-$th atom and N is the total number of atoms in the system. The configurational part of the energy of the system is related to the pressure P through the virial expansion,

$$\frac{\langle P_{md} \rangle}{\rho k_B \langle T \rangle} = 1 - \frac{1}{3MNk_B\langle T \rangle} \sum_{k=1}^{N} \sum_{\alpha} \sum_{i=1}^{N-1} \sum_{j=i+1}^{N} |\boldsymbol{r}_{ij}(k\Delta t) - \boldsymbol{\alpha} L| \frac{\mathrm{d}u(|\boldsymbol{r}_{ij}(k\Delta t) - \boldsymbol{\alpha} L|)}{\mathrm{d}\boldsymbol{r}_{ij}} \tag{2.28}$$

where $u(r_{ij})$ is the two-body potential, $\boldsymbol{\alpha}$ is the edge of the computational box and this is the expression for the pressure which consider the Periodic Boundary Condition (PBC)[9] for the system. The subscript in P_{md} means that is the pressure obtained from the simulations, and it must be correct by another term (namely

[9] See Allen and Tildesley [1987]; Haile [1992] for a definition of the PBC

P_{LR}, hence $P = P_{md} + P_{LR}$) if the two-body potential used is a truncated potential. This calculation of the pressure is used in (N, P, T) simulation to be sure to sample the correct points in the phase space (i.e., having the correct pressure during the simulation).

2.2.2.2 Thermodynamic response functions

The response functions in a thermodynamic system measure the response of the system to a change in some macroscopic quantities. Thus, they are expressed as derivatives of some macroscopic properties of the system. The most considered in MD simulations are the isometric heat capacity C_v, the adiabatic compressibility κ_s and thermal pressure coefficient defined as follows:

$$
\begin{aligned}
C_v &= \left(\frac{\partial E}{\partial T}\right)_V, \\
\kappa_s &= -\frac{1}{V}\left(\frac{\partial V}{\partial P}\right)_S, \\
\gamma_v &= \left(\frac{\partial P}{\partial T}\right)_V.
\end{aligned}
$$

One way to obtain these quantities is to calculate the functional dependence of the two variables involved by using a number of simulations and then calculate the derivatives analytically (if the points obtained are interpolated with some function) or numerically. The main problems with this approach is that one needs more than one simulation to obtain a reliable description of this functional dependence. For the adiabatic compressibility κ_s there is another issue which involves the definition of a simulation of constant entropy. Therefore, it is preferred to evaluate the derivative analytically via statistical mechanics because with this approach only a simulation is needed. It was shown by Lebowitz et al. [1967] how the fluctuation in the canonical ensemble are related to those in a molecular dynamics isolated system and they obtained for an isolated system containing spherical molecules:

$$
C_v^{*^R} = \frac{\left\langle (\delta \mathcal{U}^*)^2 \right\rangle}{NT^{*^2} - \frac{2}{3}\left\langle (\delta \mathcal{U}^*)^2 \right\rangle} \tag{2.29}
$$

where C_v^R means that the ideal part contribution to the isometric heat capacity is

removed (i.e. $C_v = C_v^R - 2/3$). For the adiabatic compressibility and the thermal pressure coefficient it was obtained (cf. Haile [1992] for a complete derivation):

$$\kappa_s = \left(\frac{2}{3}P + \rho k_B T + \langle\theta\rangle - \frac{N}{\rho k_B T}\langle(\delta P)^2\rangle\right) \tag{2.30}$$

$$\gamma_v^* = \frac{2}{3}\left(\rho^* - \frac{1}{T^{*^2}}\langle\delta E_k^*\delta P^*\rangle\right) \tag{2.31}$$

where the star means that we are considering reduced unit[10] and θ is equal to

$$\theta = \frac{1}{9V}\sum_{i<j} r_{ij}\frac{\partial^2 u(r_{ij})}{\partial r_{ij}^2} \tag{2.32}$$

These are the most important quantities to calculate, because all the other thermodynamic response functions (e.g. isobaric heat capacity, volume expansivity, sonic velocity, isothermal compressibility) can be obtained by these with the law of the classic thermodynamics.

2.2.2.3 Entropic properties

Determination of entropy (S), Gibbs energy (G), Helmholtz energy (A) and chemical potential (μ) is one of the most difficult problem in MD simulations. This difficulty arises from the fact that this quantities are not defined as the time averages of some function along the trajectory but they are function of the volume of the accessible phase space for the system:

$$\begin{aligned} S &= k_B \ln \Omega(N, V, E) \\ G &= -k_B T \ln Z(N, P, T) \\ A &= -k_B T \ln Q(N, V, T) \\ \mu &= \frac{G}{N} \end{aligned}$$

[10] Reduced units are widely used in MD and consist in multiply the variables with some constants to make them dimensionless

The way to obtain these quantities starts from considering that in an isolated system the following equation holds:

$$\mathrm{d}S = \frac{\mathrm{d}E}{T} + \frac{P}{T}\mathrm{d}V - \frac{\mu}{T}\mathrm{d}N \tag{2.33}$$

By determining the temperature, pressure or density dependence of energy, volume or number of particles keeping the other two constants, by performing a set of simulations it is possible to integrate the appropriate thermodynamic relation and obtaining the entropic properties. If we perform a set of simulations at constant volume and number of molecules and at different temperatures it is possible to obtain the dependence of energy from the temperature and by the integration we obtain the value of S [11]

$$S(E_2) - S(E_1) = \int_{E_1}^{E_2} \frac{\mathrm{d}E}{T}$$

The simulation with a variable number of molecules can be used to obtain the entropic properties with the test particle method and the coupling parameter method[12].

2.3 Mesoscale model: Boltzmann Equation

The information obtained at the molecular level is very useful, but the computational costs associated do not allow for the simulation of a system at large scales (e.g., chemical reactor scale).

As already mentioned coarse-graining allows one to simulate large systems but the simulation of large-scale system requires the use of meso-scale and macro-scale models. Since macro-scale models are directly calculated from meso-scale models let us renew meso-scale models first.

Knowledge of the position $\mathbf{q}$, and momentum $\mathbf{p}$ of the N particles, allows one to calculate the Number Density Function (NDF), $f(t, \mathbf{x}, \mathrm{v})$, usually written in Eulerian (i.e. non-generalized Lagrangian coordinates) with the following meaning: $f(t, \mathbf{x}, \mathrm{v})\mathrm{dvd}\mathbf{x}$ represents the expected number of particles in a position comprised

[11] Strictly speaking we do not obtain an absolute value of the entropy, but a difference between two different states of the system.

[12] Cf. Haile [1992] for an extensive description of these methods

between $\mathbf{x}$ and $\mathbf{x} + \mathrm{d}\mathbf{x}$ and velocity between v and v + dv. The NDF can be easily calculated from MD simulations, by building an histogram of the velocity distribution in the three spatial directions. The main idea of meso-scale models, based on the NDF, is to calculate the NDF directly without describing the details of each single atom/molecule. Therefore, instead of solving the equations of motion of N atoms/molecules, one simple equation describing the evolution of the NDF is solved. This equation is the so-called Boltzmann Equation (BE) and reads as follows:

$$\frac{\partial f}{\partial t} + v_j \frac{\partial f}{\partial x_j} + \frac{A_j}{m} \frac{\partial f}{\partial v_j} = C(f, g) \tag{2.34}$$

where $\mathbf{A}(\mathbf{x}, \mathrm{v}, t) = (A_1, \ldots, A_n)$ is the external force field acting on each atom/molecule, m is the mass of the atom/molecule and C is the term which gives the rate of change of f due to atom/molecule interactions. We know from MD that these interactions are governed by force field and their corresponding potential. Altough, theoretically every type of interaction can be included, most of the developments refer to the simplest potential: the hard sphere potential. With this potential molecules do not see each other until they "collide":

$$V(\boldsymbol{r}) = \begin{cases} 0 & if\ |\boldsymbol{r}| > b \\ +\infty & if\ |\boldsymbol{r}| \leq b \end{cases}$$

where b is the so-called molecular diameter. As we will see, this description defines a collisional term and a collision kernel that can eventually be extended also to other potential. The interaction term reads as follows:

$$C(f, g) = \frac{1}{2} \int_{\mathbb{R} \times S^{n-1}} q(\upsilon, \theta)(f' g'_\star + f'_\star g' - f g_\star - f_\star g) \mathrm{dv}_\star \mathrm{d}\theta \tag{2.35}$$

and is often referred to as "collisional" integral (since with the hard sphere potential molecules collide), where

$$f' = f(t, \mathbf{x}, \mathrm{v}'), \quad f'_\star = f(t, \mathbf{x}, \mathrm{v}'_\star), \quad f_\star = f(t, \mathbf{x}, \mathrm{v}_\star)$$

and similarly for g. v, v', $\mathrm{v}_\star$, $\mathrm{v}'_\star$ are the velocities of the pair of colliding particles before and after the collisions obtained by considering the conservation

of linear momentum (Eq. (2.36)), energy (Eq. (2.37)):

$$\mathrm{v} + \mathrm{v}_\star = \mathrm{v}' + \mathrm{v}'_* \tag{2.36}$$

$$|\mathrm{v}|^2 + |\mathrm{v}_\star|^2 = |\mathrm{v}'|^2 + |\mathrm{v}'|^2 \tag{2.37}$$

and of angular momentum from which one obtains

$$\mathrm{v}' = \mathrm{v} - ((\mathrm{v} - \mathrm{v}_\star) \cdot \omega)\omega \tag{2.38}$$

$$\mathrm{v}'_\star = \mathrm{v}_\star + ((\mathrm{v} - \mathrm{v}_*) \cdot \omega)\omega \tag{2.39}$$

where $\omega \in S^{n-1}$

$$\upsilon = |\mathrm{v} - \mathrm{v}_\star| \tag{2.40}$$

$$\cos\theta = \frac{1}{\upsilon}(\mathrm{v} - \mathrm{v}_\star) \cdot \omega \tag{2.41}$$

as geometrically represented in Fig. 2.4. These equations are valid for conservative systems where interaction do not dissipate energy[13]. Moreover, as in MD interactions are considered pair-wise addictive, or in other words, the collision integral operates on binary-collisions[14]. The function $q(\upsilon, \theta)$ is the collision kernel which is determined by the interaction potential between two colliding particles. In the case of the hard sphere potential the kernel is simply equal to

$$q(\upsilon, \theta) = C\upsilon \quad \text{with } C > 0 \ ,$$

whereas in the case of other potential it assumes different forms[15].

In order to derive such equations we need to define the concept of local equilibrium. Local equilibrium is represented by a local distribution function f^e such

[13] To describe dissipative systems an elastic coefficient is generally introduced

[14] Eq. (2.35) is derived also by using additional simplifications often labelled *Stosszahlansatz*. Among them the most important is that the porbability of having a collision, or in other words of having a molecule in $\mathbf{x}$ with relative velocity v' and another one at a distance equal to the molecular diameter with velocity v, is equal to the product of $f(t, \mathbf{x}, \mathrm{v})$ and $f(t, \mathbf{x}, \mathrm{v}')$.

[15] In the case of other potentials, interactions among molecules are not collisions, but can be treated as collisions by defining the instant of collision as instant of minimum distance between molecules and v, v' and $\mathrm{v}_\star$, $\mathrm{v}'_\star$ as the velocities of the molecules at sufficiently long time interval before and after the collision.

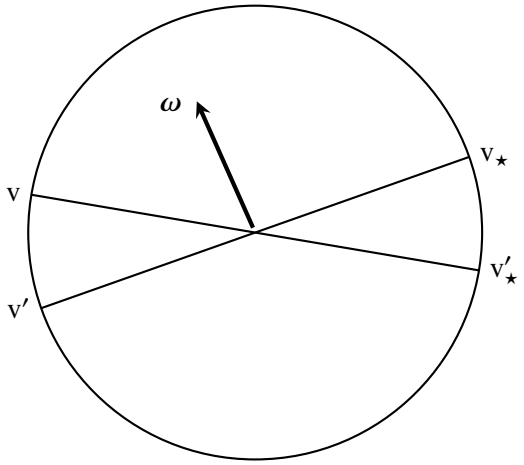

Figure 2.4: The geometry of collision in the center of mass reference frame

that the gain and the lose are balanced, hence the collision term becomes zero:

$$C(f^e, g^e) = 0$$

From this equation one obtains the detailed balance condition:

$$f'g' = fg \tag{2.42}$$

which becomes, by taking the logarithm:

$$\ln f' + \ln g' = \ln f + \ln g \tag{2.43}$$

that is, the distribution function is collision invariant, it does not change under the effect of collisions. Therefore, at the equilibrium $\ln f$ must be function of the quantity invariants in the collisions: number, momentum, energy:

$$\ln f = \alpha + \beta_i v_i + \frac{1}{2}\eta|\mathrm{v}|^2 \tag{2.44}$$

where $\alpha,\ \beta_i,\ \eta$ are five Lagrange multipliers which relates the distribution function to five hydrodynamic fields: density, momentum and energy. Hence, this multipliers are computed by imposing for the moment of the distribution func-

tion:

$$
\begin{aligned}
m \int_{\mathbb{R}^3_{\mathrm{v}}} f(\mathrm{v})\mathrm{dv} &= \rho(t, \mathbf{x}) \\
m \int_{\mathbb{R}^3_{\mathrm{v}}} v_\alpha f \mathrm{dv} &= \rho(t, \mathbf{x}) U_\alpha(t, \mathbf{x}), \quad \alpha = 1, 2, 3 \\
m \int_{\mathbb{R}^3_{\mathrm{v}}} \frac{1}{2} |\mathrm{v}|^2 f \mathrm{dv} &= \rho(t, \mathbf{x}) e(t, \mathbf{x})
\end{aligned}
$$

where ρ is the fluid density, U_α is the macroscopic flow component velocity in the α direction and ρe the energy density. From the previous equations one obtains[16] that exist one and only one equilibrium distribution and this is the Maxwellian distribution:

$$
f^e = \mathcal{M}_{(\rho,u,\theta)}(\mathrm{v}) \equiv \frac{\rho}{(2\pi\theta^2)^{\frac{3}{2}}} \exp\left(\frac{\left|\boldsymbol{v} - \boldsymbol{U}\right|^2}{2\theta^2} \right) \tag{2.45}
$$

where $\left|\boldsymbol{v} - \boldsymbol{U}\right|$ is the magnitude of the so-called peculiar speed which represents the relative speed of the molecules with respect to the fluid. The quantity

$$
\theta = \sqrt{\frac{k_B T}{m}}
$$

is the thermal speed associated with the fluid temperature T. It is interesting to observe that this distribution is exactly the ensemble distribution function of Table 2.1 for the (N, V, T) ensemble in the case of Hamiltonian equal to the kinetic energy only (as in the case of the hard sphere potential).

2.3.1 Length scale

The approach to equilibrium is controlled by the following time-scales [Succi, 2001]:

- $\tau_{int} \approx {}^{b}/_{v}$: duration of collisional event
- $\tau_\mu \approx {}^{\lambda}/_{v}$: mean flight-time between two successive collisions

[16] This is a (non-rigorous) sketch of the proof of the famous H-theorem due to Boltzmann, see App. A for a more detailed discussion

- $\tau_h \approx \min[L/u, l_M^2/\nu]$: minimum hydrodynamic (convective, diffusive) time-scale

where b is the molecule diameter, λ is the mean-free path and L is a typical length at macroscopic scale. These three time-scales give a rough estimates of the relaxation time: to obtain the particle distribution function from the many-body distribution function ($f_{(1,2,\dots,N)} \rightarrow f_1$ (τ_{int}) which is relatively fast, especially for very dilute system), to obtain the equilibrium distribution from the starting distribution (τ_μ) $f_1 \rightarrow \mathcal{M}(v; u, T)$ and to obtain from the local equilibrium distribution function with space-time dependent flow speed and temperature to a global Maxwellian with constant speed and temperature $\mathcal{M}(v; u, T) \rightarrow \mathcal{M}(v; u, T)$.

2.3.2 Solution of the Boltzmann equation

Because of the high non-linearities in the BE (e.g. the collision term) it is very difficult to find a solution of this equation in more realistic situations far from equilibrium. One of the most used techniques is the perturbation theory: we choose a parameter ϵ and we expand the distribution function f in series of powers of ϵ:

$$f = \sum_{n=0}^{\infty} \epsilon^n f_n \tag{2.46}$$

This technique is called perturbation theory because we assume that the value of f_0 is the equilibrium value (i.e. the Maxwellian distribution). Hence, the remaining part of the power expansion can be seen as a perturbation from the equilibrium. The resulting solution in general is not convergent to the exact solution of the BE [Cercignani, 1988] but is only asymptotic to a solution of the BE at the decrease of the value of ϵ. In one of the most used expansions ϵ is the ratio between the mean-free path of the particles λ and a macroscopic dimension of the system L, or in other words the Knudsen number $K_n = \lambda/L$. If we consider the adimensional BE:

$$\frac{\partial f}{\partial t} + v_j \frac{\partial f}{\partial x_j} = \frac{1}{\epsilon} C(f, g) \tag{2.47}$$

and we substitute the power expansion we obtain

$$\sum_{n=1}^{\infty} \epsilon^n \left(\frac{\partial f_{n-1}}{\partial t} + v_j \frac{\partial f_{n-1}}{\partial x_j} \right) = \sum_{n=0}^{\infty} \epsilon^n C_n \tag{2.48}$$

In the Chapman-Enskog procedure the power series is truncated to the first term

$$f \approx f_0 + \epsilon f_1$$

Accordingly, it is possible to show by using the H-theorem and taking the moment of the distribution function f that two conservation equations involving only macroscopic quantities can be written. These are the continuity equation,

$$\nabla \cdot (\rho \mathbf{U}) = \mathbf{0}, \tag{2.49}$$

and the momentum balance equation:

$$\frac{\partial \rho \mathbf{U}}{\partial t} + \nabla \rho \mathbf{U}\mathbf{U} = -\nabla \rho + \nabla \underline{\Sigma} + \mathbf{f} \tag{2.50}$$

where ρ is the density of the fluid, $\boldsymbol{f}$ are the external forces acting on the fluid and $\underline{\Sigma}$ is the so-called viscous stress tensor. In the case of constant density, negligible external force acting on the fluid and Newtonian fluid the famous Navier-Stokes equation is obtained:

$$\frac{\partial U_i}{\partial t} + U_j \frac{\partial U_i}{\partial x_j} = \frac{\partial}{\partial x_j}\left(\nu \frac{\partial U_i}{\partial x_j}\right) - \frac{1}{\rho}\frac{\partial p}{\partial x_j} \tag{2.51}$$

where $U_i \quad i = 1, 2, 3$ is the i-th component of the velocity vector, ν is the kinematic viscosity, p the pressure and where the Einstein summation convention for the index (i.e., repeated indices imply summation) is used.

The rigorous derivation is very difficult and is beyond the scope of this work and is extensively treated elsewhere. The purpose of this section is only to show how from the atomistic description it is possible to go with continuity to a macroscopic description. In fact, the basic hypothesis which allows to move from the mesoscopic description obtained through the NDF to a macroscopic description in terms of velocity and density (which turn out to be averages of instantaneous velocities and positions of molecules) is the scale at which the problem is considered, quantified by the Knudsen number.

The description of the properties of a fluid are based on the fundamental continuum hypothesis that can be resumed as: *all the macroscopic proprieties of the fluid (i.e. pressure, density, temperature, velocity) are always considered well-defined also in the limit of the dimension of the control volume that tends to*

zero. Practically, we are treating our system not considering its atomistic nature and approximating it as one continuum field. This hypothesis mathematically allows and justifies the operation of spatial derivation of the macroscopic quantity of the fluid. Hence, if we consider its point-wise density $\rho(\mathbf{x}, t)$ we can think meaningfully that at point $\mathbf{x}$ in space at the time t there is matter even if in all likelihood there is nothing at all. In a similar way it is possible to consider the difference in properties at distance smaller than that of the molecular scale, which leads to the definition of derivatives and therefore to the notion of gradients

$$\frac{\partial \rho}{\partial x_j} = \lim_{\Delta x_j \to 0} \frac{\rho(x_j + \Delta x_j, t) - \rho(x_j, t)}{\Delta x_j}. \tag{2.52}$$

As mentioned, the validity of this approximation[17] is evaluated by the already introduced Knudsen number K_n. If $K_n \lll 1$ the system can be treated as a continuum while for $K_n \approx 1$ tools of the statistical mechanics must be considered. Practically, this condition is often satisfied in the systems usually considered by fluid dynamics at standard conditions. If we consider for example a pipe of 10^{-4} m of diameter[18] at standard pressure and temperature the mean free path of air molecules is of the order of 10^{-9} m. Hence, in this case we obtain $K_n \approx 10^{-5}$.

2.4 Macroscale model: Computational Fluid Dynamics

Computational Fluid Dynamics (CFD) refers to the mathematical models used in the numerical resolution of the equation governing the motion of a fluid treated as a continuum, i.e., by solving the Navier-Stokes or Euler equations. The main goal of CFD is then to find the velocity field describing the flow inside a given

[17] To be rigorous we shall consider a small volume δV_0 around the point $\mathbf{x}$ whose dimension is a finite quantity. This volume is very small compared with the macroscopic dimension of the system (e.g. of the order of 10^{-9} m) and yet contains enough molecules to consider the average value of the properties in the volume independent from the number of molecules. Hence the dimension Δx_j in the limit in Eq. (2.52) should not tend to zero but to Δx_{j_0}

$$\frac{\partial \rho}{\partial x_j} = \lim_{\Delta x_j \to \Delta x_{j_0}} \frac{\rho(x_j + \Delta x_j, t) - \rho(x_j, t)}{\Delta x_j}$$

[18] The usual dimensions considered in fluid dynamics are certainly greater than this, that is only considered as a rough estimation of the validity of the continuum hypothesis.

domain. The basic equations solved with CFD encodes the two very general laws (derived from the BE)

- conservation of mass (continuity equation, from now on C-E)
- conservation of momentum (Navier-Stokes equation, from now on NS-E)
- conservation of energy.

corresponding to the moments of order zero, one and two of the Boltzmann equation.

There are different mathematical models used to obtain a numeric solution of these set of equations and they differ in the computational cost required, details of the scale resolved and accuracy of the solution. The most complete tool for the resolution of the C-E and NS-E under turbulent conditions is Direct Numerical Simulation (DNS) which offers the greater accuracy for the solution and is used in the so-called "numerical experiments" for the determination of the flow field in a given domain. However, its huge computational cost makes it infeasible for all but the simplest systems. Large Eddy Simulation (LES) and the Reynolds-Averaged Navier-Stokes (RANS) equations approach grant a lesser computational effort by using some approximation. LES uses the concept of low-pass filtering applied to NS-E with which the small scales of the solution are filtered-out. The smallest scales are then modelled with different approaches. RANS is based on the concept of Reynolds average with which only the average value of the velocity is considered in the determination of the flow field. This leads to some closure problems related to the fluctuating part of the velocity which need to be modelled.

The model used in this work to describe the flow field of the system under investigation is the RANS approach and will be analysed in the subsequent part of this chapter.

2.4.1 Basic Equations

Although some of the problems discussed in later Chapters involve flows with variable density, here the discussion is limited to constant density (i.e., incompressible) flow.

For an incompressible fluid the C-E will results to be

$$\nabla \cdot (\mathbf{U}) = \mathbf{0}, \tag{2.53}$$

in which **U** is the velocity vector of the fluid. The above equation states that for an incompressible fluid the local volume dilatation is zero, or rather the flow field is solenoidal. The NS-E equation reads as

$$\frac{\partial U_i}{\partial t} + U_j \frac{\partial U_i}{\partial x_j} = \frac{\partial}{\partial x_j}\left(\nu \frac{\partial U_i}{\partial x_j}\right) - \frac{1}{\rho}\frac{\partial p}{\partial x_j} \tag{2.54}$$

where ρ is the density of the fluid, $U_i \quad i = x_1, x_2, x_3$ is the i-th component of the velocity vector, ν is the kinematic viscosity and p the pressure. The boundary conditions for the NS-E are

- **Impermeability condition:** $\mathrm{U} \cdot \mathbf{n} = 0$
- **No-slip condition:** $\mathrm{U} - \mathbf{n}(\mathrm{U} \cdot \mathbf{n}) = 0$

where **n** is the normal of the surface. These conditions together lead to $\mathrm{U} = 0$. This equation must be coupled with the Poisson equation for the pressure to rewrite the pressure term in closed form:

$$\nabla^2 p = -\rho \frac{\partial U_i}{\partial x_j}\frac{\partial U_j}{\partial x_i} \tag{2.55}$$

the derivation of this equation is presented in App. B.

There are two different kinds of regimes of motion of the fluid, the laminar regime and the turbulent regime. The laminar regime is the most simple case to consider because the fluid flows in parallel streamlines with no interaction of fluid from one plane to another. There are no swirls nor eddies: for some of the simplest problems analytical solutions are also available. However, the most interesting case is the turbulent regime. In fact, most mixers used in practical applications are designed to reach turbulent flow since, as we will see in the later part of the work, the turbulent regime highly increases the mixing efficiency.

Under turbulent conditions the flow field represented by $\mathrm{U}(\mathbf{x}, t)$ is chaotic, that is to say that even if the same experiment is repeated under the same con-

ditions[19], the flow field obtained will be not the same. The average values of the quantity involved however, as the velocity, will be the same in all the experiments, but the instant values in space and time will be different. This behaviour originates from the high non-linearities present in the NS-E (i.e., the second term in Eq. (2.54)). The motion of the fluid is deterministic, because it is governed by the C-E and NS-E , but the non-linear term makes the solution very sensitive from the initial and boundary conditions, very small differences in the initial or boundary conditions from one experiment to another grow exponentially, and lead to very different value of the instantaneous and local velocity[20]. Therefore, turbulent flow is better described by considering the function $\mathrm{U}(\mathbf{x}, t)$ as a stochastic function. Hence, in the next session of the chapter there will be a brief excursus on the theory of the random variables and random processes.

2.4.1.1 Reynolds average

In the turbulent regime, velocity, pressure and local composition of the fluid can be considered random[21] variables. Hence, it is possible to define an average and a fluctuation for each of these quantities. This average value can be time independent, i.e. stationary, or can evolve with time. Anyway, these fluctuations of the local proprieties of the fluid in turbulent regime are small compared to the average value. Henceforth, it is more useful to describe the motion of the fluid with respect to his averaged quantity [Kays et al., 2005]. The velocity $\mathbf{U}(\mathbf{x}, t)$ in a turbulent system can be decomposed as sum of two terms, the average value and the fluctuation. This decomposition is called Reynolds decomposition:

$$\mathbf{U}(\mathbf{x}, t) = \langle \mathbf{U}(\mathbf{x}, t) \rangle + \mathbf{u}(\mathbf{x}, t) . \tag{2.56}$$

[19] One must remember that initial conditions are always subjected to some errors and uncertainties. Thus, "same" must be intended in operative way.

[20] In his essay "Science and Method" Poincaré [1903] wrote: "If we knew exactly the laws of nature and the situation of the universe at the initial moment, we could predict exactly the situation of that same universe at a succeeding moment. but even if it were the case that the natural laws had no longer any secret for us, we could still only know the initial situation approximately. If that enabled us to predict the succeeding situation with the same approximation, that is all we require, and we should say that the phenomenon had been predicted, that it is governed by laws. But it is not always so; it may happen that small differences in the initial conditions produce very great ones in the final phenomena. A small error in the former will produce an enormous error in the latter. Prediction becomes impossible, and we have the fortuitous phenomenon."

[21] In the sense specified in the previous Section.

In the above equation the average is intended as the Reynolds average (RA) of the random variable $\mathbf{U}$

$$\langle \mathbf{U}(\mathbf{x}, t) \rangle = \frac{1}{\Delta t} \int_{t_0}^{t_0+\Delta t} \mathbf{U}(\mathbf{x}, t)\, dt. \tag{2.57}$$

where t_0 is an arbitrary initial time. Then, Reynold average is a time average of a quantity over a certain time interval Δt in a point of the domain $\mathbf{x}$.

From the definition of Reynolds average, one obtains that if $\boldsymbol{u}$ is the fluctuating part of a quantity, its RA is always zero

$$\frac{1}{\Delta t} \int_{t_0}^{t_0+\Delta t} u \, \mathrm{d}t = \frac{1}{\Delta t} \int_{t_0}^{t_0+\Delta t} [\mathrm{U}(\mathbf{x}, t) - \langle \mathrm{U} \rangle] \, \mathrm{d}t = 0$$

where the last equality follows by considering that the average is a constant and it can be brought outside the integral.

2.4.2 One-point PDF

The velocity field $\mathbf{U}(\mathbf{x}, t)$ can be characterized by a one-point PDF $f_{\mathbf{U}}(\mathbf{V}; \mathbf{x}, t)$[22]; if we fix a point in the quadri-dimensional space $\mathbf{x}, t$ the PDF is defined as:

$$\begin{aligned} f_{\mathbf{U}}(\mathbf{V}; \mathbf{x}, t)\, d\mathbf{V} &= f(V_1, V_2, V_3; \mathbf{x}, t)\, dV_1 dV_2 dV_3 \\ &= P[V_1 \leq U_1(\mathbf{x}, t) < V_1 + dV_1 \\ &\cap V_2 \leq U_2(\mathbf{x}, t) < V_2 + dV_2 \\ &\cap V_3 \leq U_3(\mathbf{x}, t) < V_3 + dV_3]. \end{aligned} \tag{2.58}$$

This is the probability that in a fixed point in space, and in a fixed instant of time, the components U_1, U_2, U_3 of the vector $\mathbf{U}$ are included in the interval $V_i \leq U_i(\mathbf{x}, t) < V_i + dV_i$, with $i = 1, 2, 3$. In the case of homogeneous fully developed turbulence[23], we can write the PDF as $f_{\mathbf{U}}(\mathbf{V}; t)$, which is a nearly-Gaussian distribution [Fox, 2003]. Hence, it is possible to completely define this

[22] semicolon ; divides the independent variable V from the fixed quantities $\mathbf{x}$ and t. Besides, with the term "one-point" we are considering a point in the four dimensional space $(\mathbf{x}, t)$

[23] The turbulence is homogeneous when the averages are invariant with respect to spatial translation.

distribution through its vector of expected values $\boldsymbol{\mu}$ and the covariance tensor $\mathbf{C}$:

$$\mu(t) \equiv \langle \mathbf{U}(\mathbf{x}, t) \rangle \equiv \iiint_{-\infty}^{+\infty} \mathbf{V} f((V); \mathbf{x},) \, dV_1 dV_2 dV_3, \tag{2.59}$$

$$C_{ij}(t) \equiv \langle u_i(\mathbf{x}, t) u_j(\mathbf{x}, t) \rangle = \\ = \iiint_{-\infty}^{+\infty} (V_i - \langle U_i \rangle)(V_j - \langle U_j \rangle) f_{\mathbf{U}}((V); t) \, d\mathbf{V}. \tag{2.60}$$

C_{ij} is also known as the Reynolds stress tensor or the autocorrelation tensor and gives quantitative information about the correlation time of the turbulent signal.

2.4.3 Two-point PDF

It is possible to define a two-point PDF in the same way of the previous section:

$$f_{\mathbf{U},\mathbf{U}^*}(\mathbf{V}, \mathbf{V}^*; \mathbf{x}, \mathbf{x}^*, t) \, d\mathbf{V} d\mathbf{V}^* \equiv \mathrm{P}[(\mathbf{V} \leq \mathbf{U}(\mathbf{x}, t) < \mathbf{V} + d\mathbf{V}) \\ \cap (\mathbf{V}^* \leq \mathbf{U}(\mathbf{x}^*, t) < \mathbf{V}^* + d\mathbf{V}^*)] \tag{2.61}$$

This kind of PDF gives a measure of the correlation between two different velocities in two different points of the space in a given instant. This function is used to calculate the characteristic dimension or the shape of the turbulent structure; for distances $|\mathbf{x} - \mathbf{x}^*|$ lower than the spatial correlation value, the value of the correlation will be near to one, whilst for values of the correlation greater than the spatial correlation value, the correlation fast decays to zero. Such a spatial correlation will prove to be very important because it is the starting point for the energy cascade model. The spatial correlation function is

$$R_{ij}(\mathbf{r}, t) \equiv \langle u_i(\mathbf{x}, t) u_j(\mathbf{x}^*, t) \rangle \tag{2.62}$$

where $\mathbf{r} \equiv \mathbf{x}^* - \mathbf{x}$; if $\mathbf{r} = 0$, or rather $\mathbf{x} = \mathbf{x}^*$, the Reynolds stress tensor is obtained. By considering homogeneous isotropic turbulence[24] the correlation function can be expressed in terms of transversal autocorrelation function (g) and longitudinal autocorrelation function (f)

$$R_{ij}(\mathbf{r}, t) = \frac{2k}{3} \left(g(r, t) \delta_{ij} + [f(r, t) - g(r, t)] \frac{r_i r_j}{r^2} \right) \tag{2.63}$$

[24] The turbulence is isotropic if the quantity involved are invariant with respect to the rotation.

where

$$f(r,t) \equiv \frac{3}{2k} R_{11}(r\mathbf{e}_1, t) \tag{2.64}$$

$$g(r,t) \equiv \frac{3}{2k} R_{22}(r\mathbf{e}_1, t) \tag{2.65}$$

and $\mathbf{e}_1$ is the versor in direction x_1. Longitudinal and transversal autocorrelation functions for isotropic and homogeneous turbulence are related by the following equation

$$g(r,t) = f(r,t) + \frac{r}{2}\frac{\partial}{\partial r} f(r,t) \tag{2.66}$$

from which one obtains that $R_{ij}(\mathbf{r}, t)$ is completely determined by the longitudinal autocorrelation function f. In the same way, it is possible to define a temporal correlation function

$$\begin{aligned} f_{\mathbf{U},\mathbf{U}^*}(\mathbf{V}, \mathbf{V}^*; \mathbf{x}, t, t^*)\, d\mathbf{V} d\mathbf{V}^* \quad &\equiv \quad \mathrm{P}[(\mathbf{V} \leq \mathbf{U}(\mathbf{x}, t) < \mathbf{V} + d\mathbf{V}) \\ &\cap \quad (\mathbf{V}^* \leq \mathbf{U}(\mathbf{x}, t^*) < \mathbf{V}^* + d\mathbf{V}^*)] \end{aligned} \tag{2.67}$$

which is used in the description of a steady-state turbulent flow. This function quantify the scales for the times correlations of the turbulent flow.

2.4.4 Energy cascade theory

The energy and the anisotropies of the flow in a turbulent system are distributed among the different length scales, which range from the macroscale (order of meters) to microscale (order of micrometer). The energy cascade theory states that the kinetic energy enters in the system at the macroscale, is transferred and conserved to the microscale where is dissipated by macromolecular viscosity.

In a turbulent flow there are characteristic structures of the liquid in motion which are called eddies. These represent regions of the fluid in which the turbulent motion is concentrated. They can have very different characteristic length-scales l, in fact the biggest eddies have a dimension l_0 comparable with the macroscale of the flow, $\mathcal{L}$, and velocity of the order of magnitude of $u_0 \equiv u(l_0)$. At this scale, the Reynolds number ($Re_0 \equiv u_0 l_0/\nu$) is very high, hence the effect of viscosity is negligible. The biggest eddies are unstable and are divided in smaller

eddies till they become stable. By reducing the dimension, the Reynolds number decreases as well. At the smallest scales the effect of the viscosity becomes important.

2.4.4.1 Turbulent energy spectrum

The definition of turbulent energy spectrum involves the definition of the tensor of the spectrum of the velocity. This is related to the spatial correlation function Eq. (2.62) by the Fourier transform

$$\mathbf{\Phi}_{ij}(\kappa, t) = \frac{1}{(2\pi)^3} \int\int\int_{-\infty}^{+\infty} \mathbf{R}_{ij}(\mathbf{r}, t) \mathrm{e}^{-i\kappa\mathbf{r}} d\mathbf{r} \tag{2.68}$$

where κ is the wave number with dimension m^{-1}. When $\mathbf{r} = 0$ Eq. (2.62) is equal to the Reynolds stress tensor, then the quantity $\mathbf{\Phi}_{ij}(\kappa, t)$ corresponds to the amount of the stress described in the Reynolds tensor located in the point κ in the wave space at time t. The turbulent kinetic energy spectrum is obtained by the velocity spectrum integrating on the spherical shell in the wave space at distance κ from the origin:

$$E_u(\kappa, t) = \int\int\int_{-\infty}^{+\infty} \frac{1}{2} \left[\Phi_{11}(\kappa, t) + \Phi_{22}(\kappa, t) + \Phi_{33}(\kappa, t)\right] \delta(\kappa - \mid \kappa \mid) d\kappa. \tag{2.69}$$

By integrating with respect to the whole space of the wave number one obtains the turbulent kinetic energy:

$$k(t) = \int_0^{+\infty} E_u(\kappa, t) \mathrm{d}\kappa = \frac{1}{2} \left(\langle u_1^2 \rangle + \langle u_2^2 \rangle + \langle u_3^2 \rangle \right), \tag{2.70}$$

then $E_u(\kappa, t)d\kappa$ represents the quantity of kinetic energy contained in eddies characterized by wave numbers in between κ and $\kappa + \mathrm{d}\kappa$. The turbulent energy spectrum can be divided into three parts (see Fig. 2.5):

1. Energy containing range for $0 \leq \kappa \leq \kappa_{EI}$;
2. Inertial range for $\kappa_{EI} \leq \kappa \leq \kappa_{DI}$, where $E_u(\kappa) \sim \kappa^{5/3}$;
3. Dissipation range for $\kappa_{DI} \leq \kappa$, where $E_u(\kappa)$ has an exponential decay.

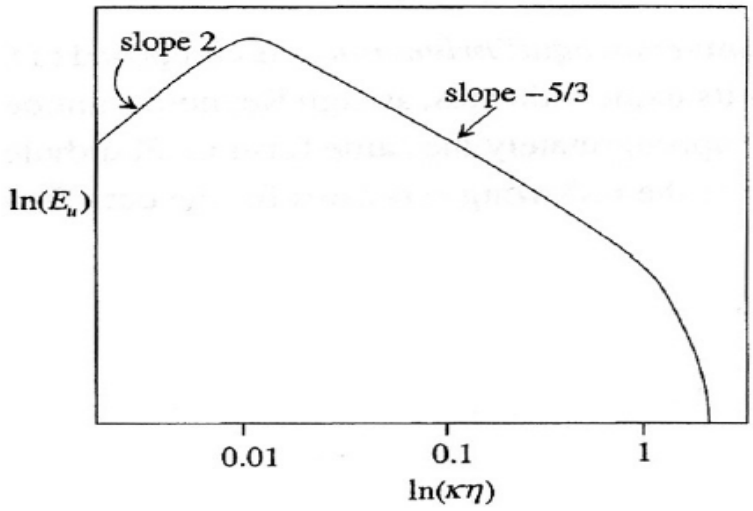

Figure 2.5: Model for the turbulent energy spectrum for $Re = 500$ [Fox, 2003]

The first part of the spectrum is dominated by the biggest eddies which possess the lowest wave number and with a dimension that satisfy $l_{EI} < l < 6l_0$. In the inertial range the eddies have an intermediate dimension $l_{DI} < l_{EI} < l$ and here is where the energy is transferred to the smallest scale. In the dissipation range the smallest eddies with dimension $l < l_{DI}$ can be found and this is the scale at which the viscosity is not longer negligible. The characteristic dimension of the smallest eddies is proportional to the Kolmogorov scale and they are characterized by a velocity, dimension and existence time given by:

$$\eta = (\nu^3/\varepsilon)^{1/4}, \tag{2.71}$$

$$u_\eta = (\varepsilon\nu)^{1/4}, \tag{2.72}$$

$$\tau_\eta = (\nu/\varepsilon)^{1/2}. \tag{2.73}$$

where k is the turbulent kinetic energy and ϵ is the turbulent dissipation rate.

At Kolmogorov scale we have that $Re_k = \eta u_\eta/\nu = 1$, or rather the turbulent and viscosity dissipation equal each other. If we define the turbulent Reynolds number as

$$Re_L \equiv \frac{k^2}{\varepsilon\nu} \tag{2.74}$$

and the integral scale of the turbulence as

$$L_u \equiv \frac{k^{3/2}}{\varepsilon} \tag{2.75}$$

the ratio between the Kolmogorov scale and the integral scale for the turbulence can be expressed by the Reynolds number

$$\frac{\eta}{L_u} = Re_L^{-3/4} \tag{2.76}$$

Eventually, one can derive the integral time for turbulence resulting in:

$$\tau_u = \frac{k}{\varepsilon} \tag{2.77}$$

and representing the characteristic time-scale with which eddies are dissipated.

One of the most important results for turbulent flows has been postulated by Kolmogorov: at high values of Re_L and κ, $E_u(\kappa)$ is universal and depends only from the kinematic viscosity ν and the dissipation rate ε. At high Reynolds number values the smallest scales are locally isotropic even in inhomogeneous flows. Kolmogorov also postulated that for high Reynolds number $E_u(\kappa)$ will depend on ε only. It is important to remind here that the dissipation rate of the turbulent kinetic energy can be expressed with the tensor s_{ij}:

$$s_{ij} \equiv \frac{1}{2}\left(\frac{\partial u_i}{\partial x_j} + \frac{\partial u_j}{\partial x_i}\right) \tag{2.78}$$

as

$$\varepsilon = 2\nu\langle s_{ij} s_{ij}\rangle \tag{2.79}$$

ε is related to $E_u(\kappa, t)$ by the following relation

$$\varepsilon(t) = 2\nu \int_0^\infty \kappa^2 E_u \kappa, t d\kappa = \int_0^\infty D_u(\kappa, t) d\kappa \tag{2.80}$$

where $D_u(\kappa, t)$ is the turbulent energy dissipation spectrum.

2.4.5 Averaged Equations

One of the most used approach in deriving transport equations for turbulent flow, is the Reynolds average. Starting from the continuity equation, Eq. (2.53), and by applying the Reynolds average and decomposition, one obtains:

$$\nabla \cdot \langle \mathrm{U} \rangle = 0 \tag{2.81}$$

$$\nabla \cdot \mathbf{u} = 0. \tag{2.82}$$

Both the average velocity field and the fluctuating velocity field are solenoidal[25]. By applying the Reynolds average and decomposition to NS-E one obtains:

$$\frac{\partial \langle U_i \rangle}{\partial t} + \langle U_j \rangle \frac{\partial \langle U_i \rangle}{\partial x_j} + \frac{\partial \langle u_j u_i \rangle}{\partial x_j} = -\frac{1}{\rho} \frac{\partial \langle P \rangle}{\partial x_j} + \Gamma \nabla^2 \langle U_i \rangle \tag{2.83}$$

The term $\Gamma \nabla^2 \langle U_i \rangle$ which represents the molecular transport is proportional to Re_L^{-1}, hence it can be neglected in the limit of high Reynolds number. The pressure term appears in non-closed form, therefore one needs to apply the Reynolds average to Poisson equation for the pressure (Eq. (2.55)):

$$\begin{aligned} \nabla^2 \langle P \rangle &= -\rho \left\langle \frac{\partial U_i}{\partial x_j} \frac{\partial U_j}{\partial x_i} \right\rangle \\ &= \frac{\partial \langle U_i \rangle}{\partial x_j} \frac{\partial \langle U_j \rangle}{\partial x_i} + \left\langle \frac{\partial u_i}{\partial x_j} \frac{\partial u_j}{\partial x_i} \right\rangle \\ &= \frac{\partial \langle U_i \rangle}{\partial x_j} \frac{\partial \langle U_j \rangle}{\partial x_i} + \frac{\partial^2 \langle u_i u_j \rangle}{\partial x_i \partial x_j}. \end{aligned} \tag{2.84}$$

The only terms in Eq. (2.83) and in Eq. (2.84) which appear in non-closed form are the Reynolds stress tensor $\langle u_i u_j \rangle$, which is a second order symmetric tensor , i.e. $\langle u_i u_j \rangle = \langle u_j u_i \rangle$ [Fox, 2003].

2.4.5.1 Reynolds tensor stress transport equation

Since the Reynolds stress tensor is the only non-closed term in Eq. (2.83) and Eq. (2.84) we need to close this term to be able to solve the equation. The starting point to find a way to close this term is to obtain a transport equation for the

[25] We are considering incompressible fluid, $\rho = cost$.

Reynolds stress tensor. The first step is to consider the equation for the fluctuating part of the velocity:

$$\frac{\partial u_i}{\partial t} + U_k \frac{\partial u_i}{\partial x_k} + u_k \frac{\partial U_i}{\partial x_k} = \nu \nabla^2 u_i - \frac{1}{\rho} \frac{\partial p}{\partial x_k} + \frac{\partial (u_i u_k)}{\partial x_k}. \tag{2.85}$$

From the above equation it is possible to obtain (the complete derivation is presented in App. C):

$$\frac{\partial \langle u_i u_j \rangle}{\partial t} + \langle U_k \rangle \frac{\partial \langle u_i u_j \rangle}{\partial x_k} + \frac{\partial \langle u_i u_j u_k \rangle}{\partial x_k} = \mathcal{P}_{ij} + \Pi_{ij} + \nu \nabla^2 \langle u_i u_j \rangle - \varepsilon_{ij}. \tag{2.86}$$

$\nu \nabla^2 \langle u_i u_j \rangle$ represents the molecular transport and is proportional to Re_L^{-1}, hence can be neglected for high value of the Reynolds number, $\mathcal{P}_{ij}$ is the source term for the production of the stresses due to the mean velocity gradient, ε_{ij} describes how the velocity fluctuations are dissipated at the scales near the Kolmogorov scales, and Π_{ij} is the correlation term between the pressure and velocity fluctuations. This term can be further decomposed into two different parts:

$$\Pi_{ij} = \mathcal{R}_{ij} - \frac{\partial \mathcal{T}_{kij}^{(p)}}{\partial x_k} \tag{2.87}$$

where

$$\mathcal{R}_{ij} \equiv \left\langle \frac{p}{\rho} \left(\frac{\partial u_i}{\partial x_j} + \frac{\partial u_j}{\partial x_i} \right) \right\rangle \tag{2.88}$$

is the source term for the stresses due to the pressure fluctuations and

$$\mathcal{T}_{kij}^{(p)} \equiv \frac{1}{\rho} \langle u_i p \rangle \delta_{jk} + \frac{1}{\rho} \langle u_j p \rangle \delta_{ik} \tag{2.89}$$

is the term of diffusion of the stresses due to pressure fluctuations.

2.4.6 Turbulence models

The closure of the term due to stress tensor was a fundamental part of the developing of this theory. The RANS approach uses the turbulent viscosity concept proposed by Boussinesq in 1877 [Pope, 2000] which is valid for high Reynolds numbers, where convection and diffusion are negligible and production and dissipation of the Reynolds stresses are in equilibrium. Boussinesq main hypothesis

was to consider the motion of the turbulent structure similar to the molecular motion. Hence, he found an expression to link the Reynolds stress tensor to the value of the average velocity $\langle \mathbf{U} \rangle$. This assumption is valid only under certain conditions:

- the turbulent characteristic scales must be much smaller than the scale of the system. Let us define:

$$L = \frac{|dU_j/dx_i|}{|d^2U_j/dx_i^2|} \tag{2.90}$$

  as the macro-scale dimension. This first hypothesis corresponds to the fact that the Knudsen number for the turbulence must be very small

$$Kn = \frac{l_m}{L} \ll 1; \tag{2.91}$$

  where l_m is the mixing length (i.e., of an eddy)

- turbulence must be isotropic.

Following the Boussinesq derivation it is possible to show that the deviatoric part of the Reynolds stress tensor is proportional to the mean deformation rate:

$$-\rho\langle u_i u_j \rangle + \frac{2}{3}\rho k \delta_{ij} = \rho\nu_T \left(\frac{\partial \langle U_i \rangle}{\partial x_j} + \frac{\partial \langle U_j \rangle}{\partial x_i} \right) = 2\rho\nu_T \langle S \rangle_{ij}$$

where ν_T is the turbulent viscosity and where:

$$\langle S \rangle_{ij} = \frac{1}{2} \left(\frac{\partial \langle U_i \rangle}{\partial x_j} + \frac{\partial \langle U_j \rangle}{\partial x_j} \right).$$

Therefore, one obtains for the NS-E averaged with the RA:

$$\frac{\partial \langle U_i \rangle}{\partial t} + \langle U_j \rangle \frac{\partial \langle U_i \rangle}{\partial x_j} = \frac{\partial}{\partial x_i} \left[\nu_{\text{eff}} \left(\frac{\langle U_i \rangle}{\partial x_j} + \frac{\partial \langle U_j \rangle}{\partial x_i} \right) \right] - \frac{1}{\rho} \frac{\partial p_m}{\partial x_i}, \tag{2.92}$$

in which we can define an effective viscosity $\nu_{\text{eff}}(\mathbf{x}, t) = \nu + \nu_T(\mathbf{x}, t)$ and $p_m = \langle p \rangle + \frac{2}{3}\rho k$ is the modified pressure. Now the closure problem concerns the turbulent viscosity term which needs to be calculated. There are several models to perform

this task labelled with the number of equations involved. Here we consider the two-equation model called standard $k-\varepsilon$.

2.4.6.1 $k-\varepsilon$ model

In this model the turbulent viscosity is calculated as a function of the kinetic turbulent energy and the kinetic turbulent dissipation rate ε:

$$\nu_T = C_\mu \frac{k^2}{\varepsilon} \tag{2.93}$$

where C_μ is a numerical constant. In order to obtain a transport equation for ε we start from Eq. (2.85) which can be rewritten as:

$$\frac{\partial u_i}{\partial t} = \mathcal{N}_i(\mathbf{U}, \mathbf{u}, p). \tag{2.94}$$

The evolution equation for s_{ij} is therefore given by:

$$2\frac{\partial s_{ij}}{\partial t} = \frac{\partial}{\partial x_i}\frac{\partial u_j}{\partial t} + \frac{\partial}{\partial x_j}\frac{\partial u_i}{\partial t} = \frac{\partial \mathcal{N}_j}{\partial x_i} + \frac{\partial \mathcal{N}_i}{\partial x_j}. \tag{2.95}$$

From Eq. (2.79) we obtain the equation for the evolution of ε:

$$\frac{\partial \varepsilon}{\partial t} = 4\nu \left\langle s_{ij}\left(\frac{\partial \mathcal{N}_j}{\partial x_i} + \frac{\partial \mathcal{N}_i}{\partial x_j}\right)\right\rangle, \tag{2.96}$$

This equation is not much useful because the terms to model are very complex; it is simpler to obtain a description of the evolution of ε based on physical considerations and dimensional analysis. In this equation there will be a source term, a dissipation term and a turbulent convective term, resulting in:

$$\frac{\partial \varepsilon}{\partial t} + \langle U_j \rangle \frac{\partial \varepsilon}{\partial x_j} = \frac{\partial}{\partial x_j}\left[(\nu + \frac{\nu_T}{\sigma_\varepsilon})\frac{\partial \varepsilon}{\partial x_j}\right] + \frac{\varepsilon}{k}(C_{\varepsilon 1}\mathcal{P} - C_{\varepsilon 2}\varepsilon); \tag{2.97}$$

this equation is coupled with the transport equation for the turbulent kinetic energy

$$\frac{\partial k}{\partial t} + \langle U_j \rangle \frac{\partial k}{\partial x_j} = \frac{\partial}{\partial x_j}\left[(\nu + \frac{\nu_T}{\sigma_\varepsilon})\frac{\partial k}{\partial x_j}\right] + \mathcal{P} - \varepsilon. \tag{2.98}$$

$\mathcal{P}$ is the production term for the turbulent kinetic energy and is defined as follows:

$$\mathcal{P} = -\langle u_i u_j \rangle \frac{\partial \langle U_i \rangle}{\partial x_j}. \tag{2.99}$$

Eq. (2.98) states that the kinetic turbulent energy is produced at the macro-scale thanks to mean velocity gradients and dissipated at the Kolmogorov scale by ε. In the transport equation for the dissipation rate of the turbulent kinetic equation the term σ_ε is the turbulent Prandtl number, whereas $C_{\varepsilon 1}$ and $C_{\varepsilon 2}$ are two numerical constants. In the $k-\varepsilon$ model these constants are equal to $C_\mu = 0.09$ whereas $C_{\varepsilon 1} = 1.44$ and $C_{\varepsilon_2} = 1.92$. These values are obtained by interpolating experimental data on different types of flow and represent a good trade-off between different situations that can occur in practice. The different turbulent models based on the hypothesis of turbulent viscosity are applied to a great variety of problems related to turbulent flow and they showed to be the cheapest and most robust.

Anyway the presence of the empirical constant make this model reliable only for flow with isotropic fully developed turbulence. Hence, other models were developed to obtain more accurate results. The Renormalization Group (RNG) $k-\varepsilon$ and the realizable models $k-\varepsilon$ are the most used in this framework. For a review of these models see Valerio et al. [1998].

2.4.6.2 Wall condition

RANS model needs to be coupled with an accurate description of the interaction between the flow and the wall in which it is contained. A turbulent flow is very sensitive to the presence of the wall. In fact, the average component of the velocity is modified to satisfy the non-slip velocity condition to the wall and the modification to the velocity field are propagated even far from the wall. In the zone near the wall the viscous damping reduces the tangential component of the fluctuating part of the velocity whereas the non-slip velocity condition reduces the normal component of the fluctuating part of the velocity. Therefore, the correct condition of the flow near the wall must be very carefully placed in order to obtain correct results for the turbulent flow.

The region near the wall can be divided in three zones. The first is the closest to the wall and is called the viscous sublayer where the flow is always laminar and transport is controlled by molecular phenomena (i.e., viscosity). The most

external region is the region where the turbulent phenomena become important. In the intermediate region there is no prevalence among the laminar and turbulent descriptions.

There are two main approaches to model the wall region in a bounded domain. The first is the Near Wall Model where the turbulence models are modified to take into account the viscous layer near the wall, whereas in the second approach some semi-empirical functions (called wall functions) are used to connect the viscous layer and the region where the turbulence is completely developed. The second approach is the cheapest and will be described here.

The standard wall functions describe the dimensionless velocity u^+ as a logarithmic law:

$$u^+ = \frac{\langle v_t \rangle}{u_\tau} = \frac{1}{\kappa_k} \ln y^+ + B, \tag{2.100}$$

where $\langle v_t \rangle$ is the averaged velocity in the direction parallel to the wall and, u_τ is the deformation rate,

$$u_\tau = \sqrt{\frac{\tau_w}{\rho_f}}. \tag{2.101}$$

τ_w is then the deformation stress to the wall, $\kappa_K = 0.41$ is the von Karman constant; B is an empirical constant related to the thickness of the laminar flux to the wall. In this functions, the dimensionless distance to the wall is used

$$y^+ = \frac{u_\tau y}{\nu} \tag{2.102}$$

where y is the coordinate perpendicular to the wall. The velocity field is then modelled by considering the RANS approach for the bulk and the wall function Eq. (2.100) for distance $10 < y^+ < 50$. Below $10 = y^+$ a linear relation between the dimensionless velocity and the distance from the wall $u^+ \propto y^+$ is assumed. Wall functions are valid for high Reynolds numbers; at small values of the Reynolds number the Near Wall model must be used. In this model the whole domain is divided in a viscous region and in a turbulent region without an intermediate region. The position of the interface between the two regions with respect to the wall is determined by a function which depends from the wall Reynolds turbulent number Re_y:

$$Re_y \equiv \frac{\rho y \sqrt{k}}{\nu}. \tag{2.103}$$

where y is the length of the normal to the wall. In the region with fully developed turbulence ($Re_y > Re_y^*; Re_y^* = 200$) the $k-\varepsilon$ model is used. In the region near the wall where the viscous effects become important a one-equation model is used. In this model the transport equations are equal to those of the $k-\varepsilon$ except for the turbulent viscosity ν_t. The new turbulent viscosity $\nu_{t,2layer}$ is defined as:

$$\nu_{t,2layer} = \rho C_\nu l_\nu \sqrt{k}, \tag{2.104}$$

where l_ν is given by:

$$l_\nu = yC_l\left(1 - \exp\left(-\frac{Re_y}{A_\nu}\right)\right), \tag{2.105}$$

and where $A_\nu = 70$ and $C_l = \kappa C_\nu^{\frac{3}{4}}$. The turbulent viscosity will then be:

$$\nu_{t,enh} = \lambda_\varepsilon \nu_t + (1 - \lambda_\varepsilon)\nu_{t,2layer}. \tag{2.106}$$

The function λ_ε is defined as:

$$\lambda_\varepsilon = \frac{1}{2}\left[1 + \tanh\left(\frac{Re_y - Re_y^*}{A}\right)\right] \tag{2.107}$$

The constant A is given by:

$$A = \frac{|\Delta Re_y|}{\tanh(0.98)} \tag{2.108}$$

where $\Delta Re_y = (Re_y - Re_y^*)$. The turbulent dissipation rate is given by

$$\varepsilon = \frac{k^{\frac{3}{4}}}{l_\varepsilon} \tag{2.109}$$

where l_ε is

$$l_\varepsilon = yC_l\left(1 - \mathrm{e}^{-\frac{Re_y}{A_\varepsilon}}\right) \tag{2.110}$$

where $A_\varepsilon = 2C_l$. Near the wall the enhanced wall functions which couple the linear and logarithmic law are used

$$u^+ = \mathrm{e}^{\Gamma} u_{lin}^+ + \mathrm{e}^{\frac{1}{\Gamma}} u_{log}^+ \tag{2.111}$$

where Γ is the composition function defined as:

$$\Gamma = \frac{a(y^+)^4}{1 + by^+}$$

and where a and b depend from the specific system (i.e., they depend from the roughness of the surface).

2.4.7 Turbulent mixing

NS-E expresses a physic conservation principle. In this specific case the NS-E expresses the conservation of momentum in the system. This basic physic principle of the conservation of some quantity can be generalized in a way that every conserved quantity obey to the same equation which has a common structure even if the single term can vary from one case to another. This general transport equation will contains the transient term (time derivatives of the quantity), the diffusion and convective terms and the source term (which is the only term which can be very different from one system to another). For a generic scalar (or vector) quantity $\boldsymbol{\phi} = \phi_1, \phi_2, \ldots, \phi_n$ it is possible to write:

$$\frac{\partial \phi_\alpha}{\partial t} + U_j \frac{\partial \phi_\alpha}{\partial x_j} = \frac{\partial}{\partial x_j}\left(\Gamma_\alpha \frac{\partial \phi_\alpha}{x_j}\right) + S_\alpha(\boldsymbol{\phi}). \tag{2.112}$$

In NS-E the source term is represented by the pressure field, instead in the Eq. (2.112) this term needs to be written explicitly. This will lead to the closure problem for this equation that will be considered in the Chap. 3.

As already done in Sec. 2.4.4.1 it is possible to define the scalar spectrum $E_\phi(\kappa, t)$ from which it is possible to obtain all the characteristic scales of the mixing. Two important spatial scales able to describe the turbulent mixing are the integral mixing scale L_ϕ and the Batchelor scale λ_B. The Batchelor scale is defined as function of the Kolmogorov scale[26] η and the number of Schmidt which is defined as $Sc = \nu/\Gamma$ where ν is the kinematic viscosity and Γ the molecular diffusivity:

$$\lambda_B \equiv \mathrm{Sc}^{-\frac{1}{2}}\eta. \tag{2.113}$$

The scalar integral scale characterizes the biggest structure in the system and can

[26] Cf. Eq. (2.71).

be considered in two different ways:

1. initial condition: the scalar field is initialized with a scale equal to L_ϕ which results independent from the turbulent velocity field

2. turbulent mixing: during the mixing scalar eddies will be created with a characteristic dimension equal to L_ϕ approximately equal to L_u

On the other hand, the Batchelor scale characterize the smallest structures in the scalar field where the molecular diffusion is balanced by the turbulent mixing. In a liquid system where $Sc \gg 1$ the scalar field contains a lot of structure thinner than the turbulent velocity field. For domains of the scalar with dimension greater than the Batchelor scale the molecular diffusion is negligible. Accordingly, a fluid which is not pre-mixed will remain segregated at scale greater that the Batchelor scale. Therefore, in a reactive system the chemical reaction term will be strongly dependent from mixing. In a fully developed turbulent flow the rate of dissipation of a scalar eddy of dimension l_ϕ depends on its size relatively to integral turbulent scale L_u and Kolmogorov scale η. For scalar eddies in the inertial subrange (i.e., $\eta < l_\phi < L_u$), the micromixing velocity can be approximated as [Fox, 2003]:

$$\gamma(l_\phi) = \left(\frac{\varepsilon}{\nu}\right)^{\frac{1}{2}} \left(\frac{\eta}{l_\phi}\right)^{\frac{2}{3}} \quad \text{for} \quad \eta \leq l_\phi \leq L_u. \tag{2.114}$$

By recallig the Eq. (2.76) the mixing velocity at the integral scale of the turbulence can be written as:

$$\gamma(L_u) \approx \frac{\varepsilon}{k}; \tag{2.115}$$

whereas at the Kolmogorov scale:

$$\gamma(\eta) \approx \left(\frac{\varepsilon}{\nu}\right)^{\frac{1}{2}} = \mathrm{Re}_L^{\frac{1}{2}} \gamma(L_u). \tag{2.116}$$

At high Reynolds number the mixing at the Kolmogorov scale is faster than the mixing at the integral scale. If the scalar eddies have a dimension smaller than the Kolmogorov scale $l_\phi < \eta$, a different situation occurs, and the turbulent eddies compress the scalar structure until they reach the Bacthelor scale. At this scale the molecular diffusion becomes prevalent and eliminates all the scalar gradients leading to an homogenization of the scalar value inside the system. The

micromixing rate can be expressed for dimension of the scalar structure between Kolmogorov and Batchelor scale as:

$$\gamma(l_\phi) = \left(\frac{\varepsilon}{\nu}\right)^{\frac{1}{2}} \quad \text{per} \;\; l_\phi \leq \eta. \tag{2.117}$$

2.4.7.1 One-point composition PDF

As the velocity field, the scalar field can be described with the tools of statistical analysis by employing the PDF. Hence, it is possible to define $f_{\mathbf{U},\phi}(\mathbf{V}, \psi; \mathbf{x}, t)$ as:

$$\begin{aligned} f_{\mathbf{U},\phi}(\mathbf{V}, \psi; \mathbf{x}, t) \equiv & P[(\mathbf{V} \leq \mathbf{U}(\mathbf{x}, t) < \mathbf{V} + \mathrm{d}\mathbf{V}) \cap \\ & (\psi \leq \phi(\mathbf{x}, t) < \psi + \mathrm{d}\psi)]. \end{aligned} \tag{2.118}$$

Anyway, it is possible to use a one-point composition PDF:

$$f_\phi(\psi; \mathbf{x}, t) \equiv P[\psi \leq \phi(\mathbf{x}, t) < \psi + \mathrm{d}\psi], \tag{2.119}$$

which can be obtained by integrating the PDF defined in Eq. (2.118) on all the phase space:

$$f_\phi(\psi; \mathbf{x}, t) = \iiint_{-\infty}^{\infty} f_{\mathbf{U},\phi}(\mathbf{V}, \psi; \mathbf{x}, t).$$

Unlike the turbulent velocity field, the composition PDF can not be assimilated to a known distribution because it evolves during the process due to the turbulent mixing and the molecular diffusion. In the case of binary mixing the average value of the scalar is constant during all the process obtaining $\langle\phi(\mathbf{x}, t)\rangle = \langle\phi(\mathbf{x}, 0)\rangle = p_1$, where p_1 represents the volume fraction of the scalar field with value $\phi(\mathbf{x}, 0) = 1$. The mixing rate can be quantified by considering the scalar variance $\langle\phi'^2\rangle$ defined as

$$\langle\phi'^2(\mathbf{x}, t)\rangle \equiv \int_{-\infty}^{+\infty} (\psi - \langle\phi\rangle)^2 f_\phi(\psi; t)\mathrm{d}\psi, \tag{2.120}$$

and in the case of binary mixing the variance is equal to $\langle\phi'^2(\mathbf{x}, 0)\rangle = p_1(1 - p_0)$, where p_0 is equal to $\phi(\mathbf{x}, 0) = 0$. When the time $t \to \infty$ the PDF collapses on the average value, hence $\langle\phi'^2(\mathbf{x}, \infty)\rangle = 0$ and

$$f_\phi(\psi; \infty) = \delta(\psi - p_1). \tag{2.121}$$

For all the intermediate times, variance will be a decreasing function of time. It is possible to define the amount of segregation which represents a measure of the non-homogeneity of the scalar field at molecular scale:

$$I(t) \equiv \frac{\langle \phi'^2(\mathbf{x}, t) \rangle}{\langle \phi'^2(\mathbf{x}, 0) \rangle}, \tag{2.122}$$

the rate of change of $I(t)$ is determined from the scalar spectrum described in the next Sections.

2.4.7.2 Two-point composition PDF

One-point PDF is not able to give information about the mixing scales needed by the description of the decreasing rate of the scalar variance. Hence, two-point PDF, which give information about the spatial correlation of the scalar, is used. These are defined in accordance with the Reynolds decomposition of a generic field in an average and a fluctuating part[27]:

$$\phi'(\mathbf{x}, t) \equiv \phi(\mathbf{x}, t) - \langle \phi(\mathbf{x}, t) \rangle, \tag{2.123}$$

as

$$R_\phi(\mathbf{r}, t) \equiv \langle \phi'(\mathbf{x}, t) \phi'(\mathbf{x}^*, t) \rangle, \tag{2.124}$$

where $\mathbf{r} = \mathbf{x} - \mathbf{x}^*$. If $\mathbf{r} = \mathbf{0}$ the one-point statistics described in the previous section is again obtained[28]. As the spatial correlations of the turbulent velocity described in the Sec. 2.4.3, spatial correlations of the scalar quantity give the information of the mixing scales. If a correlation exists between two points $\mathbf{x}$ and $\mathbf{x}^*$, with value of the propriety equal to ϕ', at distance $l_\phi = |\mathbf{x} - \mathbf{x}^*|$, there will be inside the fluid some domains with value of the propriety equal to ϕ'. In a homogeneous and isotropic scalar field, the correlation function will depend only from the distance of the points considered $r \equiv \mathbf{r}$ hence, $R_\phi(r, t)$. The integral scale of the scalar L_ϕ can be obtained by the normalized correlation function f_ϕ defined as:

$$f_\phi(r, t) \equiv \frac{R_\phi(r, t)}{R_\phi(0, t)}. \tag{2.125}$$

[27] Cf. Sec. 2.4.1.1.

[28] $R_\phi(\mathbf{0}, t)$ is the scalar variance.

The integral dimension of the scalar domain is defined as:

$$L_\phi = \int_0^\infty f_\phi(r,t)\mathrm{d}r. \tag{2.126}$$

2.4.7.3 Scalar spectrum

The scalar spectrum $\Phi_\phi(\boldsymbol{\kappa}, t)$ is connected to the spatial correlation function Eq. (2.124) through the Fourier transform:

$$\Phi_\phi(\boldsymbol{\kappa},t) = \frac{1}{(2\pi)^3}\iiint_{-\infty}^{+\infty} R_\phi(\boldsymbol{r},t)\mathrm{e}^{-i\boldsymbol{\kappa}\boldsymbol{r}}\mathrm{d}\boldsymbol{r}, \tag{2.127}$$

$$R_\phi(\boldsymbol{r},t) = \iiint_{-\infty}^{+\infty} \Phi_\phi(\boldsymbol{\kappa},t)\mathrm{e}^{i\boldsymbol{\kappa}\boldsymbol{r}}\mathrm{d}\boldsymbol{\kappa}. \tag{2.128}$$

If $\boldsymbol{r} = \mathbf{0}$ the spatial correlation function is the covariance of the scalar, thus it is possible to derive the relation between the latter and the scalar spectrum which results to be:

$$R_\phi(\mathbf{0},t) = \langle\phi'^2\rangle(t)\iiint_{-\infty}^{+\infty} \Phi_\phi(\boldsymbol{\kappa},t)\mathrm{e}^{i\boldsymbol{\kappa}\boldsymbol{r}}\mathrm{d}\boldsymbol{\kappa}. \tag{2.129}$$

$\Phi_\phi(\boldsymbol{\kappa}, t)\mathrm{d}\boldsymbol{\kappa}$ is the amount of variance localized in the point $\boldsymbol{\kappa}$ of the wave number space at the time t. The energy spectrum of the scalar is thus defined starting from the scalar spectrum and by integration over the wave number space:

$$E_\phi(\kappa,t) = \iiint_{-\infty}^{+\infty} \Phi_\phi(\boldsymbol{\kappa},t)\delta(\kappa - |\boldsymbol{\kappa}|)\mathrm{d}\kappa, \tag{2.130}$$

where the integration domains are the spherical shells in the wave number space at distance κ from the origin. In an isotropic scalar field one obtains for the scalar energy spectrum

$$\Phi_\phi(\kappa,t) = \frac{E_\phi(\kappa,t)}{4\pi\kappa^2}. \tag{2.131}$$

At high Reynolds number it can be assumed that the smallest scales of the scalar field are isotropic [Fox, 2003]. As in the case of turbulent velocity it is possible to consider that the biggest structures are formed at the smallest wave number, or rather at the biggest spatial scales. These structures have a directionality which is lost as one goes down towards the smallest scales (biggest wave numbers). At the smallest spatial scales these structures are dissipated by the molecular diffusion

(which is analogous to molecular viscosity in the case of turbulent velocity). The variance can be written as:

$$\langle \phi'^2 \rangle(t) = \int_0^\infty E_\phi(\kappa, t) \mathrm{d}\kappa; \tag{2.132}$$

the value of the scalar energy spectrum represents the amount of variance at wave number κ. For isotropic turbulence the integral scalar scale is connected to the scalar energy spectrum by:

$$L_\phi(t) = \frac{\pi}{2\langle \phi'^2 \rangle} \int_0^\infty \frac{E_\phi(\kappa, t)}{\kappa} \mathrm{d}\kappa. \tag{2.133}$$

The scalar energy spectrum can be divides in different zones, as the turbulent energy spectrum. However, in this case the dependence on the Schmidt number together with the Reynolds number must be considered. If $\mathrm{Sc} \gg 1$ as in the case of liquids, Batchelor wave number κ_B is higher than Kolmogorov wave number κ_η because $\kappa = \mathrm{Sc}^{1/2}\kappa_\eta$. If Reynolds number is sufficiently high there will be a range of wave numbers in which neither the molecular viscosity nor the molecular diffusion will have effect.

As consequences, the scalar energy spectrum and the turbulent energy spectrum have the same shape in this region of the spectrum. As already done in the description of the turbulent energy spectrum the region with the smallest wave numbers to $\kappa_{EI}$is called scalar energy-containing range. The next regions are the inertial-convective subrange and the inertial-diffusive sub-range. The last part of the spectrum is composed by the viscous-convective sub-range and viscous-diffusive sub-range for the highest wave numbers, greater than κ_η. In Fig. 2.6 is shown the dependence of the spectrum shape from the Reynolds number. If $\mathrm{Re} = 1$ the integral scale of turbulence and the Kolmogorov scale are equal, hence in the scalar energy spectrum there will not be inertial convective subrange and for $\kappa > 1$ it will be composed only by the vicous convective subrange scale which decrease as $E_\phi \sim \kappa^{-1}$, followed by an exponential decay in the viscous-diffusive subrange near the wave number κ_B equal to the Batchelor scale ($\kappa_B = \mathrm{Sc}^{1/2}\mathrm{Re}^{3/2}$). For $\mathrm{Re} = 10$ there is not a definite region corresponding to the inertial-convective subrange. For $\mathrm{Re} = 100$ inertial convective subrange begins to form in the region of wave number near the value $\kappa = \mathrm{Re}^{3/2}$ and it decays as $E_\phi \sim \kappa^{-5/3}$. This region is followed by the viscous-convective sub-range where $E_\phi \sim \kappa^{-1}$ and from

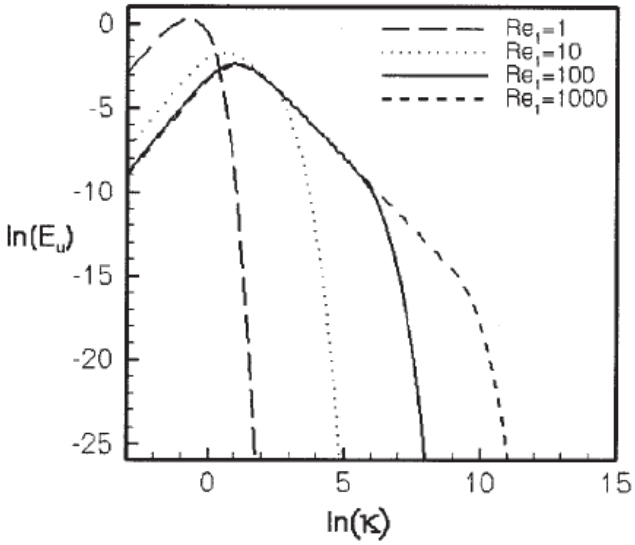

Figure 2.6: Dependence of the shape of the scalar energy spectrum from the Reynolds number with fixed Schmidt number Sc = 1000 [Liu and Fox, 2005]

the viscous-diffusive sub-range. For the Re = 1000 the scalar spectrum is completely developed and all the four regions are clearly visible. As the case of the turbulent energy spectrum in the regime of turbulence completely developed, the law of $-5/3$ is distinguishable in the shape of the spectrum as shown in Fig. 2.6.

Chapter 3

CFD simulation of nanoparticles precipitation[1]

In this part of the thesis a model for precipitation of polymer nanoparticles in solvent-displacement processes is presented and validated. The model is based on computational fluid dynamics coupled with a population balance model. The standard $k-\epsilon$ turbulence model in combination with the enhanced wall treatment approach is used to describe mixing and particle formation in a confined impinging jets reactor. The interaction between turbulent fluctuations and particle formation (i.e., micro-mixing) is modelled with the so-called direct quadrature method of moments coupled with the interaction and exchange with the mean approach, whereas the population balance model is solved by using the quadrature method of moments. The model is used here for the first time to model the precipitation of polymer nanoparticles of poly-ε-caprolactone via solvent-displacement with acetone and water as solvent and anti-solvent. Particle formation is described with the nucleation (by using the Classical Nucleation Theory), molecular growth and aggregation steps and a discussion on the effect of the polymer molecules behaviour in the system is presented and its effect on the results of the models is shown. The relevant rates are derived from first principles and most of the parameters appearing in the model are identified through independent measurements or from theory. Results show good agreement with experimental

[1] This chapter has been published in a shorted version in the *Chemical Engineering Science*

data and prove that the approach is very interesting, but further work is needed because, as shown, molecular characteristics of the polymer molecules can not be neglected and need to be linked with the macroscopic description of the system obtained by computational fluid dynamics. Strategies to assess the value of some missing model parameters via multi-scale modelling are also discussed.

3.1 Introduction

As anticipated, among the different processes used in the production of nanoparticles, solvent-displacement, also called flash-precipitation, is a very common technique in the production of these systems due to the possibility of using solvents with low toxicity (e.g., acetone or short-chain alcohols) and to the overall reproducibility [Fessi et al., 1989]. This process involves mixing of two solutions, the solvent and the anti-solvent (sometimes referred to as non-solvent). The solvent contains in molecular solution the particle-forming substances: drug, polymer and additives. The anti-solvent consists of a fluid miscible with the solvent in which the polymer and drug are not soluble. Solvent and anti-solvent are mixed together leading to the formation of the particles. In this work water is used as anti-solvent, conversely acetone and PCL will be used as solvent and polymer. In this first modelling attempt the presence of the drug molecules is neglected, although their effect is sometimes important [Lince et al., 2011c].

Although the amount of experimental data gathered on these and similar processes is impressive, there is still a number of issues that have to be addressed. Mathematical models are very useful in this context, since in combination with experiments, they typically help in addressing all the relevant questions and clarifying the most important uncertainties. The ideal model should describe accurately the molecular scale, for taking into account the kinetic and thermodynamic factors, as well as the reactor scale, for describing the inevitable effects of large-scale gradients. These gradients, related to inhomogeneous conditions within the mixer, are important also when very efficient mixing devices are used, because the particle formation process here investigated is often very fast if not almost instantaneous.

A very interesting approach is that based on the use of computational fluid dynamics (CFD). As concerns the production of polymer nanoparticles by solvent displacement, the particle formation process can be included in this framework

following two strategies. In the first one the process is described as self-assembly (or ordered aggregation) of the molecules of polymers in nanoparticles of increasingly larger size [Cheng et al., 2010]. This model has been coupled with CFD obtaining interesting results, although the very different time-scales of the particle formation (i.e., self-assembly) process and of mixing make the numerical solution of the model very stiff [Cheng and Fox, 2010]. With the second technique the process is modelled by using the classic theory of nucleation in which polymer molecules overcome an energy barrier, forming the nuclei of the nanoparticles, growing subsequently due to molecular growth and aggregation.

The aim of this work is to develop a predictive model (of the second type) capable of simulating the formation of particles in solvent displacement processes considering not only nucleation and molecular growth as in previous works [Woo et al., 2006, 2009] but also particles aggregation. It is particularly important to stress here that this modelling approach has never been used in the past for the simulation of polymer nanoparticle precipitation processes, more complex than other widely known precipitation processes (e.g. barium sulphate). In fact, the behaviour of polymeric chains depends on several parameters, such as process (e.g., temperature, solvent non-solvent ratio, initial polymer concentration) and molecular parameters (e.g., distribution of molecular weight, length of chains). Therefore, particular emphasize is given here to the nanoprecipitation of PCL in a CIJR considering also the influence of different anti-solvent to solvent ratios. This approach can theoretically be applied for the investigation of any precipitation or crystallization process (carried out through solvent-displacement) and therefore the validity and conclusions of this work apply to a wider research area. The processes involved are described from first principle and the parameters and properties needed to quantify their rates are highlighted in the discussion. Strategies to obtain these quantities through independent experiments and other modeling techniques are thoroughly described.

The turbulent flow in the CIJR is described via the Favre-Averaged Navier-Stokes equation approach. It is important to remind here that this part of the work is based on the conclusions of previous works where the flow field in CIJR has been extensively analysed from the experimental and modelling viewpoint [Gavi et al., 2010; Icardi et al., 2011a,b].

The influence of turbulent mixing on particle formation is modelled by using the mixture fraction approach and the closure problem is overcome by using the

Direct Quadrature Method Of Moments (DQMOM) coupled with the Interaction and Exchange with the Mean (IEM). The population balance model, describing the evolution of the particles, is solved by using the Quadrature Method Of Moments (QMOM) that allows to consider a smaller number of equations (in comparison to other approaches like those used for example in Woo et al. [2009]) preserving the overall accuracy.

This Chapter is organized as follows: after discussing some theoretical background the test case is presented and results are discussed. Eventually predictions are validated with experiments and some conclusions are drawn.

3.2 Theoretical background

The mixture density is not constant in solvent-displacement processes and varies from that of the solvent (i.e., acetone in this case, ρ_A) to that of the anti-solvent (i.e., water, ρ_W) according to the following equation:

$$\overline{\rho}(\langle\xi\rangle) = \frac{1}{\left(\frac{\langle\xi\rangle}{\rho_A} + \frac{(1-\langle\xi\rangle)}{\rho_W}\right)} \tag{3.1}$$

where $\langle\xi\rangle$ is the Favre averaged mixture fraction representing the mass fraction of acetone in the water-acetone mixture. This quantity, which is conserved along the system, is also known as Shvab-Zel'dovich variable [Lam and Bellam, 2003].

The steady-state Favre-averaged continuity and Navier-Stokes equations read as follow:

$$\frac{\partial}{\partial x_j}\left(\overline{\rho}\langle\mathbf{U}\rangle\right) = 0, \tag{3.2}$$

$$\frac{\partial}{\partial x_j}(\overline{\rho}\langle\mathbf{U}\rangle\langle\mathbf{U}\rangle) = -\frac{\partial\langle p\rangle}{\partial x_j} + \frac{\partial}{\partial x_j}\left((\mu+\mu_t)\frac{\partial\langle\mathbf{U}\rangle}{\partial x_j}\right), \tag{3.3}$$

where $\langle\mathbf{U}\rangle$ is the Favre-averaged velocity, $\langle p\rangle$ is the Favre-averaged pressure, μ and μ_t represent the molecular and turbulent viscosity respectively and $\overline{\rho}$ is the point-wise density that depends on the local composition.

3.2.1 Particle formation kinetics

The formation of the nuclei of the growing nanoparticles is described as a standard homogeneous primary nucleation process, whose driving force is the saturation ratio (S), defined as follows:

$$S(\xi) = \frac{c_s(\xi, m^{(3)})}{c_{s,eq}(\langle\xi\rangle)} \tag{3.4}$$

in which $c_s(\xi, m^{(3)})$ is the local solute (i.e., polymer in our case) concentration, $m^{(3)}$ is the third-order moment of the Particle Size Distribution (PSD) whose meaning will be clarified in the following parts of this work, and $c_{s,eq}(\xi)$ is its solubility or equilibrium concentration at the same point. Both quantities are generally a function of space since they both depend on the local composition of the mixture of the solvent and anti-solvent. The equilibrium concentration is obtained by experimental data as will be shown later. Conversely, the local solute concentration is calculated as the difference between the amount coming from the solvent stream (from its initial concentration in the solvent and the mixture fraction) and the amount that precipitates during the process (quantified by $m^{(3)}$):

$$c_s(\xi, m^{(3)}) = c_{s,in}\xi - \frac{\rho_s m^{(3)}}{6M_w\pi} \tag{3.5}$$

where M_w is the molecular weight of the polymer and ρ_s is the density of the solid nanoparticles. It is worth mentioning that this simplified approach is valid only if there is no accumulation of solute molecules in the liquid phase and if the solid nanoparticles and the liquid share the same velocity field (as in this case where particles are small and have a density very similar to that of the suspending fluids).

3.2.1.1 Nucleation

As anticipated, only homogeneous primary nucleation is considered, due to the high saturation ratio levels reached in this work. According to the classical theory [Mersmann, 1999] the nucleation rate reads as follows:

$$J(S) = \frac{2D}{d^5}\exp\left(-\frac{16\pi\gamma^3\tilde{v}^2}{3k_B^3T^3[\ln S]^2}\right) \tag{3.6}$$

where D is the molecular diffusion of solute (the explicit expression can be found in [Bird et al., 2002]), d is its molecular diameter, k_B is the Boltzmann constant, T is the absolute temperature, γ is the interfacial tension between the already formed particles and the solution; finally $\tilde{v}$ is the solute molecular volume. The size of the nuclei is instead computed as:

$$x_c(S) = 4\gamma \frac{\tilde{v}}{k_B T} \frac{1}{\ln S}. \tag{3.7}$$

The equation Eq. (3.6) will be derived in Chap. 4 along with a discussion of the hypothesis employed in the CNT and a possible extension of this theory to better describe the formation of particles by polymer molecules.

3.2.1.2 Molecular growth

Single solute molecules can be added to a growing particle through a molecular growth process. The molecules in solution are transported towards the growing nuclei where they are incorporated. This transport is due to a concentration gradients of the solute $\Delta c_s = c_s - c_{eq}$ between the bulk and the surface of the particle. This gradient can be decomposed in two contributions:

- concentration gradient between the bulk c_s and the solution layer which encloses the particles c_I which is responsible for the motion of the solute molecules from the bulk to the surface of the particle
- concentration gradient between the solution layer around the particle and the surface of the particles c, $(c - c_I)$

The mass flux towards the surface of the particle is given by:

$$\dot{m} = k_m M_W (c - c_I) = k_r M_w (c_I - c_{eq}), \tag{3.8}$$

where k_m is the matter transfer coefficients, M_w is the molecular weight of the polymer, k_r is the constant associated to the integration rate of new molecules into the growing particle. If $k_m \gg k_r$, growth is controlled by the integration and the concentration of the solute at the interface can be considered the same as those in the bulk, or rather $c_s \approx c_I$. Otherwise, if $k_m \ll k_r$ process is controlled by the matter transfer towards the particle and we obtain for the interface concentration $c_I \approx c_{s,eq}$. Because for these kinds of system the values of saturation

ratio reached inside the chamber are very high an instantaneous integration step of one solute molecule into the particle can be considered. Hence, for the typical size of the particle considered, lower than 1 μm, the rate-limiting step for the growth process is the diffusion of solute molecules towards the particle (diffusion controlled growth).

Growth rate can be expressed as:

$$G = \frac{\mathrm{d}L}{\mathrm{d}t} \tag{3.9}$$

where L is the characteristic length of the particle which is function of time. The variation of volume v_p with times is connected to the mass flow by the following relation:

$$G = \frac{\mathrm{d}L}{\mathrm{d}t} = 2\frac{M_w}{\rho_p} k_m c_{eq}(S - 1). \tag{3.10}$$

If we consider the relative slip velocity between particle to be zero it is possible to consider the asymptotic value of the Sherwood number $Sh = 2$ [Armenante and Kirwan, 1989]. This assumption is valid for small particles as those considered in this work, with characteristic dimension smaller than 1 μm. Hence, k_m can be expressed as:

$$k_m = \frac{ShD}{L} = \frac{2D}{L}. \tag{3.11}$$

And by substituing Eq. (3.11) in Eq. (3.10) one obtains

$$G(S, L) = \frac{2\mathrm{Sh}DM_w c_{s,eq}}{L\rho}(S - 1), \tag{3.12}$$

It is worth mentioning that for the system under investigation, the large dimension of solute molecules (i.e., PCL) reduces the growth rate to very small values, leaving to nucleation (and aggregation) the role of controlling the overall processes. We shall come back to this aspect later on.

3.2.1.3 Aggregation

The last process that particles undergo is aggregation, due to their frequent collisions. This process is a complex phenomenon which depends on a number of different factors involving the interactions between particles and fluid, particle and particles or the Reynolds number of the fluid (i.e., the fluid is in laminar or

turbulent conditions). This process can be resumed in two different steps:

- collision between particles
- adhesion between particles if the resulting attractive force is greater that the thermal motion and the drag of the fluid.

Let us consider a particle of radius L and a particle of radius λ of volume v_L and v_λ respectively (from now on the particles will be identified with their radius, i.e., the particle L means "the particle with radius equal to L"). Once they collide a new particle $L+\lambda$ with volume $v_{L+\lambda}$ is formed. The collision rate can be expressed as:

$$\dot{N} = \beta_{L,\lambda} n_L n_\lambda, \tag{3.13}$$

where $\beta_{L,\lambda}$ is the aggregation kernel, n_L and n_λ are the number for unit volume of particles L and λ respectively [Mei and Hu, 1999]. The functional form of $\beta_{L,\lambda}$ must be evaluated in accord with the motion of the particles. There are different collision mechanisms possibly involved that lead to different expressions for the aggregation kernel. In this work two mechanisms are considered:

- Brownian aggregation or perikinetik aggregation
- turbulent aggregation or orthokinetic aggregation.

Brownian aggregation occurs when the particles are small enough to not be affected by the motion of the fluid. Let us consider the particles of radius λ fixed in a reference frame, and a flux of particles with radius L which go through the space occupied by the fixed particle. The flux of particle L towards particle λ in the unit time is:

$$\dot{F} = 4\pi R_{L,\lambda} D_L \tag{3.14}$$

where D_L is the diffusion coefficient of the particles L obtained from the Einstein equation[2] and $R_{L,\lambda}$ is the radius of collision for the particle L and λ which can be considered equal to the sum of the radius of the two particles

$$R_{L,\lambda} = r_L + r_\lambda. \tag{3.15}$$

If attractive forces between particles are present the radius of collision between particles can be greater than that defined in the previous equation. Anyway, the

[2] Eq. (4.28)

error committed in neglecting the contribution of those attractive forces is small [Elimelech et al., 1995]. Actually, the particle λ is not fixed but is also subject to Brownian motion. Hence, in Eq. (3.14) D_L must be substituted with the mutual diffusion coefficient $D_{L,\lambda}$

$$D_{L,\lambda} = D_L + D_\lambda$$

obtaining for the number of collisions in the unit time the expression:

$$\dot{N} = 4\pi(L + \lambda)D_{L,\lambda}n_L n_\lambda. \tag{3.16}$$

By comparing this expression with Eq. (3.13) the Brownian aggregation kernel is obtained:

$$\beta_B(L, \lambda) = \frac{2kT}{3\mu}\frac{(L + \lambda)^2}{L\lambda}. \tag{3.17}$$

The turbulent aggregation mechanism was derived from Smoluchowski [1917] that obtained the collision velocity of two spherical particles in a laminar flow. Afterward, his approach was extended to turbulent flows [Saffman and Turner, 1956]. In a laminar flow the collision rate of a particle L and a particle λ which moves with relative velocity $w_{r_{L,\lambda}}$ is proportional to the flux of particles L towards a spherical surface with radius equal to the collision radius defined in Eq. (3.15), as shown in Fig. 3.1. The theory developed by Saffman and Turner [1956] can be applied to systems with homogeneous isotropic turbulence obtaining for the aggregation rate:

$$\dot{N}_{L,\lambda} = n_L n_\lambda 2\pi(L + \lambda)^2\langle|w_r|\rangle, \tag{3.18}$$

where $\langle|w_r|\rangle$ is the average value of relative velocity between particles L and λ and for particles of dimension smaller than the Kolmogorov scale[3] can be calculated as follows:

$$\langle\mid w_r \mid\rangle = \langle\mid u_{Lr} - u_{\lambda r} \mid\rangle \approx (L + \lambda)\left\langle\frac{\partial u_r}{\partial r}\right\rangle = (L + \lambda)\left(\frac{2}{15\pi}\frac{\varepsilon}{\nu}\right)^{1/2}, \tag{3.19}$$

where u_{Lr} and $u_{\lambda r}$ are the components of the velocity in the r direction of the particles L and λ which represents the distance between the two particles, ε is the turbulent kinetic dissipation rate and ν is the kinematic viscosity of the fluid. Moreover, if particle inertia (leading to local accumulation and clustering) is ne-

[3]For a definition of Kolmogorov scale see Eq. (2.71).

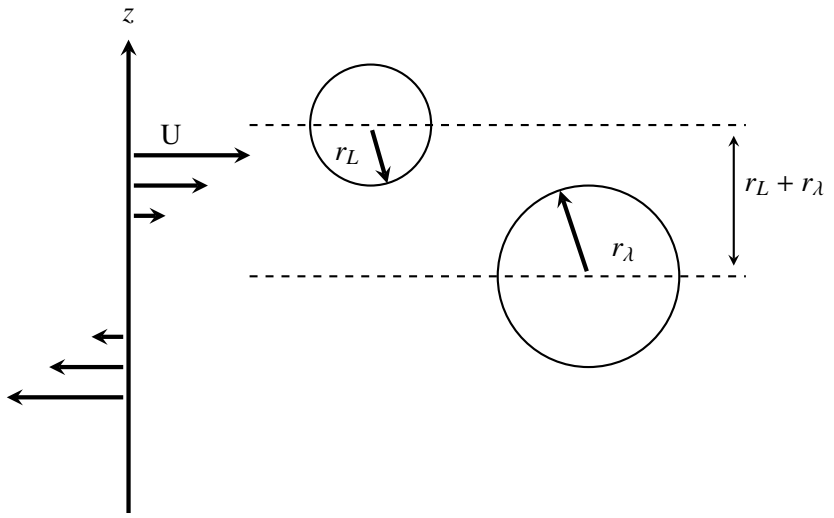

Figure 3.1: Model for the aggregation in a laminar flow. Particles on the strem line aggregate if they are at a distance smaller than the collision radius [Elimelech et al., 1995]

glected the turbulent aggregation kernel can be calculated with the following expression [Saffman and Turner, 1956; Wang et al., 2005; Marchisio et al., 2003a; Adachi et al., 1994]:

$$\beta_T(L,\lambda) = 1,294(L+\lambda)^3\left(\frac{\varepsilon}{\nu}\right)^{1/2}. \tag{3.20}$$

Brownian aggregation is generally important for particles smaller than 1 μm. A way to quantify the relative significance among the Brownian and turbulent kernel is through the Péclet number (Pe). When $Pe << 1$ turbulent mechanism is negligible, when $Pe >> 1$ Brownian mechanism is negligible.

These kernels quantify the collision frequency but since not all collisions lead to a successful aggregation event, an efficiency must be introduced. The efficiency accounts for the balance between repulsive forces, due to the electrical double layer and the drainage of the fluid, and attractive Van der Waals forces; it typically ranges from zero (no aggregation) to one (every collision produces an aggregate). Here we only consider the two limiting cases of no aggregation (i.e., zero efficiency) and complete aggregation (i.e., unitary efficiency) to carry out an estimation of the role of the aggregation mechanism in this process. Although

it is possible to consider a model for describing the efficiency of aggregation for small particles [Fuchs, 1934], and this case is discussed for a completely different particulate system in a previous work [Gavi et al., 2010], since in this case this approach is used with polymer particles it seems more sensible to compare experiments with predictions obtained under the two limits (i.e. aggregation efficiency equal to zero and one), to assess the validity of the overall approach. In a real system with an aggregation efficiency that ranges from zero to one, one would expect to obtain experimental data sets bounded by these two limiting cases. This will allow to estimate the effect of aggregation on the final nanoparticle size and to carry out a validation of the model.

3.2.1.4 Other parameters

The rates of the processes thus far described, derived from first principles, can be calculated when all the parameters appearing in Eqs. (3.4) to (3.20) are defined. For the particular case investigated here, as well as in the most common solvent-displacement processes the chemical nature of the solute (i.e., PCL) and of the suspending mixture (i.e., water and acetone) defines most of these constants. The ones adopted in this work are reported in Tab. 3.1.

Among the different parameters there are some that must be determined independently. For example, the interface tension (γ) and the equilibrium concentration of PCL ($c_{s,eq}$) used in the model are derived from experimental data obtained by Lince et al. [2008]. Both the interface tension and equilibrium concentration of PCL are function of the water molar fraction, X_{W}, of the suspending mixture that is in turn a function of the mixture fraction:

$$X_{\mathrm{W}} = \frac{(1-\xi)}{\rho_W V_{mol,\mathrm{W}}} \left(\frac{\xi}{\rho_A V_{mol,\mathrm{A}}} + \frac{1-\xi}{\rho_W V_{mol,\mathrm{W}}} \right)^{-1} \tag{3.21}$$

where $V_{mol,\mathrm{A}}$ and $V_{mol,\mathrm{W}}$ are the molecular volume of acetone and water respectively. The interfacial tension is obtained fitting data reported in [Lince et al., 2008], resulting in the following equation:

$$\gamma(\xi) = 54.122\, X\mathrm{w}^2(\xi) - 46.773\, X_{\mathrm{W}} + 32.33. \tag{3.22}$$

The equilibrium concentration of PCL in water was also obtained by the data reported in [Lince et al., 2008], resulting in the following expression for the range

of the polymer concentration we are interested in:

$$c_{s,eq}(\xi) = 1200 \exp\left[-14.533 X_W\right], \tag{3.23}$$

The molecular viscosity μ is instead calculated as follows:

$$\mu(\xi) = \exp\left[(1 - X_W)\ln\mu_A + X_W \ln\mu_W\right], \tag{3.24}$$

where μ_A and μ_W are the viscosity of pure acetone and pure water.

3.2.2 Turbulence-particle formation interactions

In Sec. 2.4.7 the transport equation for a generic scalar was introduced (Eq. (2.112)). If the scalar considered is a reactive scalar the problem of the closure of the source term arises. If we consider a flow with turbulence completely developed in which there is a second order reaction $A + B \longrightarrow P$, the transport equation for the two reactants is:

$$\frac{\partial \phi_\alpha}{\partial t} + U_j \frac{\partial \phi_\alpha}{\partial x_j} = \Gamma_\alpha \frac{\partial^2 \phi_\alpha}{\partial x_j^2} - k\phi_A\phi_B, \tag{3.25}$$

where $\alpha = A, B$ and k_2 is the kinetic constant of the reaction. If the Reynolds average[4] is applied to the previous equations one obtains the average and fluctuating part of the concentrations of the two reactants:

$$\frac{\partial \langle\phi_\alpha\rangle}{\partial t} + \langle U_j\rangle \frac{\partial \langle\phi_\alpha\rangle}{\partial x_j} = \frac{\partial}{\partial x_j}\left[(\Gamma_t + \Gamma_\alpha)\frac{\partial \langle\phi_\alpha\rangle}{\partial x_j}\right] - k(\langle\phi_A\rangle\langle\phi_B\rangle + \langle\phi'_A\phi'_B\rangle) \tag{3.26}$$

As it is possible to see the chemical source term $\langle S(\phi)\rangle = -k_2(\langle\phi_A\rangle\langle\phi_B\rangle + \langle\phi'_A\phi'_B\rangle)$ does not appear in closed form. In addition, one must consider the relation between turbulence of the flow and chemical reactions. In fact, a chemical reaction is a process which occurs at molecular scale, hence is highly sensible to the micro-scale mixing. More precisely, for slow reactions[5], the concentration of the reactants can be considered constant and equal to their average value. This im-

[4] The results presented at the end of this Chapter are obtained by solving the Favre averaged equations. Since in this section our main goal is only to present the model, a sketch of the derivation performed with the Reynold Average is presented, in order to simplify the theory.

[5] In this contest, "slow" is relative to the characteristic time of mixing.

Symbol	Definition/Value	Unit
c_s	Eq. 3.5	$\mathrm{kmol/m^3}$
$c_{s,eq}$	Eq. 3.23	$\mathrm{kmol/m^3}$
M_w	14000	kg/mol
k_B	1.38×10^{23}	$\mathrm{JK^{-1}}$
γ	Eq. 3.22	$\mathrm{J/m^2}$
T	300	K
ρ_A	780.85	$\mathrm{kg/m^3}$
ρ_W	993.68	$\mathrm{kg/m^3}$
ρ_s	1146	$\mathrm{kg/m^3}$
$\overline{\rho}$	Eq. 3.1	$\mathrm{kg/m^3}$
μ	Eq. 3.24	Pa s
μ_A	0.00031	Pa s
μ_W	0.00085	Pa s
$V_{mol,\mathrm{A}}$	0.074	$\mathrm{m^3/mol}$
$V_{mol,\mathrm{W}}$	0.055	$\mathrm{m^3/mol}$
D	$\frac{k_B T}{12\pi\mu d}$	$\mathrm{m^2/s}$
d	$2(\tilde{v}\frac{3}{4\pi})^{\frac{1}{3}}$	$\mathrm{m^3}$
Sh	2	–

Table 3.1: Definition and numerical values of the different parameters appearing in the model.

ply that the covariance $k\langle\phi'_A\phi'_B\rangle$ is negligible with respect to $k\langle\phi_A\phi_B\rangle$, or rather $k\langle\phi'_A\phi'_B\rangle \ll k\langle\phi_A\phi_B\rangle$. On the opposite side there are the instantaneous reactions[6] where the mixture is no longer homogeneous but the fluid is divided in different domain at different concentration and thus with different reaction rates. In this case $k\langle\phi_A\phi_B\rangle = 0$ from which one obtains $k\langle\phi'_A\phi'_B\rangle = -k\langle\phi_A\rangle\langle\phi_B\rangle$ and the covariance is at its maximum value.

However, in general, the fluctuating term $\langle\phi'_A\phi'_B\rangle$ needs to be closed. This closure problem is particularly complex due to the non-linear nature of the process and can be successfully overcome by employing a presumed mixture fraction Probability Density Function (PDF) approach. This method consists in assuming a functional form for the PDF and in solving the transport equations for the parameters that define the PDF itself; in this work the DQMOM-IEM [Fox, 1998, 2003; Marchisio and Fox, 2005] is used. In DQMOM-IEM the PDF is approximated with the summation of a finite number (N_e) of Dirac delta functions $\delta[\boldsymbol{\phi} - \boldsymbol{\phi}_i(\mathbf{x})]$:

$$f_{\boldsymbol{\phi}}(\mathbf{x};\boldsymbol{\phi}) = \sum_{i=1}^{N_e} p_i(\mathbf{x})\boldsymbol{\delta}[\boldsymbol{\phi} - \boldsymbol{\phi}_i(\mathbf{x})] \tag{3.27}$$

where

$$\boldsymbol{\delta}[\boldsymbol{\phi} - \boldsymbol{\phi}(\mathbf{x})] = \prod_{\alpha=1}^{N} \delta[\phi_\alpha - \phi_{\alpha_i}(\mathbf{x})]$$

and N is the dimension of the vector $\boldsymbol{\phi}$.

This corresponds to the division of the reactive environment in N_e environments each of which is characterized by a different volume fraction. In each environment every chemical species is present with concentration equal to $\phi_{\alpha,n}$. The volume fraction in each environment is defined as

$$s_{\alpha,n} = p_n\phi_{\alpha,n}$$

The weight p_n and the volume fraction evolve in accordance with the following

[6] "Instantaneous" is relative to the characteristic time of mixing.

transport equations:

$$\frac{\partial p_n}{\partial t} + \langle U_i \rangle \frac{\partial p_n}{\partial x_i} = \frac{\partial}{\partial x_i}\left(\Gamma_t \frac{\partial p_n}{\partial x_i}\right) + G_n(\mathbf{p}) \tag{3.28}$$

$$\frac{\partial s_{\alpha,n}}{\partial t} + \langle U_i \rangle \frac{\partial s_{\alpha,n}}{\partial x_i} = \frac{\partial}{\partial x_i}\left(\Gamma_t \frac{\partial s_{\alpha,n}}{\partial x_i}\right) + \mathbf{M}_{\alpha,n}(\mathbf{p}, \mathbf{s}_n) + p_n S_\alpha(\phi_n), \tag{3.29}$$

where $G_n(\mathbf{p})$ and $\mathbf{M}_{\alpha,n}(\mathbf{p}, \mathbf{s}_n)$ are functions defined in terms of probability of flux r_n outside the environment n. This probability quantifies the interactions between the environments. If one considers two environments it is possible to write:

$$G_1 = r_2 - r_1 \tag{3.30}$$

$$G_2 = r_1 - r_2 \tag{3.31}$$

and

$$M_{\alpha,1} = r_2 \phi_{\alpha,2} - r_1 \phi_{\alpha,1} \tag{3.32}$$

$$M_{\alpha,2} = r_1 \phi_{\alpha,1} - r_2 \phi_{\alpha,2} \tag{3.33}$$

The mass and volume must be conserved, hence one obtains

$$\sum_n G_n = 0 \tag{3.34}$$

$$\sum_n M_{\alpha,n} = 0 \tag{3.35}$$

and because the probabilities are normalized, the total probability must be equal to one

$$\sum_n p_n = 1,$$

thus, one of the Eq. (3.28) is redundant. The explicit expression of r_n depends from the particular micromixing model adopted.

3.2.2.1 Direct Quadrature Method Of Moments

In the DQMOM-IEM model the transport equations for the parameters defined by the PDF considered in Eq. (3.27) are solved. Each delta function is a node of a quadrature approximation and it can be thought as a reactive environment with

volume fraction p_n and local concentration of $\phi_{\alpha,n}$. The principal characteristic of these methods is to force the zeroth, first and second order moment of the PDF to be correctly predicted. Let us start from the transport equation of the PDF:

$$\frac{\partial f_\phi}{\partial t} + \langle U_i \rangle \frac{\partial f_\phi}{\partial x_i} - \frac{\partial}{\partial x_i}\left(\Gamma_t \frac{\partial f_\phi}{\partial x_i}\right) = -\frac{\partial}{\partial \psi_\alpha}[S_\alpha(\boldsymbol{\psi}) + \langle \Gamma_\alpha \nabla^2 \phi_\alpha | \boldsymbol{\psi} \rangle f_\phi], \tag{3.36}$$

where we choose the IEM method as micromixing model:

$$\langle \Gamma_\alpha \nabla^2 \phi_\alpha | \psi \rangle = \gamma(\langle \phi_\alpha \rangle - \psi_\alpha), \tag{3.37}$$

in which γ is the micromixing rate. In the case of single scalar ($N = 1$) and $\boldsymbol{\phi} = \phi$ if Eq. (3.27) is substituted in Eq. (3.36) one obtains, after some algebraic manipulation:

$$\sum_{n=1}^{N_e} [\delta(\psi - \phi_n) + \delta'(\psi - \phi_n)\phi_n]a_n - \sum_{n=1}^{N_e} \delta'(\psi - \phi_n) b_n = \sum_{n=1}^{N_e} \delta''(\psi - \phi_n) c_n + S(\psi),$$

where the following substitutions were used:

$$a_n = \frac{\partial p_n}{\partial t} + \langle U_i \rangle \frac{\partial p_n}{\partial x_i} - \frac{\partial}{\partial x_i}\left(\Gamma_t \frac{\partial p_n}{\partial x_i}\right) \tag{3.38}$$

$$b_n = \frac{\partial p_n \phi_n}{\partial t} + \langle U_i \rangle \frac{\partial p_n \phi_n}{\partial x_i} - \frac{\partial}{\partial x_i}\left(\Gamma_t \frac{\partial \phi_n p_n}{\partial x_i}\right) \tag{3.39}$$

$$c_n = p_n \Gamma_t \frac{\partial \phi_n}{\partial x_i} \frac{\phi_n}{\partial x_i}, \tag{3.40}$$

and where $\delta'(x)$ and $\delta''(x)$ are the first and second derivatives of the dirac delta function $\delta(x)$. The k-th moment of Eq. (3.38) defined as:

$$\langle \phi^k \rangle = \int_0^{+\infty} \psi^k f_\phi(\psi) d\psi, \tag{3.41}$$

is calculated by using the following properties of the Dirac delta function:

$$\int_0^{+\infty} \delta(\psi - \phi_n)\psi^k)d\psi = \phi_n^k$$
$$\int_0^{+\infty} \delta'(\psi - \phi_n)\psi^k)d\psi = -k\phi_n^{k-1}$$
$$\int_0^{+\infty} \delta''(\psi - \phi_n)\psi^k)d\psi = k(k-1)\phi_n^{k-2}.$$

A linear equation in a_n and b_n is obtained:

$$(1-k)\sum_{n=1}^{N_e} \phi_n^k a_n + k\sum_{n=1}^{N_e} \phi_n^{k-1} b_n = \langle S_k^{(N_e)} \rangle + \langle C \rangle_k, \tag{3.42}$$

with

$$\langle S_k^{(N_e)} \rangle = \int_0^{+\infty} \psi^k S(\psi)d\psi = -k\sum_{n=1}^{N_e} p_n \phi_n^{k-1} S(\phi_n) \tag{3.43}$$

$$\langle C \rangle_k = k(k-1)\sum_{n=1}^{N_e} \phi_n^{k-2} c_n. \tag{3.44}$$

If we consider $N_e = 2$, when $k = 0$ in Eq. (3.42) we obtain that $a_1 + a_2 = 0$. Hence the value of a_0 and a_1 can be arbitrary chosen and the most convenient choice is to put $a_1 = a_2 = 0$. The other terms, b_1 and b_2, are calculated by using the transport equation of the first and second order moment ($k = 1, 2$) of the PDF obtained by Eq. (3.42) in which Eqs. (3.43) and (3.44) are substituted:

$$k\sum_{n=1}^{N_e} \phi^{k-1}(b_n + p_n S(\phi_n)) = k(k-1)\sum_{n=1}^{N_e} \phi^{k-2} c_n \quad k = 1, k = 2 \tag{3.45}$$

from which results that:

$$b_1 = \frac{c_1 + c_2}{\phi_2 - \phi_1} = -b_2$$

Eventually, the DQMOM-IEM with two environments and one scalar (ϕ) consists of the following three transport equations:

$$\frac{\partial p_1}{\partial t} + \langle U_i \rangle \frac{\partial p_1}{\partial x_i} - \frac{\partial}{\partial x_i}\left(\Gamma_t \frac{\partial p_1}{\partial x_i}\right) = 0 \qquad (p_2 = 1 - p_2) \tag{3.46}$$

$$\frac{\partial p_1\phi_1}{\partial t} + \langle U_i \rangle \frac{\partial p_1\phi_1}{\partial x_i} - \frac{\partial}{\partial x_i}\left(\Gamma_t \frac{\partial p_1\phi_1}{\partial x_i}\right) = \gamma p_1 p_2[\phi_2 - \phi_1] + p_1 S(\phi_1) + \frac{c_1 + c_2}{\phi_2 - \phi_1} \tag{3.47}$$

$$\frac{\partial p_2\phi_2}{\partial t} + \langle U_i \rangle \frac{\partial p_2\phi_2}{\partial x_i} - \frac{\partial}{\partial x_i}\left(\Gamma_t \frac{\partial p_2\phi_2}{\partial x_i}\right) = \gamma p_1 p_2[\phi_1 - \phi_2] + p_2 S(\phi_2) + \frac{c_1 + c_2}{\phi_1 - \phi_2} \tag{3.48}$$

The generalization to a multi-variate case is straightforward

$$\frac{\partial p_1\phi_{\alpha,1}}{\partial t} + \langle U_i \rangle \frac{\partial p_1\phi_{\alpha,1}}{\partial x_i} - \frac{\partial}{\partial x_i}\left(\Gamma_t \frac{\partial p_1\phi_{\alpha,1}}{\partial x_i}\right) = \gamma p_1 p_2[\phi_{\alpha,2} - \phi_{\alpha,1}] + p_1 S_\alpha(\boldsymbol{\phi}) + \frac{c_{\alpha,1} + c_{\alpha,2}}{\phi_{\alpha,2} - \phi_{\alpha,1}}$$

$$\frac{\partial p_2\phi_{\alpha,2}}{\partial t} + \langle U_i \rangle \frac{\partial p_2\phi_{\alpha,1}}{\partial x_i} - \frac{\partial}{\partial x_i}\left(\Gamma_t \frac{\partial p_2\phi_{\alpha,2}}{\partial x_i}\right) = \gamma p_1 p_2[\phi_{\alpha,1} - \phi_{\alpha,2}] + p_2 S_\alpha(\boldsymbol{\phi}) + \frac{c_{\alpha,1} + c_{\alpha,2}}{\phi_{\alpha,1} - \phi_{\alpha,2}}$$

with

$$c_{\alpha,n} = p_n \Gamma_t \frac{\partial \phi_{\alpha,n}}{\partial x_i} \frac{\phi_{\alpha,n}}{\partial x_i}. \tag{3.49}$$

The micromixing rate γ at the right hand side is expressed by the following relation [Corrsin, 1964]

$$\gamma = \frac{C_\phi}{2} \frac{\varepsilon}{k}. \tag{3.50}$$

where C_ϕ is the mechanical-to-scalar ratio calculated as a function of the local Reynolds number [Gavi et al., 2007a], ε is the turbulent dissipation rate and k is the turbulent kinetic energy. The third term is the correction term that derives from the finite-mode representation and allows to correctly predict the evolution of the moments of the PDF [Wang and Fox, 2004].

In this work the number of environments chosen is $N_e = 2$ and by considering

as the scalar quantity the local composition identified by the local mixture fraction, ξ_n, the presumed PDF in which each delta function is a node of a quadrature approximation or a fluid environment of volume fraction, p_n results in the following expression:

$$f_\xi(\mathbf{x};\xi) = \sum_{i=1}^{N_e} p_i(\mathbf{x})\delta[\xi - \xi_i(\mathbf{x})], \tag{3.51}$$

where f_ξ is the mixture fraction PDF. In this case three equations must be solved and the first equation is the transport equation for the weight of the first node (or volume fraction of the first environment) averaged according to the Favre average:

$$\frac{\partial}{\partial x_j}(\overline{\rho}\langle\mathbf{U}\rangle p_1) - \frac{\partial}{\partial x_j}\left(\Gamma_t \frac{\partial p_1}{\partial x_j}\right) = 0 \tag{3.52}$$

Γ_t is the turbulent diffusivity, calculated through a turbulent $Sc^{(t)}$ taken equal to 0.7. Recalling that the PDF integrates to unity, the sum of the probabilities for each environment must be equal to one and therefore no transport equation for p_2 must be solved since: $p_2 = 1 - p_1$

The second and third equations are the transport equations for the mixture fraction in each of the two environments:

$$\frac{\partial}{\partial x_j}(\overline{\rho}\langle\mathbf{U}\rangle p_1\xi_1) - \frac{\partial}{\partial x_j}\left(\Gamma_t \frac{\partial}{\partial x_j}(p_1\xi_1)\right) = \gamma_M p_1 p_2[\xi_2 - \xi_1]\overline{\rho} + \frac{\Gamma_t}{\xi_1 - \xi_2}\left(p_1 \frac{\partial \xi_1}{\partial x_j}\frac{\partial \xi_1}{\partial x_j} + p_2 \frac{\partial \xi_2}{\partial x_j}\frac{\partial \xi_2}{\partial x_j}\right), \tag{3.53}$$

$$\frac{\partial}{\partial x_j}(\overline{\rho}\langle\mathbf{U}\rangle p_2\xi_2) - \frac{\partial}{\partial x_j}\left(\Gamma_t \frac{\partial}{\partial x_j}(p_2\xi_2)\right) = \gamma_M p_1 p_2[\xi_1 - \xi_2]\overline{\rho} + \frac{\Gamma_t}{\xi_2 - \xi_1}\left(p_1 \frac{\partial \xi_1}{\partial x_j}\frac{\partial \xi_1}{\partial x_j} + p_2 \frac{\partial \xi_2}{\partial x_j}\frac{\partial \xi_2}{\partial x_j}\right). \tag{3.54}$$

By using this approach the average mixture fraction can be calculated as:

$$\langle\xi\rangle(\mathbf{x}) = \int_0^1 f_\xi(\mathbf{x};\xi)d\xi = p_1(\mathbf{x})\xi_1(\mathbf{x}) + p_2(\mathbf{x})\xi_2(\mathbf{x}) \tag{3.55}$$

whereas the mixture fraction variance (or small-scale variance, SSV)

$$\langle \xi'^2 \rangle(\mathbf{x}) = \int_0^1 (\xi - \langle \xi \rangle)^2 \, f_{\xi}(\mathbf{x}; \xi) d\xi = p_1(\mathbf{x}) p_2(\mathbf{x}) \, (\xi_1(\mathbf{x}) - \xi_2(\mathbf{x}))^2 \tag{3.56}$$

which is very important in quantifying the segregation at the molecular scale of water and acetone molecules.

Besides molecular segregation, the segregation at the reactor scale is also very important and can be quantified through the difference between the actual value of the mean mixture fraction $\langle \xi \rangle$ and the value of the mixture fraction when the solvent and anti-solvent are completely mixed, $\overline{\xi}$:

$$\langle \xi'^2 \rangle_{LS}(\mathbf{x}) = \left(\langle \xi \rangle(\mathbf{x}) - \overline{\xi} \right)^2, \tag{3.57}$$

resulting in a quantity that is often referred to as large-scale variance (LSV).

The SSV, $\langle \xi'^2 \rangle$, and the LSV, $\langle \xi'^2 \rangle_{LS}$, quantify the level of mixedness in the solvent-displacement process and when they are both equal to zero the system is defined as perfectly micro- and macro-mixed.

3.2.2.2 Scalar-to-mechanical ratio

The term C_ϕ is defined as:

$$C_\phi = \frac{k \varepsilon_\phi}{\varepsilon \langle \phi'^2 \rangle} = \frac{2 \tau_u}{\tau_\phi} \tag{3.58}$$

and represents the adimensional expression for the mixing time of the scalar τ_ϕ where $\tau_u = {}^{k}/_{\varepsilon}$ is the integral time scale of the turbulence. For a fixed Schmidt number, C_ϕ is function of the local Reynolds number:

$$Re_l = \frac{k}{(\varepsilon \nu)^{1/2}}. \tag{3.59}$$

In the standard equal-scales model, for high local Reynolds number (i.e., $Re_l > 1000$, system with fully developed turbulence) it is assumed that $C_\phi \approx 2$. However, in systems with $Sc \gg 1$ as in the liquids by assuming $C_\phi \approx 2$ the micromixing velocity in Eq. (3.50) is overestimated. Hence, we do not consider the constant value of C_ϕ but a different route is taken. The value of C_ϕ is obtained

by integrating over all the scalar spectrum[7] $E_\phi(\kappa)$ obtaining the dependence of C_ϕ from the local Reynolds number. This dependence was obtained by Liu and Fox [2005] by assuming $Sc = 1000$ and is reported in Fig. 3.2. The shape of

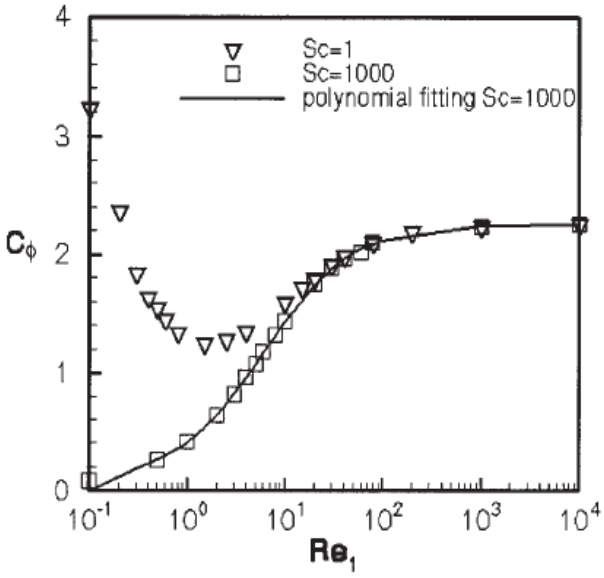

Figure 3.2: Dependence of C_ϕ from local Reynolds number for gases Sc = 1 (▽) and for liquids Sc = 1000 (□) [Liu and Fox, 2005]

the spectrum has a great influence on C_ϕ especially for low Reynolds numbers as it is possible to see from Fig. 3.2. The dependence of C_ϕ from Re_l can be approximated by the following expression [Liu and Fox, 2005]

a_0	a_1	a_2	a_3	a_4	a_5	a_6
0.4093	0.6015	0.5851	0.09472	-0.3903	0.1461	-0.01604

Table 3.2: Interpolation coefficient for C_ϕ [Liu and Fox, 2005]

[7] Cf. Sec. 2.4.7.3

$$C_\phi = \sum_{n=0}^{6} a_n (\ln_{10} Re_l)^n \quad \text{for} \quad Re_l \leq 0,2 \tag{3.60}$$

where the values of a_n are reported in Table 3.2.

3.2.3 Population balance model

In the analysis of a system of particles the behaviour of a population of particles is described by considering the behaviour of a single particle. The population of particles is described by using the density of an extensive variable, usually the number of particle. The basic assumption for the population balance model is that exists a numerical density function of the particles in a specified domain.

In order to describe the characteristics and behaviour of the particles it is possible to use two different kinds of coordinates, the internal and external ones: the internal coordinates $\boldsymbol{\xi} \equiv (\xi_1, \xi_2, \ldots, \xi_d)$ represent d different quantities associated to the particles, as the velocity or characteristic dimension. On the other hand, the external coordinates $\mathbf{x} \equiv (x_1, x_2, x_3)$ are the positions of the particles in the physical domain. We define the state vector of the particles as $(\boldsymbol{\xi}, \mathbf{x})$ which represents internal and external coordinates. Let us now consider the set $\boldsymbol{\Omega}_{\boldsymbol{\xi}}$ as the domain for the internal coordinates and $\boldsymbol{\Omega}_{\mathbf{X}}$ as the domain for the external coordinates which represent a subset of the physical space.

The population of particles can be seen as distributed randomly in the $d + 3$-dimensional space which includes the external and internal coordinates. We can define the vector $\mathbf{Y}(\mathbf{x}, t) \equiv [Y_1(\mathbf{x}, t), Y_2(\mathbf{x}, t), \ldots, Y_c(\mathbf{x}, t)]$ which is function of the external coordinates $\mathbf{x}$ and of time only.

Therefore, let us assume that such a numerical density function exists:

$$E[n(\boldsymbol{\xi}; \mathbf{x}, t)] \equiv f_1(\boldsymbol{\xi}; \mathbf{x}, t), \quad \boldsymbol{\xi} \in \boldsymbol{\Omega}_{\boldsymbol{\xi}}, \quad \mathbf{x} \in \boldsymbol{\Omega}_{\mathbf{x}}, \tag{3.61}$$

the first member is the expected value of the numerical density function $n(\boldsymbol{\xi}; \mathbf{x}, t)$ at a given instant whilst $f_1(\boldsymbol{\xi}; \mathbf{x}, t)$ is the average value of the numerical density function. This definition implies that the average value of the particles in the infinitesimal volume $\mathrm{d}V_{\boldsymbol{\xi}}\mathrm{d}V_{\mathbf{x}}$ in the state $(\boldsymbol{\xi}, \mathbf{x})$ is $f_1(\boldsymbol{\xi}; \mathbf{x}, t)\mathrm{d}V_{\boldsymbol{\xi}}\mathrm{d}V_{\mathbf{x}}$. The function $f_1(\boldsymbol{\xi}; \mathbf{x}, t)$ is assumed to be sufficiently smooth to be derivable in all its arguments.

The total number of particles in the system is defined as Ramkrishna [2000]:

$$\int_{\mathbf{\Omega}_\xi} dV_\xi \int_{\mathbf{\Omega}_\mathbf{x}} dV_x f_1(\boldsymbol{\xi}, \mathbf{x}, t) \tag{3.62}$$

The total number of particles for unit volume in the physical space is given by:

$$N(\mathbf{x}, t) = \int_{\mathbf{\Omega}_\xi} dV_\xi f_1(\boldsymbol{\xi}, \mathbf{x}, t) \tag{3.63}$$

If we are interested in obtaining the value of the numerical density of the particles of a certain class in a subset A_ξ of $\mathbf{\Omega}_\xi$ one must integrate the numerical density function in the given subset.

3.2.3.1 Population Balance Equation

In this paragraph the population balance equation (PBE) will be derived for the monodimensional case. The only internal coordinate cosidered is the dimension of the particles $\xi \equiv L$ which corresponds to the radius of the particles in the case of spherical particles and it can varies from 0 to $+\infty$. It is also assumed that the particles are uniformly distributed in the space, hence the numerical density is independent from external coordinates.

In the first part of the derivation the independence of the characteristics of the particles (size) from the environment will be assumed in order to simplify the derivation of the main equations of the model. Hence, the saturation ratio in our system will be considered constant and therefore nucleation rate and growth rate will be constant with respect to this parameter. In the system we are considering this hypothesis is seldom verified, hence at the end of this Section the generalization will be showed.

In Eq. (3.9) the growth rate of a particle with size L was defined. Let us consider a region A_L of the space of the internal coordinates which corresponds to an interval $[a, b]$; the number of particles in this interval changes with time: the size of some particles can increase beyond b or rather it can decrease below a. The variation of the number of particles in the interval characterized by a length $a \leq L \leq b$ can be expressed as:

$$G(b, t) f_1(b, t) - G(a, t) f_1(a, t), \tag{3.64}$$

where $f_1(b,t)$ is the numerical density function. The two terms in the above equation can be seen as a flux of particles, the first entering in a, the second leaving the set from b. Hence, this equation represents the net flux with size between a and b. If other processes, which result in a change of the size of the particles, are not present, it is possible to write for the numerical balance in the same interval:

$$\frac{\mathrm{d}}{\mathrm{d}t}\int_a^b f_1(L,t)dL = G(b,t)f_1(b,t) - G(a,t)f_1(a,t) \tag{3.65}$$

which can be rewritten as[8]:

$$\int_a^b \left[\frac{\partial f_1(L,t)}{\partial t} + \frac{\partial}{\partial L}\left(G(L,t)f_1(\xi,t)\right)\right]dL = 0. \tag{3.66}$$

Because the integration interval $[a,b]$ is arbitrary, is required for the integrand to be zero to fulfil the equality. Hence:

$$\frac{\partial f_1(L,t)}{\partial t} + \frac{\partial}{\partial L}\left(G(L,t)f_1(\xi,t)\right) = 0 \tag{3.67}$$

An initial condition and a contour condition must be added to this equation. As initial condition is often considered that there are no particles in the system at time zero ($t = 0$), i.e., $f_1(L,0) = 0$ for each $L \geq 0$. Let $J(t)$ be the nucleation velocity for unit time, as contour condition it is assumed that the new particles have size $L = x_c$. Hence it is possible to write:

$$G(x_c,t)f_1(x_c,t) = J(t). \tag{3.68}$$

If Eq. (3.67) is integrated over all the possibles sizes of the particles, by remembering that for $L < x_c$ there are no particles in the system, one obtains:

$$\frac{\mathrm{d}N}{\mathrm{d}t} = \frac{\mathrm{d}}{\mathrm{d}t}\int_{x_c}^{+\infty} f_1(L,t)dL = G(0,t)f_1(0,t) - G(\infty,t)f_1(\infty,t) = J(t) \tag{3.69}$$

The last equality follows by considering that particles can increase their number

[8]Because we have supposed regular and smooth function.

only by nucleation, and by recalling Eq. (3.68) we can conclude that

$$G(\infty, t) f_1(\infty, t) = 0, \tag{3.70}$$

which is called regularity condition. This equation states that for arbitrary large size the growth of the particles and the numerical density of the particles must be zero. In deriving Eq. (3.67) it was not considered the born and death of particle in the interval $[a, b]$. Therefore, it is possible to extend this derivation by adding the generation term for the particles $h(L, t)$. The net generation of the particles in the interval $[L, L + dL]$ will be $h(L, t)dL$. The explicit form of $h(L, t)$ will depend on the particular model used for the aggregation and breakage considered. Accordingly it is possible to write Eq. (3.66) as:

$$\int_a^b \left[\frac{\partial f_1(L,t)}{\partial t} + \frac{\partial}{\partial L} \left(G(L,t) f_1(x,t) \right) - h(L,t) \right] dL = 0. \tag{3.71}$$

from which the PBE becomes:

$$\frac{\partial f_1(L,t)}{\partial t} + \frac{\partial}{\partial L} \left(G(L,t) f_1(x,t) \right) = h(L,t). \tag{3.72}$$

As contour and initial conditions Eqs. (3.68) and (3.70) still hold. If we consider the total numeric balance

$$\frac{dN}{dt} = J(t) + \int_{x_c}^{+\infty} h(L,t) dL \tag{3.73}$$

the regularity condition on the numerical density function still hold. Now, let us eliminate the starting hypothesis of constant saturation ratio and let us say that the behaviour of the particles will depend from this variable too. If we put $Y \equiv S$ we found that:

- the nucleation rate will depend from S also, thus $J = J(S, t)$;
- the growth rate will depend from S also, thus $G = G(S, t)$;
- growth process decreases the saturation ratio proportionally with the size

of the particles:

$$\frac{\mathrm{d}S}{\mathrm{d}t} = -\int_{x_c}^{+\infty} \alpha(L)G(L,S,t)f_1(L,t)dL; \tag{3.74}$$

- the source term can depend from S also. It will be considered in the next Section.

Accordingly, we obtain:

$$\frac{\partial f_1(L,t)}{\partial t} + \frac{\partial}{\partial L}\left(G(L,S,t)f_1(x,t)\right) = h(L,S,t) \tag{3.75}$$

The initial condition is the same as the previous case ($f_1(L,0) = 0$ for each $L \geq 0$ at $t = 0$), whereas for the contour condition we must add the dependence of the nucleation and growth term from the saturation ratio:

$$G(x_c,S,t)f_1(x_c,t) = J(S,t). \tag{3.76}$$

Eq. (3.74) must be considered with the equation which describes the saturation ratio variation due to nucleation and particles growth:

$$\frac{dS}{dt} = -\int_{x_c}^{+\infty} \alpha(L)G(L,S,t)f_1(L,t)dL \tag{3.77}$$

Eventually, an initial condition for the saturation ratio must be added to complete the description of the problem. A complete and more general derivation of the population balance can be found in Ramkrishna [2000].

3.2.3.2 Source term analysis

In the previous Section the number of particles in the interval $[a,b]$ varied thanks to a flux of particles in or outside the interval considered. In this Section the birth and death process of particles which can occur in all the points of the phase space will be analysed. The physical phenomena underlying the birth and death processes are the aggregation and breakage respectively. Even if in this kind of systems the breakage of the particle is a rare events which can be neglected a short description of this process will still be made.

The aggregation frequency is the probability for unit time that two particles in some point of the space aggregate, or rather the fraction of couples of particles which aggregates for unit time. This definition must be slightly modified because in the population balance the external coordinates do not compare explicitly in the equation. It is possible to assume that the population of particles is small enough that in an infinitesimal interval of time $\mathrm{d}t$ the probability that more than two particles at the same time aggregates is negligible[9]. Let us define the probability that a particle in the state $(L, \mathbf{x})$ and a particle in the state $(L', \mathbf{x}')$ at the instant t with local value of saturation ratio S will aggregate in the time interval $[t, t + \mathrm{d}t]$ as:

$$\beta(L, \mathbf{x}, L', \mathbf{x}'; S, t)\mathrm{d}t. \tag{3.78}$$

The previous definition holds for an ordinate pair of particles. However, from a physical point of view there is no difference between the order of the particles in the aggregation. Hence, the aggregation probability $\beta(L, \mathbf{x}, L', \mathbf{x}'; S, t)$ must be symmetric under exchange of particles:

$$\beta(L, \mathbf{x}; L', \mathbf{x}'; S, t) = \beta(L', \mathbf{x}'; L, \mathbf{x}; S, t). \tag{3.79}$$

In order to formulate the birth and death term in the population balance it is necessary to identify the state of the particles which is formed by the aggregation (or breakage) process. Therefore, if we call the two aggregating particles A and B and the resulting particle from the aggregation process C it is assumed that it is possible to determine the state of B by giving the state of A and C[10]. Hence, by using the state of the new formed particle $(L, \mathbf{x})$ and the state of one of the aggregating particles $(L', \mathbf{x}')$ the state of the other particles of the couple is given by $[\tilde{L}(L, \mathbf{x}|L', \mathbf{x}'), \tilde{\mathbf{x}}(L, \mathbf{x}|L', \mathbf{x}')]$. It is possible to define the density distribution function of the number of couples $f_2(L, \mathbf{x}; L', \mathbf{x}', t)$ which represents the number of distinct particles at time t per unit volume localized at the coordinate $(L, \mathbf{x})$ and

[9]The probability that more than two particles aggregates in an infinitesimal interval of time is of the order of $O(\mathrm{d}t^2)$, hence negligible with respect to $\mathrm{d}t$. Let us remind here that a term is said to be of order $O(\mathrm{d}t^n)$ if this condition holds: $\lim_{dt\to 0} \frac{\mathrm{d}t^n}{\mathrm{d}t^k} = \begin{cases} 0, & k < n \\ \infty, & k = n \end{cases}$

[10]By recalling the symmetry requirements on the aggregation probability one obtains that this definition is symmetrical, i.e., it is completely equivalent to say "it is possible to determine the state of A by giving the state of B and C"

$(L', \mathbf{x}')$ respectively. The source term for the production of particles in the volume $(L, \mathbf{x})$ of the phase space is denoted as $h^+(L, \mathbf{x}, S, t)$ which is function of the coordinates of the two colliding particles $(L', \mathbf{x})$ and $[\tilde{L}(L, \mathbf{x}|L', \mathbf{x}'), \tilde{\mathbf{x}}(L, \mathbf{x}|L', \mathbf{x}')]$. Therefore, one must transform these coordinates in the coordinates $(L, \mathbf{x})$ by using the Jacobian of the transformation. It is possible to write[11]:

$$h^+(L, \mathbf{x}, t) = \int_{\Omega_\xi} dV_{\xi'} \int_{\Omega_x} \frac{1}{\delta} dV_{x'} \beta(\tilde{L}, \tilde{\mathbf{x}}; L', \mathbf{x}', t) f_2(\tilde{L}, \tilde{\mathbf{x}}; L', \mathbf{x}', t) \frac{\partial(\tilde{L}, \tilde{\mathbf{x}})}{\partial(L, \mathbf{x})} \quad (3.80)$$

where δ is the number of times that the same couples are considered in the integration interval, hence the term $1/\delta$ corrects for the multiples of the same couple. The death term for the particle $h^-(L, \mathbf{x}, S, t)$ is defined as:

$$\int_{\Omega_\xi} dV_{\xi'} \int_{\Omega_x} \frac{1}{\delta} dV_{x'} \beta(L', \mathbf{x}'; L, \mathbf{x}, S) f_2(L', \mathbf{x}'; L, \mathbf{x}, t) \quad (3.81)$$

In the previous equations, the function $\beta(\tilde{L}, \tilde{\mathbf{x}}; L', \mathbf{x}')$ must vanish for state $(L', \mathbf{x}')$ in which $(\tilde{L}, \tilde{\mathbf{x}})$ has non physical values. Once the death and birth term of the particles are written explicitly we can substitute $h^+ - h^-$ in Eq. (3.72) to obtain the final form for the population balance. In is important to highlight here that the equation obtained is not in closed form because the function f_2 is not known. In order to close this equation we can consider the following approximation:

$$f_2(L', \mathbf{x}'; L, \mathbf{x}, t) = f_1(L', \mathbf{x}', t) f_1(L, \mathbf{x}, t) \quad (3.82)$$

The latter equation states that there are no statistical correlation between different states of particles at every t. This approximation is more accurate as the dilution of the system increases, because interactions between particles are the lowest as possible.

A particle of size L is created by the aggregation of two particles of size $\sqrt[3]{L^3 - L'^3}$ and L' respectively with an aggregation frequency of $\beta(\sqrt[3]{L^3 - L'^3}, L')$. The source term for the aggregation $h(L, t)$ is equal to the difference between the

[11] Because the aggregation kernel does not depend form the saturation ratio we omit it in the definition of the birth and death terms.

birth term which expresses the formation of particles of size L

$$h^{+}(L,t) = \frac{L^2}{2}\int_0^L \frac{\beta(\sqrt[3]{L^3-L'^3},L')f_1(L',\mathbf{x}',t)f_1(\sqrt[3]{L^3-L'^3},\tilde{\mathbf{x}},t)}{(L^3-L'^3)^{\frac{2}{3}}}dL', \quad (3.83)$$

and the death term $h^{-}(L,t)$ which expresses the disappearing from the system of a particle of size L

$$h^{-}(L,t) = f_1(L,t)\int_0^{\infty}\beta(L,L')f_1(L',t)dL'. \quad (3.84)$$

Therefore, it is obtained for the source term

$$\begin{aligned} h(L,t) = {} & \frac{L^2}{2}\int_0^L \frac{\beta(\sqrt[3]{L^3-L'^3},L)f_1(L',\mathbf{x}',t)f_1(\sqrt[3]{L^3-L'^3},\tilde{\mathbf{x}},t)}{(L^3-L'^3)^{\frac{2}{3}}}dL' \\ & - f_1(L,t)\int_0^{\infty}\beta(L,L')f_1(L',t)dL' \end{aligned} \quad (3.85)$$

where $\beta(L,\lambda)$ is the aggregation kernel, calculated as the summation of the Brownian and turbulent shear kernels reported in Eqs. (3.17) and (3.20). A more extensive treatment of the aggregation-breakage process can be found in [Marchisio et al., 2003b].

3.2.3.3 Quadrature method of moments

By applying the Favre average to the PBE the averaged-PBE equation is obtained. The functional form of the nucleation, molecular growth and aggregation term was already obtained in Sec. 3.2.1.1 to 3.2.1.3. Hence, the final equation appears to be:

$$\begin{aligned} \frac{\partial\overline{\rho}\langle f_1(L;\mathbf{x},t)\rangle}{\partial t} + \langle U_j\rangle\frac{\partial\overline{\rho}\langle f_1(L;\mathbf{x},t)\rangle}{\partial x_j} = {} & \frac{\partial}{\partial x_j}\left[\Gamma_t\frac{\partial\langle f_1(L;\mathbf{x},t)\rangle}{\partial}\right] + \overline{\rho}\langle J(S)\rangle \\ & + \overline{\rho}\left(\frac{\partial}{\partial L}\left[\langle G(S,L)\rangle f_1(L;\mathbf{x},t)\right] + \langle h(L;\mathbf{x},t)\rangle\right). \end{aligned} \quad (3.86)$$

In this particular application the PBE is usually written as a continuity state-

ment for the Favre-averaged PSD $\langle n \rangle(L;\mathbf{x})$ [Ramkrishna, 2000]

$$\frac{\partial}{\partial x_j}(\overline{\rho}\langle \mathbf{U} \rangle \langle n \rangle(L;\mathbf{x})) = \frac{\partial}{\partial x_j}\left(\Gamma_t \frac{\partial}{\partial x_j}\langle n \rangle(L;\mathbf{x})\right) + \overline{\rho}\langle J(S) \rangle + \overline{\rho}\left(\frac{\partial}{\partial L}\left(\langle G(S,L)n(L;\mathbf{x}) \rangle\right) + \langle B \rangle(L;\mathbf{x}) + \langle D \rangle(L;\mathbf{x})\right), \quad (3.87)$$

where $\langle J \rangle$ is the Reynolds-averaged nucleation rate and $\langle B \rangle(L;\mathbf{x})$ and $\langle D \rangle(L;\mathbf{x})$ are the Reynolds-averaged birth and death rates due to aggregation (Eqs. (3.83) and (3.84)) and where the temporal dependence in the PSD was removed because we are considering a steady-state problem.

Closer observation of Eq.(3.87) highlights the presence of different closure problems related to the effect of turbulent fluctuations on particle transport, nucleation, growth and aggregation. The closure problem related to particle transport is overcome by introducing the turbulent diffusivity, Γ_t, fixed equal to that of the other scalars involved due to the very small Stokes number of the particles analyzed in this study [Baldyga and Orciuch, 2001]. For the very same reason the particle velocity can be assumed equal to that of the fluid mixture, $\langle \mathbf{U} \rangle$, and therefore the system can be treated as pseudo-homogeneous.

The Eq. (3.87) will be solved with the QMOM whose validity in this kind of problems was already investigated [Marchisio et al., 2003a]. The QMOM solves the PBE by using the first n moments of the PSD and the closure problem is overcome by a quadrature approximation. Therefore, the PBE is transformed into a transport equation of the moment of the PSD and all the terms are written as function of the same moments. Let us defune the k-th moment of the PSD as[12]

$$m^{(k)}(\mathbf{x}) \equiv \int_0^{+\infty} n(L;\mathbf{x}) L^k dL \quad (3.88)$$

and the k-th Reynolds-averaged moment of the PSD as:

$$\langle m^{(k)} \rangle(\mathbf{x}) \equiv \int_0^{\infty} \langle n \rangle(L;\mathbf{x}) L^k dL, \quad (3.89)$$

[12] In general they are function of the time t also

The quadrature approximation is based on the following equation:

$$m_k \approx \sum_{i=1}^{N_d} w_i L_i^k$$

in which the weights (w_i) and the abscissas (L_i) are determined through the Product-Difference (PD) algorithm [Gordon, 1968] from the lowest order moments. PD algorothm is based on the minimization of the error committed by replacing Eq. (3.88) with its approximate expression. From the first N_d moments is possible to determine the $N_d/2$ abscissas and the $N_d/2$ weights which minimizes this error. These are obtained by a tri-diagonal matrix with rank equal to $N_d/2$ whose eigenvalues are the abscissas and the first square component of its eigenvectors are the weights of the quadrature approximation [Marchisio et al., 2003b]. If N_d nodes are considered for the quadrature approximation it is possible to use the moments from order $k = 0$ to order $2N_d - 1$. In this work $N_d = 2$ from which one obtains:

$$m_k = \sum_{i=1}^{N_d=2} w_i L_i^k = w_1 L_1^k + w_2 L_2^k.$$

The knowledge of w_i and L_i^k is sufficient to close the transport equation of the moments

$$\langle U_i \rangle \frac{\partial m_k(\mathbf{x})}{\partial x_i} - \frac{\partial}{\partial x_i}\left[\Gamma_t \frac{\partial m_k(\mathbf{x})}{\partial x_i}\right] = (x_c)^k J(\mathbf{x}) + \overline{B}^{(k)}(\mathbf{x}) - \overline{D}^{(k)}(\mathbf{x}) + \int_0^{+\infty} k L^{k-1} G(L) n(L;\mathbf{x}) dL$$

where $J(\mathbf{x})$ is the nucleation rate and where

$$\overline{B}^{(k)}(\mathbf{x}) = \frac{1}{2} \int \int_0^{+\infty} \beta(L,\lambda)(L^3 + \lambda^3)^{\frac{k}{3}} n(L;\mathbf{x}) n(\lambda;\mathbf{x})\, dL\, d\lambda \tag{3.90}$$

$$\overline{D}^{(k)}(\mathbf{x}) = \int_0^{+\infty} L^k n(L;\mathbf{x}) \int_0^{+\infty} \beta(L,\lambda) n(\lambda;\mathbf{x})\, d\lambda\, dL. \tag{3.91}$$

are the moments of birth and death of particles. The Favre averaged transport

equation for the moments results to be:

$$\frac{\partial}{\partial x_j}(\overline{\rho}\langle \mathbf{U}\rangle\langle m^{(k)}\rangle(\mathbf{x})) - \frac{\partial}{\partial x_j}\left(\Gamma_t \frac{\partial}{\partial x_j}(\langle m^{(k)}\rangle(\mathbf{x}))\right) = \overline{\rho}(x_c)^k\langle J(S)\rangle + \overline{\rho}\left(k\int_0^{+\infty} L^{k-1}\langle G(S,L)n(L;\mathbf{x})\rangle\, dL + \langle \overline{B}^{(k)}\rangle(\mathbf{x}) - \langle \overline{D}^{(k)}\rangle(\mathbf{x})\right), \quad (3.92)$$

where $\langle m^{(k)}\rangle$ is represented in the two environments of the DQMOM-IEM as $m_1^{(k)}$ and $m_2^{(k)}$ resulting in:

$$\langle m^{(k)}\rangle(\mathbf{x}) = p_1(\mathbf{x})m_1^{(k)}(\mathbf{x}) + p_2(\mathbf{x})m_1^{(k)}(\mathbf{x}). \quad (3.93)$$

Applying this definition the resulting transport equations for the weighted moment in the first node/environment, introducing the quadrature approximation and recalling the definition of Brownian and turbulent kernels for aggregation (Eqs. (3.17) and (3.20)), reads as follows:

$$\frac{\partial}{\partial x_j}\left(\overline{\rho}\langle \mathbf{U}\rangle p_1 m_1^{(k)}(\mathbf{x})\right) - \frac{\partial}{\partial x_j}\left(\Gamma_t \frac{\partial}{\partial x_j}\left(p_1 m_1^{(k)}(\mathbf{x})\right)\right) = \frac{\Gamma_t}{m_1^{(k)} - m_2^{(k)}}\left(p_1 \frac{\partial m_1^{(k)}}{\partial x_j}\frac{\partial m_1^{(k)}}{\partial x_j} + p_2 \frac{\partial m_2^{(k)}}{\partial x_j}\frac{\partial m_2^{(k)}}{\partial x_j}\right) + \overline{\rho}\left(\gamma_M(m_2^{(k)} - m_1^{(k)}) + p_1(x_{c,1})^k J(S_1) + k\sum_{\alpha=1}^{N} p_1 G(S_1, L_{\alpha,1}) w_{\alpha,1} L_{\alpha,1}^{k-1}\right) + \overline{\rho}\left(\frac{p_1}{2}\sum_{\alpha=1}^{N}\sum_{\gamma=1}^{N} w_{\alpha,1}w_{\gamma,1}\beta_{\alpha,\gamma,1}[(L_{\alpha,1}^3 + L_{\gamma,1}^3)^{\frac{k}{3}} - L_{\alpha,1}^k - L_{\gamma,1}^k]\right) \quad \text{with } k \in 0,\ldots,2N-1 \quad (3.94)$$

where:

$$\beta_{\alpha,\gamma,1} = \frac{2k_B T}{3\nu_f}\frac{(L_{\alpha,1} + L_{\gamma,1})^2}{L_{\alpha,1}L_{\gamma,1}} + 1.294(L_{\alpha,1} + L_{\gamma,1})^3\left(\frac{\varepsilon}{\nu}\right)^{\frac{1}{2}} \quad (3.95)$$

and:

$$S_1 = \frac{c_s(\xi_1, m_1^{(3)})}{c_{s,eq}(\xi_1)} \quad (3.96)$$

whereas a similar equation for the second node/environment is obtained by re-

placing the subscript $i = 1$ with 2 in the previous equation. The nodes $L_{i,\alpha}$ and weights $w_{i,\alpha}$ ($\alpha = 1, \ldots, N$) of the quadrature approximation of order N are all calculated from the first $2N - 1$ moments of the PSD in each node/environment, (i.e., $m_1^{(k)}$) by using the Product-Difference algorithm [Marchisio et al., 2003b; Gordon, 1968; McGraw, 1997].

As it was previously shown [Barrett and Webb, 1998], a quadrature approximation with only few nodes describes the moment evolution accurately. In this work N is taken equal to two, because it represents a good trade off between accuracy and computational time. The first four moments represent important quantities related to particles. The 0-th is the total numerical density in the system, the second and third order moments represents the mean volumetric surface area and volume of the particles. From the moments it is also possible to define various characteristic dimensions. The ratio $d_{10} = {}^{m_1}/_{m_0}$ is a mean dimension based on the numerical density of the particles; $d_{32} = {}^{m_3}/_{m_2}$ is called the Sauter diameter and is a mean particle dimension based on the total surface area of the particles; $d_{43} = {}^{m_4}/_{m_3}$ is a mean dimension based on the volume of the particles. In this work the d_{43} will be considered because this is the value of the particle size obtained from experiments.

The set of moments could be altered during the simulation, due to the spatial discretization scheme used by the CFD code, and due to other numerical approximations. In fact, during the simulation, moments can approach non-physical values corresponding for example to negative PSD! This behaviour, called moment corruption, is clearly illustrated in the work of Wright [2007]. When this happens the moments fed to the Product-Difference algorithm might result in negative nodes, a serious threat to the stability of the simulation. In order to overcome this problem an algorithm to test the validity and consistency of the moment set (and to correct them in case of invalid set) was tested and implemented. The validity of a moment set is granted by the positiveness of the following determi-

nants [Shoahat and Tamarkin, 1963]:

$$\Delta_{i,n} = \begin{vmatrix} m_i^{(0)} & m_i^{(1)} & \cdots & m_i^{(n)} \\ m_i^{(1)} & m_i^{(2)} & \cdots & m_i^{(n+1)} \\ \cdots & \cdots & \cdots & \cdots \\ \cdots & \cdots & \cdots & \cdots \\ m_i^{(n)} & m_i^{(n+1)} & \cdots & m_i^{(2n)} \end{vmatrix} \qquad \begin{matrix} n = 2, 3, \ldots \\ i = 1, 2 \end{matrix} \tag{3.97}$$

$$\Delta_{i,n}^{(1)} = \begin{vmatrix} m_i^{(1)} & m_i^{(2)} & \cdots & m_i^{(n+1)} \\ m_i^{(2)} & m_i^{(3)} & \cdots & m_i^{(n+2)} \\ \cdots & \cdots & \cdots & \cdots \\ \cdots & \cdots & \cdots & \cdots \\ m_i^{(n+1)} & m_i^{(n+2)} & \cdots & m_i^{(2n+1)} \end{vmatrix} \qquad \begin{matrix} n = 3, 4 \ldots \\ i = 1, 2 \end{matrix} \tag{3.98}$$

For the first four moments of the PSD ($m^{(0)}$, $m^{(1)}$, $m^{(2)}$, $m^{(3)}$) this condition is equivalent to the convexity of the function $\ln(m^{(k)})$ versus k. In practice a difference table of the function $\ln(m^{(k)})$ is built and the previous condition is checked by testing that all the elements in the column of the second order difference are positive [Petitti et al., 2009]. If the test fails the moments are corrected before being passed to the Product Difference (PD) algorithm. The moments are recovered using the Minimum Square Algorithm (MSA) proposed by McGraw [McGraw, 2006], based on identifying the moment of order k^* whose change maximizes the smoothness of the function $\ln(m^{(k)})$. This detection and correction algorithm was shown to be very efficient for a different multiphase system and is employed for this application, conferring greater stability to the CFD code.

The closure problem related instead to the other terms is treated with the presumed PDF approach previously introduced (i.e., DQMOM-IEM) coupled with

the QMOM for the population balance model.

3.3 Operating conditions and numerical details

A sketch of the reactor investigated in this work is shown together with the computational grid in Figure 3.3 (d_j = 1 mm). The grid was created by using GAM-

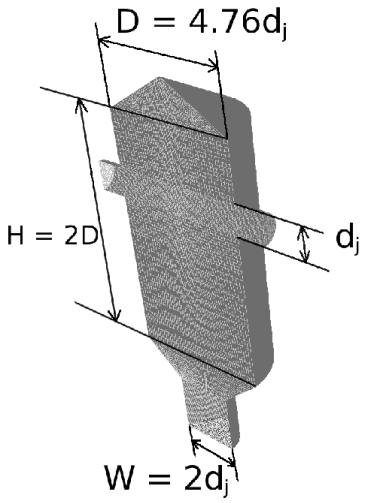

Figure 3.3: Sketch of the CIJR geometry investigated in this work and final grid used in the simulations.

BIT 2.4 and the simulations were performed with FLUENT 12.0. Only half of the real geometry was described by using the hypothesis of plane-symmetry. Inlets of the mixer were extended for 2 mm to take into account back-mixing that could probably occur. Otherwise outlet was extended for 3 mm. The grid consists of 120, 000 cells refined near the impinging plane and in an annular region around the jets by using the gradient adaptation approach. The independence of the solution from the grid was already tested [Gavi et al., 2007a]. The employed spatial numerical scheme is a first-order upwind scheme and the pressure-velocity coupling was solved with the SIMPLE algorithm. The standard $k - \varepsilon$ turbulence model coupled with the Enhanced-Wall Treatment approach was used, since it was shown to be the best approach for this system [Gavi et al., 2007b]. Outlet boundary conditions assume zero normal gradients for all flow variables, except

pressure, implying that outflow boundary values are not imposed but are calculated from the interior. The DQMOM-IEM and QMOM model were implemented via User Defined Functions (UDF) in Fluent.

In order to test the model at different levels of turbulence, different operating conditions were considered. The ratio between the water and the acetone inlet flow rates (indicated as $R = \dot{V}_W/\dot{V}_A$) was in this work fixed equal either to one or two. The water inlet stream flow rate in the simulations was varied from 10 mL/min to 120 mL/min. Because of the low value of the Reynolds number in the inlet tube, the inlet flow was considered laminar and a parabolic profile was imposed. The temperature of the system is assumed constant and equal to 303 K.

The solvent-displacement process simulated in this work consists of mixing a solution of acetone containing poly-ε-caprolactone (PCL) characterized by a molecular weight $M_w = 14000\,\mathrm{kg/kmol}$ with a water solution. Four different initial concentrations of PCL in acetone, $c_{in,PCL} = 0.25\,\mathrm{mg\,mL^{-1}}$, $0.5\,\mathrm{mg\,mL^{-1}}$, $2.5\,\mathrm{mg\,mL^{-1}}$, $5\,\mathrm{mg\,mL^{-1}}$, were considered.

As already reported all the model parameters were independently identified and their final value is reported in Table 3.1.

There is a parameter that deserve a special attention: the molecular volume of the solute molecule, $\tilde{v}$. It is very difficult to obtain experimentally this value and there are no models useful to describe it in dependence of the environment in the reactor (i.e. $\tilde{v}$ is a function of the water molar fraction). In this work we use a constant value of the molecular volume, treating it as fitting parameter, showing the dependence of the results from it. The range of $\tilde{v}$ is between 2.0 and $2.6 \cdot 10^{-28}\,\mathrm{m^3}$. One suitable way to obtain this parameter seems to be the atomistic simulation of the solute by using the Molecular Dynamics. In the next Chapter it will be shown how it is possible to obtain these parameters from MD simulations and how to couple them with the CFD description of the system as long as a new formulation of the nucleation rate which relax some of the approximations used in the derivation of the classic law (i.e., obtained from CNT, Eq. (3.6))

3.4 Results and discussion

Let us start discussing the model predictions concerning the flow field in the CIJR. Figure 3.4 reports the contour plots of the velocity magnitude across the symmetry plane for three different inlet water flow rates and for the two values

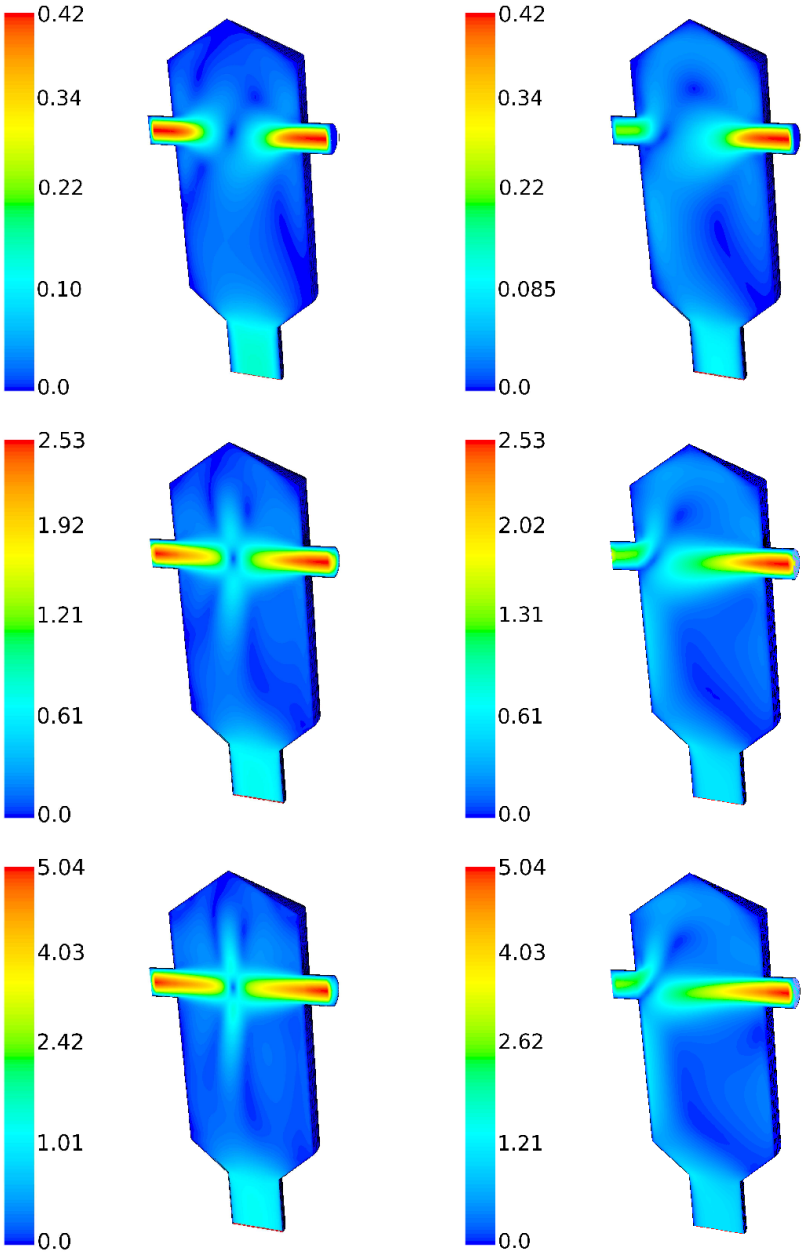

Figure 3.4: Contour plots of the velocity magnitude (m s^{-1}) predicted by the model with the standard $k - \varepsilon$ turbulence model for $R = 1$ (left) and $R = 2$ (right) and for different inlet water flow rates (from top to bottom: 10 mL min^{-1}, 60 mL min^{-1} and 120 mL min^{-1}).

of R considered in this work. In the figure the acetone inlet is on the left and the water inlet is on the right. As it is seen the two inlet streams collide in the cylindrical chamber forming an impinging plane. The impinging plane does not stand at the centre of the chamber even for $R = 1$, but is actually shifted to the left, towards the acetone inlet, because of the higher density of water. It is useful to remind here that only by including the variation of density into the CFD model this effect can be accounted for and this explains why it was not evidenced in previous works where an average constant density value was considered [Woo et al., 2009]. In obtaining this results the mixture density fluctuations in the mixer were neglected. Results show that a non-constant average mixture density must be considered, conversely it is good a approximation to neglect density fluctuations. An increase in the value of R accentuates this effect and in the second case the impinging plane is completely shifted near the inlet of the acetone stream. The region around the impingement of the two streams is where the turbulent kinetic energy is generated and quickly dissipated; as it is possible to see in the figures as the flow rate is increased this region becomes very thin resulting in even higher turbulent kinetic energy dissipation rates. Results also show that the confinement of the two inlet streams is such that the central part of the chamber, characterized by very high mixing rates, is not by-passed, resulting in overall good performances in terms of both macro- and micro-scale mixing. These conclusions are confirmed by the results reported in Figures 3.5 and 3.6, were the contour plots on the symmetry plane of the small-scale mixture fraction variance, $\langle \xi'^2 \rangle$, and of the large-scale mixture fraction variance, $\langle \xi'^2 \rangle_{LS}$, are reported for some of the cases investigated. As clearly visible, mixing at every scale improves when increasing the flow rate of the inlet streams. The large-scale variance is created by the different compositions of the two inlet streams and has its maximum value at the inlets. It then approaches very quickly zero, as soon as the two inlet streams enter the mixing chamber. Mixing is a cascade process and in fact the variance generated and then dissipated at the macro-scale is transferred at the micro-scale. In turn the small-scale variance is quickly dissipated in the confined region around the impingement plane.

Although mixing in these devices is very efficient, some gradients at the macro- and micro-scale, that influence the particle formation process, are still present. This is illustrated in Figure 3.7 where the Favre-averaged saturation ratio, $\langle S \rangle = p_1 S_1 + p_2 S_2$, nucleation rate, $\langle J \rangle = p_1 J(S_1) + p_2 J(S_2)$, and mean

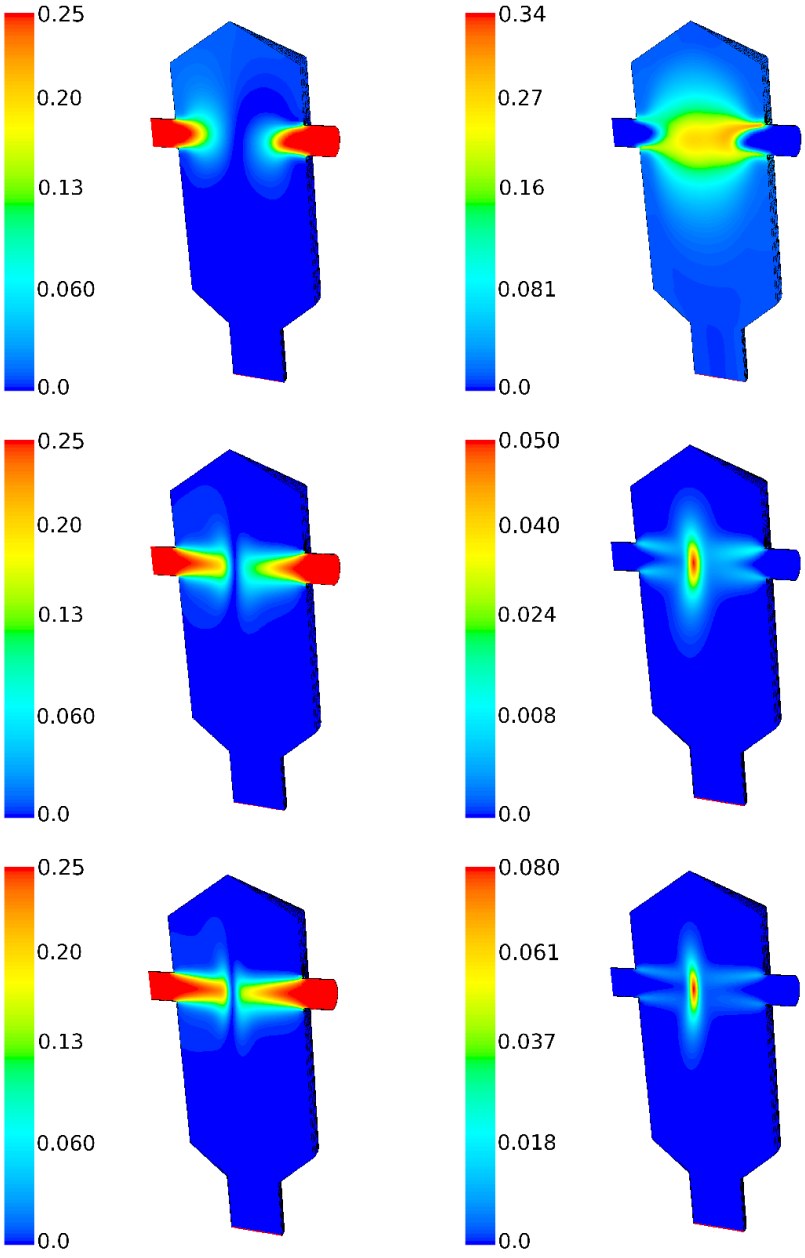

Figure 3.5: Contour plots of the large-scale mixture variance $\langle \xi'^2 \rangle_{LS}$ (left) and of the small-scale mixture fraction variance $\langle \xi'^2 \rangle$ (right) predicted by the model for $R = 1$ and for different inlet water flow rates (from top to bottom: 10 mL min^{-1}, 60 mL min^{-1} and 120 mL min^{-1}).

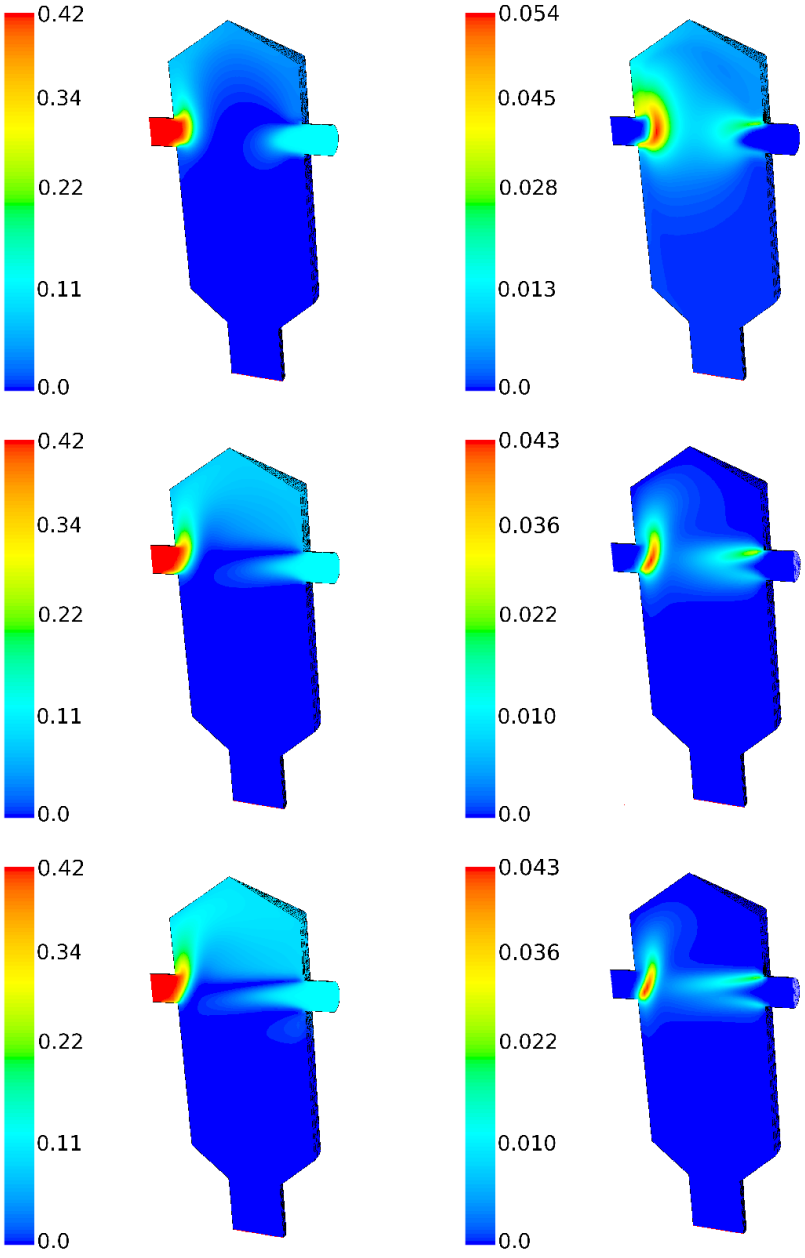

Figure 3.6: Contour plots of the large-scale mixture variance $\langle \xi'^2 \rangle_{LS}$ (left) and of the small-scale mixture fraction variance $\langle \xi'^2 \rangle$ (right) predicted by the model for $R = 2$ and for different inlet water flow rates (from top to bottom: 10 mL min^{-1}, 60 mL min^{-1} and 120 mL min^{-1}).

nanoparticle size, $d_{43} = \langle m^{(4)} \rangle / \langle m^{(3)} \rangle$, are reported at different inlet water flow rates. As it is seen saturation ratio is built-up as the acetone stream (containing the polymer) is mixed with water. The resulting nucleation rate (which is a non-linear function of saturation ratio) is also very different from point to point, resulting in a quite inhomogeneous spatial distribution. On the contrary the final mean nanoparticle size is characterized by a more uniform spatial distribution, especially at higher flow rates. These results confirm that mixing under these operating conditions is fast enough to homogenize the particles produced within the CIJR. This is proved by the fact that the global mixing time (reported in Figure 3.8) is always smaller than the residence time, readily calculated by the flow rate, resulting in values between 1 to 4 seconds. However, mixing is not capable of completely smoothing down the saturation ratio and nucleation rate gradients. This is particularly important in this case because particle formation is almost instantaneous. Moreover, simulation results also show that an increase in the flow rates of the inlet streams (at high flow rates) results in significant improvements in the overall mixing rate but in limited changes of the final mean nanoparticle size. These concepts are illustrated in Fig. 3.8 where the characteristic times of mixing, nucleation, molecular growth and aggregation are reported versus the flow rate. As it is seen at high flow rates the mixing time becomes smaller than the molecular growth time, resulting in limited changes of the final nanoparticle size.

It is also important to highlight here that because particle formation is very fast, extracting the nucleation and growth rate under the assumption of perfect mixing would lead to large errors. For all these crystallization and precipitation processes, characterized by very fast particle formation time-scales, it is therefore suggested to identify the kinetic parameters only by using CFD models. When also aggregation plays a significant role, then the use of CFD models to extract the nucleation, growth and aggregation rates is even more important as demonstrated in a previous work by Marchisio et al. [2006]. Very similar conclusions were obtained by analyzing in the same device a fast parallel-competitive reaction by employing Large Eddy Simulation [Marchisio, 2009].

As already mentioned, the equation for the particle nucleation rate used in this work contains the polymer molecular volume. This term describes the spatial configuration of the molecule and, especially for a long chain molecule, can assume a wide range of values passing from a minimum (corresponding to a com-

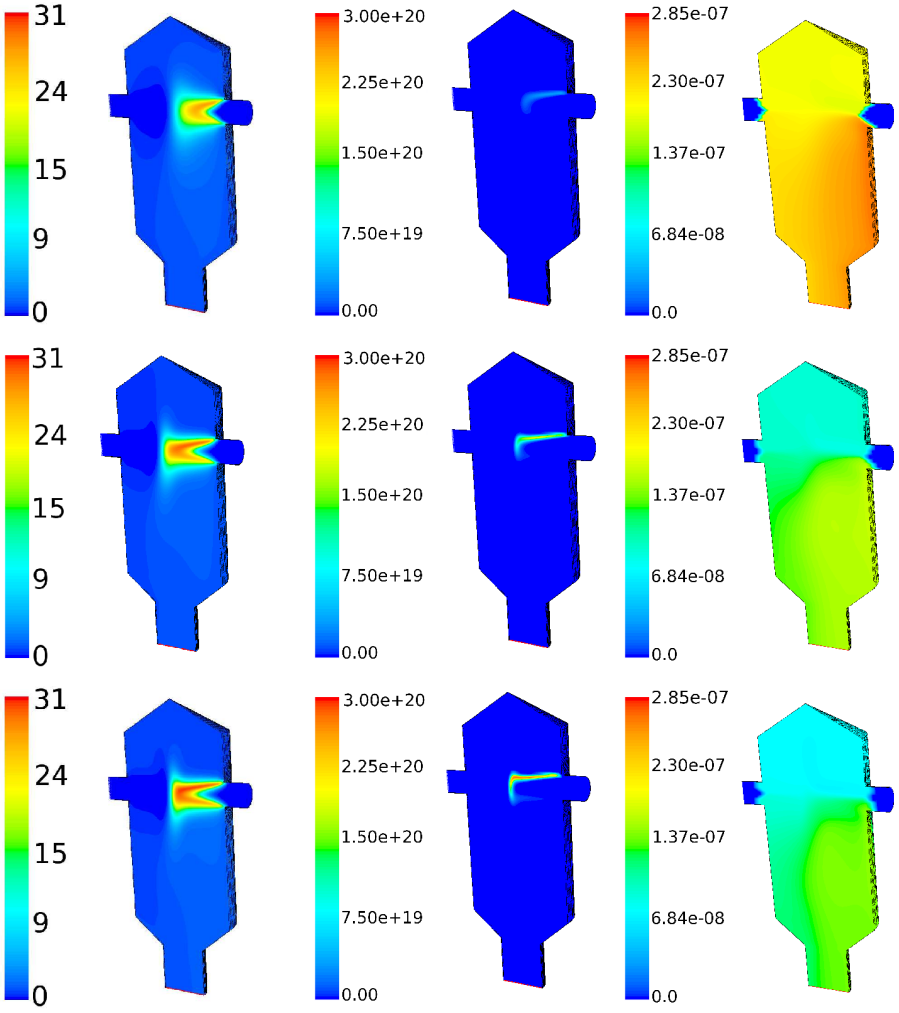

Figure 3.7: Contour plots of (from left to right) Favre-averaged, nucleation rate (s^{-1}) and mean nanoparticle size (m) predicted by the model for $R = 1$ and $c_s^0 = 0.5\,\mathrm{mg\,mL^{-1}}$ at different inlet water flow rates (from top to bottom: $40\,\mathrm{mL\,min^{-1}}$, $80\,\mathrm{mL\,min^{-1}}$, $120\,\mathrm{mL\,min^{-1}}$).

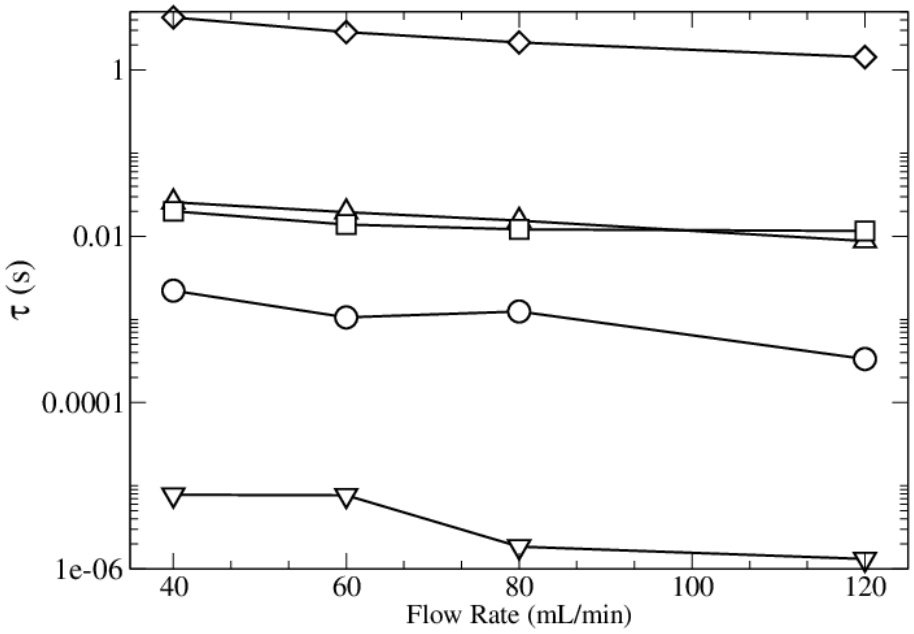

Figure 3.8: Comparison of characteristic times in CIJR for $R = 2$: residence time ($\diamond$), mixing time ($\triangle$), growth time ($\square$), aggregation time ($\circ$), nucleation time (∇)

pletely convoluted molecule) to a maximum (corresponding to a fully extended molecule). The spatial configuration for the polymer considered is strongly dependent on the composition of the solution. One can expect that the molecular volume is lower in water and higher in acetone (with which the polymer has greater affinity). In the CIJR the solution passes with continuity from pure acetone to pure water so polymer molecules flow through very different environments resulting in different values for the molecular volume. This volume, that is related to the radius of gyration of the polymer molecule, can be very difficult to determine. Previous works on similar systems, although in the context of molecular weight measurements [Lince et al., 2011b], showed that dynamic light scattering can be used to this end, but typically results in non-negligible experimental errors. An alternative way to evaluate this parameter is to resort to molecular dynamics simulations (see Chap. 5), but for the moment it is treated as fitting parameter. Moreover, although as already reported the dependence over composition should be considered, as first step a constant value throughout the CIJR is assumed in this work also with the aim of performing a sensitivity analysis of predictions with respect to this parameter.

Predictions for the mean nanoparticle size at the reactor outlet are reported in Figure 3.9 and are compared with experiments. In order to evaluate the effect of aggregation in the system under study, simulations were performed considering first only nucleation and molecular growth and then subsequently also aggregation.

The trend of both experimental results and predictions is the same for all the cases considered; the value of the mean nanoparticle size decreases with increasing the flow rate of the inlet streams, because of the influence that faster mixing has on the particle formation process [Gavi et al., 2008]. The nucleation rate is a non-linear function of the saturation ratio whereas on the contrary the growth rate is only a linear function of the saturation ratio. As the water flow rate increases, the saturation ratio increases and the increase for the nucleation rate turns out to be much larger than the corresponding increase for the molecular growth rate. This results in the formation of a larger number of smaller particles. Comparison of other moments (not reported for brevity) provides some additional information on the variance and the skewness of the PSD. Results show that increasing the flow rate of the inlet streams the width of the PSD does not change much, indicating that under the range of operating conditions investigated, mixing in the

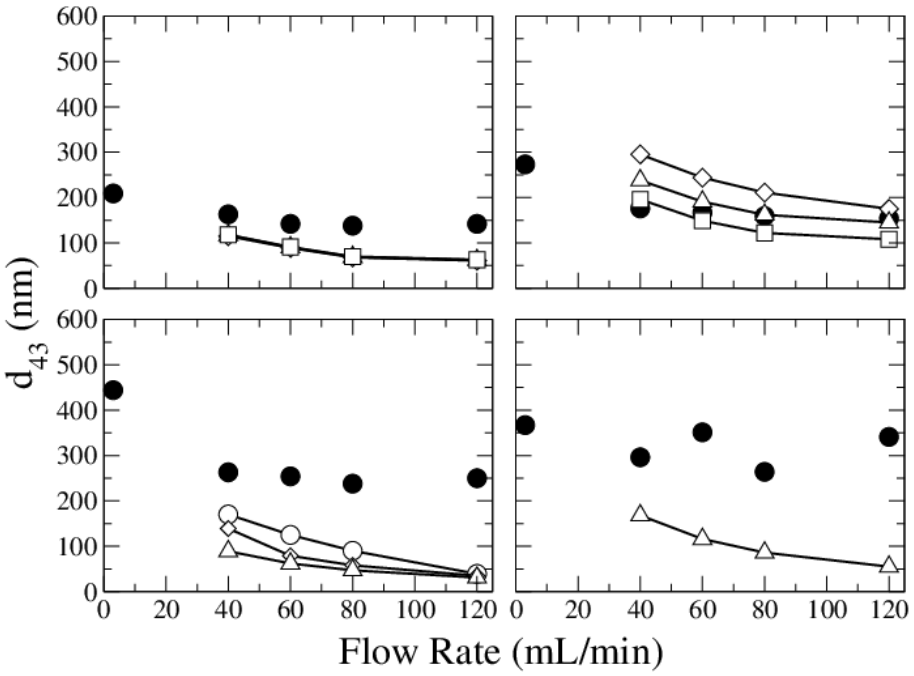

Figure 3.9: Comparison of the mean nanoparticle size at the CIJR outlet for $R = 1$ experimentally measured (•) with model predictions including only particle nucleation and molecular growth for $\tilde{\nu} = 2.1\ 10^{-28}\ m^3$ (□), $\tilde{\nu} = 2.2\ 10^{-28}\ m^3$ (△), $\tilde{\nu} = 2.46\ 10^{-28}\ m^3$ (◇), $\tilde{\nu} = 2.6\ 10^{-28}\ m^3$ (○); from left to right and top to bottom different initial polymer concentrations (in acetone) are considered: $c_{in,PCL} = 0.25 - 0.5 - 2.5 - 5.0\,mg\,mL^{-1}$.

CIJR is already very good. It is important to highlight here that, although some limitations of the DQMOM-IEM approach [Akroyd et al., 2009], this model is able to show the effects of process parameter on particle size.

Simulations performed at flow rates smaller than 40 mL min^{-1} are not compared in Figure 3.9 with experiments, since the corresponding predictions were found to be less reliable. In fact, turbulence is here modelled with the RANS approach, which assumes a fully developed turbulent flow, characterized by high local Reynolds numbers. Altough there exist more sophisticated turbulence models (i.e. LES, DNS) RANS model gives accurate results in terms of average quantities of flow field and turbulent properties of the fluid (i.e. turbulent dissipation and turbulent kinetic energy) in systems with turbulence fully developed as in the operating conditions we considered. Furthermore RANS simulations are computationally less expensive and therefore more attractive than LES and DNS.

For flow rate values smaller than 40 mL min^{-1}, the predictions for the mean flow field may be still considered as reliable, predictions for the turbulent kinetic energy and the turbulent dissipation rate might be affected by very large errors. Since the values of these two quantities greatly affect the final model predictions for particle formation and evolution, it is safer to exclude from the comparison cases obtained under these operating conditions. Fig. 3.9 reports model predictions (neglecting aggregation) for different values of the molecular volume (i.e. $\tilde{v} = 2.1 - 2.2 - 2.46 - 2.6\ 10^{-28}$ m^3). Model predictions confirm that this parameter affects the particle nucleation rate and in turn the resulting mean nanoparticle size. In fact, the nucleation rate decreases as the molecular volume $\tilde{v}$ decreases, leading to the formation of fewer nuclei in the system that then grow into bigger nanoparticles. The effect of $\tilde{v}$ is less important at low initial polymer concentrations (e.g., for $c_{in,PCL} = 0.25$ mg mL^{-1} the curves at different $\tilde{v}$ values are practically overlapping), whereas on the contrary becomes more important at high initial polymer concentrations.

In Fig. 3.10 the results for the complete model (including aggregation) are reported for all the molecular volume values considered in this work and compared with experiments. Predictions considering aggregation include both the effect of Brownian and turbulent aggregation. Comparison of model predictions neglecting (see Fig. 3.9) or including aggregation (see Fig. 3.10) highlights the role and importance of aggregation at different initial polymer concentrations. In fact, results show that aggregation is important only at high initial concentra-

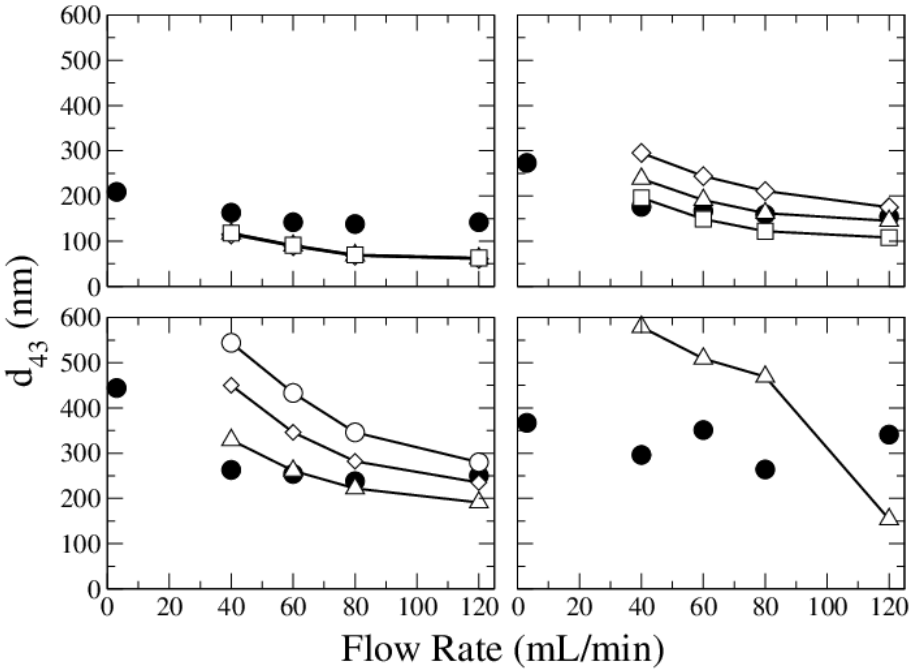

Figure 3.10: Comparison of the mean nanoparticle size at the CIJR outlet for $R = 1$ experimentally measured (•) with model predictions including particle nucleation, molecular growth and aggregation for $\tilde{v} = 2.1\ 10^{-28}\ m^3$ (□), $\tilde{v} = 2.2\ 10^{-28}\ m^3$ (△), $\tilde{v} = 2.46\ 10^{-28}\ m^3$ (◇), $\tilde{v} = 2.6\ 10^{-28}\ m^3$ (○); from left to right and top to bottom different initial polymer concentrations (in acetone) are considered: $c_{in,PCL} = 0.25 - 0.5 - 2.5 - 5.0\,mg\,mL^{-1}$.

tions, whereas at low initial concentrations aggregation does not seem to have any influence at all. This can be easily explained considering that for particles to aggregate it is necessary to have an elevate total particle number density, that is obtained only for $c_{in,PCL} \geq 2.5\,\mathrm{mg\,mL^{-1}}$. For $c_{in,PCL} < 2.5\,\mathrm{mg\,mL^{-1}}$ the resulting total particle number density is such that very few collisions occur and therefore aggregation does not take place. Similar conclusions can be drawn for $R = 2$. The results of the simulations performed at $R = 2$ for different values of the molecular volume $\tilde{v} = 2.06 - 2.1 - 2.2 - 2.46 - 2.06\ 10^{-28}\,\mathrm{m^3}$ are shown in Fig. 3.11 (considering only nucleation and molecular growth) and Fig. 3.12 (considering nucleation, molecular growth and aggregation). As it is clear from the

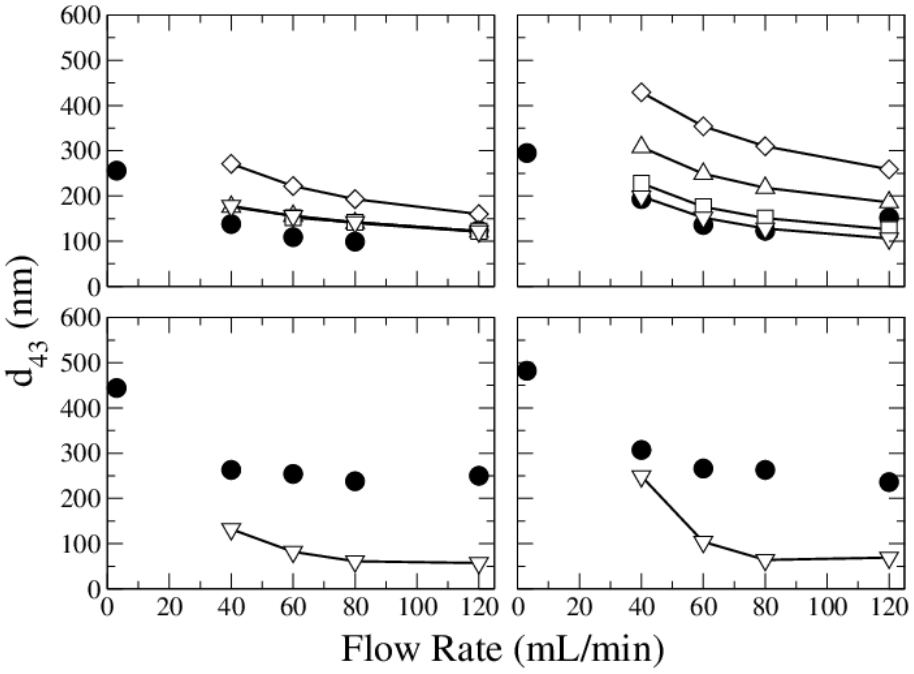

Figure 3.11: Comparison of the mean nanoparticle size at the CIJR outlet for $R = 2$ experimentally measured (•) with model predictions including particle nucleation and molecular growth for $\tilde{v} = 2.06\ 10^{-28}\,\mathrm{m^3}$ (∇), $\tilde{v} = 2.1\ 10^{-28}\,\mathrm{m^3}$ (□),$\tilde{v} = 2.2\ 10^{-28}\,\mathrm{m^3}$ (△), $\tilde{v} = 2.46\ 10^{-28}\,\mathrm{m^3}$ (◇), $\tilde{v} = 2.6\ 10^{-28}\,\mathrm{m^3}$ (○); from left to right and top to bottom different initial polymer concentrations (in acetone) are considered: $c_{in,PCL} = 0.25 - 0.5 - 2.5 - 5.0\,\mathrm{mg\,mL^{-1}}$.

comparison of Figures 3.9 and 3.10 and Figures 3.11 and 3.12 only including

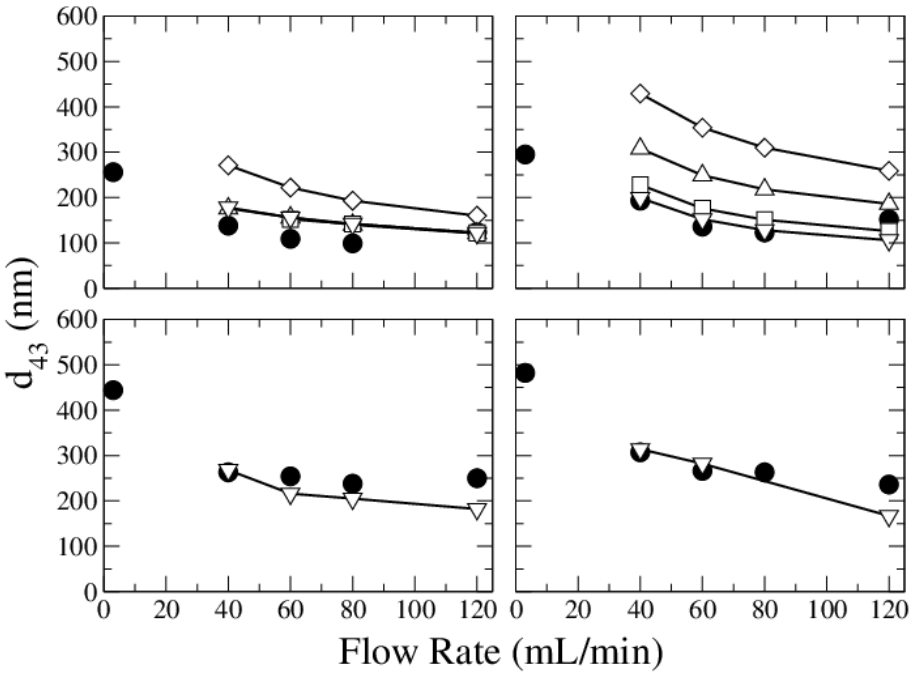

Figure 3.12: Comparison of the mean nanoparticle size at the CIJR outlet for $R = 2$ experimentally measured (•) with model predictions including particle nucleation, molecular growth and aggregation for $\tilde{\nu} = 2.06\ 10^{-28}\,\mathrm{m}^3$ (∇), $\tilde{\nu} = 2.1\ 10^{-28}\,\mathrm{m}^3$ (□), $\tilde{\nu} = 2.2\ 10^{-28}\,\mathrm{m}^3$ (△), $\tilde{\nu} = 2.46\ 10^{-28}\,\mathrm{m}^3$ (◇); from left to right and top to bottom different initial polymer concentrations (in acetone) are considered: $c_{in,PCL} = 0.25 - 0.5 - 2.5 - 5.0\,\mathrm{mg\,mL^{-1}}$.

aggregation (eventually assuming a realistic aggregation efficiency) can lead to good agreement with experiments. This is confirmed by experiments, that do not exclude the possibilities of partial aggregation inside CIJR.

The results of the performed simulations show that the value of the molecular volume that best fits the experimental data is around $\tilde{v} \approx 2.2\ 10^{-28}\,\mathrm{m}^3$ for $R = 1$ and $\tilde{v} \approx 2.06\ 10^{-28}\,\mathrm{m}^3$ for $R = 2$. In fact, one single $\tilde{v}$ value is capable of describing fairly well the situation at $R = 1$, whereas a different $\tilde{v}$ value must be chosen for $R = 2$. This is consistent with what stated earlier: being $\tilde{v}$ related to the spatial conformation of PCL molecules, one can expect that when increasing the acetone content in the CIJR (i.e., small R values), the molecular volume increases, indicating a more stretched configuration of PCL molecules. This can be considered a very crucial point for the application of this model to polymer nanoparticle precipitation, the final properties of the nanoparticles depend on the characteristics of the polymer chains that can not be longer considered independent of the environment inside the mixer.

Efficiency of this process in terms of particle formation can be considered looking at the saturation ratio at the mixer outlet. For each operating condition and flow rate, saturation ratio has a very low value, close to the unity, compared to those obtained in the impinging zone (Figure 3.7). Therefore, it can be concluded that at the mixer outlet PCL has reached the equilibrium concentration at the working temperature for the outlet mixture composition; in this condition no further precipitation is possible and the process is almost complete. Hence particle formation efficiency can be virtually considered equal to one.

In conclusion the comparison of model predictions with experimental data showed acceptable agreement, proving the validity of the approach. Indeed, the molecular volume should be transformed into a quantity dependent on the local mixture composition, in order to automatically predict larger $\tilde{v}$ values for PCL molecules in acetone-rich environments and smaller $\tilde{v}$ values for PCL molecules in water-rich environments. This is the subject of the next Chapter.

3.5 Conclusions

A CFD model for describing precipitation in solvent-displacement processes is here discussed. The procedure used requires first the quantification of the interface tension of the formed particles with the solvent and anti-solvent mixture and

of the equilibrium concentration of the considered solute. These two quantities are very important since they define the saturation ratio, which is the driving force of the entire process. Nucleation, molecular growth and aggregation rates can be written from first principles and only one parameter, the molecular volume of the polymer, cannot be independently measured and is left to fit experiments. Validation of model predictions is done in this work through comparison of the mean particle size experimentally measured in our previous work. An independent validation of the flow and turbulence field was carried out in a previous work and is not discussed here [Gavi et al., 2010].

The approach is illustrated for the precipitation of PCL nanoparticles in CIJR produced through solvent-displacement with acetone as solvent and water as anti-solvent. First the predictions for the flow field were analyzed and discussed. In a second step, nanoparticle formation was also investigated and validated. Comparison between simulation results and experimental data was carried out for numerous cases, corresponding to very different operating conditions. In particular, different values of the inlet water flow rate, inlet acetone to water flow rate ratios and initial polymer concentration, were considered. Good agreement was found in terms of the mean nanoparticle size at the reactor outlet. In particular the trend observed for the experimental data (i.e., the decrease of the mean size of the nanoparticles with the increase of the flow rate) is well reproduced by the simulations. The model highlights that at high flow rates thank to the high mixing rate, saturation ratio reaches higher values, resulting therefore in smaller particles. The comparison of model predictions neglecting or including the effect of Brownian and turbulent aggregation shows that at low initial concentrations of PCL aggregation is unimportant, because of the resulting low total particle number density, that makes the collisions very unlikely. On the contrary at high initial PCL concentrations aggregation plays a very important role and only by including its effect good agreement can be found.

The results collected also show that the RANS approach used here does not allow to rely on predictions for low flow rates, due to the fact that the turbulence model employed here overestimates the turbulent mixing rate, leading to an incorrect prediction of saturation ratio levels. For these cases other approaches should be used, such as Large Eddy Simulations that can represent a further improvement of this work.

Concluding, the most common results concerning the effect of operating con-

ditions on the precipitation process are obtained also for the precipitation of PCL (e.g. decrease of the diameter with the increase of the flow rate) but results also show that the complexity of this system (constituted by polymer chains) cannot be neglect in order to obtain quantitative predictions. This different behaviour of PCL in the mixer is probably related to the sensibly different environments in which particles are formed, highlighting the necessity of including in the model a functional dependency of this parameter over the local composition, that will be extracted from the MD simulation of the PCL.

Chapter 4

Simulation of the precipitation process [1]

The results showed in the previous chapter have shown the inadequacy of the Classical Nucleation Theory describing the nucleation rate of polymer nanoparticle precipitation in solvent-displacement processes. This chapter is devoted to the development of an improved description of polymer particle nucleation by using also Molecular Dynamics (MD) simulations. In the first section the fundamentals of the nucleation phenomenon are described by introducing the concept of the Gibbs free energy of nucleation. Following the derivation of the nucleation rate presented in Kelton et al. [1983], a modified expression with respect to the classical derivation (which we refer as Classical Nucleation Theory, CNT) of Nielsen [1964] is obtained. The final expression for the nucleation rate presented (which we refer as Augmented Nucleation Theory, ANT) is adapted to be used with polymeric systems and is very different from the expression for the nucleation rate employed in the Chap. 3 which was instead derived for crystallization of small molecules in solution. In order to emphasize the differences between the two approaches (ANT and CNT) a derivation of the nucleation rate in the framework of CNT is also presented. In subsequent parts of the chapter the atomistic model for the description of polymeric chains is also presented. This is used to

[1] This chapter has been submitted in a shorter version for publication to the *Industrial & Engineering Chemistry* Journal

quantify specific configurational and geometrical properties of nuclei constituted by polymer molecules, such as volume and external surface. Since the nucleation model is very sensitive to these quantities, their correct estimation is of primary importance. In this work the "dimension" of a polymeric chain is estimated by using the concept of radius of gyration $\mathbf{R}_g$ and the end-to-end distance $\mathbf{R}_{EE}$. Some models used to calculate $\mathbf{R}_g$ and $\mathbf{R}_{EE}$ are presented.

In the last part of the Chapter the results obtained with MD are presented. The expressions for the nucleation rate obtained with the CNT and with ANT are implemented into the CFD model and predictions are finally compared with experiments resulting in good agreement and demonstrating the validity of the approach.

4.1 Thermodynamics of Nucleation

Nucleation basically consists in a change of phase of a solute dissolved in a solution. The solute in solution forms a new particulate phase, the particle, different from the original one. Each change of phase is accompanied by a change in the Gibbs energy which can be written, at constant T and P as:

$$\Delta G = (\mu_2 - \mu_1)n$$

where n is the quantity of matter (number of solute molecules) which goes from phase 1 where the chemical potential is μ_1 to phase 2 where the chemical potential is μ_2. The Gibbs energy gives a measure of the spontaneity of this transition. If $\Delta G < 0$ the process is spontaneous whereas if $\Delta G > 0$ such a transition is impossible, $\Delta G = 0$ represents the system at equilibrium.

At the interface between two different substances (or the same substance in two different phases) the molecules are in a state of higher potential energy then the rest of the molecules in the bulk. This excess of energy is often negligible at the macroscopic scale, when the ratio between the area of the interface (A) and the volume (V) of the bulk is very low. On the other hand, nuclei in solution have a high A/V ratio therefore this contribution can not be neglected any more in the calculation of the Gibbs energy. This excess of energy in a macroscopic body is proportional to the external surface of the body (A) through the surface tension σ_n which represents the Gibbs energy per unit of area of the body and in general

is a function of the dimension of the nucleus. Therefore the change in Gibbs free energy for a nucleus will be

$$\Delta G = \Delta G_V + \Delta G_S = -(\mu_2 - \mu_1)n + A\sigma_n. \tag{4.1}$$

The difference in the chemical potential between the two phases $(\mu_2 - \mu_1)$ can be expressed through the activity of the solute a by

$$\mu_2 - \mu_1 = k_B T \ln\left(\frac{a}{a_{eq}}\right)$$

where k_B is the Boltzmann constant, T is the temperature, a_{eq} the activity of the solute at equilibrium. It is often possible to consider the activity coefficients to be one [Nielsen, 1964] and use the concentration of the solute in solution c instead

$$\mu_2 - \mu_1 = k_B T \ln\left(\frac{c}{c_{eq}}\right)$$

where c_{eq} is the equilibrium concentration of the solute. Another assumption employed is that the value of the surface tension does not change with the dimension of the sample considered. Therefore the change of Gibbs energy associated with the formation of a nucleus will be:

$$\Delta G = k_B T \ln(S)\Delta n + A\sigma \tag{4.2}$$

where $S = {}^{c}/_{c_{eq}}$ is the quantity called saturation ratio.

Starting from these results the derivation of the nucleation rate according to Kelton et al. [1983] and Nielsen [1964] is presented in the following Sections.

4.2 Stationary Nucleation

In the classical theory of nucleation it is assumed that nuclei are obtained by a series of consecutive reactions:

$$P_{n-1} + P_1 \underset{k_n^-}{\overset{k_{n-1}^+}{\rightleftharpoons}} P_n \tag{4.3}$$

$$P_n + P_1 \underset{k_{n+1}^-}{\overset{k_n^+}{\rightleftharpoons}} P_n \tag{4.4}$$

in which P_n represents a nucleus composed by n molecules whereas P_1 represents the single molecule. The rate constant of addition and loss of a molecule from a nucleus of size n are represented by k_n^+ and k_n^- respectively. It was suggested by Volmer and Weber [1926] in the early development of the theory that a critical size for the nucleus (namely n^*) exists beyond which the nucleus grows rapidly and does not flow back in the reaction scheme reported in Eqs. (4.3) to (4.4) ($n \geq n^*$). It is moreover assumed that nuclei over the critical size are removed from the solution to become new elements of the dispersed phase (i.e. particles). With this assumption the number of nucleus of size n (with $n \geq n^*$), namely $N_{n,t}$ is equal to zero. For $n \leq n^*$ $N_{n,t}$ is set equal to N_n^e which represents the equilibrium number of nuclei. N_n^e turns out to be independent of time and to be a function of the position only:

$$N_n^e(\mathbf{x}) = N_i(\mathbf{x}) \exp\left(\frac{-\Delta G_n}{k_B T}\right). \tag{4.5}$$

In the above equation k_B is the Boltzmann constant, T the temperature, $N_i(\mathbf{x})$ the number of solute molecules still in the initial phase. Accordingly, these hypotheses lead to a nucleation rate $J(\mathbf{x})$ given simply by $N_{n^*}^e \times k_{n^*}^+$.

The main hypothesis used in this approach, namely that the nuclei are removed from the solution, lead to some inconsistency, both mathematical and physical. In fact, considering the distribution of the nuclei N_n^e this function presents a discontinuity at n^* going from a finite value in n^* to zero for $n \geq n*$; moreover the nuclei should be eliminated instantaneously from the solution.

This first formulation of the nucleation theory was improved by considering nucleation as a steady state process [Becker and Döring, 1935], at constant saturation ratio. According to this approach the net rate of appearance of nuclei

constituted by n solute molecules reads as follows:

$$J_{n,t} = N_{n,t}k_n^+ - N_{n+1,t}k_{n+1}^- \tag{4.6}$$

where k_n^+ is the kinetic constant. When the system reaches the equilibrium the net rate of nuclei formation, $J_{n,t}$ is zero because at equilibrium the forward and the backward rates equal each other:

$$J_{n,t} = N_n^e k_n^+ - N_{n+1}^e k_{n+1}^- = 0 \tag{4.7}$$

However, it was pointed out by Becker and Döring [1935] the system does not reach the equilibrium, but rather a steady state distribution of nuclei will be established. In this framework, the net rate of formation will be independent from time and of the number of molecules inside the nucleus. The value of the steady-state net rate of formation of nuclei (J^s) will therefore read as follows:

$$J^s = N_n^s k_n^+ - N_{n+1}^s k_{n+1}^- \tag{4.8}$$

where N_n^s is the number on nuclei at steady state. Strictly speaking this is not a steady state, because the molecules involved in the formation of a nucleus are removed from the solution. Anyway, it is observed experimentally that nuclei are formed by a few molecules, so a sort of steady-state nucleation often occurs [Kelton et al., 1983]. In this work we consider that at time $t = 0$ s the concentration of nuclei constituted by $n > 1$ solute molecules is zero:

$$N_{1,0} = N \tag{4.9}$$

$$N_{n,0} = 0 \; n \geq 2 \tag{4.10}$$

where N represents the total number of solute molecules in solution. When the process of nucleation begins (i.e. for $t > 0$) the value of the nucleation rate goes from zero to a finite value approaching the value of J^s. From Eqs. (4.6) and (4.7) it is possible to obtain an expression for $J_{n,t}$ by eliminating the kinetic constant k_{n+1}^+ in both equations, resulting in:

$$J_{n,t} = N_n^e k_n^+ \left(\frac{N_{n,t}}{N_n^e} - \frac{N_{n+1,t}}{N_{n+1}^e} \right). \tag{4.11}$$

The kinetic constant k_n^+ represents the rate at which a nucleus composed by n molecules gets a molecule from the solution, conversely, the rate at which one molecule from the solution "jumps" in a nucleus composed by n molecules. Therefore, this term will be proportional to the frequency of the jumps of the molecules in the solution towards the nucleus and the number of sites of the nucleus able to host such molecules, which is in turn proportional to the external surface area of the nucleus. According to the relevant theory [Kelton et al., 1983], it is possible to define an average, unbiased molecular jump frequency γ at the nucleus surface in condensed system. When a molecule from the bulk enters in the nucleus, it goes through two different phases. Hence, the jump will be accompanied by a change in the free energy. If $\Delta g(n)$ is the difference between the free energy of a nucleus composed by n molecule and the free energy of a nucleus composed by $n+1$ molecule, then the following quantities can be defined [Turnbull and Fisher, 1949]:

$$\gamma_n^+ = \gamma \exp\left(-\frac{\Delta g(n)}{2k_B T}\right), \tag{4.12}$$

$$\gamma_{n+1}^- = \gamma \exp\left(+\frac{\Delta g(n)}{2k_B T}\right), \tag{4.13}$$

which represent the average jump rates of molecules in reactions in Eqs. (4.3) to (4.4)). The value of γ in the above equations is in general related to the movement of the solute molecule in the solution and is therefore proportional to the diffusion coefficient of the solute D. The complete expression for γ turns out to be [Kelton et al., 1983]:

$$\gamma = 6\frac{D}{\lambda^2}, \tag{4.14}$$

in which λ is the root-mean-squared displacement of the solute molecules and can be taken equal to the diameter of the molecule [Dirksen and Ring, 1991].

The number of sites of the nucleus able to host molecules arriving from the solution can be described by considering the number of molecules that can be placed with their centres on a sphere which encloses the nucleus. Therefore each molecule jumping on the surface of the nucleus will occupy a certain region of this surface. The number of sites H_n is then equal to the total external surface of the nucleus divided by the external surface of one molecule. By assuming that nuclei are spherical the following expression is obtained: $H_n = 4n^{2/3}$, resulting

in the following forward and backward kinetic constants:

$$k_n^+ = H_n \gamma_n^+, \tag{4.15}$$

$$k_n^- = H_{n-1} \gamma_n^-, \tag{4.16}$$

Starting from Eq. (4.11) and replacing the value of k_n^+ with the value just found in Eqs. (4.12) and (4.15) one obtains:

$$J(n) = N^e(n) H_n \gamma \exp\left(-\frac{\Delta g(n)}{2k_B T}\right)\left(\frac{N(n)}{N^e(n)} - \frac{N(n+1)}{N^e(n+1)}\right), \tag{4.17}$$

that at steady state simplifies into the following expression:

$$J^s(n)\frac{1}{N^e(n) H_n \gamma \exp\left(-\frac{\Delta g(n)}{2k_B T}\right)} = \left(\frac{N^s(n)}{N^e(n)} - \frac{N^s(n+1)}{N^e(n+1)}\right). \tag{4.18}$$

The above equation represents the number of nuclei of size n (i.e., constituted by nN solute molecules) formed per unit volume and time.

By assuming that [Becker and Döring, 1935] as $n \to 0$, $N_n \to N_n^e$ and as $n \to \infty$, $N_n^s \to 0$, the following conditions can be written: $n \leq u$, $N^s(n) = N^e(n)$ and $n \geq v$, $N^s(n) = 0$, where $u < n^* < v$. The values u and v have to be taken outside of the critical region, corresponding to the the values of n for which $(\Delta G(n) - \Delta G(n^*)) < k_B T$. Summing Eq. (4.18) over all the possible values of n, one obtains [Kelton et al., 1983]:

$$J^s \sum_u^v \frac{1}{N_n^e H_n \gamma \exp\left(-\frac{\Delta g_n}{2k_B T}\right)} = \left(\frac{N^s(u)}{N^e(u)} - \frac{N^s(v+1)}{N^e(v+1)}\right) = 1, \tag{4.19}$$

where now $J^s = \sum_n J^s(n)$ is the total nucleation rate, accounting for the nuclei constituted by n solute molecules formed and not only those of critical size n^*. An expression for the nucleation rate is finally obtained with the additional assumption that the energy barrier to be overcome by molecules entering a nucleus is null (i.e., $\Delta g(n) \approx 0$), an approximation which turns out to be more and more realistic as the size of the nucleus increases, resulting in the following expression:

$$J^s = \left(\sum_{n=u}^v \frac{d^2}{24 N n^{2/3} D \exp\left(-\frac{\Delta G_V(n) - \Delta G_A(n) - \Delta G_1}{2k_B T}\right)}\right)^{-1}, \tag{4.20}$$

to which we refer in what follows as augmented nucleation theory (ANT), where N is the number density of solute molecules. The calculation of the terms $\Delta G_V(n)$ and $\Delta G_A(n)$ is not performed as in the CNT. In fact the approximations on the shape and dimensions of the molecules in solution used in the CNT can not be used with polymer chain. A more detailed calculation of these property is needed and this will be performed by using the MD simulations. This approach will be described in details the next Section. The term ΔG_1 in the above equation is instead added in order to recover self-consistency. Some authors however pointed out that the correction is not always necessary [Oxtoby, 1992]. However, since nuclei of polymer particles probably contain less molecules than nuclei composed of small inorganic molecules the use of this correction is retained in this work.

As anticipated in this work the rate of formation of polymer particles in solvent-displacement processes will be estimated by using the simplified CNT reported in Eq. (4.35) and the more accurate ANT reported in Eq. (4.20). The values of the different parameters appearing in Eq. (4.35) are obtained from independent measurements and a fitting procedure performed in our previous work [Di Pasquale et al., 2012] and also reported in Chap. 3. The values of the parameters appearing in Eq. (4.20) will be estimated for the first time in this work by using MD simulations.

4.3 Classical Nucleation Theory: simplified theory

Lots of simplified theories were developed (for a complete overview cf. Nielsen [1964]) to simplify the summation in Eq. (4.19) and to obtain an asymptotic expression of the nucleation rate to be used in a wide range of problems. These derivations make use of some of the assumption used in the previous part of the chapter, such as the possibilities of reaching a steady-state and the existence of a critical dimension of the nuclei (n^*) beyond which the nucleation rate can be considered negligible.

4.3.1 Concentration of nuclei in solution

Following the derivation of Nielsen [1964] an expression for the concentration of nuclei in solution can be found following this reasoning. From Eq. (4.2) it is possible to consider a process of nuclei formation composed by two steps, the

total Gibbs energy of which, is given by Eq. (4.2):

1. A certain number of molecules (n) is transferred from the solution to a very large particle

2. A nucleus composed by n molecules is separated from the large crystal.

Only once nuclei are formed they are allowed to grow in larger particles. It is therefore possible to consider the nuclei as liquid diluted from molar fraction one till a solution of molar fraction x_n is obtained. The corresponding total Gibbs energy for this system will be:

$$\Delta G = \Delta G_V + \Delta G_A + k_B T \ln(x_n) \tag{4.21}$$

where the last term represents the entropy of mixing of two ideal solutions. With this approach the process considered is no longer a phase transition but rather a formation and dissolution of particles. In this case from the condition of equilibrium ($\Delta G = 0$) the whole concentration of nuclei in solution can be obtained as follows:

$$\begin{aligned} \ln(x_n) &= -\left(\frac{\Delta G_V + \Delta G_A}{k_B T}\right) \\ x_n &= \exp\left(-\frac{\Delta G_V + \Delta G_A}{k_B T}\right) \\ N_n^e &= \frac{1}{v_{sol}} \exp\left(-\frac{\Delta G_V + \Delta G_A}{k_B T}\right) \end{aligned} \tag{4.22}$$

where the last step is done by assuming the dimension of a solute molecule to be equal to those of the solvent molecules and dividing both members by $\tilde{v}_s$, namely the molecular volume of the solvent, defined as the ratio between the solvent molar volume and the Avogadro number N_A.

4.3.2 Classical form of the nucleation term

Taking a step back, starting from Eq. (4.3) the classical rates given by the mass action law can be rewritten, resulting in what follows:

$$J_{n-1,n} = k^+_{n-1,n} N_1 N_{n-1}$$

where $J_{n-1,n}$ represents the rate of formation of nuclei constituted by n molecules from the "reaction" of a nucleus of $n = 1$ molecules and a single molecule. The overall rate of this "reaction" can be written considering both the forward and the backward rates:

$$J_n = J_{n-1,n} - J_{n,n-1}, \tag{4.23}$$

where J_n is the overall rate of formation of nuclei of size n. The value of n in the previous equation ranges from 1 to n^* for the definition of critical dimension of the nuclei considered. Beyond such a value $J = 0$, while for $n \leq n^*$ the value of J is independent from n. By using again the mass action law and the concept of equilibrium, it is possible to define an equilibrium concentration for a population of nuclei composed by n molecule via the following equation:

$$k^+_{n-1,n} N_1 N^e_{n-1} = k^-_{n,n-1} N^e_n.$$

Starting from $n = 1$:

$$J = k^+_{1,2} N_1^2 - k^-_{2,1} N_2$$

it is possible to write that:

$$\begin{aligned} N_2 &= k^+_{1,2} \frac{N_1^2}{k^-_{2,1}} - \frac{J}{k_{2,1}} = \\ &= \frac{k^+_{1,2}}{k^-_{1,2}} \frac{k^-_{2,1}}{k^+_{2,1}} N^e_2 - \frac{J}{k_{2,1}} = N^e_2 \left(1 - \frac{J}{J^e_{1,2}} \right) \end{aligned}$$

where $J^e_{n-1,n} = J^e_{n,n-1}$ because the system is at equilibrium. This procedure can be repeated for different n values (i.e., $n = 2$)

$$J = k^+_{2,3} N_1 N_2 - k^-_{3,2} N_3 \tag{4.24}$$

and it is then possible to obtain, by using the relations previously found, an expression for N_2 and N_3:

$$\begin{aligned} N_3 &= k^+_{2,3} \frac{N_1 N_2}{k^-_{3,2}} - \frac{J}{k_{3,2}} = \\ &= N^e_3 \left(1 - \frac{J}{J^e_{2,1}} - \frac{J}{J^e_{3,2}} \right). \end{aligned}$$

Therefore, by induction:

$$N_n = N_n^e \left(1 - \frac{J}{J_{2,1}^e} - \frac{J}{J_{3,2}^e} - \frac{J}{J_{4,3}^e} - \ldots - \frac{J}{J_{n,n-1}^e} \right). \tag{4.25}$$

In general, the above equation is valid for any values of n but, as already pointed out, for $n > n^*$ the nucleation rate becomes negligible. Henceforth, it is possible to consider only values of $n \leq n^*$. In the above equation it is possible to put $N_m = 0$ with $m \ggg n*$ obtaining

$$J = \left(\frac{J}{J_{2,1}^e} - \frac{J}{J_{3,2}^e} - \frac{J}{J_{4,3}^e} - \ldots - \frac{J}{J_{m,m-1}^e} \right)^{-1}. \tag{4.26}$$

where

$$J_{n,n-1}^e = k_{n,n-1} N_n^e = J_{n-1,n}^e \tag{4.27}$$

in which N_n^e is given by Eq. (4.22). The kinetic constant $k_{n,n-1}$ may be simplified by considering that the only rate-limiting step of the reaction is the diffusion of the solute molecules from the bulk towards the surface of the nucleus (diffusion-controlled process). Thus it is possible to consider $k_{n,n-1}$ independent from n. From the Einstein's relation between the diffusion coefficient D of a molecule and its root-mean square displacement λ:

$$D = \frac{\lambda^2}{2t_{\text{diff}}} \tag{4.28}$$

one can identify the kinetic constant $k_{n,n+1}$ as the inverse of time of diffusion of the molecules $k_{n,n+1} = t_{\text{diff}}^{-1}$. One then obtains:

$$J = \left(\frac{2D}{\lambda^2} \right) \left(\frac{1}{v_{sol}} \right) \sum_{n=2}^{m} \exp\left(\frac{\Delta G_n}{k_B T} \right). \tag{4.29}$$

By substituting the sum with an integral and by letting $m \to \infty$ thank to the hypothesis that the argument of the summation deviates slightly from zero except for a narrow region around n^*, the equation can be further simplified. In obtaining the expression for the equilibrium concentration of nuclei we assumed that the

solvent and solute molecules have the same volume. Hence we can write:

$$\frac{1}{v_{sol}} \approx \frac{1}{d_{mol}^3}$$

where d_{mol} is the diameter of the solute molecule. The final result (for a complete derivation cf. Nielsen [1964]) of the nucleation rate law expressed in closed form is:

$$J(n^*) = \left(\frac{2D}{d_{mol}^5}\right) \exp\left(-\frac{\Delta G(n^*)}{k_B T}\right), \tag{4.30}$$

in which the mean-square displacement λ has been identified with the diameter of the solute molecule and $\Delta G(n^*)$ represents the Gibbs energy at the critical size of the nucleus.

Dirksen and Ring [1991] proposed an alternative derivation which is conceptually simpler to that proposed by Nielsen [1964] but leads at the same result reported in Eq. (4.30). The basic assumption of this derivation is that only critical nuclei exist at once in solution. The nuclei below the critical size melt away and those beyond are removed from the solution. Hence, by considering the population of the critical nuclei given by Eq. (4.22) and by using Eq. (4.3) the rate of change of the population of nuclei of critical size n^* can be written as follows:

$$\begin{aligned} J(n^*) = \frac{\mathrm{d}N(n^*)}{\mathrm{d}t} &= k^+_{n^*-1} N(n^* - 1) N(1) - k^-_{n^*} N(n^*) \\ &\approx \left[k^+_{n^*-1}\left(\frac{1}{\tilde{v}_{sol}}\right) - k^-_{n^*}\right]\left(\frac{1}{\tilde{v}_{sol}}\right) \exp\left(\frac{-\Delta G(n^*)}{k_B T}\right), \end{aligned} \tag{4.31}$$

where the last equality follows by assuming $N(n^* - 1) \approx N(n^*)$. If we consider the limiting step for the formation of a nucleus to be the diffusion of one solute molecule from the solution towards the nucleus we can further simplify the difference between the two kinetic constants, because the rate-determining step will only be the separation of one molecule from a critical nucleus. By estimating this constant with the reciprocal diffusion time through the Einstein equation an expression identical to Eq. (4.30) is obtained.

4.3.3 Free Energy of nucleation

Different strategies have been used for the calculation of the Gibbs free energy for nucleation. Sometimes this calculation is performed by considering the nuclei as spheres; the radius of a nucleus composed by n solute molecules will be then taken equal to:

$$r(n) = \left(\frac{3n\tilde{v}_s}{4\pi}\right)^{1/3}, \tag{4.32}$$

where $\tilde{v}_s$ is the molecular volume of the solute. By using this definition for the radius of a nucleus, the following expression for the Gibbs free energy associated with the formation of a nucleus is obtained:

$$\Delta G(r) = -\left(\frac{4\pi r^3}{3\tilde{v}_s}\right) k_B T \ln(S) + 4\pi r^2 \sigma. \tag{4.33}$$

By differentiating the above equation with respect to the radius r and by imposing the null condition for the first derivative (corresponding to the maximum of the Gibbs energy) the critical size of a nucleus composed by n^* solute molecules, $r^* = {}^{2\sigma\tilde{v}_s}/_{k_B T \ln(S)}$, is obtained [Dirksen and Ring, 1991]. By substituting the above expression in Eq. (4.33) the value of the Gibbs energy for the formation of the critical nucleus is obtained:

$$\Delta G(r^*) = \frac{16\pi\sigma^3\tilde{v}_s^2}{3k_B^2 T^2 \ln(S)^2}, \tag{4.34}$$

resulting in the following nucleation rate:

$$J = \left(\frac{2D}{d^5}\right) \exp\left(-\frac{16\pi\sigma^3\tilde{v}_s^2}{3(k_B T)^3 \ln(S)^2}\right). \tag{4.35}$$

Most of the parameters appearing in Eq. (4.35), referred to as CNT, can be easily determined in the case of small inorganic molecules nucleating in one single solvent, as illustrated for example in our previous work [Gavi et al., 2010]. The case of nucleation of particles constituted by large polymer molecules during solvent-displacement processes is complicated by the fact that most of the parameters (i.e., D, d, $\tilde{v}_s$) change when moving from the solvent to the anti-solvent and these dependencies are not easy to be determined. Moreover, as already highlighted, the main hypotheses used in this approach lead to some inconsistency

(e.g., the equilibrium nuclei distribution presents a discontinuity at n^*, nuclei should be eliminated instantaneously from the solution).

In what follows the use of MD for calculating the change of Gibbs free energy associated with nucleation will be discussed. The discussion starts from some preliminary considerations on polymer chains that are then applied to the problem of polymer particle nucleation.

4.4 Atomistic model for polymer chains

As stated before, the volume and surface contribution to the free energy appearing in Eq. (4.20) depends from some properties of the molecules, as the dimensions and the shape. These properties can be easily extracted from MD simulations. However, the first thing to point out is what is the meaning of dimension for a geometrical complex object such as a polymeric chain.

First, let us consider a linear chain composed by N bonds as sketched in Fig. 4.1. The position of the atom i is individuated by its position vector $\mathbf{r}_i$. The vector joining two atoms i and j will be indicated as $\mathbf{r}_{ij} = \mathbf{r}_i - \mathbf{r}_j$. The end-to-end vector $\mathbf{R}_n$ of a polymeric chain is defined as

$$\mathbf{R}_n = \sum_{i=0}^{N} \mathbf{r}_i. \tag{4.36}$$

Since the end-to-end vector will be different for different chains in the system, it turns out to be more useful to consider instead some average quantity of the end-to-end vector instead. However, if we consider an isotropic collection of chain, the average value of the end-to-end vector turns out to be zero $\langle \mathbf{R}_n \rangle = 0$, since there is no preferred direction in the orientation of the end-to-end vector.

The first non-zero average result is the average square of the end-to-end vector, called the end-to-end distance ($\mathbf{R}_{EE}$):

$$\begin{aligned} \langle \mathbf{R}_{EE}^2 \rangle \equiv \langle \mathbf{R}_n \cdot \mathbf{R}_n \rangle &= \left\langle \left(\sum_{i=0}^{N} \mathbf{r}_i \right) \cdot \left(\sum_{i=0}^{N} \mathbf{r}_i \right) \right\rangle = \\ &= \left\langle \sum_{i=0}^{N} \sum_{j=0}^{N} \mathbf{r}_i \cdot \mathbf{r}_j \right\rangle. \end{aligned} \tag{4.37}$$

Where the average must be intended as an ensemble average. As it can be seen

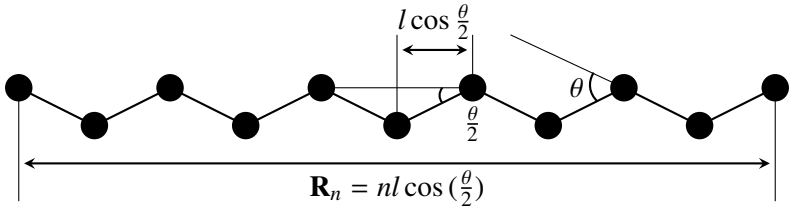

Figure 4.1: Conformation for a linear polymer chain. The chain is showed with all the torsion trans

from Fig. 4.2, the end-to-end vector defines the radius of a sphere which contains roughly all the chain.

The scalar product in Eq. (4.37) can be written in terms of the angle between the bond vectors $\mathbf{r}_i$ and $\mathbf{r}_j$, θ_{ij} as follows:

$$\mathbf{r}_i \cdot \mathbf{r}_j = r_i r_j \cos\theta_{ij},$$

which allows us to write the expression of the end-to-end distance:

$$\langle \mathbf{R}_{EE}^2 \rangle = \sum_{i=0}^{N} \sum_{j=0}^{N} \langle r_i r_j \cos\theta_{ij} \rangle, \tag{4.38}$$

where the summations can be brought out from the ensemble average.

The simplest model of an ideal polymer chain is the freely jointed chain model. In this model, it is assumed that the chain has a constant bond length $l = |\mathbf{r}_i|$ and no correlation between the direction of different bond vectors, $\langle \cos\theta_{ij} \rangle = 0$ if $i \neq j$. Therefore, from the double summation in Eq. (4.38) only N terms remain and the expression for $\langle \mathbf{R}_{EE}^2 \rangle$ reduces to

$$\mathbf{R}_{EE} = Nl^2. \tag{4.39}$$

which is the expression for the end-to-end distance for an ideal polymer molecule which follows from the hypothesis of the freely jointed chain model.

However, in a real polymer chain a correlation between vector bond, due mainly to angles between bond vectors and steric hindrance, exists. This correla-

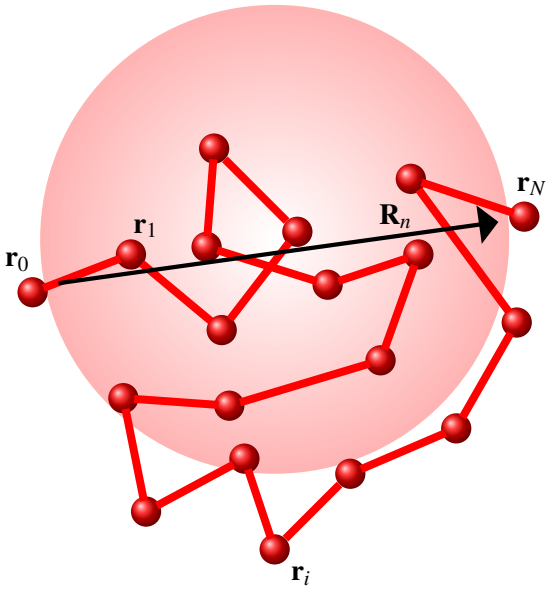

Figure 4.2: Sketch of a chain composed by $N + 1$ atoms. The end-to-end distance represents roughly a sphere that enclose all the molecule

tion decays quickly as continuing along the chain till it is zero at long distances:

$$\lim_{|i-j|\to\infty} \langle \cos\theta_{ij} \rangle = 0.$$

It can be shown (for a complete derivation cf. Rubinstein and Colby [2003]) that the sum over all the bond j for each bond i converges towards a finite quantity:

$$C_i' \equiv \sum_{j=0}^{N} \langle \cos\theta_{ij} \rangle.$$

Hence we can rewrite Eq. (4.38) as follows:

$$\langle \mathbf{R}_{EE}^2 \rangle = l^2 \sum_{i=0}^{N} \sum_{j=0}^{N} \langle \cos\theta_{ij} \rangle = l^2 \sum_{i=0}^{N} C_i' = l^2 N C_N, \tag{4.40}$$

in which

$$C_N = \frac{1}{N} \sum_{i=0}^{N} C_i' \tag{4.41}$$

is the Flory characteristic ratio. If steric hindrance between monomers separated by many bonds is ignored, the value of C_N increases with the number of monomers in the chain, until it reaches an asymptotic value C_∞ for $N \to \infty$. Hence $\langle \mathbf{R}_{EE}^2 \rangle$ can be written as:

$$\langle \mathbf{R}_{EE}^2 \rangle \approx C_\infty n l^2. \tag{4.42}$$

An universal, or rather, independent from the chemistry of the particular chain, description of the characteristic of the polymer can be obtained by using the concepts of the equivalent freely jointed chain. In this model, an equivalent chain which has the same $\mathbf{R}_{EE}$ and same $\mathbf{R}_n$ as the actual polymer but has N' freely-jointed effective bonds of length b, with $N' < N$, is defined. We can therefore write for the contour length of the polymer:

$$\mathbf{R}_n = N' b \tag{4.43}$$

from which the end-to-end distance is obtained:

$$\langle \mathbf{R}_{EE}^2 \rangle = N' b^2 = b\mathbf{R}_n = C_\infty n l^2. \tag{4.44}$$

By using the two previous equations the equivalent bond length b and the equivalent number of bonds N' can be calculated:

$$N' = \frac{\mathbf{R}_n}{C_\infty n l^2},$$
$$b = \frac{C_\infty n l^2}{\mathbf{R}_n}.$$

The equivalent bond length is called Kuhn length [Kuhn, 1936].

4.4.1 Freely Rotating chains

The freely rotating chain model is a model for ideal chains which assumes fixed bond length and bond angle (in freely jointed chain model only the bonds are fixed) and free torsion, i.e. all the possible torsion angles are equally probable ($-\pi < \phi_i < \pi$). In order to calculate the mean square end-to-end distance, reported in Eq. (4.37), the correlation between bond vectors $\mathbf{r}_i$ and $\mathbf{r}_j$ must be determined. Due to the assumption of freely rotating chain, the only correlation (i.e. the quantity that is not averaged out in an ensemble average) between a bond vector $\mathbf{r}_j$ and a bond vector $\mathbf{r}_{j+1}$ is the component of the bond vector $\mathbf{r}_j$ parallel to bond vector $\mathbf{r}_{j+1}$, $l\cos\theta$, because the normal component when the ensemble average is performed turns out to be equal to zero:

$$I_{j,j+1} = \langle \mathbf{r}_j \cdot \mathbf{r}_{j+1} \rangle = l^2 \cos\theta.$$

The correlation between the bond vector $\mathbf{r}_j$ and a bond vector $\mathbf{r}_{j+2}$ is again due only to the projection of leftover memory of bond vector $\mathbf{r}_j$ on bond vector $\mathbf{r}_{j+1}$, on bond vector $\mathbf{r}_{j+2}$:

$$I_{j,j+2} = \langle \mathbf{r}_j \cdot \mathbf{r}_{j+2} \rangle = \left\langle \left(\frac{\mathbf{r}_j \cdot \mathbf{r}_{j+1}}{|r_{j+1}|} \right) \cdot \mathbf{r}_{j+2} \right\rangle = l^2 \cos^2\theta.$$

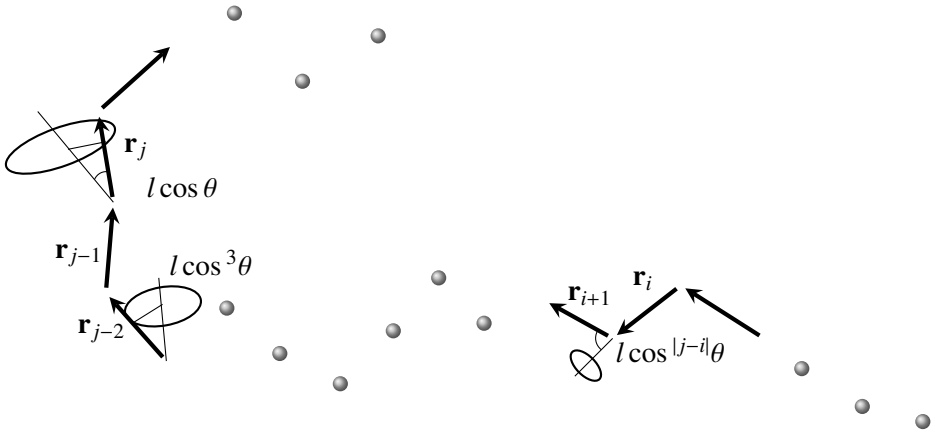

Figure 4.3: In the freely rotating chain model each bond and angle between two vector bond are fixed. Each vector bond can still freely rotate because it is assumed that all the torsion angles are equally probable

By iterating the previous argument along the chain, one obtains for a bond vector $\mathbf{r}_i$ and a bond vector $\mathbf{r}_j$ separated by $|j-i|$ bonds the following correlation:

$$I_{i,j} = \langle \mathbf{r}_i \cdot \mathbf{r}_j \rangle = l^2 \cos^{|i-j|}\theta. \tag{4.45}$$

It is now possible to obtain the end-to-end distance by combining Eq. (4.37) and Eq. (4.45) resulting in:

$$\begin{aligned}
\langle \mathbf{R}_{EE}^2 \rangle &= \sum_{i=0}^{N}\sum_{j=0}^{N} \langle \mathbf{r}_i \cdot \mathbf{r}_j \rangle = \sum_{i=0}^{N}\left(\sum_{j=0}^{i-1} \langle \mathbf{r}_i \cdot \mathbf{r}_j \rangle + \langle \mathbf{r}_i^2 \rangle + \sum_{k=i+1}^{N} \langle \mathbf{r}_i \cdot \mathbf{r}_k \rangle\right) = \\
&= \sum_{i=0}^{N} \langle \mathbf{r}_i^2 \rangle + l^2 \sum_{i=0}^{N}\left(\sum_{j=0}^{i-1} \cos^{|i-j|}\theta + \sum_{k=i+1}^{N} \cos^{|k-i|}\theta\right) = \\
&= Nl^2 + l^2 \sum_{i=0}^{N}\left(\sum_{k=0}^{i-1} \cos^{k}\theta + \sum_{k=i+1}^{N-i} \cos^{k}\theta\right).
\end{aligned} \tag{4.46}$$

It is also possible to define a scale at which the local correlation between the bond vector decays as s_p, resulting in:

$$\cos^{|j-i|}\theta = e^{|j-i|\ln\cos\theta} = e^{-\frac{|j-i|}{s_p}} \tag{4.47}$$

where $s_p = -1/\ln\cos\theta$. Since the decay is very fast, it is possible to replace the summation in Eq. (4.46) with an infinite series over k:

$$\sum_{i=0}^{N}\left(\sum_{k=0}^{i-1}\cos^k\theta + \sum_{k=i+1}^{N-i}\cos^k\theta\right) \approx$$
$$\approx 2\sum_{i=0}^{N}\sum_{k=0}^{\infty}\cos^k\theta =$$
$$= 2N\sum_{k=0}^{\infty}\cos^k\theta = 2N\frac{\cos\theta}{1-\cos\theta} \tag{4.48}$$

from which one obtains the final results for the end-to-end distance of the freely rotating chain

$$\langle \mathbf{R}_{EE}^2\rangle = Nl^2 + 2N\frac{\cos\theta}{1-\cos\theta}. \tag{4.49}$$

4.4.2 Other models

There are several other models for the description of polymer chains and for a complete review cf. Rubinstein and Colby [2003]. Here, only the simplest and widely known were analysed and discussed. A brief description of the other models is summarized in Table 4.1, along with the basic assumptions and some results.

Models	FJC	FRC	HR	RIS
Bond length l	Fixed	Fixed	Fixed	Fixed
Bond angle θ	Free	Fixed	Fixed	Fixed
Tosion angle ϕ	Free	Free	Controlled by $V(\phi)$	t, g^+, g^-
Next ϕ is independent?	Yes	Yes	Yes	No
C_∞	1	$\frac{1+\cos\theta}{1-\cos\theta}$	$\left(\frac{1+\cos\theta}{1-\cos\theta}\right)\left(\frac{1+\langle\cos\theta\rangle}{1-\langle\cos\theta\rangle}\right)$	Specific

Table 4.1: Assumption and prediction for C_∞ for the principal ideal chain models: FJC freely jointed chain, FRC freely rotating chain, HR indered rotation, RIS rotational isomeric state. $V(\phi)$ represents the dihedral potential associated with the torsional angles of the chain. t, g^+, g^- represent the different orientation of the chain: trans, gauche +, gauche − [Rubinstein and Colby, 2003].

4.4.3 Radius of gyration

A second type of measure that can be used to quantify the dimension of a chain is the radius of gyration, $\mathbf{R}_g$, which represents the square second moment around the centre of mass of the chain. $\mathbf{R}_g$ gives more detailed information about the shape of the chain and the distribution of the monomers around the centre of the chain, identified with the Centre Of Mass (COM). The COM of a chain is defined as

$$\mathbf{r}_B = \frac{1}{\sum_{i=0}^{N} m_i} \sum_{i=0}^{N} m_i \mathbf{r}_i$$

where m_i is the mass of the i-th atom. Then, $\mathbf{R}_g$ is given by

$$\mathbf{R}_g^2 = \frac{1}{\sum_{i=0}^{N} m_i} \sum_{i=0}^{N} m_i (\mathbf{r}_i - \mathbf{r}_B)^2$$

Again, it is more useful to define an ensemble averaged radius of gyration $\langle \mathbf{R}_g^2 \rangle$

$$\begin{aligned} \langle \mathbf{R}_g^2 \rangle &= \left\langle \frac{1}{\sum_{i=0}^{N} m_i} \sum_{i=0}^{N} m_i (\mathbf{r}_i - \mathbf{r}_B)^2 \right\rangle = \\ &= \frac{1}{\sum_{i=0}^{N} m_i} \sum_{i=0}^{N} m_i \left\langle (\mathbf{r}_i - \mathbf{r}_B)^2 \right\rangle = \\ &= \frac{1}{2\left(\sum_{i=0}^{N} m_i\right)^2} \sum_{i,j=0}^{N} m_i \left\langle (\mathbf{r}_i - \mathbf{r}_j)^2 \right\rangle \end{aligned} \tag{4.50}$$

where the average can be exchanged with the mean and the last equality is detailed in App. D. For non-fluctuating objects the average is not necessary. However, the relative position of atoms in a polymer chains are not fixed in time, hence an averaged value is needed.

An analytical expression for the radius of gyration can be obtained by considering an ideal linear chain. In this case, the summation over the monomers in Eq. (4.50) can be substituted with an integration over the contour of the chain. The coordinate i and j of the atoms are replaced with the continuous variables u

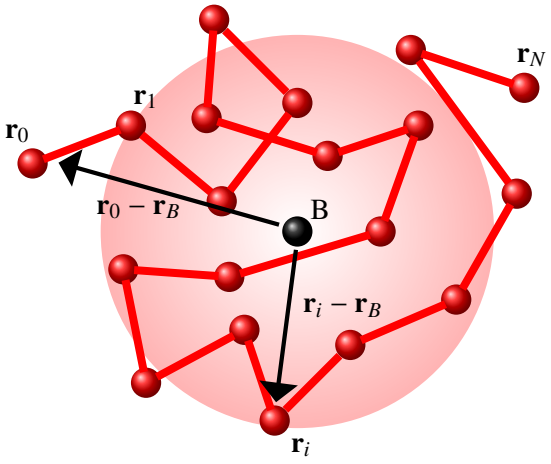

Figure 4.4: Sketch of a chain composed by $N + 1$ atoms. B stands for the center of mass of the chain. The radius of gyration can be considered as the average between all the vector connecting each atoms to the center of mass, and represents roughly the sphere that occupies the same volume of the polymer

and v:

$$\sum_{i=0}^{N} \rightarrow \int_0^N \mathrm{d}u \qquad \sum_{j=0}^{N} \rightarrow \int_0^N \mathrm{d}v$$

from which we can obtain the integral form of the mean-square radius of gyration

$$\langle \mathbf{R}_g^2 \rangle = \frac{1}{N^2} \int_0^N \int_0^N \langle (\mathbf{r}(u) - \mathbf{r}(v))^2 \rangle \mathrm{d}v \mathrm{d}u \tag{4.51}$$

in which $\mathbf{r}(u)$ is the position vector corresponding to the contour coordinate u. The mean square distance between u and v along the contour of the chain can be calculated by considering each section $u - v$ as a shorter ideal chain and by assuming that the rest of the chain does not affect the behaviour of this short chain. Therefore, the mean square end-to-end distance of an ideal chain is given by:

$$\langle (\mathbf{R}(u) - \mathbf{R}(v))^2 \rangle = (v - u) b^2. \tag{4.52}$$

Then, it is possible to calculate the radius of gyration by integration and with a

change of variable $v' = v - u$ and $u' = N - u$

$$\begin{aligned}\langle \mathbf{R}_g^2 \rangle &= \frac{b^2}{N^2}\int_0^N \int_0^N \langle (\mathbf{r}(u) - \mathbf{r}(v))^2 \rangle \mathrm{d}v\mathrm{d}u = \frac{b^2}{N^2}\int_0^N \int_0^N v'\mathrm{d}v'\mathrm{d}u \\ &= \frac{b^2}{N^2}\int_0^N \frac{N-u}{2}\mathrm{d}u = \frac{b^2}{2N^2}\int_0^N (u')^2 = \\ &= \frac{b^2}{2N^2}\frac{N^3}{3} = \frac{Nb^2}{6}. \end{aligned} \tag{4.53}$$

From Eq. (4.39) the important relation between the mean square end-to-end distance and the mean-square radius of gyration is also obtained:

$$\langle \mathbf{R}_{EE}^2 \rangle = \frac{Nb^2}{6} = \frac{\langle \mathbf{R}_{EE}^2 \rangle}{6}. \tag{4.54}$$

$\mathbf{R}_g$ consists of 3 components $\mathbf{R}_{g_x}$, $\mathbf{R}_{g_y}$, $\mathbf{R}_{g_z}$, which are defined as follows:

$$\langle \mathbf{R}_{g_\alpha}^2 \rangle = \left\langle \frac{1}{\sum_{i=0}^N m_i} \sum_{i=0}^N m_i (r_{i_\alpha} - r_{B_\alpha})^2 \right\rangle, \quad \alpha = x, y, z \tag{4.55}$$

where r_{i_α} is the component of the position vector of atom i and r_{B_α} is the component of the position vector of the COM. To obtain a description of the variation of $\mathbf{R}_{g_x}$, $\mathbf{R}_{g_y}$, $\mathbf{R}_{g_z}$ the shape factor s are defined:

$$\langle S_x \rangle = \frac{\langle \mathbf{R}_{g_x}^2 \rangle}{\langle \mathbf{R}_g^2 \rangle}, \tag{4.56}$$

$$\langle S_y \rangle = \frac{\langle \mathbf{R}_{g_y}^2 \rangle}{\langle \mathbf{R}_g^2 \rangle}, \tag{4.57}$$

$$\langle S_z \rangle = \frac{\langle \mathbf{R}_{g_z}^2 \rangle}{\langle \mathbf{R}_g^2 \rangle} \tag{4.58}$$

which can be considered almost independent from the dimension of the chain [Mazur et al., 1973]. This quantity gives some information about the shape of the molecules in solution. In fact if there is no preference on the disposition of the chain it will approach their ideal value of 1/3.

4.4.4 Polymer in solution

The radius of gyration of a polymer chain is not constant in all the environments (with environment we refers to the different solvents in which a polymer chains can be immersed), but it is instead highly sensitive to the nature of the solvent. In the process we consider, due to the fast mixing of the solvent and anti-solvent, the polymer experiences a number of different environments which range from pure acetone to pure water. Therefore it is crucial to evaluate this dependence. The relation between the radius of gyration and the solvent in which the polymer is immersed, can be evaluated through the Flory theory [Flory, 1953] which expresses the polymer size (in term of radius of gyration) as a function of the number of monomers, through the following universal power law:

$$\mathbf{R}_g \propto N^{\nu}. \tag{4.59}$$

The affinity of the polymer with the solvent, which can be taken in account by considering the excluded volume of the polymer, modifies the Flory exponent ν, only for $\nu > 0$, or rather for any good polymer solvent. The Flory theory leads to a value of $\nu = 3/5$ for a real chain in good solvents and a value of $\nu = 1/2$ for an ideal chain. This can be summarized as [Flory, 1953]: "the better the solvent the greater the swelling of the molecule. Conversely, the poorer the solvent the smaller the molecule". However the value of ν can change slightly from one polymer to another as shown in Cotton et al. [1974] for polystyrene.

4.4.5 Nucleation barrier

The concepts showed in the previous Sections (i.e Radius of gyration, Flory exponent) turn out to be very useful in the calculation of the nucleation rate, since by using them it is possible to overcome the assumption of spherical molecules used, for example, in the previously mentioned derivation of the Gibbs energy in the CNT. It is important to remind here that although this assumption seems to be valid for virtually all the systems in which an inorganic salt is precipitated, it is questionable in the case of precipitating polymer molecules [Di Pasquale et al., 2012]. In fact, polymer chains are characterized by different behaviors depending on the environment (i.e. solvent versus anti-solvent) in which they are dissolved, as they can be more or less unfolded or entangled.

MD is used in this work to calculate the value for the radius of gyration of the polymer molecule, $\mathbf{R}_g$; this value is then used to estimate the dimension of the nuclei and their external surface that in turn are used to calculate the volume and surface contributions to the Gibbs free energy. Since polymer molecules are not rigid as small inorganic molecules, they can rearrange themselves in the nucleus, resulting in non-additive volumes and surfaces, when they assemble together forming a nucleus. Due to this fact, it seems reasonable to consider each nucleus composed by n polymer molecules of m monomers each as a single molecule of $n \times m$ monomers. One problem that arises by using this approach is that in the real nucleus the polymer molecules are not linked together as in our representation. If one considers the number of ways in which n single molecules can be rearranged, the result is greater than the number of configurations in which a single molecule can be rearranged. This may lead to an overall underestimation of the nucleus size, whose effect is probably more consistent on the volume terms than on the surface terms for the calculation of Gibbs free energy.

In this work this problem is overcome by adopting the following strategy: a correction (of the order of magnitude of n) is applied only to the volume contribution to the Gibbs free energy, whereas the surface contribution is calculated without applying any correction. Therefore the final volume and surface contributions to the Gibbs free energy appearing in Eq. (4.20) read as follows:

$$\Delta G_V(n) = n^2 k_B T \ln(S), \tag{4.60}$$

$$\Delta G_A(n) = A_s(n)\sigma, \tag{4.61}$$

where $A_s(n)$ is the external surface of the ellipsoid with semi-principal axes of length equal to $\mathbf{R}_{g_x}$, $\mathbf{R}_{g_y}$, $\mathbf{R}_{g_z}$ corresponding to a nucleus constituted by n molecules. These hypotheses will be the validated a-posteriori by comparing simulations with experimental results.

4.5 Operating conditions investigated and simulation details for MD and CFD

The simulations carried out in this work refer to the precipitation of poly-ϵ-caprolactone (PCL) nanoparticles in CIJM by using acetone and water as solvent and anti-solvent. Simulation predictions are compared with experiments taken

from our previous work [Lince et al., 2008].

MD simulations are performed with the GPL code Gromacs [van der Spoel et al., 2005]. The systems simulated are two different chain lengths of PCL composed by $m = 10$ and $m = 30$ monomers respectively (from now on PCL-10 and PCL-30) in different environments characterized by different molar fractions of water, X_W, in water-acetone mixtures. One monomer is composed by 18 atoms and is shown in Fig. 4.5, hence the dimensions of the chain for PCL-10 and PCL-30 are of 188 and 548 atoms respectively (each chain is closed by a methyl group). The simulated time is reported in Table 4.2. The force field used is the OPLS-AA [Jorgensen et al., 1996] for both acetone and PCL molecules and SPC [Berendsen et al., 1983] for water. The simulations are carried in the (N, P, T) ensemble with a temperature of 300 K and a pressure of 1 bar with the Berendsen thermostat and barostat. The temperature relaxation time used is $\tau_T = 0.1$ ps, and the pressure relaxation time was set to $\tau_P = 0.5$ ps. In Table 4.3 the dimensions of the systems simulated in pure water and pure acetone is reported.

	pure water	pure acetone
PCL-10	85 ns	70 ns
PCL-30	60 ns	70 ns

Table 4.2: Simulated time for all the environment conditions and for all the systems considered

	pure water	pure acetone
PCL-10	7169	1512
PCL-30	22635	1193

Table 4.3: Dimension of the system simulated in number of solvent molecules

CFD simulations are carried out by using Ansys/Fluent 12.0 commercial software. Turbulence is modeled by using the RANS approach and DQMOM-IEM is used to describe the interaction between turbulence and particle formation. The precipitation of the PCL particles is described by the PBM solved with QMOM.

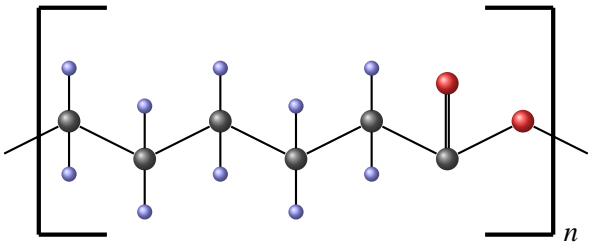

Figure 4.5: Representation of one monomer of PCL. Black spheres represent carbon, light blue spheres represent the hydrogen and the red spheres represent the oxygen

DQMOM-IEM and QMOM are implemented in the CFD code by resorting to user-define scalars and functions. The pressure-velocity coupling was solved with the SIMPLE algorithm, whereas the standard $k-\epsilon$ turbulence model coupled with the enhanced-wall treatment approach was used. The simulations presented in this work are limited to the case of water flow rate of $120\,\mathrm{mL\,min^{-1}}$ and of water-to-acetone flow rate ratio of $R = 2$. The initial polymer concentration considered is of $c^0_{PCL} = 2.5\,\mathrm{mg\,mL^{-1}}$.

4.6 Results and discussion

Before discussing the results for MD simulations of PCL molecules, the force field used for the solvent was tested by performing a simulation under the same conditions but without any other molecule inside the simulation box. Some results are sketched in Fig. 4.6 where the radial distribution functions for oxygen and carbon atoms of the acetone molecule are compared with a reference solution[Freitas et al., 1999]. As it is possible to see good agreement is obtained. The final density obtained with the simulation is $784 \pm 2\,\mathrm{kg\,m^{-3}}$, which is in agreement with the experimental density of acetone at $T = 300$ K of $779\,\mathrm{kg\,m^{-3}}$.

The main results for PCL are shown in Table 4.4 where radius of gyration, $\mathbf{R}_g$, and the Flory exponents, ν, are reported for the two extreme environments of pure water and pure acetone. All the properties are calculated by averaging over the trajectory and the calculation starts when the value of the property is stabilized, i.e. after an equilibration period. Fig. 4.7 shows the time evolution of the radius of gyration after the equilibration period for the entire simulation. As

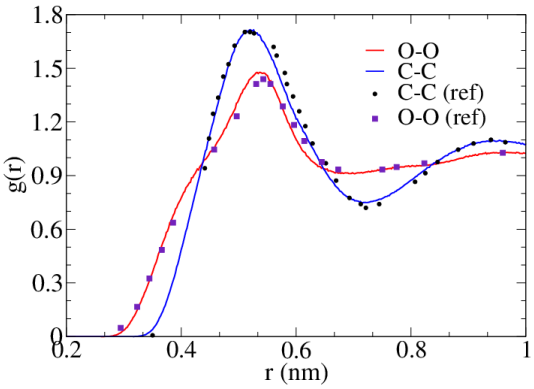

Figure 4.6: Radial distribution function for liquid acetone; carbon-carbon sites: MD simulations perfromed in this work (blue solid line), referenceFreitas et al. [1999] (filled circles); oxygen-oxygen sites: MD simulations performed in this work (red solid line), referenceFreitas et al. [1999] (filled squares).

it is seen the radius of gyration grows with the size of the polymer chain and is larger in acetone than in water. Moreover the Flory exponent is smaller in water than in acetone.

	pure Water		pure Acetone	
	PCL 10	PCL 30	PCL 10	PCL 30
$\mathbf{R}_g$	0.63 ± 0.04	0.87 ± 0.01	1.2 ± 0.2	1.96 ± 0.37
ν	0.292		0.489	

Table 4.4: $\mathbf{R}_g$ in (nm) obtained from the MD simulations for PCL molecules (constituted by $m = 10$ and $m = 30$ monomers) in pure water and pure acetone.

Additional information is gained by analysing the three components of $\mathbf{R}_g$, that better account for the preference of orientation of the chain when it deviates from the spherical shape (i.e., when is completely uncoiled as in a good solvent). This preference is measured by the average shape factors, of Eq. (4.56), reported in Table 4.5. These shape factors are average values for PCL-10 and PCL-30, since simulations have confirmed that they do not depend on the size of the polymer chain. Results show that in pure water shape factors in the three directions

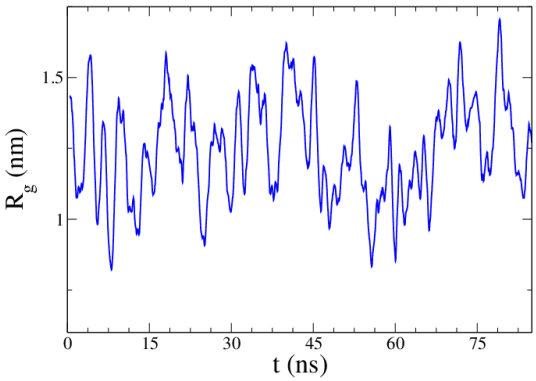

Figure 4.7: Time evolution of the radius of gyration for PCL-10 in pure acetone.

are similar to each other and close to $1/3$, whereas in pure acetone one of them is much lager than the others.

pure Water			pure Acetone		
$\langle S_x \rangle$	$\langle S_y \rangle$	$\langle S_z \rangle$	$\langle S_x \rangle$	$\langle S_y \rangle$	$\langle S_z \rangle$
0.497 ± 0.036	0.300 ± 0.014	0.196 ± 0.026	0.717 ± 0.009	0.204 ± 0.004	0.062 ± 0.01

Table 4.5: Average shape factors for PCL in pure water and pure acetone.

Summarizing, results reported in Tabs. 4.4 and 4.5 show that, as expected, convolution of PCL is greater in water than in acetone. In fact, in pure acetone PCL molecules are more stretched out, whereas in pure water are more entangled. Moreover, results show that for PCL molecules in acetone one direction is preferred among the others, or in other words, the polymer is uncoiled in this environment, whereas the shape factors for PCL molecules in water are very close to those of spheres. These conclusions are qualitatively confirmed by observation of Fig. 4.8 where a sketch of the results obtained for the MD simulation of PCL-10 in acetone (on the left) and water (on the right) is reported.

The fact that in environments rich in water PCL molecules are close to spheres further confirms the validity of some of the assumptions used in the derivation of Eq. (4.20), namely the calculation of the pre-exponential term. In fact, most of the nucleation occurs in the regions of the CIJM characterized by large saturation ratios. These regions are typically located near the water inlet and are therefore

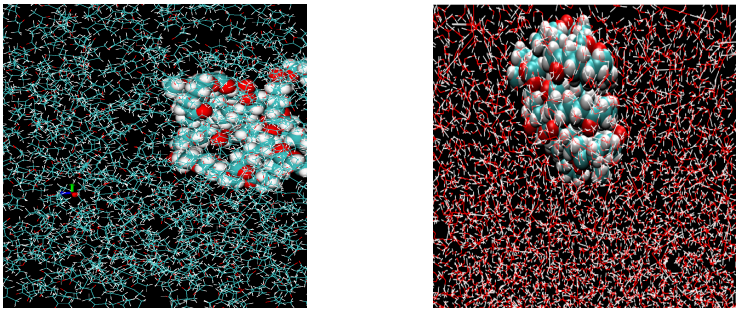

Figure 4.8: Sketch of the results obtained for the MD simulation of PCL in acetone (on the left) and water (on the right).

characterized by elevate water molar fraction values.

The behavior of PCL-10 in different environments can be more effectively summarized in Fig. 4.9, where the variation of the PCL molecular volume (calculated from the radius of gyration) is reported as a function of the water molar fraction in a mixture of water and acetone, ranging from pure water (i.e., $X_w = 100$ %) to pure acetone (i.e., $X_w = 0$ %).

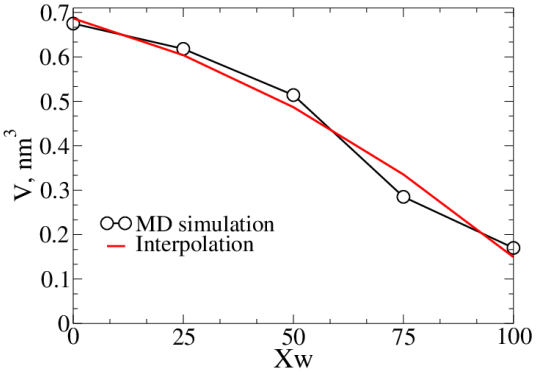

Figure 4.9: Molecular volume (nm^3) of PCL-10 calculated using the three components of the radius of gyration versus the water molar fraction X_w (%).

As already mentioned the results obtained from the MD simulations are finally used to calculate the nucleation rate by using the ANT of Eq. (4.20); simulations with the CNT of Eq. (4.35) are also considered. Although many tests with different operating conditions were performed, only one flow rate 120 mL min^{-1} and only one water-to-acetone ratio $R = 2$ is here presented for brevity. Both nu-

cleation rates are adopted in the PBM implemented in the CFD code and results are compared with experiments.

It is important to remind here that results are here obtained from MD simulations performed for PCL-10 and PCL-30, whereas the PCL used in the experiments (and in our CFD simulations) has a molecular weight of 14000 kg mol^{-1} corresponding to about 120 monomers. Therefore instead of running time consuming MD simulations for the full chain corresponding to the molecular weight of 14000 kg mol^{-1}, MD simulations for smaller chains were run, and results extrapolated from PCL-10 and PCL-30. We are aware of the potential limit of this extrapolation, that will be therefore validated in our future work.

CFD simulation results are reported in Fig. 4.10, where the contour plots on the symmetry plane of the CIJM of saturation ratio, nucleation rate and mean particle size are plotted. Results obtained with Eq. (4.20) are compared with those obtained with Eq. (4.35)) with a value of the molecular volume of the polymer obtained from the fitting procedure performed in our previous work Di Pasquale et al. [2012].

Closer observation of Fig. 4.10 reveals that the contour plots of the mean particle size obtained with the two approaches is quite similar. In fact, the mean particle size in the CIJM outlet obtained with Eq. (4.20) is equal to d_{43} = 178 nm whereas the same value resulting from Eq. (4.35) is d_{43} = 182 nm. Both values must be compared with an experimental value of 210 nm.

The main differences lie in the contour plot of nucleation rate and saturation ratio. As it is shown, nucleation of the particles inside the CIJM takes place in a very narrow region near the water inlet, where the highest values and gradients of saturation ratio are detected. Predictions with Eq. (4.20)) result in smaller nucleation rates, when compared with predictions obtained with Eq. (4.35).

As far as the predictions for the saturation ratio are concerned, at the outlet of the CIJM a value near unity is predicted in both cases. This means that both nucleation rates predict that all polymer in excess with respect to the equilibrium concentration precipitates before exiting from the CIJM, which seems to be in agreement with experimental evidence. The shape of the region with the highest saturation ratio seems very similar and the main difference is in the absolute value of S. With Eq. (4.35) the saturation ratio is twice the value of that obtained with Eq. (4.20). Also this result seems to confirm that Eq. (4.20) gives a more realistic description of the nucleation process, since the nucleation of the polymer

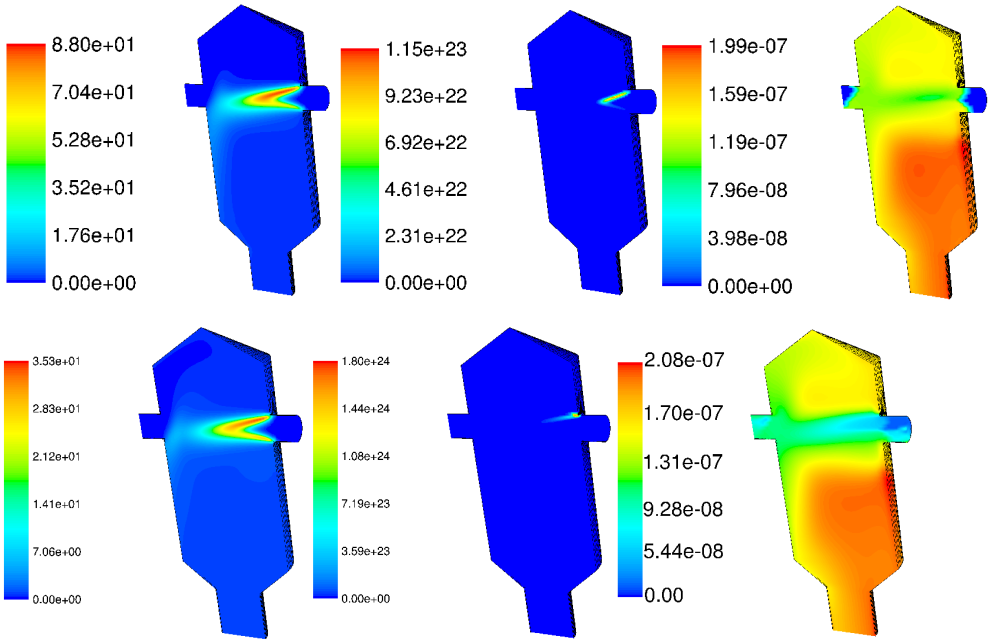

Figure 4.10: Comparison of the results obtained with Eq. (4.20) (top) with the results obtained with Eq. (4.35) (bottom); from left to right: contour plot of the saturation ratio (−), nucleation rate ($m^{-3}s^{-1}$) and mean particle size on the symmetry plane of the CIJM; water flow rate: 120 mL min^{-1}, water-to-acetone flow rate ratio $R = 2$, and initial PCL concentration, $c^0_{PCL} = 2.5$ mg mL^{-1}

particles, due to the large dimension of the polymer chains constituting the nuclei should be slower than that of smaller molecules.

It is interesting to compare now the predictions of the CNT reported in Eq. (4.35) with the predictions obtained by using the ANT of Eq. (4.20), with the surface contribution calculated via MD simulations as explained above for a different operating conditions of the mixer (i.e. different water inlet flow rate and different water-to-acetone ratio).

Let us start with the saturation ratio, whose contours in the symmetry plane of the CIJR are reported in Fig. 4.11 for different inlet flow rates of the water (left inlet) and acetone (right inlet) streams. Although the mixing efficiency increases with the increase of the flow rate, from 40 to 120 $\mathrm{mL\,min^{-1}}$, as also highlighted by Di Pasquale et al. [2012], the saturation ratio obtained with the CNT seems not to be affected much by the change in the flow field conditions. A much stronger influence is instead predicted by the ANT, that quantifies a change of the saturation ratio from 60 to 90, when the water flow rate is increased from 40 to 120 $\mathrm{mL\,min^{-1}}$. Fig. 4.12 compares instead the contours of the predicted nucleation rate on the symmetry plane of the CIJR, for the ANT (left) and the CNT (right), for different water inlet flow rates and for a constant water-to-acetone flow rate of $R = 2$. It is important to remind here that in the CNT, resulting in Eq. (4.35), the value of $\tilde{v}$ was tuned in order to reach agreement with the experiments (in term of the final mean particle size). As already mentioned the fitting resulted in $\tilde{v} = 2.06\ 10^{-28}\,\mathrm{m^3}$ for $R = 2$. In the case of the ANT, resulting in Eq. (4.20), instead no attempt to tune or fit the parameters was done, as all of them were derived from the theory and from MD simulations. As visible from Fig. 4.12, and as confirmed by the theoretical findings of Nielsen [1964], the CNT overestimates the nucleation rate (with respect to ANT) of one order of magnitude.

The comparison, in terms of the contours of the final mean particle size, d_{43}, in the symmetry plane of the CIJR as predicted by the ANT (left) and by the CNT (right) for different water inlet flow rates and for a constant water-to-acetone flow rate ratio of $R = 2$, is reported is Fig. 4.13. As it is seen the two approaches result in very similar values of the final mean particle size. However, this is artificially obtained in the CNT, by fitting the value of $\tilde{v}$ appearing in Eq. (4.35). This results in higher nucleation rates (as evident from Fig. 4.12) that makes the overall simulation very unstable and produce some unphysical predictions. One

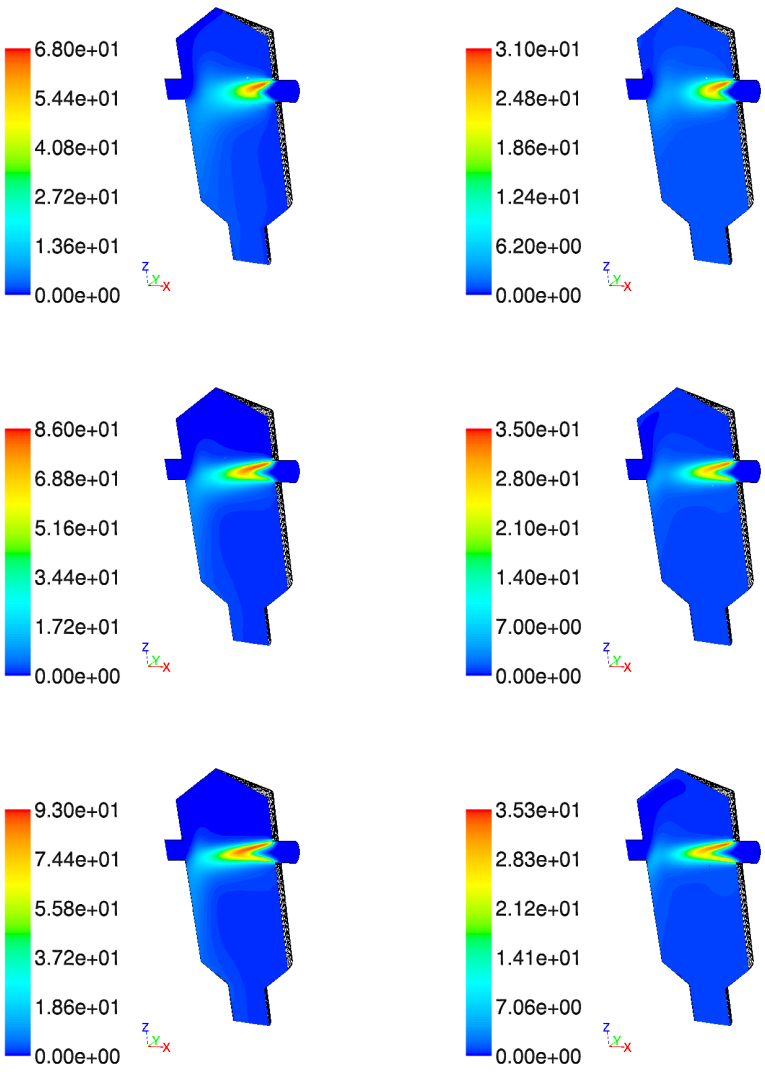

Figure 4.11: Contour plots of the saturation ratio predicted by the ANT (left) and the CNT (right) for $R = 2$ and for different inlet water flow rates (from top to bottom: 40 mL min^{-1}, 80 mL min^{-1} and 120 mL min^{-1}).

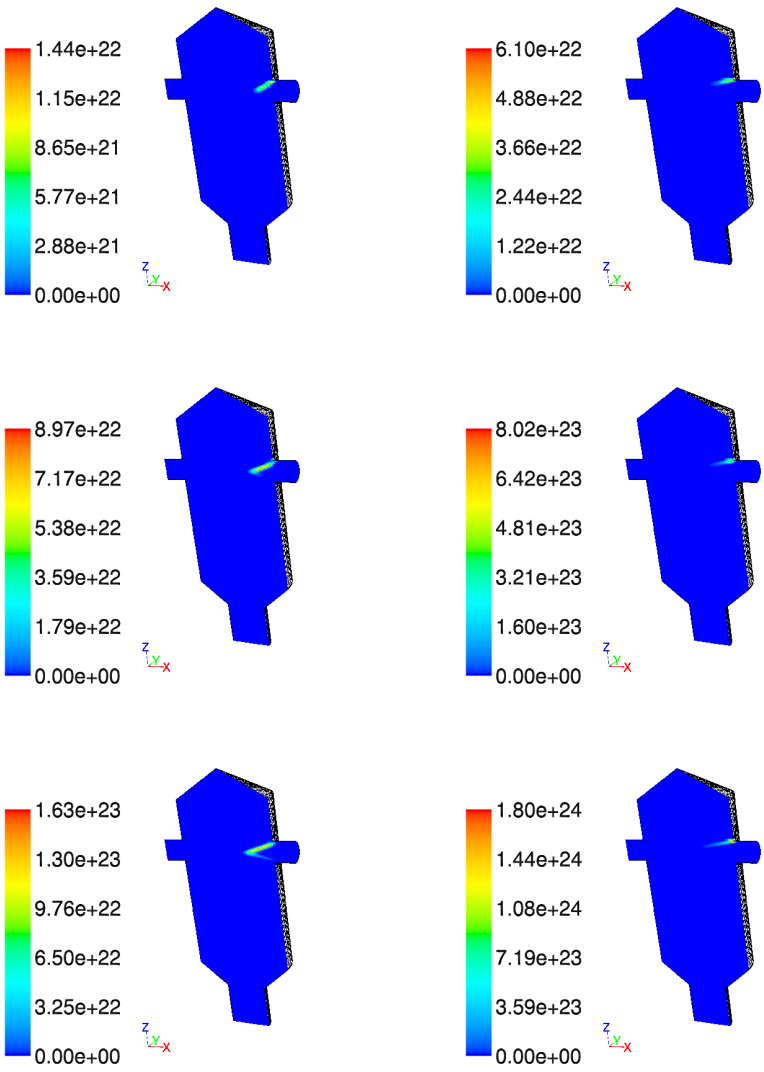

Figure 4.12: Contour plots of the nucleation rate (in $m^{-3}s^{-1}$) predicted by the ANT (left) and the CNT (right) for $R = 2$ and for different inlet water flow rates (from top to bottom: 40 mL min^{-1}, 80 mL min^{-1} and 120 mL min^{-1}).

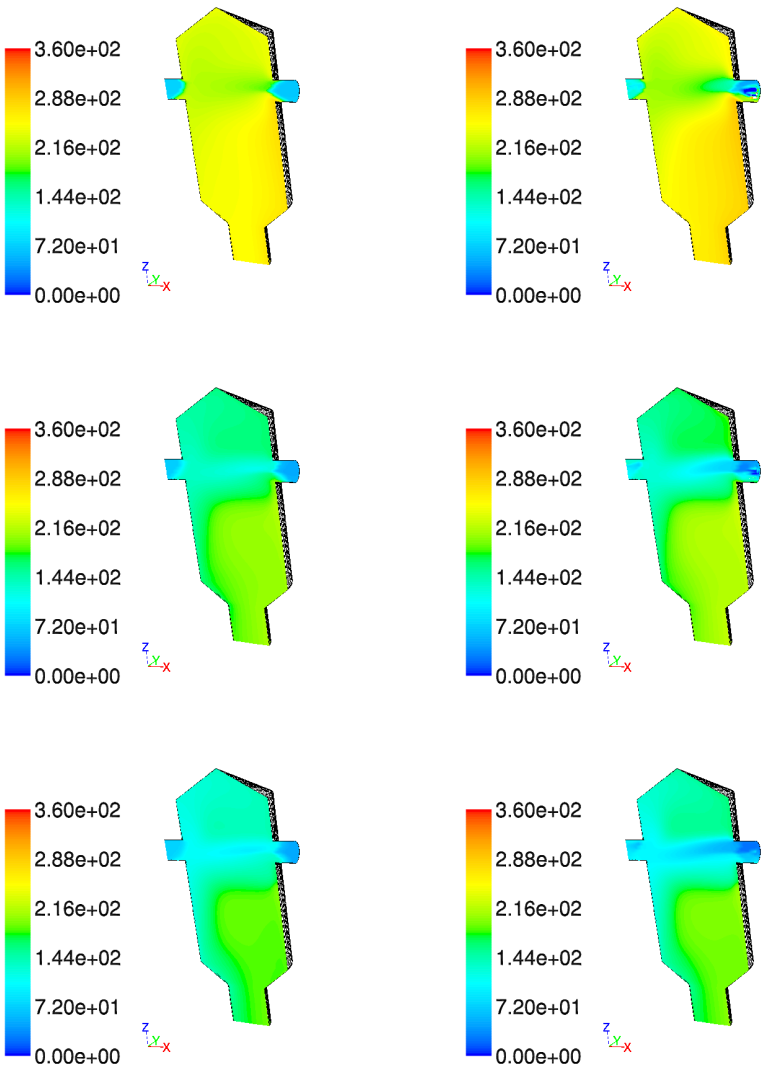

Figure 4.13: Contour plots of the mean particle size (nm) predicted by the ANT (left) and the CNT (right) for $R = 2$ and for different inlet water flow rates (from top to bottom: 40 mL min^{-1}, 80 mL min^{-1} and 120 mL min^{-1}).

of them is visible in Fig. 4.13, where in some regions (as for example at the inlets of the CIJR) large variations on the predicted values of d_{43} are detected.

Most of these issues are instead cured by the ANT that results in smoother and more reasonable contours for the mean particle size, caused in turn by more reasonable contours for the nucleation rate, and resulting in more stable simulations. It is important to remind once more that no fitting is done with the ANT, since the parameters appearing in it are all estimated from the theory and from MD simulations.

Similar conclusions can be drawn for different R values. Fig. 4.14 shows a detail of the contour plot of the nucleation rate for $R = 1$ and $R = 2$ and for the CNT and ANT. The region of the reactor in which nucleation occurs is larger with the ANT model, but this difference is more evident for the results of $R = 1$. However, it is worth mentioning that when the CNT is employed a different fitted value of $\tilde{v} = 2.20\ 10^{-28}\ \mathrm{m}^3$ has to be used, whereas the ANT can be used with the very same parameters reported in Table 4.5 and in Table 4.4. The final comparison with experiments, in terms of the mean particle size at the outlet of the CIJR, is reported for $R = 1$ in Fig. 4.15 and for $R = 2$ in Fig. 4.16. As it is possible to see both the ANT and the CNT result in acceptable agreement with experiments for $R = 1$ and $R = 2$, but with the CNT a different set of parameters are necessary ($\tilde{v} = 2.2\ 10^{-28}\ \mathrm{m}^3$ for $R = 1$ and $\tilde{v} = 2.06\ 10^{-28}\ \mathrm{m}^3$ for $R = 2$) whereas with the ANT the same set of parameters was used. Moreover, the ANT is completely derived from first principles (i.e. theory and MD simulations) whereas with the CNT some tedious and time consuming fitting is necessary.

4.7 Conclusions

In this part of the work the precipitation of polymer nanoparticles of PCL, in a solvent displacement process with acetone and water as solvent and anti-solvent carried out in a CIJM, is simulated by using a PBM implemented in the CFD code Ansys/Fluent. As highlighted by our previous work the nucleation rate plays a crucial role in determining the final predictions and the CNT seems to be inadequate to describe the formation of particles constituted by large polymer molecules.

In this work a more adequate nucleation rate (ANT) was derived, starting from the same fundamental principles of the CNT, but without adopting some

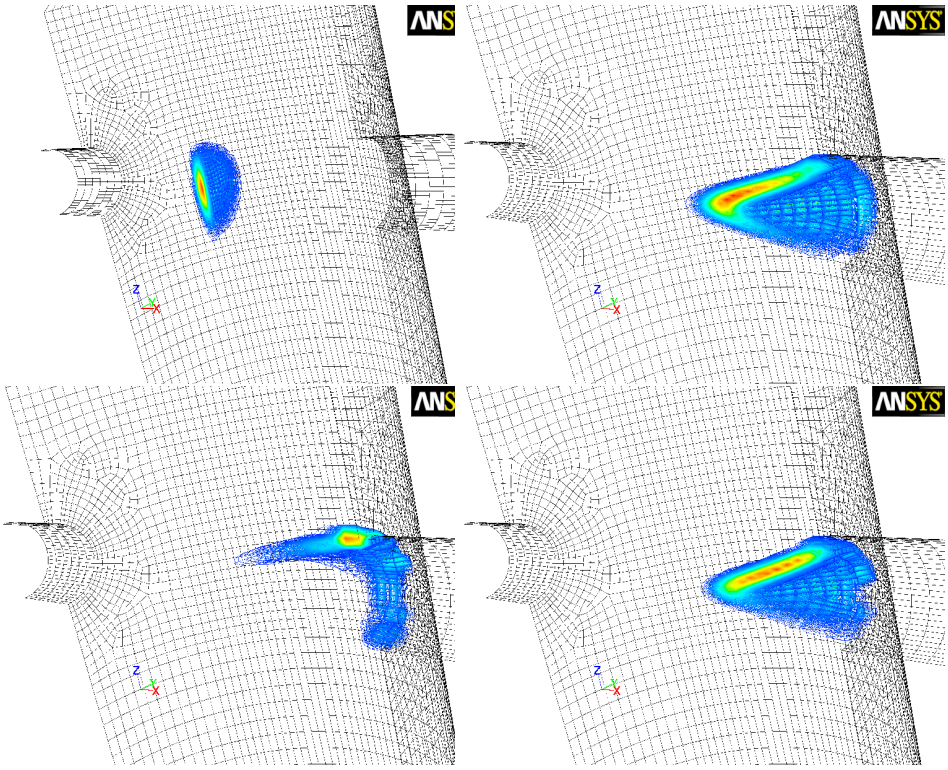

Figure 4.14: Contour plots of the nucleation rate J (in $m^{-3}s^{-1}$) predicted by the CNT (left) and the ANT (right) for $R = 1$ (top) and $R = 2$ (bottom) and for a water flow rate of 120 mL min^{-1}). The maximum value showed for J (red contour) is: $6.2 \cdot 10^{23}$ ($R = 2$, CNT), $2.4 \cdot 10^{22}$ ($R = 2$, ANT), $1.8 \cdot 10^{24}$ ($R = 2$, CNT), $1.6 \cdot 10^{23}$ ($R = 2$, ANT)

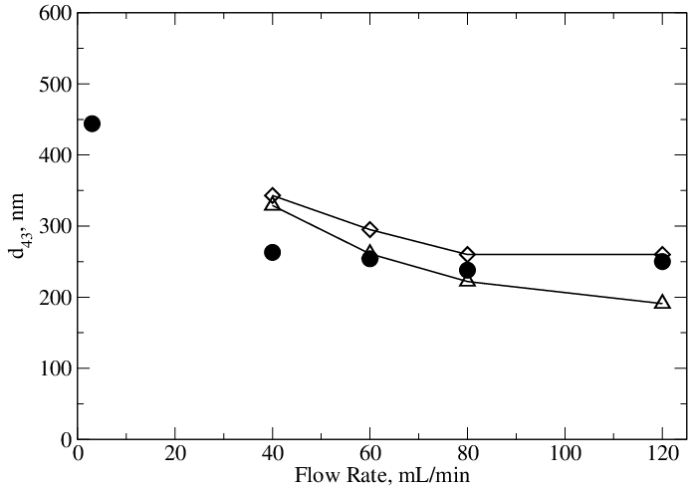

Figure 4.15: Comparison of the mean nanoparticle size at the CIJR outlet for $R = 1$ experimentally measured (•) with the predictions of the CNT (with $\tilde{\nu} = 2.2\ 10^{-28}\ \mathrm{m}^3$ (⋄)) and with the ANT (△)

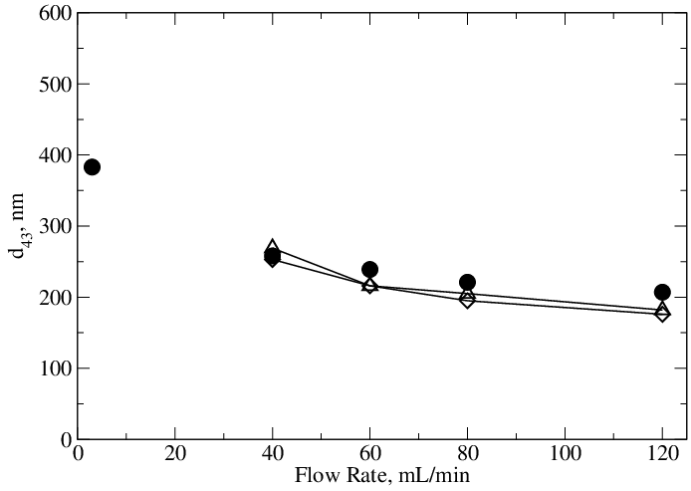

Figure 4.16: Comparison of the mean nanoparticle size at the CIJR outlet for $R = 2$ experimentally measured (•) with the predictions of the CNT (with $\tilde{\nu} = 2.06\ 10^{-28}\ \mathrm{m}^3$ (⋄)) and with the ANT (△)

important approximations. The many parameters appearing in this nucleation rate have been estimated with MD simulations carried out in simulation boxes containing PCL, acetone and water molecules with different compositions and resulting in different environments ranging from pure water to pure acetone. These different simulation boxes represent the different local compositions that fluid elements of water and acetone would see when mixing together in the CIJM.

The predictions of ANT (with unknown parameters estimated with MD) have been compared with predictions obtained with the CNT (with unknown parameters estimated through fitting with experiments performed in our previous work [Di Pasquale et al., 2012]) and with experiments. The comparison shows that although both models predict very similar values for the final mean particle size, predictions with the ANT, reported in Eq. (4.20), are more realistic. In fact, in order to match experiments the nucleation rate derived from the CNT reported in Eq. (4.35)), needed to assume unreasonably large values, making the CFD code very unstable. Moreover, use of Eq. (4.20) with unknown parameters estimated a-priori with MD simulations, represents a fully predictive approach preferable to the use of Eq. (4.35) with unknown parameters estimated from a long and time consuming fitting procedure.

Next steps of this work include MD simulations performed with molecules larger than PCL-10 and PCL-30 in order to verify the extrapolation necessary to extract information concerning PCL molecules corresponding to a molecular weight of 14000 $\mathrm{kg\,mol^{-1}}$, MD simulations performed with larger simulation boxes to verify the absence of constraint effects due to the size of the simulation box and CFD simulations performed under different operating conditions (i.e., water flow rate, water-to-acetone flow rate ratio, initial polymer concentration) in order to complete the validation of the model via comparison with experiments.

Chapter 5

Hybrid Atomistic/CG model[1]

To further investigate the problem of polymer particles nucleation it would be very useful to simulate systems including more than simple polymer molecule, requiring therefore some form of coarse-graining. Moreover the presence of the drug molecules (neglected in this work) and their interactions with polymer molecules would require the description of only part of the polymer molecule as coarse-grained, leaving some other parts completely described. This is very useful, especially when copolymers (block, or grafted) are employed [Valente et al., 2012b,c; Lince et al., 2011a,d]. With this ambitious goal in mind we have developed a simple hybrid model for macromolecules where the single molecules are modelled with both atoms and coarse-grained beads. In this initial validation of the method two simpler systems are investigated: polystyrene and polyethylene melts, for which the coarse-grained potentials have been developed using the Iterative Boltzmann Inversion procedure (IBI). Our results show that it is possible to couple the two potentials without modifying them and that the mixed model preserves the local and the global structure of the melts in each of the cases presented. The degree of resolution present in each single molecule seems to not affect the robustness of the model. The mixed potential does not show any bias and no cluster of particles of different resolution has been observed after simulation of the order of 100 ns.

The application of this method to systems including solvent and anti-solvent

[1] This chapter has been published in a shorted version in the *Journal of Chemical Physics*

molecules, as well as drug molecules, will instead be investigated in a future work.

5.1 Overview

The ability to combine a detailed description of the chemistry of a molecular model with an efficient exploration of the conformation space is a key point in simulating realistic systems. This is particularly true in the case of soft materials where phenomena taking place at different length scales (ranging from few picoseconds to microseconds and beyond) are responsible for their global properties. Due to the current computational power, all-atom (AA) simulations, which naturally describe the chemical details, are often constrained in time scale up to 100 ns and limited in the number of atoms. In order to overcome this problem coarse-grained (CG) methods have been developed in the past 10 years to expand at the same time the size and the time scale of the simulations [Müller-Plathe, 2002; Tschop et al., 1998; Gubbins and Moore, 2010]. These reduce the degrees of freedom (DOF) of the model collecting several atoms in one super-atom or bead. Although these models have proved to be very useful in predicting different type of material properties, in some cases the lack of atomistic details is such a limitation that the AA simulations are preferred, even though their use reduces the dimension of the system and the type of phenomena that can be investigated. Typically, the atomistic resolution of the model is vital when hydrogen bonds or specific chemical interactions act among the atoms [Bock et al., 2007; Karimi-Varzaneh et al., 2008]. This is for example the case when polymers are in contact with a metal surface or another polymer where the detailed description of the polymer/metal or polymer/polymer interface is necessary to predict the level of adhesion [Delle Site et al., 2004]. The atomistic resolution is equally important in investigating the encapsulation/release mechanism of a drug through synthetic or bio membranes [Discher et al., 2007], the biocompatibility of synthetic polymers or the gene delivery mechanism where protein segment or DNA strands are put in contact with polymers or dendrimers [Smith, 2008]. In these latter cases the interplay between the organic molecule and the soft material is driven by specific chemical interactions that should not be coarse-grained away. The solution to tackle simulations where the detailed description of the model is as important as the exploration of large time scale is in devising a multiscale ap-

proach where atoms and CG beads are integrated in the same molecular model. Initial attempts in this direction have been made simulating models with fixed dual resolution, partitioning them in two regions among which there is no mass transfer. Abrams et al. [2003] devised the first multiscale model of such a kind to study the adsorption of bisphenol-A-polycarbonate liquids in contact with a nickel surface Their approach combines within the same model the short range interactions responsible for the adsorption of the chain ends onto the surface (extracted from Car-Parrinello molecular dynamics simulations) with the long range interactions responsible for the chain configurations (described with a coarse-grained potential). This dual-resolved model where only the last monomer of each chain was modelled atomistically while the rest of the chain was represented by coarser beads enables to model both the orientation relative to the surface of the absorbed terminal groups and the effect that such adsorption has on the global structure of the liquid. Neri et al. [2005] developed also a multiresolved model in order to study the conformational space of two globular proteins in their native state. In this model the key residues of the active site of the protein were treated with atomic detail while the rest of the protein was described at coarser level using a generic bead and spring model. Therefore in this pioneering attempt the coarser part of the model added to describe the long protein molecule, does not retain any chemical details and the protein is treated as a generic soft polymeric chain. Other hybrid models with two non-interchanging regions of different resolutions have been proposed: Shi et al. [2006] investigated the structure of an atomistic resolved peptide channel embedded in a CG model lipid bilayer surrounded by CG water molecules, while Michel et al. [2008] devised a AA-CG model that is able to reproduce the partition coefficients of small molecules (described at atomic level) in coarse-grained solvent (water or octane). Recently, a comprehensive test of the applicability of these mixed models in simulating liquid and complex biological environment has been carried out [Rzepiela et al., 2011]. The atomistic force field has been mixed with four different CG potentials and the results showed that these models work well reproducing the global structure and the thermodynamic properties reasonably well. Recently a model similar to what proposed by [Neri et al., 2005] has been also used to simulate a DNA strand in implicit solvent [Machado et al., 2011], while the equation of motion for the coupled atomistic/coarse-grained system has been formally derived using the Zwanzig's projector method [Español, 2009]. More sophisticated

AA-CG models have been also proposed [Praprotik et al., 2008; Nielsen et al., 2010a]. Their most important feature is that they all allow an on-the-fly change in the model resolution depending on the spatial position of the molecules. Praprotnik et al. [2005] proposed a simulation technique, Adaptive Resolution Scheme (AdResS), for liquids in which a water molecule spatially adapts its molecular resolution as a function of its position in the simulation box. Recently Nielsen et al. [2010b] proposed a new method, which couples a rotational dynamics of the atomistic fragments represented by each CG bead with the CG dynamics, to simulate polymers in dilute solution. This method also adopts a new paradigm to overcome the problem of the fluctuations of the total energy of the model during the simulation caused by the change in the total number of DOFs [Nielsen et al., 2011; Praprotnik et al., 2011]. The development of hybrid models for dense polymer melts where the single macromolecules can be treated with different level of details depending on their positions would represent an enormous advantage in computational time in any case where interfacial properties are sought. Such new intramolecular hybrid models however pose several new questions related to their thermodynamic properties that might differ from the hybrid models of simple liquids. In this Chapter we present an AA-CG model for polymer melts where the AA and CG force fields are combined. We will use here as test case to validate the approach melts of polyethylene (PE) and atactic-polystyrene (PS). The method is implemented in the code IBIsCO [Karimi-Varzaneh et al., 2011] and has been developed to be generic and applicable to any type of macromolecular systems. In this initial attempt the resolution of the single molecule does not change during the simulation and the aim of this work is primarily to verify whether the bonded and non-bonded part of the two force fields can be mixed to form a homogeneous single phase system.

5.2 Theoretical background

5.2.1 Development of the coarse-grained potential for the polymer melts

For the construction of the hybrid model, the coarse-grained part of the macromolecule is modelled using a force field developed using the Iterative Boltzmann Inversion procedure. Here we briefly explain the basic concept of the technique but extensive discussions on this procedure and others used to develop CG mod-

els can be found in several references [Müller-Plathe, 2002; Karimi-Varzaneh and Müller-Plathe, 2012; Karimi-Varzaneh et al., 2012; Voth, 2008].

5.2.1.1 Radial Distribution Function

Let us consider a liquid with density ρ at temperature T and imagine to observe the rest of the system from one of the atom while it moves in the system and count the number of the other atoms surrounding the chosen atom at different distances from it. Since we are considering a fluid, the distribution of the atoms around will be on the average simmetrical around a center (i.e., around the chosen atom). However, the mean number of atoms found in an infinitesimal volume $\mathrm{d}V$ at distance r from the central molecule, in general is not the product $\rho \mathrm{d}V$ because the presence of the central molecule will perturb its surroundings. As example, if we consider the atoms to be hard-sphere with radius a we will not find any atoms at distance[2] $r < a$. This correlation is lost at high distance as the potential goes to zero, and at these distances the mean number of molecules $\rho \mathrm{d}V$ in the volume $\mathrm{d}V$ is approached.

It is possible to specify the mean number of molecules observed in a volume $\mathrm{d}V$ as $\rho g(r)\mathrm{d}V$ where $g(r)$ is the so-called Radial Distribution Function (RDF) and it can be considered a measure of the amount of deviation of the density from its mean values in the surroundings of an atom. Therefore, the RDF satisfy these proprieties

$$g(r) \to 0 \;\; as \; r \to 0$$
$$g(r) \to 1 \;\; as \; r \to +\infty$$

RDF is a very important quantity in MD simulation because it can be obtained by X-ray diffraction experiments, hence it become one of the common way to test the reliability of the simulation[3]. In McQuarrie [2000] is shown how the X-ray diffraction is related to RDF and is shown that the scattering $P(\theta)$ through an angle θ is proportional to the function $h(r) = g(r) - 1$ through the Fourier transform

$$P(\theta) \propto \int (g(r) - 1) e^{i\mathbf{s}\cdot\mathbf{r}} \mathrm{d}\mathbf{r}$$

[2] Actually in most of the potentials used in MD atoms can be considered hard sphere at distance shorter than their radius.

[3] Or rather, the reliability of the force field employed

The RDF can be obtained by considering a system composed by N molecules, at temperature T and volume V. Let us start with the definition of probability to find the system in a certain configuration $\mathrm{d}\mathbf{q}\mathrm{d}\mathbf{p}$ (see Table 2.1):

$$\frac{e^{-\frac{\mathcal{H}}{k_B T}}}{\int e^{-\frac{\mathcal{H}}{k_B T}} \mathrm{d}\mathbf{q}\mathrm{d}\mathbf{p}}$$

If this equation is integrated over the momenta one obtains:

$$P^{(N)}(\mathbf{r})\mathrm{d}\boldsymbol{r} = \frac{e^{-\frac{\mathcal{U}}{k_B T}} \mathrm{d}\mathbf{r}}{Z_N}$$

where

$$Z_N = \int e^{-\frac{\mathcal{H}}{k_B T}} \mathrm{d}\mathbf{q}$$

is called the configurational integral. $P^{(N)}(\mathbf{q})$ is the probability of finding the atom (labelled with) 1 in $\mathrm{d}r_1$, the atom (labelled with) 2 is in $\mathrm{d}r_2$ and so on until the atom N in $\mathrm{d}r_N$. Thus, the probability to find the atom 1 in $\mathrm{d}r_1$, the atom 2 in $\mathrm{d}r_2$ and so on until the atom n in $\mathrm{d}r_n$ irrespective of the configuration of the remaining $N - n$ atoms is:

$$P^{(n)}(\boldsymbol{r})\mathrm{d}r_1\mathrm{d}r_2 \ldots \mathrm{d}r_n = \mathrm{d}r_1\mathrm{d}r_2 \ldots \mathrm{d}r_n \frac{\int e^{-\frac{\mathcal{U}}{k_B T}} \mathrm{d}r_{n+1} \ldots \mathrm{d}r_N}{Z_N} \tag{5.1}$$

If we want to obtain the probability that any atom is in $\mathrm{d}r_1$, any atoms[4] is in $\mathrm{d}r_2$ and so on until $\mathrm{d}r_n$, irrespective of the position of the other $N - n$ atoms you just need to multiply Eq. (5.1) by $N!/(N-n)!$ which is the number of way to arrange n objects taken form a set of N objects (n-permutation of N). Hence we obtain:

$$\rho^{(n)}(\boldsymbol{r}_1, \boldsymbol{r}_2, \ldots, \boldsymbol{r}_n) = \frac{N!}{(N-n)!} P^{(n)}(\mathbf{q}) \tag{5.2}$$

[4] Except the atom already found in $\mathrm{d}r_1$.

Now, it is possible to define a correlation function $g^{(n)}(\boldsymbol{r}_1, \boldsymbol{r}_2, \ldots, \boldsymbol{r}_n)$ as

$$\rho^{(n)}(\boldsymbol{r}_1, \boldsymbol{r}_2, \ldots, \boldsymbol{r}_n) = \rho^n g^{(n)}(\boldsymbol{r}_1, \boldsymbol{r}_2, \ldots, \boldsymbol{r}_n) \tag{5.3}$$

If the molecules were independent one from another, the correlation function $g^{(n)}(\boldsymbol{r}_1, \boldsymbol{r}_2, \ldots, \boldsymbol{r}_n)$ would be equal to unity, and hence $\rho^{(n)} = \rho^n$. When n is small compared to N it is possible to write [Hill, 1986]:

$$\frac{N!}{\rho^n (N-n)!} = V^n \left[1 + O\left(\frac{1}{N}\right)\right]$$

obtaining:

$$g^{(n)}(\boldsymbol{r}_1, \boldsymbol{r}_2, \ldots, \boldsymbol{r}_n) = V^n \frac{\int e^{-\frac{\mathcal{U}}{k_B T}} \mathrm{d}q_{n+1} \ldots \mathrm{d}q_N}{Z_N}. \tag{5.4}$$

The RDF is the correlation function with $n = 2$. In a liquid with spherically symmetric molecule this correlation function depends upon only the relative distances between molecule one and two [McQuarrie, 2000] ($\boldsymbol{r}_{12} = \boldsymbol{r}_2 - \boldsymbol{r}_1$). Therefore $\rho g(r) 4\pi r^2 \mathrm{d}r$ is the number of atoms between $\boldsymbol{r}$ and $\boldsymbol{r} + \mathrm{d}\boldsymbol{r}$.

5.2.1.2 Iterative Boltzmann Inversion

From the correlation function $g^{(n)}(\boldsymbol{r}_1, \boldsymbol{r}_2, \ldots, \boldsymbol{r}_n)$ obtained in the previous section it is possible to define a quantity $w^{(n)}(\boldsymbol{r}_1, \ldots, \boldsymbol{r}_n)$ [McQuarrie, 2000; Hill, 1986] as

$$g^{(n)}(\boldsymbol{r}_1, \boldsymbol{r}_2, \ldots, \boldsymbol{r}_n) \equiv e^{-\frac{w^{(n)}(\boldsymbol{r}_1, \ldots, \boldsymbol{r}_n)}{k_B T}} \tag{5.5}$$

The physical meaning of $w^{(n)}$ can be obtained as follows. Let us substitute the previous equation in Eq. (5.4):

$$e^{-\frac{w^{(n)}(\boldsymbol{r}_1, \ldots, \boldsymbol{r}_n)}{k_B T}} = V^n \frac{\int e^{-\frac{\mathcal{U}}{k_B T}} \mathrm{d}r_{n+1} \ldots \mathrm{d}r_N}{Z_N}. \tag{5.6}$$

and by taking the logarithm of both side and then by differentiating with respect

to the position of one of the n molecules $1, \ldots, n$ (say i) we obtain

$$-\nabla_i w^{(n)} = \frac{\int e^{-\frac{\mathcal{U}}{k_B T}} (-\nabla_i \mathcal{U}) \mathrm{d}r_{n+1} \ldots \mathrm{d}r_N}{\int e^{-\frac{\mathcal{U}}{k_B T}} \mathrm{d}r_{n+1} \ldots \mathrm{d}r_N} \quad \text{with} \quad i = 1, 2, \ldots, n \tag{5.7}$$

$-\nabla_i \mathcal{U}$ is the force acting on atom i for any fixed configuration $\boldsymbol{r}_1, \ldots, \boldsymbol{r}_{i-1}, \boldsymbol{r}_{i+1}, \ldots, \boldsymbol{r}_N$, thus the right-hand side of the previous equation is the mean value of the force $f_i^{(n)}$ acting on particle i averaged over the different configurations of the $N - n$ atoms not in the fixed set:

$$f_i^{(n)} = -\nabla_i w^{(n)}. \tag{5.8}$$

Therefore, $w^{(n)}$ is the potential which gives the mean force acting on particle i and is called Potential of Mean Force (PMF). $w^{(2)}$ is the potential between two particles keeping the other $N - 2$ fixed. If the density of the system is very low this two particles will not be affected by the other particles and in the limit of $\rho \to 0$ we obtain $w^{(2)}(\boldsymbol{r}) \to \mathcal{U}(\boldsymbol{r})$.

The PMF can be defined for any correlation among independent degrees of freedom of the system (e.g., bonds, bending and dihedral angles) and is the basis of the Boltzmann inversion method used in CG simulation. The IBI procedure develops the bead-bead interactions using these structural properties obtained from detailed atomistic simulations performed on the system of small size. The atomistic system is mapped into bead, that is to say that some atoms are grouped together to form a supramolecular system called bead, which is treated exactly as one atom. Hence, the beads will experience some forces which are derived from a CG force-field. In order to obtain the potential acting between the beads it was proposed by Soper [1996] to invert Eq. (5.5) in which we consider a generic pair correlation function $P(q)$, where q is the generic degree of freedom, obtaining:

$$w(q) = -k_B T \ln P(q). \tag{5.9}$$

The problem with the previous equation is that $w(q)$ is not a potential energy but a free energy, except in the case of zero density (which is not of practical in-

terests). Therefore, in order to obtain the correct potential, it was proposed by Reith et al. [2003] to use an iterative procedure in which the potential is correct at each step. Therefore, distributions of bond distances, angles, torsions (when necessary), and radial distribution functions, are subjected to a Boltzmann inversion (see Eq. (5.9)) to find the corresponding potentials of mean force which, to become the effective, pairwise potential used in the simulation is then iteratively optimized against these structural information. Therefore from the Boltzmann inversion of the pair distributions $P(r)$, a first initial guess, $V_1(q)$, for the CG potential is obtained. This can be written by using Eq. (5.9):

$$V_1(q) = -k_B T \ln P(q) \tag{5.10}$$

where k_B is the Boltzmann constant and T is the temperature.

As said above, $V_1(r)$ does not represent the correct potential energy of the system but needs to be improved, and this can be done by adding to it the correction term $-k_B T \ln [P_1(r)/P(r)]$, where $P_1(r)$ is the distribution obtained from the simulation performed using $V_1(r)$ as potential energy and $P(r)$ is the target (atomistic) distribution. This step can be iterated

$$V_{i+1}(q) = V_i(q) - k_B T \ln [P_1(q)/P(q)] \tag{5.11}$$

thus obtaining an algorithm, as sketched in Fig. 5.1. The IBI potential can be "corrected" against the system pressure so that it can reproduce the correct mass density at atmospheric conditions. To correct the pressure a linear weak perturbation is added to the attractive long range part of the potential [Reith et al., 2003]

$$\Delta V(r) = A\left(1 - \frac{r}{r_{cut}}\right) \tag{5.12}$$

where A is a small constant and its value is positive or negative depending on whether the pressure is above or below the target value. The IBI CG potential used for the a-PS melt in this work is that one already developed by Qian et al. [2008]. For the polyethylene melt the IBI CG potential has instead to be developed and the details about the chosen mapping scheme and CG simulation results are reported below.

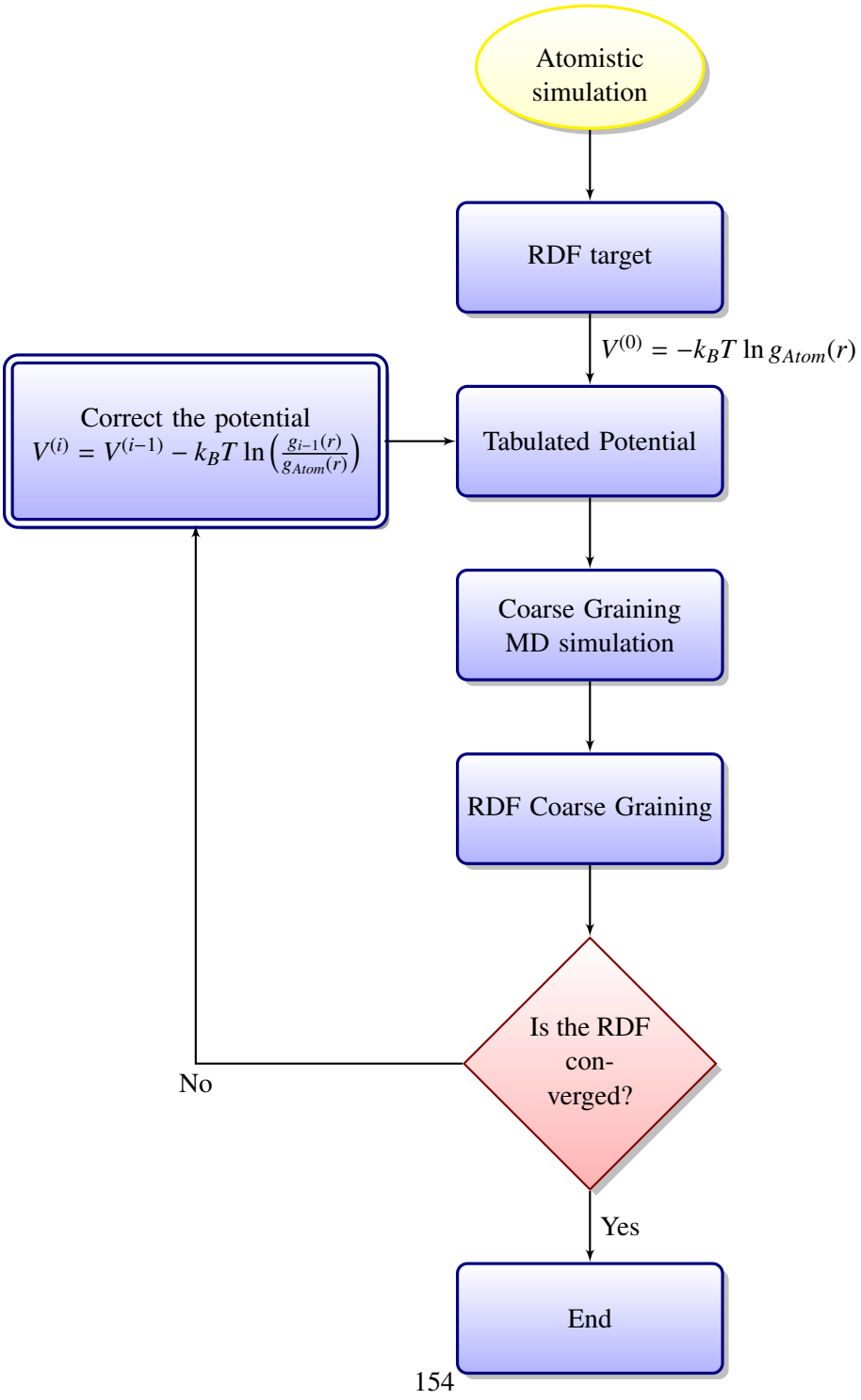

Figure 5.1: Flowchart of the Iterative Boltzmann Inversion

5.2.2 Construction of the hybrid model

Our hybrid model consists of beads and atoms embedded into the same macromolecular chain (see Fig. 5.2). The intermolecular potential that acts among the CG beads is that derived from the Iterative Boltzmann Inversion (IBI) procedure [Müller-Plathe, 2002]. The IBI technique develops the CG force field starting exclusively from structural properties (radial distribution functions and pair distributions of distances and bending angles) obtained from accurate atomistic simulations and CG models obtained in this way are able to predict structural, dynamic and thermodynamic properties of linear polymers, dendrimers and complex liquids [Qian et al., 2009; Chen et al., 2007; Carbone et al., 2007, 2008]. From now on we label the generic part of the chain (atom or bead) as *element*. Its nature is defined only by its index for which we remind to Fig. 5.2.

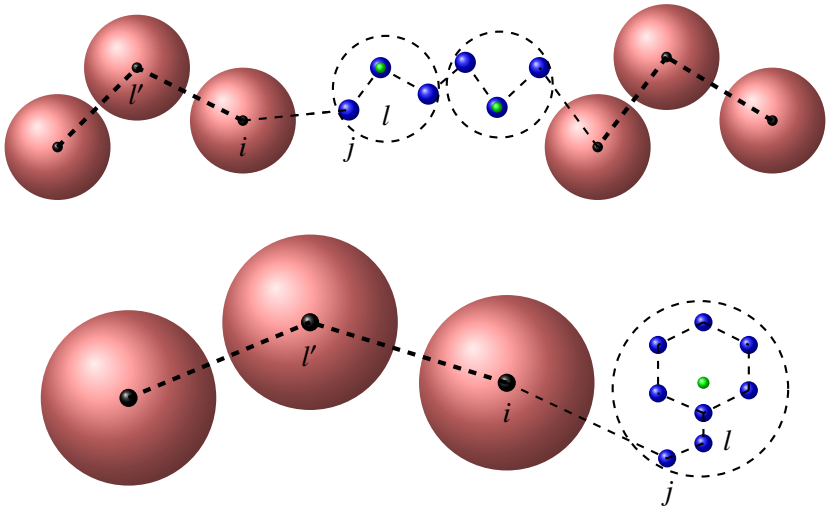

Figure 5.2: Example of possible structure of the hybrid models for polyethylene (top) and polystyrene (bottom) chain: the black filled circles represent the centres of mass of the coarse-grained beads while the green filled circles represent the position of the virtual sites in the atomistic fragment of the polymer chain. In this example the polymer chain is formed by six coarse-grained (represented by the red filled spheres) and two atomistic (represented by their contour showed with dotted line which enclose the atoms) resolved monomers (i.e., $N_m^{CG} = 6$ and $N_m^{AA} = 4$) for the PE and three coarse-grained (represented by the red filled spheres) and one atomistic (represented by their contour showed with dotted line which enclose the atoms) resolved monomers (i.e., $N_m^{CG} = 3$ and $N_m^{AA} = 1$) for the PS. The labels i, j, l, and l' indicate the particles involved in the bonded force field interactions (see Eq. (5.14))

An important advantage of using the IBI procedure in a hydrid AA-CG model is the fact that it should guarantee a balanced mass transfer between the atomic and CG resolved region. The IBI potential in fact corresponds by construction to the same state point of the atomistic model [Praprotnik et al., 2005]. However, recent detailed simulations performed on liquid water [Fritsch et al., 2011; Wang et al., 2009] have showed that the same IBI potential cannot reproduce at the same time both the correct pressure and water isothermal compressibility leading to unphysical fluctuations in the CG region and therefore unbalanced mass transfer across the simulation box. One of the aims of this work is to test if similar fluctuations in the particle density distribution can be seen also in the polymer case and check whether our model induces any transient flow of particles from one region of the box to another.

The potential energy (V^{total}) of our model can be written as

$$V^{total} = V_{AA} + V_{CG} + V^{bonded}_{AA-CG} + V^{nonbonded}_{AA-CG} \tag{5.13}$$

where V_{AA} and V_{CG} represent the potential energies (bonded and nonbonded) of the atomistic and CG part respectively whereas the last two terms (V^{bonded}_{AA-CG} and $V^{nonbonded}_{AA-CG}$) represent the cross terms potentials. V^{bonded}_{AA-CG} ensures that the connectivity of the chain is maintained and comprises the stretching (V^{str}_{AA-CG}) and bending term. V^{bonded}_{AA-CG} takes the following form

$$V^{bonded}_{AA-CG} = V^{str}_{AA-CG} + V^{bend}_{AA-CG} = \frac{1}{2}K_s\left(\boldsymbol{r}_{ij} - \boldsymbol{r}^0_{ij}\right)^2 + \frac{1}{2}K_s\left(\theta - \theta^0\right)^2 \tag{5.14}$$

where $\boldsymbol{r}_{ij} = \boldsymbol{r}_i - \boldsymbol{r}_j$ and $\boldsymbol{r}_i$ and $\boldsymbol{r}_j$ are the position vectors of the element j and i (see Fig. 5.2), $\boldsymbol{r}^0_{ij}$ is the corresponding equilibrium distance set equal to the atomistic simulation reference. Similarly θ is the angle between three elements (which can be represented by two atoms and one bead $\widehat{ijl}$ or two beads and one atom $\widehat{l'ij}$) and θ^0 is the corresponding equilibrium angle as extracted from the atomistic simulation. K_s and K_b are the equilibrium constants that have been set equal to those corresponding to the CG potential previously fitting the tabulated IBI force fields to harmonic functions. Our choice of the values of K_s and K_b is based on atomistic simulation results (being the IBI potentials developed from them) however it might be possible that other values of these constants can be used as long as they are able to reproduce the correct structural features of the

atomic resolved part. The V^{bonded}_{AA-CG} is the only potential through which atoms and beads directly interact. All the other mixed interactions are mediated by the virtual sites (VS). Because the IBI potential is derived from atomistic models, the CG mapping scheme is built on the chain atomic structure and each bead centre of mass corresponds either to a specific atom or to the centre of mass of all the atoms lumped up in it. Thus, it is easy to identify in the atomistic resolved part of the chain the positions of the virtual beads and use them as pinning position to collect any mixed interactions. The $V^{nonbonded}_{AA-CG}$ acts between CG beads in the low resolved region and VS in the atomistic one and is set equal to the non-bonded IBI potential acting among pairs of beads ($V^{nonbonded}_{AA-CG} = V^{nonbonded}_{CG-CG}$). The resulting forces acting on the virtual site i, (F_i), is distributed among the atoms belonging to the virtual bead weighing on their masses:

$$f_{i,j} = \frac{m_{i,j}}{\sum_{i=k}^{N_i^A} m_k, i} F_i, \quad j = 1, \ldots, N_A \tag{5.15}$$

where $f_{i,j}$ is the force acting on the j-th atom of the $i - th$ bead, $m_{i,j}$ is its corresponding mass and N_i^A is the total number of atoms belonging to the i-th virtual bead. Finally due to the fact that typically the distance at which the non-bonded interactions are switched off is larger in the CG models than in the atomistic ones, two non-bonded interactions cut-off distances are implemented separately for the atom-atom and the bead-bead interactions.

5.3 System details

In this Section a description of the systems simulated and details of the atomistic and coarse-grained force fields will be given. Sec. 5.3.1 and 5.3.2 contain the description of the model (i.e., force field employed) on the fully resolved system (i.e., pure atomistic or pure CG).

5.3.1 Polyethylene

The details of the atomistic force field and simulations used as a reference for the development of the CG bead-bead interactions and for the part of the molecule modelled at the atomistic resolution are reported in Carbone et al. [2010] and here only briefly mentioned. The atomistic force field is the united-atom force

field reported by Smit et al. [1995]. The equilibrated simulation box of the melt of polyethylene is constructed using the fine-graining technique described in Carbone et al. [2010]. The procedure quickly relaxes high molecular weight polymer melts introducing the atoms into a melt of "parent" random walk chains. Initially the atomistic fragment whose length is equal to the persistence length of the polymer (for polyethylene 1.6 nm) is gradually inserted in each bead of the random walk chain and then an equilibration protocol involving a series of molecular dynamics simulations follows. The procedure requires the knowledge of the persistence length value for the specific polymeric system under investigation and its approximated bulk density value. For the CG mapping scheme three methylene units are merged into one CG bead whose centre of mass is located on the second methylene group (see Fig. 5.2). The CG force field is developed using the IBI procedure [Reith et al., 2003] using as pair distributions to generate the CG bonded potentials distances and angles connecting the beads (no explicit torsions are included in the potential) and radial distribution functions (RDF) among beads not belonging to the same polymer chain to obtain the non-bonded interactions. The pressure optimization of the CG potential is performed using Eq. (5.12) and the structure-based iterations of Eq. (5.11) are performed concurrently until the target pressure (1atm) is obtained. The CG force field predicts a bulk density of 780 kg/m^3 at atmospheric pressure, in agreement with the atomistic reference and in reasonable agreement with the experimental one [Carbone et al., 2010; Mavrantzas et al., 1999]. The comparison between the pair distributions obtained from the reference atomistic simulation and the CG one are reported in Figs. 5.3 to 5.5.

The perfect agreement between the distributions showed in Figs. 5.3 to 5.5 guarantees that the iterative procedure has converged. Although the CG potential is optimized against pressure, the simulations of the hybrid model are carried out in the canonical ensemble.

5.3.2 Polystyrene

The atomic interactions in the atomistic resolved part of the polymer chain are described using the Transferable Potentials for Phase Equilibria Force Field (TraPPE) united atoms model which reproduces the density of PS over a range of temperatures [Harmandaris et al., 2006]. Several CG models for a-PS melts are

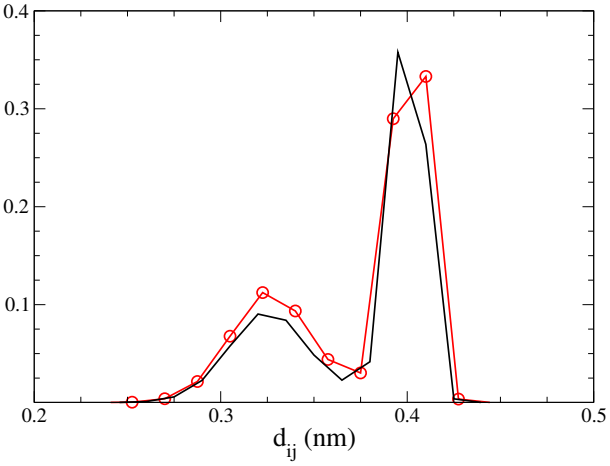

Figure 5.3: Polyethylene melt: comparison between the distributions of the bead-bead bond distance extracted from the atomistic simulation (black solid line) and the coarse-grained one (red empty circles)

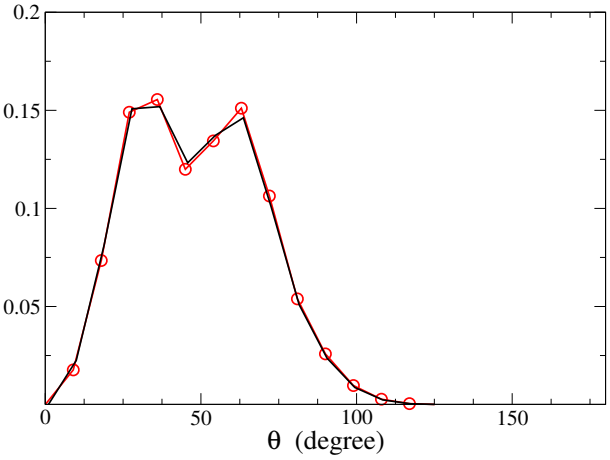

Figure 5.4: Polyethylene melt: comparison between the distributions of the plane angle connecting three beads extracted from the atomistic simulation (black solid line) and the coarse-grained one (red empty circles)

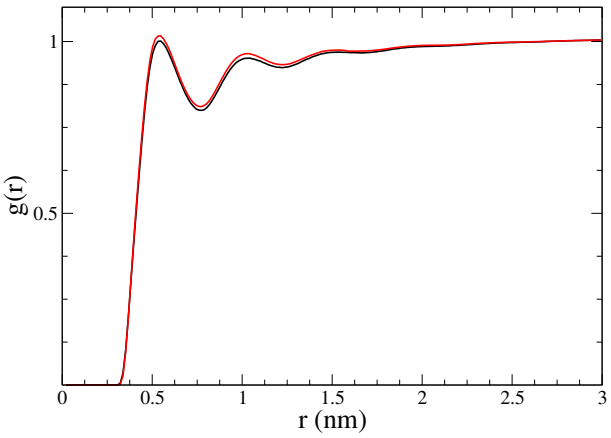

Figure 5.5: Polyethylene melt: comparison between the radial distribution functions between the beads extracted from the atomistic simulation (black solid line) and the coarse-grained one (red line)

present in the literature [Karimi-Varzaneh et al., 2012; Qian et al., 2008; Carbone et al., 2010; Harmandaris et al., 2006; Milano and Müller-Plathe, 2005; Sun and Faller, 2006]. We employ for our hybrid model the CG force field reported by Qian et al. [2008] that has the advantage of using a simple mapping scheme (one bead corresponds to one monomer unit). Atoms in each PS monomer are merged into one CG bead located at the centre of mass of the repeat unit. The CG superatoms are distinguished as R and S according to their absolute configuration of the parent monomers. This CG force field has been developed using the IBI procedure and although developed and optimized at a specific thermodynamic state (temperature and ambient pressure) is transferable for a range of temperature of 100 K ca.

5.4 Simulation details

All the simulations are carried out using a modified version of the IBIsCO code [Karimi-Varzaneh et al., 2011] able to handle all the features necessary to simulate the hybrid model. A summary of the simulations performed is reported in Table 5.1.

5.4.1 Polyethyelene

The system, composed by 20 PE chains of 160 monomers each, is simulated in the canonical ensemble at the same temperature at which the CG force field has been developed (450 K). The density of the system is set equal to the experimental one (780 kg/m^3). This density value is also reproduced by the CG force field at atmospheric pressure. The nonbonded interactions are truncated beyond 1.6 nm for the bead-bead and bead-virtual site and beyond 1.0 nm for atom-atom interactions. Neighbours list is updated every 20 time step. A single time step of 1 fs is employed to integrate the equation of motion for any type of interactions. For the harmonic functions used to model the bonded interactions between atoms and virtual sites (see Eq. (5.15)) the following constants are used: K_s = 7800 kJ/(nm^{2}mol), d_0 = 0.3 nm, K_b = 80 kJ/(rad^{2}mol) and θ = 130°. All the simulations have been run in the canonical ensemble (T=450K) using the Berendsen thermostat [Berendsen et al., 1984] with a coupling time of 0.2 ps for the atomistic, the coarse-grained and dual resolved model.

5.4.2 Polystyrene

The system, composed by 15 PS chains of 80 monomers each, is simulated in the canonical ensemble at the same temperature at which the CG force field has been developed (500 K). The density of the system is set equal to the experimental one 940 kg/m^3 [Qian et al., 2008]. The nonbonded interactions are truncated beyond 1.6 nm for the bead-bead and bead-virtual site and beyond 1.0 nm for atom-atom interactions. A timestep of 1 fs is used to integrate the equation of motion. Neighbours list is updated every 20 time steps. In the hybrid model the atom-VS bonding interactions (Eq. (5.13)) are described with harmonic potential functions with K_s = 1200 kJ/(nm^{2}mol), d_0 = 0.4 nm, K_b = 200 kJ/(rad^{2}mol) and θ = 113°. All the simulations have been run in the canonical ensemble (T = 500 K) using the Berendsen thermostat [Berendsen et al., 1984] with a coupling time of 0.2 ps for the atomistic, the coarse-grained and dual resolved model.

5.4.3 Hybrid models

The hybrid models are constructed starting from a well relaxed atomic resolved simulation box, from which the atoms that will be coarse-grained away are selected and substituted with CG beads. This procedure is used in the present work since our aim is to test the performances of the hybrid models, however a pre-existing atomistic structure it not a pre-requisite for using the hybrid model. All the chains are modelled with the same amount of coarse-grained (N_m^{CG}) and atomistic (N_m^{AA}) monomers, and can be thought as a copolymer arranged in a $CG - AA - CG$ tri-block structure. During the simulation the resolution of the monomer is not allowed to change and the chains can move freely within the simulation box. Since the reduction of the number of degrees of freedom within the polymer chain could impact on the model performances, for both polyethylene and polystyrene three different hybrid models each characterized by a different N_m^{CG}/N_mAA ratio ($N_m^{CG}/N_mAA \approx 0.5$ for PE-1 and PS-1, $N_m^{CG}/N_mAA \approx 1$, for PE-2 and PS-2 and $N_m^{CG}/N_mAA \approx 3$ for PE-3 and PS-3) are simulated. The initial AA configurations used to build the hybrid model and to start the simulations are different for all the systems and, is some cases (see for example PE-1 and PE-2) chosen also slightly far from the equilibrium one in order to be sure that the hybrid model has the time to relax and reaches its equilibrium configuration. The length of the simulations and the number of atomistic and coarse-grained resolved monomer per chain are reported in Table 5.1. The simulations are performed until the single chain radius of gyration and end-to-end distance values reach a plateau. The energy profiles obtained from the simulations performed using the hybrid models do not in fact show any drift and they mainly oscillate around an equilibrium value (see Figs. 5.6 and 5.7).

5.5 Results

5.5.1 Single chain properties

In order to test the robustness of the hybrid models we compare their structural properties with the corresponding ones calculated on the mono-resolved, both fully atomistic and CG, models. Figs. 5.8 and 5.9 report the values obtained for the radius of gyration (Rg) and end-to-end distance (Ree) calculated for the different hybrid models for both polyethylene and polystyrene. In the figures, the

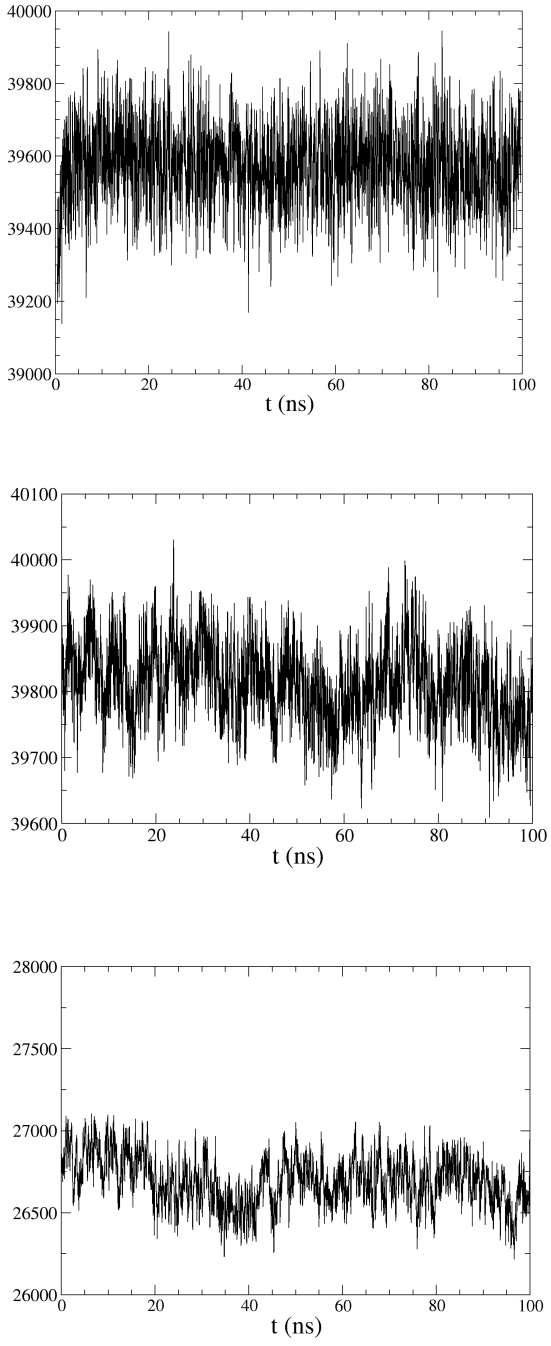

Figure 5.6: Energy profile (in kJ/mol) of the hybrid model PE-1 during the 100 ns of simulation. From the top: stretching energy, bending energy, non-bonded energy

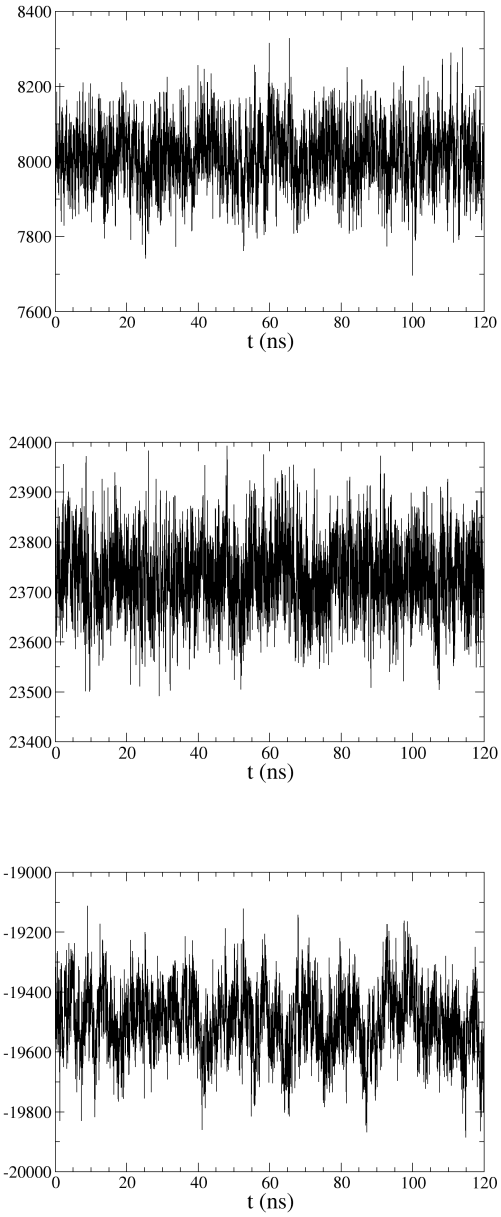

Figure 5.7: Energy profile (in kJ/mol) of the hybrid model PS-1 during the 120 ns of simulation. From the top: stretching energy, bending energy, non-bonded energy.

Model Name	N_m^{AA}	N_m^{CG}	Number of chain in the Box	Length of simulation [ns]
PE-1	60	100	20	100
PE-2	80	80	20	100
PE-3	110	50	20	80
PS-1	20	60	15	120
PS-2	40	40	15	120
PS-3	60	20	15	120

Table 5.1: List of systems simulated in this work. In the table: N_mAA and N_mCG represent respectively the number of atomic and coarse-grained resolved monomers per chain

mean values obtained for Rg and Ree from the CG and AA simulations are also reported. The corresponding averaged value of Rg and Ree are reported in Table 5.2 along with their errors. From the table it can initially be noticed that in the case of polystyrene the values obtained from the pure AA and CG model are very similar with each other and agree with previous data [Carbone et al., 2010; Harmandaris et al., 2006]. On the contrary, for polyethylene the AA and CG models predict a slightly different Rg and Ree values and, in particular, the CG model predicts a Rg around 10% larger than the atomistic one (it should be also noticed however that the errors associated with the CG results are also quite high due to the softness of the inter-bead potential). Both the Rg values obtained for the AA and CG model agree well with previous (atomistic) simulations results within their errors [Carbone et al., 2010; Smit et al., 1995; Mavrantzas and Theodorou, 1998]. This small discrepancy in the Rg and Ree values of the two monoresolved models makes the comparison with the hybrid model results more interesting. Indeed the three polyethylene hybrid models show a trend in their values of Rg and Ree that follows the percentage of atomistic details they retain: the PE-3 model in which 68% of the monomers in a single chain are atomic resolved, is characterized by a Rg more similar to that characteristic of the AA model. On the contrary when the number of CG resolved beads along the chain is increased (PE-2 and PE-3) the chain shows Rg and Ree more similar to that of the pure CG model. The polystyrene hybrid models show instead all very similar Rg and Ree

PE					
	pure Atomistic	Pure CG	PE-1	PE-2	PE-3
Rg [Å]	38.6 ± 0.5	42.4 ± 2.2	41.2 ± 1.1	43.0 ± 1.2	38.4 ± 1.0
Ree [Å]	90.1 ± 2.3	105 ± 8.9	107.3 ± 2.8	107.0 ± 2.8	91.8 ± 2.4
PS					
	pure Atomistic	Pure CG	PE-1	PE-2	PE-3
Rg [Å]	23.5 ± 0.5	23.5 ± 1.5	21.2 ± 0.7	21.1 ± 0.7	22.0 ± 0.8
Ree [Å]	60.0 ± 3.0	55.8 ± 6.2	52.6 ± 1.9	53.8 ± 1.9	50.7 ± 1.8

Table 5.2: Radius of gyration (Rg) and end-to-end distance (Ree) of the various systems simulated. The averaged values have been calculated over the last part of the trajectory.

and seem to present a slightly more collapsed conformation compared with the monoresolved models.

A detailed picture of the organization of the atoms within the chain fragment modelled atomistically can be gained from the intra-chain radial distribution function (RDF). Fig. 5.10 shows the comparison between the intra-RDFs calculated between all the carbon atoms of the central atomistic resolved block for the models PE-1 and PS-1 and the corresponding ones calculated from the pure AA simulations. In the figure, taking into account that each hybrid model contains a different number of atoms depending on its level of resolution, the distributions have been renormalized by a factor $f = N_{At}/N_{hyb}$ where N_{At} is the number of atoms of the hybrid model and N_{tot} is the total number of atoms in the system. Although the PE-1 and PS-1 models predict Rg values respectively $\approx$ 10% larger and $\approx$ 6% smaller than those obtained from the AA model, the RDFs match quite well the target (AA) ones. Perfect agreement is also obtained when the same RDFs are calculated for the hybrid models that retain more atomistic details (PE-2 and 3 and PS-2 and 3) (not showed). This good match between the RDFs indicates that the atomistic and CG force field can be merged seamless and that the atomistic structure of the hybrid model is not subjected to any strain due to the presence of the CG beads attached to it.

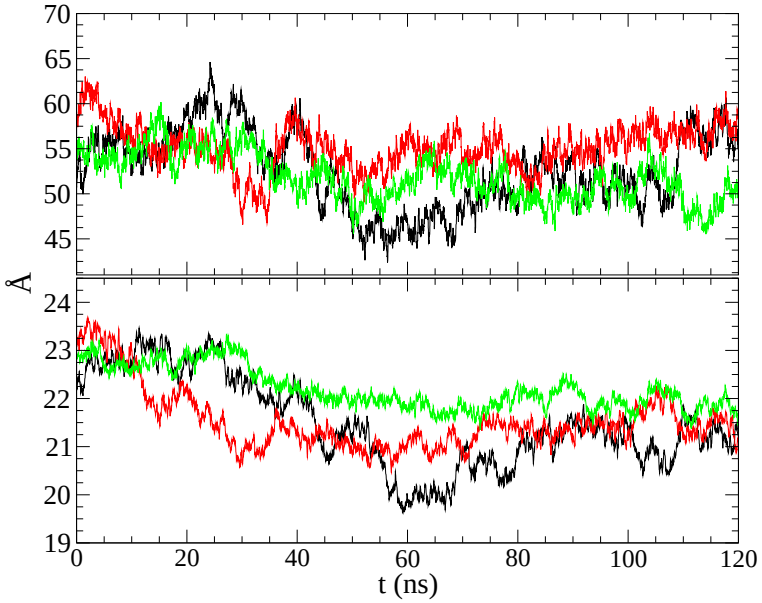

Figure 5.8: End-to-end distance (Ree) (top) and radius of gyration (Rg) (bottom) for the polystyrene hybrid models PS-1 (black), PS-2 (red) and PS-3 (green).

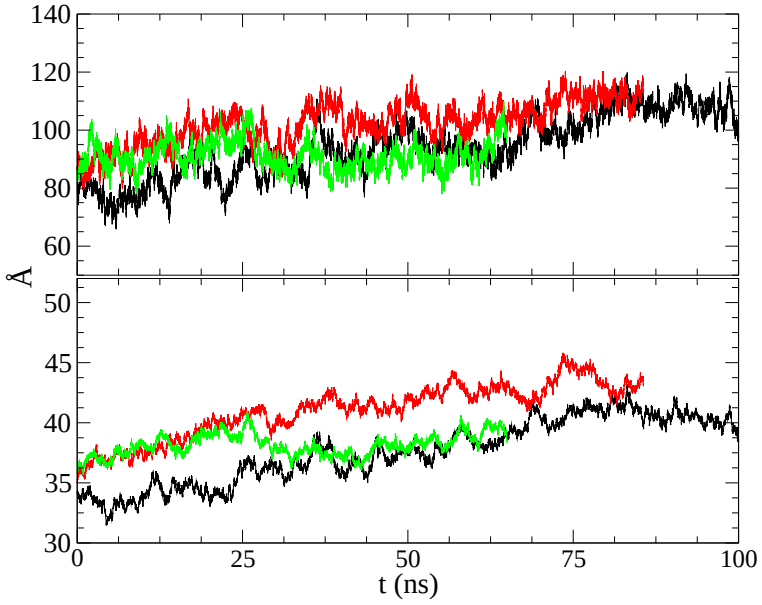

Figure 5.9: End-to-end distance (Ree) (top) and radius of gyration (Rg) (bottom) for the polystyrene hybrid models PE-1 (black), PE-2 (red) and PE-3 (green).

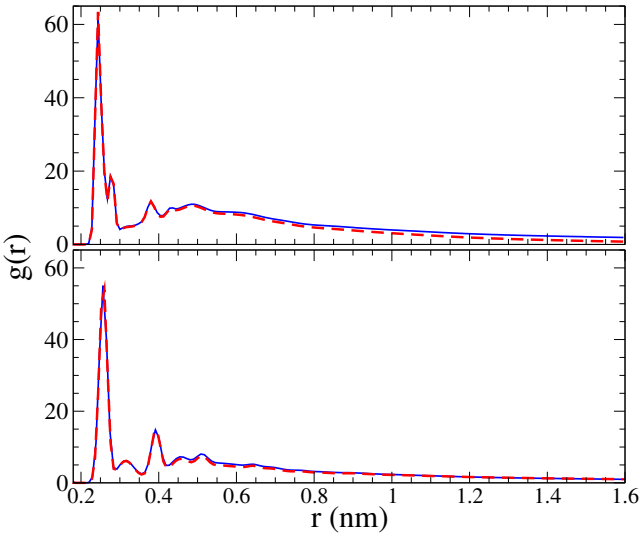

Figure 5.10: Comparison between intra radial distribution function (RDF) g(r), obtained for the pure atomistic and the hybrid model. The intra-RDF of the hybrid simulation is calculated by considering only the atomistic part in each chain. From top to bottom: Polystyrene (PS-1 only), Poly-Ethylene (PE-1 only). The blue solid line indicates the pure atomistic model. The red dashed line indicates the hybrid model

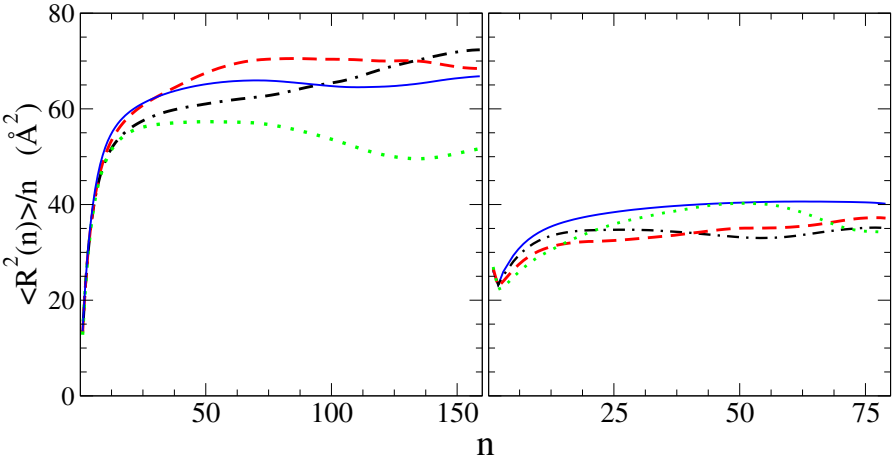

Figure 5.11: Mean squared internal distance calculated for the pure coarse-grained model (solid blue line), PE-1 and PS-1 model (black, dash-dotted line), PE-2 and PS-2 (dashed red line) and PE-3 and PS-3 (green dotted line). The left graph to polyethylene, right graph corresponds to polystyrene.

Although the averaged structural single chain properties of the hybrid models agree reasonably well with those corresponding to the monoresolved ones, the fact that the polymer chain is composed by both soft CG beads and atoms might have an effect on the internal flexibility of the chain that might not be uniform along the chain. One way to look at this effect is to calculate the mean square internal distance, MSID, among the beads of the chain. For a well equilibrated homopolymer melt, the value of MSID increases monotonically with the number of bonds along the chain towards a plateau value [Auhl et al., 2003]. Fig. 5.11 reports the MSID as a function of the number of chain beads, calculated for the CG and the three hybrid models for which the calculations are performed on a trajectory formed only by CG beads and VS (the atoms are excluded from the calculations). From the figure it can be initially noticed that the pure CG models are well equilibrated at all intermediate intra-chain distances and that, when the curves are normalized by the averaged bead-bead distance (0.35 nm for both polyethylene and polystyrene), the MSID calculated for both polyethylene and polystyrene (blue solid line in the figures) agree well with previous results obtained on polymer melts of similar molecular weight [Carbone et al., 2010; Harmandaris et al., 2006]. Therefore the MSID calculated for the pure CG models can be used as target curves and compared with the results obtained for the hybrid models. For polyethylene the MSID curves calculated for the hybrid models perfectly match at short distances ($n < 10$) with the target one and then start to slightly deviate. Again the curve corresponding to the model with more atomic resolved monomers (PE-3) is the one that more clearly depart from the target curve in agreement with its low Ree (see Table 5.2). On the contrary in the polystyrene case, the MSID calculated for the hybrid models deviate from the target CG one at any distances. All the curves lie beneath the target CG one in agreement with their low Ree values (see Table 5.2) and show quite different behaviour. Again the model that retains the highest number of atomic resolved monomers (PS-3) is the one that deviates from the target curve the most, while that characterized by the highest number of CG beads follows more closely, at least at short n, the shape of target curve. In the case of polystyrene the evident discrepancy between the chain behaviour at short, intermediate and long distances shown by the hybrid and the monoresolved model, might be ascribed to the intrinsic difference between the coarse-grained part of the chain (described through spherical beads connected with soft bonds) and the atomistic part where bulky pendant groups

(the phenyl rings) make the chain quite stiff. For the polyethylene, on the contrary, the structural difference between the atomic and coarse-grained block is less relevant and consequently the behaviour of the MSID is less affected.

5.5.2 Structural properties of the melt

The global organization of the polymer melts is assessed calculating the inter-chain RDF. Also in this case, as for the calculation of the MSID, due to the dual resolution of the chain that incorporates beads and atoms, a proper comparison with the hybrid model can be only made at the CG resolution level. Thus for the calculation of the RDFs (showed in Fig. 5.12) of the hybrid models, only beads and virtual sites are included. From the figure it can be clearly seen that the hybrid models maintain correctly the global structure of the polymer melts at long as well as at short distances. Also in this case, for both the polyethylene and polystyrene the amount of atomistic details included in the CG model does not evidently affect the result and only a small increase in the height of the first peak of the RDF is visible, as showed in Figs. 5.13 and 5.14. This small difference can be explained considering that a CG bead occupies a larger effective volume than its corresponding atomistic fragment which therefore can pack more tightly.

The good agreement between the inter- and intra-RDFs calculated from the hybrid and mono-resolved models (Figs. 5.10 and 5.12) suggests that there is no bias between the two intermolecular potentials and that the correct particle density is maintained within the simulation box. Recently Rzepiela et al. [2011] simulated a mixture of atomistic and CG liquid butane (where a butane molecule was modelled as a single CG bead) and found that the IBI force field contains a bias in its interactions and does not mix equally with the atomistic potential over-estimating the bead-bead interactions and favouring the formation of clusters of particles of the same resolution. In particular the authors found that the RDFs calculated between the CG butane molecules and the atomistic ones differed in the height of the first peak, indicating the formation of cluster of particles of the same type in the simulation box. Therefore, in order to investigate whether non-physical clustering of fraction of polymer chains takes place also in the polymer case, we calculate the total (intra- and inter- chain) RDFs between the beads and the all the CG sites (i.e. beads and VS) and compare them with those obtained between the VS and all the CG sites. If the CG and atomistic potential mix well,

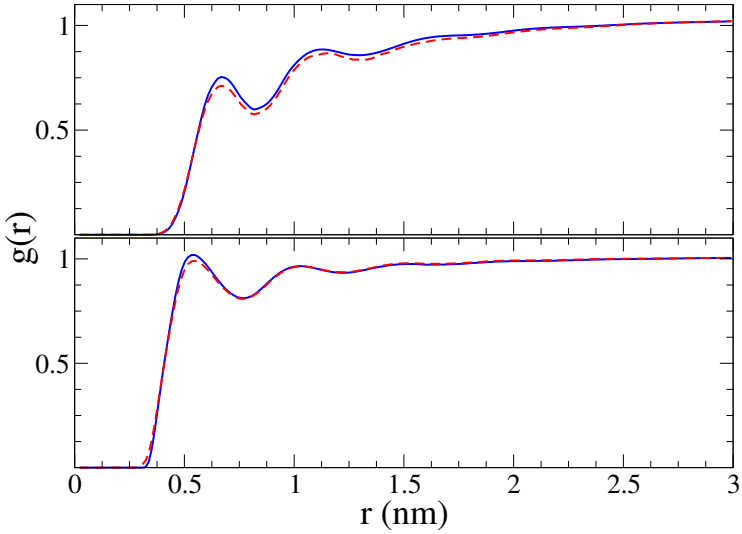

Figure 5.12: Comparison between inter-radial distribution function (RDF), $g(r)$, obtained for the pure coarse-grained and the hybrid model. The inter-RDF of the hybrid model is calculated by coarse-graining the atomistic part of each chain. From top to bottom: polystyrene (PS-1 only), polyethylene (PE-1 only). In the plot the blue solid line indicates the pure CG model, the red dashed line indicates the hybrid model.

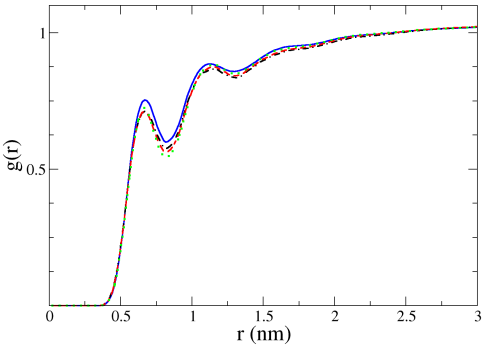

Figure 5.13: Comparison between the radial distribution functions (g(r)) obtained from the three hybrid models of the polystyrene melts and that calculated for the pure coarse-grained model: PS-1 (black dashed line), PS-2 (red dashed line), PS-3 (green dotted line), pure CG (solid blue line)

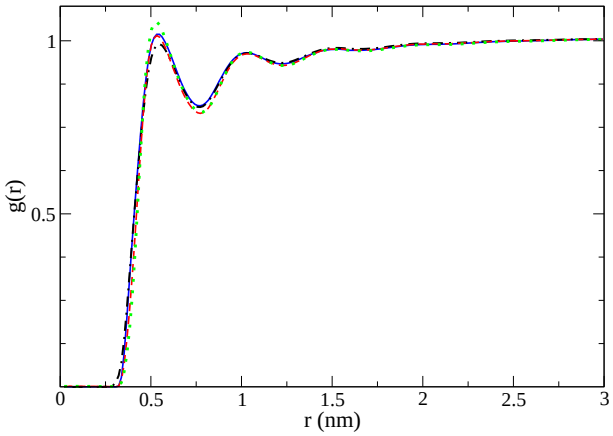

Figure 5.14: Comparison between the radial distribution functions (g(r)) obtained from the three hybrid models of the polyethylene melts and that calculated for the pure coarse-grained model: PE-1 (black dashed line), PE-2 (red dashed line), PE-3 (green dotted line), pure CG (solid blue line)

the two RDFs should match indicating that beads and atoms do not have any preference in choosing the resolution of their surrounding environment. Fig. 5.15 shows the results of the RDFs calculated for the only PE-1 and PS-1 as very similar results are obtained for the other models investigated. In the figure the total RDFs (intra- and inter- chains) calculated between all the CG sites (beads and VS) is also reported for comparison. It can be noticed that the three curves match perfectly at all distances for both the polyethylene and polystyrene cases. Here it is important to notice that for a perfect mix the simulations need to be performed for more than 50 ns since the system, although with reduced number of degrees of freedom, takes long time to equilibrate. The different quality of force field mixing obtained using our PE or PS IBI potentials compared with the butane case Rzepiela et al. [2011] may be explained observing the shape of the non-bonded IBI potentials (shown in Fig. 5.16). In fact, since the IBI force field is a structure-based potential, if the RDF from which the potential is developed presents narrow peaks, as for example in the case of simple liquid systems where one molecule is associated to one CG bead, the resulting potential will be probably characterized by a deep energy wells at short distance. On the contrary IBI potentials developed for polymer melts are often characterized by very soft interactions mirroring the usually not structured RDFs (see for example in Fig. 5.12,

blue line where the intermolecular RDFs used to develop the IBI potential for PE and PS are shown). We may therefore conclude that soft intermolecular potentials may mix well with atomistic ones not favouring one type of interaction over the other. In order to further verify that there is no bias in the mixed potential, we calculate the number density distribution ($\rho_{num} = N/V$, where N is the number of CG beads or VS present in a specific simulation box slab and V is slab volume) for beads and VS (i.e. atoms) separately across the simulation box. Fig. 5.17 shows the results obtained for the PS-2 model across the x-axis but the same results are obtained if the distributions are calculated across the y- and z- directions or for any of the hybrid models reported in Table 5.1. As it can be seen from the Figure the distribution of CG beads and atoms is homogeneous across the box confirming that there is not artificial mass transfer during the simulations within the system. As mentioned above, recently it has been shown that in the case of simple liquids such as water, if the coarse-grained force field cannot reproduce the correct isothermal compressibility (κT), unphysical large fluctuations in the particle density occur in the region of the box associated with the model with high κT (i.e. the coarse-grained one) [Fritsch et al., 2011; Wang et al., 2009]. In the case of polymer melts the pressure corrected IBI potential has also failed to reproduce the correct κT, however in this case the magnitude of the mismatch between the correct value and that predicted by the CG force field seems to depend on the choice of the beads size and, maybe, on the nature of the polymeric system as well [Carbone et al., 2008]. In this work, although atoms and beads are mixed within the simulation box, we can preliminary test whether there is any difference in the particle number fluctuation, calculated as the standard deviation of the averaged number of particles N (where N can be CG beads and/or VS) within one subvolume (slab) of the simulation box, between the monoresolved models (AA and CG) and the hybrid one. The results for the polystyrene and polyethylene melts, shown in Fig. 5.18, seem to indicate that the local density fluctuations in the monoresolved and hybrid models are fairly similar and very small fluctuation are visible across the simulation box. It should be noticed, however, that for the polystyrene we have found that a CG mapping scheme similar to that used in the present work here underestimates the κT of two orders of magnitude [Carbone et al., 2008]. This result may indicate that the fact that the atoms and beads are bonded together makes the interface between two differently modelled regions smoother than in the case of simple liquid.

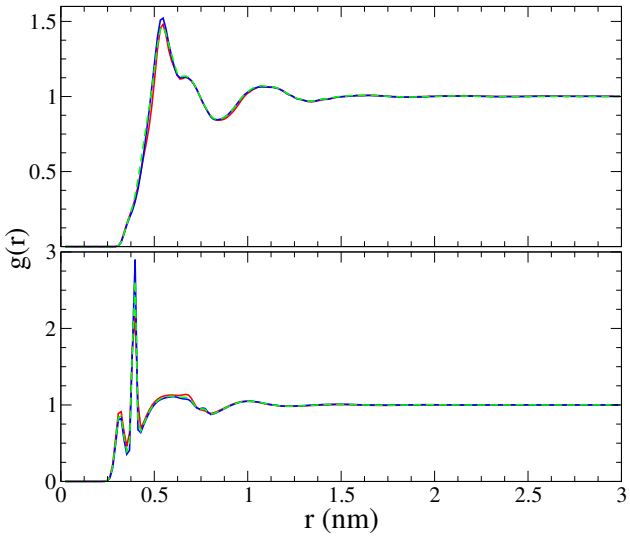

Figure 5.15: Intra and inter- radial distribution functions g(r) calculated on the hybrid models (PS-1 (top), PE-1 (bottom)) between virtual sites and all the coarse-grained sites (red line), all coarse-grained site and all coarse-grained sites (green line), beads and all coarse-grained sites (blue line).

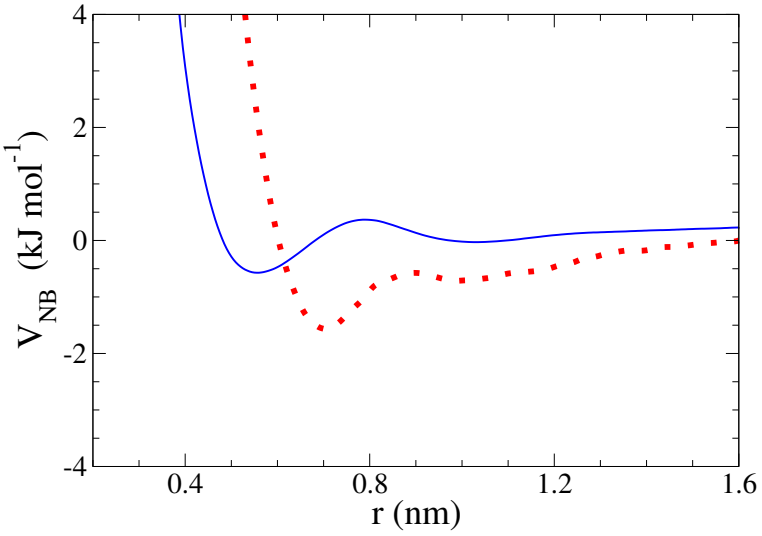

Figure 5.16: The IBI coarse-grained potential between polystyrene beads (dotted red line) and polyethylene beads (solid blue line)

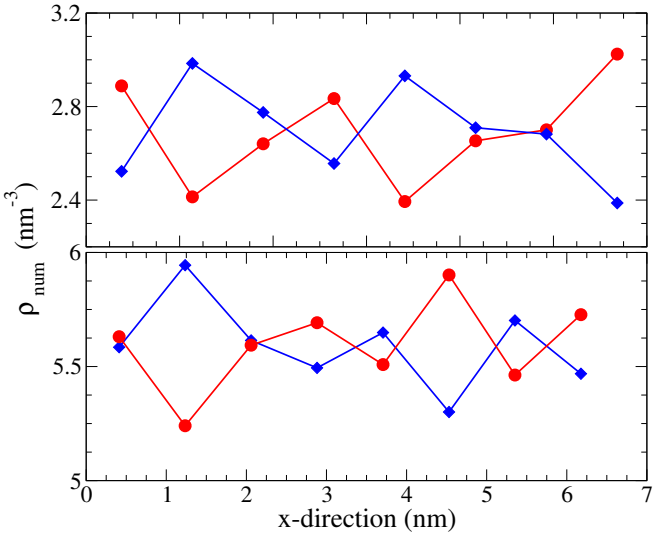

Figure 5.17: Numerical density profile across the simulation box along the x-axis calculated separately for the coarse-grained beads (◆) and virtual sites (●). The results refer to the PS-2 (top) and PE-2 (bottom) model.

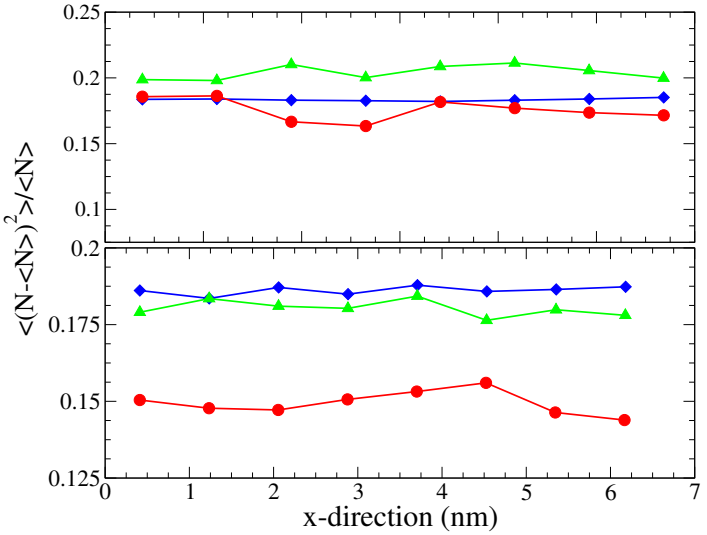

Figure 5.18: Particle number (N) fluctuation across the simulation box along the x-axis for pure atomistic (●), pure coarse-grained (◆) and hybrid (green triangles) model of and polystyrene, PS-2, (top) polyethylene, PE-2, (bottom). For the hybrid model both CG beads and virtual sites have been included in the calculation. The results obtained for the full atomistic model have been obtained from a trajectory of 16 ns and 10 ns respectively for polystyrene and polyethylene.

5.6 Further Development

This section is intended to present some further development of the hybrid model presented in this Chapter. These new features are the Multiple Time Step (MTS) which in our intention will speed up the hybrid simulations and a new fastest backmapping procedure which will be able to rebuild the atomistic detail of a coarse-grained system. The backmapping procedure will in turn be used to obtain an on-the-fly change of the degrees of freedom of the system, assuring a high flexibility of the hybrid model.

A CG potential is developed by considering a time step used in the integration of the equations of motion larger than those normally used in a fully atomistic simulation. However, in an hybrid system the shorter time step must be used. Hence, even if we have a sensible decreasing in the computational time by coarse graining some degrees of freedom of the system we have a waste of computational time represented by the fact that we must use a shorter time step even for the CG part of the system whose equation of motion can be instead integrated less frequently. These considerations are the base of the development of an algorithm able to split the integration of motion between the two different systems, or the Multiple Time Step (MTS) algorithm. A very promising way to perform this splitting is to approximate the force acting on the CG part of the system (which can be considered smoother function of time than the force acting on atoms) by using a series Taylor expansion:

$$F_{CG-CG}(t_0 + k\Delta t) \approx \sum_{i=0}^{h} \frac{(k\Delta t)^i}{i!} \left(\frac{\partial^{(i)} F_{CG-CG}}{\partial t^{(i)}} \right)_{t_0} \qquad k = 1, \ldots, m \tag{5.16}$$

where h is the order of the truncation of the Taylor series and F_{CG-CG} represents the force acting between two beads. In the multiple time step scheme the equation of motion is thus integrated every Δt for each atom-atom interactions and only every $m\Delta t$ for the bead-bead ones.

The backmapping procedure will allow to rebuild the atomistic details from a CG system by using the geometrical constraints of the atomistic structure. Starting from the CG molecules, by using a two step algorithm, a monomer (which represents the mapped atoms) is translated into the position occupied by the bead and then rotated to allow the atoms belonging to the monomer to occupy the correct positions. All these rigid movements (translation and rotation) are obtained

by geometrical constraints that the new monomer must fulfil to be reinserted in the chain.

5.7 Summary and Conclusions

In this Chapter a simple hybrid model for complex macromolecular systems was devised and tested. The model consists of coarse-grained (CG) beads and atoms embedded into the same single molecule where the bonded and non-bonded components of the atomistic and CG potential are mixed. The model was tested using the CG potential derived using the iterative Boltzmann inversion procedure that develops the interactions from atomistic simulations. Several features, such as the definition of two separate cut-off distances and the creation of two neighbour lists for respectively the atom-atom and bead-bead interactions, have been also introduced into the simulation code in order to take advantage of the reduced number of degrees of freedom of the hybrid model and the consequent speed up in the cpu time of the simulations. Two different polymeric systems, polyethylene and atatic-polystyrene melts, characterized by different chemical structure and chain flexibility have been tested and modelled with three different atoms/beads ratios and the structural properties of the resulting hybrid models have been tested against the mono-resolved model ones. Our results showed that the CG potential derived using the IBI procedure merges extremely well with the atomistic one. The equilibrium properties of the hybrid models match well with those of the mono-resolved ones although the two polymeric systems show different features. In the case of polyethylene a clear trend towards the radius of gyrations and end-to-end distance values characteristic of the AA model is showed by that hybrid system containing a high percentage of atomistic resolved monomers. This trend is not showed by polystyrene as the AA and CG models predict both the same single chain structural properties. We also observed that, maybe due to the evident topological difference between the atomic and CG blocks, in the case of polystyrene the mean-squared internal distance calculated for the hybrid models departs from that obtained from the pure CG one at all distances. On the contrary the polyethylene hybrid models present a curve more similar, and exactly overlapping at short distance, to the one obtained from the monoresolved model. A detailed analysis of the structure has showed that the mixed AA/CG potential does not introduce any bias in the simulation and that

atoms and beads are evenly distributed among the simulation box. These results indicate that no evident interfaces are present in the hybrid models that behave as single homogeneous systems.

Chapter 6

Conclusions

The thesis focuses on the use of multiscale modelling tools applied to the precipitation of polymeric nanoparticles for pharmaceutical applications. In any multiscale approach the same system is modelled at different length- and time-scales, ranging from nanometers to meters and from picoseconds to seconds.

In particular, we focus on different computational techniques, including Molecular Dynamics (MD), used to describe the motion of atoms and molecules and Computational Fluid Dynamics (CFD), used in the description of the system at macroscopic level. In Chap. 2 a description of these methods was given, along with a description on how it is possible to pass with continuity from the detailed atomistic description, to the averaged continuum approach. In subsequent Chapters it is also discussed that these methodologies far from be isolated one from another are instead intimately related and their use should depend on how many details one wants to consider. In our case for example a CFD model seems to be inadequate in treating systems like the ones presented here, because of the complex behaviour of the macromolecular chains.

The precipitation of polymeric nanoparticles takes place in a Confined Impinged Jet Mixer (CIJR) whose description was given in Chaps. 1 and 3. The process used to produce the nanoparticles (i.e., the solvent displacement) is described in Chap. 3. In this work we considered as polymer, poly-ϵ-caprolactone, and as solvent and anti-solvent acetone and water respectively. Initially (see Chap. 3), the problem was treated by using only CFD along with a Population Balance model (PBM) and the Classical Nucleation Theory (CNT) to model the

precipitation of nanoparticles. Even if CFD is able to correct describe the flow field and mixing inside the CIJM, the CNT seems not be able to correctly describe the nucleation of the particles. Hence, as we show in the last part of the Chapter, a new approach is needed to overcome this problem.

Therefore, the CFD description of the system and the equations used to model the precipitation of the polymer at the macro scale are coupled with a description of the behaviour of PCL in different solvents obtained from MD. The information extracted, which in this case is mainly related to the configuration of the molecules in solvent, is inserted in the CFD model. At the same time, the nucleation law obtained by CNT, was redefined and some approximation relaxed to take into account the complex behaviour of a macromolecular chain in solution. The final model was tested and some results presented at the end of the Chap. 4.

In order to obtain a better description of our polymeric system with atomistic details, one needs to simulate a system as close as possible to the real one. However, the simulation of a system of the size of those considered at macro scale level is not feasible, mainly due to the computational time required. In the last years a number of methods which allow to reduce the computational time of MD simulations by eliminating some degrees of freedom (i.e, Coarse-Grained (CG) methods) were devised. The main disadvantage of these methods is that by eliminating some degrees of freedom of the system, some useful information can be coarse-grained away. In Chap. 5 a new hybrid model able to speed up the MD simulation by coupling an atomistic description of the system with a CG description is presented and validated. In this first attempt to asses such a method a simpler test case was chosen, a melt of poly-styrene and poly-ethylene.

In a future development of this work, results obtained by this latter hybrid methodologies will be extended to the precipitating system investigated in Chaps. 3 to 4.

Ringraziamenti

Remember when you were young,
you shone like the sun
Shine on you crazy diamond.
Now there's a look in your eyes,
like black holes in the sky . . .
"Shine On You Crazy Diamond", **Pink Floyd**

Alla soglia dei 28 anni mi ritrovo spesso a pensare a come tutto questo sia nato e in che modo è terminato. Alle persone che hanno attraversato la mia strada. A quelle che hanno tentato di intralciarla, e a quelle che me l'hanno resa più facile. Il dottorato, questo dottorato, è stata un'esperienza fondamentale nella mia formazione, dalla quale ho cercato di apprendere il massimo, e alla quale sono molto grato.

Ma senza altri giri di parole, veniamo ai ringraziamenti. Sicuramente il primo va ai miei relatori, Daniele, Prof. Barresi e Paola, che mi hanno guidato in questo periodo di formazione, non solo scolastica, e alla mia famiglia, ai miei genitori e ai miei fratelli, che mi hanno permesso, con i loro sforzi, di poter arrivare fin qui.

Antonio, Martina, Alessandro, Valerio, Elena, Ilaria, compagni di serate, per la maggior parte delle volte passate a mangiare. Marco Sangermano che non manca mai di scherzare ogni volta che lo incrocio nei corridoi durante una delle mie innumerevoli (beh la tesi è finita, ora posso dirlo) pause caffè.

Un ringraziamento a Dario, Emanuele, Arnaldo con i quali ho condiviso alcuni dei momenti più divertenti di cui ho memoria e Annalaura che mi ha aiutato

ad ambientarmi nel freddo clima inglese di Manchester.

Un ulteriore ringraziamento è per Carlotta, sempre pronta a sorbirsi le mie (spesso inutili) paranoie e farmele dimenticare con tutti gli ottimi manicaretti che prepara.

Infine da ultimo, ma non certo per importanza, c'è Palma Martina che da due anni si porta dietro la croce del mio dottorato e che ringrazio per l'enorme pazienza che dimostra quando ha a che fare con me. D'altronde io non mi fidanzerei mai con uno come me al contrario suo.

Purtroppo non posso citarvi tutti e spero che non me ne vogliate se non lo faccio e vi ringrazio collettivamente ora.

Appendix A

Boltzmann H-theorem

H-theorem is one of the most important and most controversial results in all the theory developed by Boltzmann. This theorem represents the first unification theory between the model describing the atomistic scale and the model describing the macro-scale.

Theorem (Boltzmann H-theorem)**.** *Assume that* $f \equiv f(v) > 0$ *almost everywhere (a.e.) is rapidly decaying and such that* $\ln f$ *has polynomial growth as* $|v| \to +\infty$. *Then, this relation for the functional* $H(f)$ *holds:*

$$H(f) \equiv -\int_{\mathbb{R}^3} C(f,g) \ln f dv \geq 0.$$

Moreover, the following conditions are equivalent:

$$H(f) = 0 \Leftrightarrow C(f,g) = 0 \ \text{ almost everywhere } \Leftrightarrow f \ \text{ is a Maxwellian distribution}$$

i.e., there exist $\rho, \theta > 0$ *and* $u \in \mathbb{R}^3$ *such that:*

$$f(v) = \mathcal{M}_{(\rho,u,\theta)}(v) \equiv \frac{\rho}{(2\pi\theta^2)^{\frac{3}{2}}} \exp\left(\frac{\left|\boldsymbol{v} - \boldsymbol{U}\right|}{2\theta^2}\right) \text{ a.e. in } v \in \mathbb{R}^3$$

The proof of the H-theorem uses the definition of function which are collision invariants

Definition. *A function collision invariant is a measurable function* ϕ *defined a.e.*

on $\mathbb{R}^3$ *that satisfies:*

$$\phi(v) + \phi(v_\star) - \phi(v') - \phi(v'_\star) = 0 \quad a.e.\ in\ (v, v_*, \omega)$$

where $(v, v_\star, \omega)$ *are defined in Eqs.* (2.38) *and* (2.39)

and the sequent Lemma and Proposition

Lemma. *Let* $\phi \geq 0$ *a.e. be such* $(1 + |v|^2)\phi \in L^1(\mathbb{R}^3)$. *If*

$$\phi'\phi'_\star = \phi\phi_\star \quad for\ a.e.\ (v, v_\star, \omega)\ in\ \mathbb{R}^3 \times \mathbb{R}^3 \times \mathbb{S}^2$$

then ϕ *is either a.e.* 0 *or a Maxwellian.*

Proposition. *A function* ϕ *is collision invariant if and only if there exists five constants* $a_0, a_1, a_2, a_3, a_4, a_5 \in \mathbb{R}$ *such that*

$$\phi(v) = a_0 + a_1 v_1 + a_2 v_2 + a_3 v_3 + a_4 |v|^2 \quad a.e.\ in\ \mathbb{R}^3$$

The importance of the H-theorem is in the demonstration that the Boltzmann equation has a basic feature of non-reversibility. The law of the classic mechanic are, in fact, time reversible, i.e. by reversing the time arrows the equation must lead to the same solution (i.e. the trajectory is covered in the backward direction). The thermodynamic is an irreversible process, i.e. once the equilibrium is reached it is not possible to obtain again the initial configuration of the system. Situation resumed in the second law of thermodynamics. But if we identify the functional $H(f)$ with the entropy we can see that even if starting from a classic description of the system we can obtain the irreversible behaviour of a thermodynamic system. The implication of the H-theorem are much deeper than the naive interpretation given here and for a complete discussion and some mathematical proof of the theorem cf. Cercignani [1988]; Succi [2001]; Golse [2005]

Appendix B

Poisson pressure equation

The pressure is a thermodynamic quantity related to temperature and density of a system. Anyhow, in non-compressible system there is no connection between pressure and density and a different way to close the pressure term in the NS-E must be considered.

Let us start from the NS-E equation in vectorial form and apply the divergence operator

$$\nabla\cdot\left(\frac{\partial \mathrm{U}}{\partial t} + (\mathrm{U}\cdot\nabla)\mathrm{U}+\right) = \nabla\cdot\left(\nu\nabla^2\mathrm{U} - \frac{1}{\rho}\nabla p\right) \tag{B.1}$$

let us rearrange the equation to obtain:

$$\left(\frac{\partial}{\partial t} + \mathrm{U}\cdot\nabla - \nu\nabla^2\right)\nabla\cdot\mathrm{U} = -\frac{1}{\rho}\nabla^2 p - \nabla\cdot\nabla(\mathrm{U}\cdot\mathrm{U}). \tag{B.2}$$

Now, by using Eq. (2.53) we obtain

$$\frac{1}{\rho}\nabla^2 p = -\nabla\cdot\nabla(\mathrm{U}\cdot\mathrm{U}). \tag{B.3}$$

Hence from the previous equation it can be concluded that the satisfaction of the Poisson equation for the pressure is a necessary and sufficient condition for a solenoidal velocity field to remain solenoidal [Pope, 2000].

Appendix C

Reynolds stress tensor equation

In this part the Eq. (2.86) will be derived. We start from the transport equation for the fluctuating part of the velocity u, Eq. (2.85)

$$\frac{\partial u_i}{\partial t} + U_k \frac{\partial u_i}{\partial x_k} + u_k \frac{\partial \langle U_i \rangle}{\partial x_k} = \nu \nabla^2 u_i - \frac{1}{\rho} \frac{\partial p'}{\partial x_k} + \frac{\partial (u_i u_k)}{\partial x_k}. \tag{C.1}$$

First, we multiply the above equation by u_j; then we consider another equation equal to Eq. (2.85) but in which we replace the index i with index j:

$$\frac{\partial u_j}{\partial t} + U_k \frac{\partial u_j}{\partial x_k} + u_k \frac{\partial \langle U_j \rangle}{\partial x_k} = \nu \nabla^2 u_j - \frac{1}{\rho} \frac{\partial p'}{\partial x_k} + \frac{\partial (u_j u_k)}{\partial x_k}. \tag{C.2}$$

We multiply this last equation by u_i obtaining the following equations:

$$u_j \frac{\partial u_i}{\partial t} + u_j U_k \frac{\partial u_i}{\partial x_k} + u_j u_k \frac{\partial \langle U_i \rangle}{\partial x_k} = \nu u_j \nabla^2 u_i - \frac{1}{\rho} u_j \frac{\partial p'}{\partial x_k} + u_j \frac{\partial (u_i u_k)}{\partial x_k} \tag{C.3}$$

$$u_i \frac{\partial u_i}{\partial t} + u_i U_k \frac{\partial u_i}{\partial x_k} + u_i u_k \frac{\partial \langle U_i \rangle}{\partial x_k} = \nu u_i \nabla^2 u_j - \frac{1}{\rho} u_i \frac{\partial p'}{\partial x_k} + u_i \frac{\partial (u_i u_k)}{\partial x_k}. \tag{C.4}$$

We now sum Eqs. (C.3) to (C.4) obtaining:

$$\begin{aligned} u_j\frac{\partial u_i}{\partial t} + u_i\frac{\partial u_i}{\partial t} \quad & + u_j U_k\frac{\partial u_i}{\partial x_k} + u_i U_k\frac{\partial u_i}{\partial x_k} + u_j u_k\frac{\partial \langle U_i\rangle}{\partial x_k} + u_i u_k\frac{\partial \langle U_j\rangle}{\partial x_k} \\ = \nu u_j\nabla^2 u_i \quad & + \nu u_i\nabla^2 u_j - \frac{1}{\rho}u_j\frac{\partial p'}{\partial x_k} - \frac{1}{\rho}u_i\frac{\partial p'}{\partial x_k} + \\ & + u_j\frac{\partial(u_i u_k)}{\partial x_k} + u_i\frac{\partial(u_i u_k)}{\partial x_k}. \end{aligned} \tag{C.5}$$

The various term in Eq. (C.5) can be rewritten, considering the proprieties of the derivatives and the fact that the fluctuating velocity field is solenoidal as

$$\begin{aligned} u_j\frac{\partial u_i}{\partial t} + u_i\frac{\partial u_i}{\partial t} &= \frac{\partial(u_i u_j)}{\partial t} \\ u_j U_k\frac{\partial u_i}{\partial x_k} + u_i U_k\frac{\partial u_i}{\partial x_k} &= U_k\frac{\partial(u_i u_j)}{\partial x_k} \\ u_j\frac{\partial(u_i u_k)}{\partial x_k} + u_i\frac{\partial(u_i u_k)}{\partial x_k} &= \frac{\partial(u_i u_j u_k)}{\partial x_k} \\ u_j\nabla^2 u_i + \nu u_i\nabla^2 u_j &= \nabla^2(u_i u_j) - 2\left(\frac{\partial u_i}{\partial x_k}\frac{\partial u_j}{\partial x_k}\right) \end{aligned}$$

Therefore Eq. (C.5) becomes

$$\begin{aligned} \frac{\partial(u_i u_j)}{\partial t} + U_k\frac{\partial(u_i u_j)}{\partial x_k} + u_j u_k\frac{\partial\langle U_i\rangle}{\partial x_k} + u_i u_k\frac{\partial\langle U_j\rangle}{\partial x_k} = \\ \nu\left(\nabla^2(u_i u_j) - 2\left(\frac{\partial u_i}{\partial x_k}\frac{\partial u_j}{\partial x_k}\right)\right) - \frac{1}{\rho}\left(u_j\frac{\partial p'}{\partial x_k} + u_i\frac{\partial p'}{\partial x_k}\right) + \frac{\partial(u_i u_j u_k)}{\partial x_k}. \end{aligned} \tag{C.6}$$

If we now apply the Reynolds average to the previous equation we obtain:

$$\begin{aligned} \frac{\partial\langle u_i u_j\rangle}{\partial t} + \langle U_k\rangle\frac{\partial\langle u_i u_j\rangle}{\partial x_k} + \frac{\partial\langle u_i u_j u_k\rangle}{\partial x_k} = -\left(\langle u_i u_k\rangle\frac{\partial\left\langle U_j\right\rangle}{\partial x_k} + \langle u_j u_k\rangle\frac{\partial\langle U_i\rangle}{\partial x_k}\right) \\ - \frac{1}{\rho}\left\langle u_i\frac{\partial p'}{\partial x_j} + u_j\frac{\partial p'}{\partial x_i}\right\rangle + \nu\nabla^2\langle u_i u_j\rangle - 2\nu\left\langle\frac{\partial u_i}{\partial x_k}\frac{\partial u_j}{\partial x_k}\right\rangle. \end{aligned} \tag{C.7}$$

We can define

$$\mathcal{P}_{ij} \equiv -\langle u_i u_k \rangle \frac{\partial \left\langle U_j \right\rangle}{\partial x_k} - \langle u_j u_k \rangle \frac{\partial \langle U_i \rangle}{\partial x_k}$$
$$\Pi_{ij} \equiv -\frac{1}{\rho} \left\langle u_i \frac{\partial p'}{\partial x_j} + u_j \frac{\partial p'}{\partial x_i} \right\rangle$$
$$\varepsilon_{ij} \equiv 2\nu \left\langle \frac{\partial u_i}{\partial x_k} \frac{\partial u_j}{\partial x_k} \right\rangle$$

from which we obtain at the very end

$$\frac{\partial \langle u_i u_j \rangle}{\partial t} + \langle U_k \rangle \frac{\partial \langle u_i u_j \rangle}{\partial x_k} + \frac{\partial \langle u_i u_j u_k \rangle}{\partial x_k} = \mathcal{P}_{ij} + \Pi_{ij} + \nu \nabla^2 \langle u_i u_j \rangle - \varepsilon_{ij} \tag{C.8}$$

Appendix D

Radius of Gyration

Here, the Eq. 4.50 is derived.

It is possible to prove the equality by using this identity

$$
\begin{aligned}
\sum_{i,j=0}^{N} (\mathbf{r}_i - \mathbf{r}_j)^2 &= \sum_{i,j=0}^{N} [(\mathbf{r}_i - \mathbf{r}_B) - (\mathbf{r}_j - \mathbf{r}_B)]^2 = \\
&= \sum_{i,j=0}^{N} [(\mathbf{r}_i - \mathbf{r}_B) - (\mathbf{r}_j - \mathbf{r}_B)]^2 = \\
&= \sum_{i,j=0}^{N} (\mathbf{r}_i - \mathbf{r}_B)^2 - \sum_{i,j=0}^{N} (\mathbf{r}_i - \mathbf{r}_B) \cdot (\mathbf{r}_j - \mathbf{r}_B) + \sum_{i,j=0}^{N} (\mathbf{r}_j - \mathbf{r}_B)^2 = \\
&= 2(N+1) \sum_{i=0}^{N} (\mathbf{r}_i - \mathbf{r}_B)^2 - 2 \sum_{i=0}^{N} (\mathbf{r}_i - \mathbf{r}_B) \cdot \sum_{j=0}^{N} (\mathbf{r}_j - \mathbf{r}_B) = \\
&= 2(N+1) \sum_{i=0}^{N} (\mathbf{r}_i - \mathbf{r}_B)^2
\end{aligned}
$$

where the last equality follow by considering

$$\begin{aligned}\sum_{i=0}^{N}(\mathbf{r}_i-\mathbf{r}_B) &= \sum_{i=0}^{N}\left(\mathbf{r}_i-\frac{1}{N+1}\sum_{k=0}^{N}\mathbf{r}_k\right)\\ &= \frac{1}{N+1}\left[\sum_{i=0}^{N}\left((N+1)\mathbf{r}_i-\frac{1}{N+1}\sum_{k=0}^{N}\mathbf{r}_k\right)\right]\\ &= \frac{1}{N+1}\left(\sum_{i=0}^{N}(N+1)\mathbf{r}_i-\sum_{k=0}^{N}(N+1)\mathbf{r}_k\right)=0.\end{aligned}$$

In this derivation a unitary mass for the atoms is considered, for the sake of simplify the calculation, but the extension to the general case is straightforward.

Bibliography

C. F. Abrams, L. Delle Site, and K. Kremer. Dual-resolution coarse-grained/atomistic simulation of the bisphenol-a-polycarbonate/nickel interface. *Phys.Rev.E*, 67:21807, 2003.

Y. Adachi, M.A. Cohen Stuart, and R. Fokkink. Kinetics of turbulent coagulation studied by means of end-over-end rotation. *J. Colloid Interface Sci.*, 165:310, 1994.

J. Akroyd, A. J. Smith, L. R. McGlashan, and Kraft M. Numerical investigation of dqmom-iem as a turbulent reaction closure. *Chem. Eng. Sci.*, 65:1915–1924, 2009.

M. P. Allen and D. J. Tildesley. *Computer Simulation of Liquids*. Clarendon Press, 1987.

P.M. Armenante and D.J. Kirwan. Mass transfer coefficient to microparticles in agitates systems. *Chem. Eng. Sci.*, 44:2781, 1989.

V. I. Arndold. *Mathematical Method of Classical Mechanics*. Springer, 1989.

R. Auhl, R Everaers, G.S. Grest, K. Kremer, and S.J. Plimpton. Equilibration of long chain polymer melts in computer simulations. *Journal of Chemical Physics*, 119:12718, 2003.

J. Baldyga and W. Orciuch. Some hydrodynamic aspects of precipitation. *Powder Technol.*, 121:9, 2001.

J.C. Barrett and N.A. Webb. A comparision of some approximate methods for solving the aereosol general dynamic equation. *Journal of Aereosol Science*, 29:31, 1998.

R. Becker and W. Döring. Kínetische Behandlung der Keimbildung in übersättigten Dämpfen. *Ann. Phys.*, **24**:719, 1935.

H. J. C. Berendsen, J. P. M. Postma, W. F. van Gusteren, and J. Hermans. *Intermolecular Forces*. B. Pullman, 1983.

H.J.C. Berendsen, J.P.M Postma, W.F.V. Gunsteren, Di Nola A., and J.R. Haak. Molecular dynamics with coupling to an external bath. *Journal of Chemical Physics*, 81:3684, 1984.

R.B. Bird, W.E. Stewart, and E.N. Lightfoot. *Transport Phenomena*. John Wiley & Sons, Inc.: New York, 2002.

H. Bock, K. E. Gubbins, and H.L. Klapp. Coarse Graining of Nonbonded Degrees of Freedom. *Phys. Rev. Lett.*, 98:4, 2007.

L. Brannon-Peppas and J. O. Blanchette. Nanoparticle and targeted systems for cancer therapy. *Adv. Drug Delivery Rev.*, 56:1649, 2004.

P. Carbone, F. Negri, and F. Müller-Plathe. A Coarse-grained Model for Polyphenylene Dendrimers: Switching and Backfolding. *Macromolecules*, 40: 7044, 2007.

P. Carbone, H.A. Karimi-Varzaneh, X. Y. Chen, and F. Müller-Plathe. Transferability of coarse-grained force fields: the polymer case. *Journal of Chemical Physics*, 128:64904, 2008.

P. Carbone, H.A. Karimi-Varzaneh, and F. Müller-Plathe. Fine-graining without coarse-graining: an easy and fast way to equilibrate dense polymer melts. *Faraday Discussion*, 144:25, 2010.

C. Cercignani. *The Boltzmann Equation and Its Application*. Springer-Verlag, 1988.

H.K. Chan and P.C.L. Kwok. Production methods for nanodrug particles using the bottom-up approach. *Advanced Drug Delivery Reviews*, 63:406, 2011.

X.Y. Chen, P. Carbone, W.L. Cavalcanti, G. Milano, and F. Müller-Plathe. Viscosity and Structural Alteration of a Coarse-grained model of Polystyrene under Steady Shear Flow Studied by Reverse Nonequilibrium Molecular Dynamics. *Macromolecules*, 40:8087, 2007.

J. C. Cheng and R. O. Fox. Kinetic modelling of nanoprecipitation using CFD coupled with a population balance. *Industrial & Engineering Chemistry Reasearch*, 49:10651, 2010.

J. C. Cheng, R. D. Vigil, and R. O. Fox. A competitive aggregation model for flash nanoprecipitation. *J. Colloid Interface Sci.*, 351:330, 2010.

Y. J. Choi, S. T. Chung, M. Oh, and H. S. Kim. Investigation of cristallization in a Jet Y-Mixer by a hybrid computational fluid dynamics and process simulation approach. *Cristal Growth & Design*, 5:959, 2005.

S. Corrsin. The isotropic turbulen mixer: part II. Arbitrary Schmidt number. *A.I.Ch.E. Journal*, 10:870, 1964.

J. P. Cotton, D. Decker, B. Farnoux, and G. Jannink. Experimental Determination of the Excluded-Volume Exponent in Different Environments. *Phys. Rev. Lett*, **32**:1170–1172, 1974.

T. Darden, D. York, and L. Pedersen. Particle mesh Ewald: an $N \ln(N)$ for Ewald sums in large systems. *J. Chem. Phys.*, **98**:10089, 1995.

L. Delle Site, S. Leon, and K. Kremer. BPA-PC on a *Ni*(111) Surface:The Interplay between Adsorption Energy and Conformational Entropy for different Chain-End Modifications. *Journal of the American Chemical Society*, 126: 2944, 2004.

N. Di Pasquale, D.L. Marchisio, and A.A. Barresi. Model validation for precipitation in solvent-displacement processes. *Chemical Engineering Science*, **84**: 671, 2012.

J. A. Dirksen and T. A. Ring. Fundamentals of crystallization: kinetic effects on particle size distributions and morphology. *Chem. Eng. Sci.*, **46**:2389, 1991.

D. E. Discher, V. Ortiz, G. Srinivas, M. L. Klein, C. A. David, Y. Kim, S. S. Cai, P. Photos, and F. Ahmed. Emerging applications of polymersomes in delivery: From molecular dynamics to shrinkage of tumors. *Progress in Polymer Science*, 32:838–857, 2007.

M. Elimelech, J. Gregory, X. Jia, and R.A. Williams. *Particle Deposition & Aggregation*. Butterwort-Heinemann, 1995.

P. Español. Hybrid description of complex molecules. *European Physics Letters*, 88:5, 2009.

H. Fessi, F. Puisieux, J. Ph. Devissaguet, N. Ammoury, and S. Benita. Nanocapsule formation by interfacial polymer deposition following solvent displacement. *Int. J. Pharm.*, 55:R1, 1989.

P. Flory. *Principles of Polymer Chemistry*. Ithaca: Cornell Univ. Press, 1953.

R.O. Fox. On the relationship between lagrangian micromixing models and computational fluid dynamics. *Chem. Eng. Process.*, 37:521, 1998.

R.O. Fox. *Computational models for turbulent reacting flows*. Cambridge University Press, 2003.

L. C. G. Freitas, J.M.M. Cordeirob, and F.L.L. Garbujoa. Theoretical studies of liquids by computer simulations: The water-acetone mixture. *J. Mol. Liq.*, **79**: 1, 1999.

F. Fritsch, S. Poplete, C. Junghans, G. Ciccotti, L. Delle Site, and K. Kremer. Grand canonical molecular dynamics simulations. *ArXiv:1112.3151v1*, 2011.

N. A. Fuchs. Uber die stabilitat und aufladung der aerosole. *Z. Phys.*, 89:736–743, 1934.

E. Gavi, D.L. Marchisio, and A.A. Barresi. CFD modelling and scale-up of Confined Impinging Jet Reactors. *Chem. Eng. Sci.*, 62:2228, 2007a.

E. Gavi, L. Rivautella, D.L. Marchisio, M. Vanni, A.A. Barresi, and G. Baldi. CFD modelling of nano-particle precipitation in confined Impinging Jet Reactor. *Chem. Eng. Res. Des.*, 85:753, 2007b.

E. Gavi, D.L. Marchisio, and A.A. Barresi. On the importance of mixing for the production of nanoparticles. *J. Dispersion Sci. Technol.*, 29:548, 2008.

E. Gavi, D.L. Marchisio, A.A. Barresi, M.G. Olsen, and R.O. Fox. Turbulent precipitation in micromixers: CFD simulation and flow field validation. *Chem. Eng. Res. Des.*, 12:1182, 2010.

E. Gavi, D. L. Marchisio, A. A. Barresi, M. G. Olsen, and R. O. Fox. Turbulent precipitation in micromixers: CFD simulation and flow field validation. *Chem. Eng. Res. Des.*, **88**:1182–1193, 2010.

F. Golse. Hydrodynamic limits. *Europ. Math. Soc.*, 2005.

R.G. Gordon. Error bounds in equilibrium statistical mechanics. *J. Math. Phys.*, 9:665, 1968.

J. Gradl, H.C. Schwarzer, F. Schwertfirm, M. Manhart, and W. Peukert. Precipitation of nanoparticles in a T-mixer: coupling the particle population dynamics with hydrodynamics through direct numerical simulation. *Chem. Eng. Process.*, 45:908, 2006.

K. E. Gubbins and J.D. Moore. Molecular modeling of matter: Impact and prospects in engineering. *Industrial & Engineering Chemistry Research*, 49: 3026–3046, 2010.

J.M. Haile. *Molecular Dynamics Simulation*. Wiley, 1992.

V.A. Harmandaris, N.P. Adhikari, N.F.A van der Vegt, and K. Kremer. Hierarchical Modeling of Polystyrene: From Atomistic to Coarse-Grained Simulations. *Macromolecules*, 39:6708–6719, 2006.

T. H. Hill. *An introduction to Statistical Thermodynamics*. Dover Publications Inc., 1986.

R. W. Hockney and J. W. Eastwood. *Computer Simulation Using Particles*. Adam Hilger, 1988.

M. Icardi, E. Gavi, D. L. Marchisio, A. A. Barresi, M. G. Olsen, R. O. Fox, and D. Lakehal. Investigation of the flow field in a three-dimensional Confined Impinging Jets Reactor by means of microPIV and DNS. *Chem. Eng. J.*, 162: 294, 2011a.

M. Icardi, E. Gavi, D. L. Marchisio, M. G. Olsen, R. O. Fox, and D. Lakehal. Validation of LES predictions for turbulent flow in a Confined Impinging Jets Reactor. *Applied Mathematical Modelling*, 35:1591, 2011b.

B.K. Johnson and R.K. Prud'homme. Flash nanoprecipitation of organic actives and block copolymers using a confined impinging jets mixer. *Australian Journal of Chemistry*, 56:1021, 2003a.

B.K. Johnson and R.K. Prud'homme. Chemical processing and micromixing in confined impinging jets. *AIChE J.*, 49:2264, 2003b.

W. L. Jorgensen, D. S. Maxwell, and J. Tirado-Rives. Development and Testing of the OPLS All-Atom Force Field on Conformational Energetics and Properties of Organic Liquids. *J. Am. Chem. Soc.*, **118**:11225, 1996.

H. A. Karimi-Varzaneh, P. Carbone, and F. Múller-Plathe. Fast dynamics in coarse-grained polymer models: The effect of the hydrogen bonds. *Journal of Chemical Physics*, 129:154904, 2008.

H. A. Karimi-Varzaneh, H. J Qian, X. Y. Chen, P. Carbone, and F. Müller-Plathe. IBIsCO: A Molecular Dynamics Simulation Package for Coarse-Grained Simulations. *Journal of Computational Chemistry*, 32:1475, 2011.

H. A. Karimi-Varzaneh, N. van der Vegt, F. Müller-Plathe, and P. Carbone. How good are coarse-grained polymer models? a comparison for atactic polystyrene. *ChemPhysChem.*, 13:3428, 2012.

H.A. Karimi-Varzaneh and F. Müller-Plathe. Multiscale molecular methods in applied chemistry. *Top. Curr. Chem.*, 307:295, 2012.

W. Kays, M. Crawford, and B. Weigand. *Convective Heat and Mass Transfer*. The McGraw-Hill Companies Inc., 2005.

K. F. Kelton, L. Greer, and C. V. Thompson. Transient nucleation in condensed systems. *J. Chem. Phys.*, **79**:6261, 1983.

W. Kuhn. Beziehungen zwischen Molekülgröße, statistischer Molekülgestalt und elastischen Eigenschaften hochpolymerer Stoffe. *Kolloid-Zeitschrift*, **76**:258, 1936.

S. H. Lam and J. Bellam. On de-coupling of shvab-zel'dovich variables in the presence of diffusion. *Combustion and Flames*, 132:691–743, 2003.

J. L. Lebowitz, J.K. Percus, and L. Verlet. Ensemble dependence of fluctuation with application to machine computation. *Phys. Rev.*, **153**:250–254, 1967.

F. Lince, D.L. Marchisio, and A.A. Barresi. Strategies to control the particle size distribution of poly-ε-caprolactone nanoparticles for pharmaceutical applications. *J. Colloid Interface Sci.*, 322:505, 2008.

F. Lince, D.L. Marchisio, and A.A. Barresi. Smart mixers and reactors for the production of pharmaceutical nanoparticles: Proof of concept. *Chem. Eng. Res. Des.*, 87:543, 2009.

F. Lince, S. Bolognesi, D.L. Marchisio, B. Stella, F. Dosio, A.A. Barresi, and L. Cattel. Preparation of poly(MePEGCA-co-HDCA) nanoparticles with Confined Impinging Jets Reactor: experimental and modelling study. *Journal of Pharmaceutical Sciences*, 100:2391, 2011a.

F. Lince, S. Bolognesi, D.L. Marchisio, B. Stella, F. Dosio, A.A. Barresi, and L. Cattel. Preparation of poly(MePEGCA-co-HDCA) nanoparticles with confined impinging jets reactor: experimental and modelling study. *J. Pharm. Sci.*, 100:2391, 2011b.

F. Lince, S. Bolognesi, B. Stella, D.L. Marchisio, and F. Dosio. Preparation of polymer nanoparticles loaded with doxorubicin for controlled drug delivery. *Chem. Eng. Res. Des.*, 89:2410, 2011c.

F. Lince, S. Bolognesi, B. Stella, D.L. Marchisio, F. Dosio, A.A. Barresi, and L. Cattel. Preparation of polymer nanoparticles loaded with doxorubicin for controlled drug delivery. *Chemical Engineering Research & Design*, 89:2410, 2011d.

F. Lince, D. L. Marchisio, and A. A. Barresi. A comparative study for nanoparticle production with passive mixers via solvent-displacement: Use of CFD model for optimization and design. *Chem. Eng. Process.*, 50:356, 2011e.

C.A. Lipinski, F. Lombardo, B. W. Dominy, and P. J. Feeney. Experimental and computational approaches to estimate solubility and permeability in drug discovery and development settings . *Advanced Drug Delivery*, 46:3, 2001.

Y. Liu and R.O. Fox. CFD Prediction for chemical processing in a confined impinging-jets reactor. *A.I.Ch.E. Journal*, **52**:731, 2005.

Y. Liu, C. Cheng, R.K. Prud'homme, and R.O. Fox. Mixing in a multi-inlet vortex mixer (MIVM) for flash nano-precipitation. *Chem. Eng. Sci.*, 63:2829, 2008.

M. R. Machado, P.D. Dans, and S. Pantano. A hybrid all-atom/coarse grain model for multiscale simulations of DNA. *Phys. Chem. Chem. Phys.*, 13:18134–18144, 2011.

H. Maeda. SMANCS and polymer-conjugated macromolecular drugs: advantages in cancer chemotherapy. *Adv. Drug Delivery Rev.*, 46:169, 2001.

H. Maeda, T. Sawa, and T. Konno. Mechanism of tumor-targeted delivery of macromolecular drugs, including the EPR effect in solid tumor and clinical overview of the prototype polymeric drug SMANCS . *Journal of Controlled Release*, 74:47, 2001.

D. L. Marchisio, M. Soos, J. Sefcik, and M. Morbidelli. Role of turbulent shear rate distribution in aggregation and breakage processes. *AIChE J.*, 52:158, 2006.

D.L. Marchisio. Large eddy simulation of mixing and reaction in a confined impinging jet reactor. *Comput. Chem. Eng.*, 33:408, 2009.

D.L. Marchisio and R.O. Fox. Solution of population balance using the direct quadrature method of moments. *Journal of Aerosol Science*, 36:43, 2005.

D.L. Marchisio, R. D. Vigil, and R.O. Fox. Implementation of the quadrature method of moments in CFD codes for aggregation-breakage problems. *Chem. Eng. Sci.*, 58:3337, 2003a.

D.L. Marchisio, R. D. Vigil, and R.O. Fox. Quadrature method of moments for aggregation-breakage problems. *Journal of Colloid and Interface Science*, 258:322, 2003b.

D.L. Marchisio, F. Omegna, A.A. Barresi, and P. Bowen. Effect of mixing and other operating parameters in sol-gel processes. *Industrial & Engineering Chemistry Research*, 47:7202, 2008.

D.L. Marchisio, F. Omegna, and A.A. Barresi. Production of TiO_2 nanoparticles with controlled characteristics by means of a vortex reactor. *Chem. Eng. J.*, 146:456, 2009.

V. G. Mavrantzas, T.D. Boone, E. Zervopolou, and N. Theodorou. End-Bridging Monte Carlo: A Fast Algorithm for Atomistic Simulation of Condensed Phases of Long Polymer Chains. *Macromolecules*, 32:5072–5096, 1999.

V.G. Mavrantzas and D.N. Theodorou. Atomistic Simulation of Polymer Melt Elasticity: Calculation of the Free Energy of an Oriented Polymer Melt. *Macromolecules*, 31:6310, 1998.

J. Mazur, C. M. Guttman, and F. McCrackin. Monte Carlo Studies of Self-Interacting Polymer Chains with Excluded Volume. II. Shape of a Chain. *Macromolecules*, **6**:872–874, 1973.

R. McGraw. Description of aereosol dynamics by the quadrature method of moments. *Aereosol Science and Technology*, 27:255, 1997.

R. McGraw. Correcting moment sedquence for errors associated with advective transport. Available at: $http://www.ecd.bnl.gov/pubs/momentcorrection\_mcgraw2006.pdf$, 2006.

D. McQuarrie. *Statistical Mechanics*. University Science Books, 2000.

R. Mei and K.C. Hu. "On the collision rate of small particles in turbulent flows". *"Journal of Fluid Mechanics"*, **391**:256, 1999.

A. Mersmann. Crystallization and precipitation. *Chem. Eng. Process.*, 38:345, 1999.

J Michel, M. Orsi, and J. W. Essex. Prediction of Partition Coefficients by Multiscale Hybrid Atomic-Level/Coarse-Grain Simulations. *J. Phys. Chem. B*, 112: 657, 2008.

G. Milano and F. Müller-Plathe. Mapping atomistic simulations to mesoscopic models: A systematic coarse-graining procedure for vinyl polymer chains. *Journal of Physical Chemistry B*, 109:18609, 2005.

F. Müller-Plathe. Coarse-graining in polymer simulation: From the atomistic to the mesoscopic scale and back. *Chem. Phys. Chem.*, 3:754, 2002.

M. Neri, C. Anselmi, M. Cascella, and A. Maritan. Coarse-Grained Model of Proteins Incorporating Atomistic Detail of the Active Site. *Phys. Rev. Lett*, 95: 218102, 2005.

A. E. Nielsen. *Kinetics of Precipitation*. Pergamon Press, 1964.

S. O. Nielsen, R. E. Bulo, P. B. Moore, and B. Ensing. Recent progress in adaptive multiscale molecular dynamics simulations of soft matter. *Phys. Chem. Chem. Phys.*, 12:12401, 2010a.

S. O. Nielsen, P. B. Moore, P. B. Moore, and B. Ensing. Adaptive multiscale molecular dynamics of macromolecular fluids. *Phys. Rev. Lett.*, 105:237802, 2010b.

S. O. Nielsen, P.B. Moore, and B. Ensing. Nielsen, Moore, and Ensing Reply:. *Phys. Rev. Lett.*, 107:099802, 2011.

D. W. Oxtoby. Homogenous nucleation: theory and experiment. *J. Phys. Cond. Matter*, **4**:7627, 1992.

M. Petitti, A. Nasuti, D.L. Marchisio, M. Vanni, G. Baldi, N. Mancini, and F. Podenzani. Bubble size distribution modelling in stirred gas-liquid reactors with QMOM augmented by a new correction algorithm. *AIChE J.*, 56:36, 2009.

H. Poincaré. *Science and Method*. Thomas Nelson and Sons, 1903.

S.B. Pope. *Turbulent Flows*. Cambridge University Press, 2000.

M. Praprotik, L. Delle Site, and K. Kremer. Multiscale Simulation of Soft Matter: From Scale Bridging to Adaptive Resolution . *Annual Review of Physical Chemistry*, 59:545–571, 2008.

M. Praprotnik, L. Delle Site, and K. Kremer. Adaptive resolution molecular-dynamics simulation: Changing the degrees of freedom on the fly. *Journal of Chemical Physics*, 123:14, 2005.

M. Praprotnik, S. Poblete, L. Delle Site, and K. Kremer. Comment on:"Adaptive multiscale molecular dynamics of macromolecular fluids " . *Phys. Rev. Lett.*, 107:2, 2011.

H. J. Qian, P. Carbone, X.Y. Chen, H. A. Karimi-Varzaneh, C.C. Liew, and F. Müller-Plathe. Temperature-Transferable Coarse-Grained Potentials for Ethylbenzene, Polystyrene, and their mixtures. *Macromolecules*, 41:9919, 2008.

H. J. Qian, C.C. Liew, and F. Müller-Plathe. Effective control of the transport coefficients of a coarse-grained liquid and polymer models using the dissipative particle dynamics and Lowe–Andersen equations of motion. *Phys. Chem. Chem. Phys.*, 11:1962, 2009.

D. Ramkrishna. *Population Balances*. Academic Press: San Diego, 2000.

D. Reith, M. Putz, and F. Müller-Plathe. Deriving Effective Mesoscale Potentials from Atomistic Simulations. *Journal of Computational Chemistry*, 24:1624, 2003.

V. Rokhlin. A fast Algorithm for Particle Simulations. *J. of Comput. Phys.*, **73**: 315, 1987.

M. Rubinstein and R. H Colby. *Polimer Physics*. Oxford Univ. Press, 2003.

A.J. Rzepiela, M. Louhivori, C. Peter, and S. J. Marrink. Hybrid simulations: combining atomistic and coarse-grained force fields using virtual sites. *Phys. Chem. Chem. Phys.*, 13:10437–10448, 2011.

Saffman and Turner. On the collision of drops in turbulent clouds. *Journal Fluid Dynamics*, 47:7202, 1956.

Q. Shi, S. Izvekov, and G. A. Voth. Mixed Atomistic and Coarse-Grained Molecular Dynamics: Simulation of a Membrane-Bound Ion Channel. *The Journal of Physical Chemistry B*, 110:15045–15048, 2006.

J.A. Shoahat and J.D. Tamarkin. *The Problem of Moments*. American Mathematical Society: Providence, 1963.

B. Smit, S. Karaborni, and I.J. Siepman. Computer simulation of vapor-liquid phase equilibria of n-alkanes. *Journal of Chemical Physics*, 102:2126, 1995.

D. K. Smith. Dendrimers and the Double Helix - From DNA Binding Towards Gene Therapy. *Current Topics in Medicinal Chemistry*, 8:1187, 2008.

P. E. Smith and W. F. Van Gunsteren. Reaction field effects on the simulated properties of liquid water. *Molecular Simulation*, **15**:233, 1995.

M. Smoluchowski. Veruch Einer Mathematischen Theorie Der Koagulationskinetic Kolloider Lösungen. *Zeitschrift für physikalische Chemie*, 92:129, 1917.

A. K. Soper. Empirical potential monte carlo simulation of fluid structure. *Chemical Physics*, 202:295, 1996.

O. Steinhauser. Reaction field simulation of water. *Molecular Physics*, **45**:335, 1982.

S. Succi. *The Lattice Boltzmann Equation for Fluid Dynamics and Beyond*. Clarendon Press, 2001.

Q. Sun and R. Faller. Crossover from Unentangled to Entangled Dynamics in a Systematically Coarse-Grained Polystyrene Melt. *Macromolecules*, 39:812, 2006.

V. P. Torchilin. Targeted Pharmaceutical Nanocarriers for Cancer Therapy and Imaging . *The AAPS Journal*, 9:E128, 2007.

W. Tschop, K. Kremer, J. Batoulis, T. Burger, and O. Hahn. Simulation of polymer melts. I. Coarse-graining procedure for polycarbonates. *Acta Polymerica*, 49:61–74, 1998.

D. Turnbull and L. Fisher. Rate of nucleation in condensed systems. *J. Chem. Phys.*, **17**:71, 1949.

I. Valente, E. Celasco, D.L. Marchisio, and A.A. Barresi. Nanoprecipitation in confined impinging jets mixers: Production, characterization and scale up of pegylated nanospheres and nanocapsules for pharmaceutical use. *Chemical Engineering Sciences*, 77:217, 2012a.

I. Valente, I.J. Del Valle, M.T. Casas, L. Franco, A. Rodríguez-Galán, J. Puiggalí, and D.L. Marchisio. Nanospheres and Nanocapsules of amphiphilic copolymers constituted by Methoxypolyethylene Glycol Cyanoacrylate and Hexadecil Cyanoacrylate units. *Express Polymer Letters*, in press, 2012b.

I. Valente, B. Stella, D.L. Marchisio, F. Dosio, and A.A. Barresi. Production of PEGylated nanocapsules through solvent-displacement in confined impinging jets mixers. *Journal of Pharmaceutical Sciences*, 101:2490, 2012c.

S. Valerio, M. Vanni, A.A. Barresi, and G. Baldi. Engineering modelling of turbulent flows in Chemical Engineering applications. *Trends in Chemical Engineering* , 5, 1998.

D. van der Spoel, E. Lindhal, B. Hess, G. Groenhof, A. E. Mark, and H. J. C. Berendsen. Gromacs: Fast, flexible and free. *J. Comp. Chem.*, **26**:1701, 2005.

M. Volmer and A. Weber. Keimbildung in übersättigten Gebilden. *Z. Phys. Chem.*, **119**:227, 1926.

G.A. Voth. *Coarse-Graining of Condensed Phase and Biomolecular Systems*. Taylor & Francis, 2008.

H. Wang, C. Junghans, and K. Kremer. Comparative atomistic and coarse-grained study of water: what do we lose by coarse-graining? *European Physics Journal*, 28:221, 2009.

L. Wang and R.O. Fox. Comparison of micromixing models for CFD simulation of nanoparticle formation. *AIChE J.*, 50:2217, 2004.

L. Wang, R. D. Vigil, and R. O. Fox. CFD simulation of shear-induced aggreation and breakage in turbulent Taylor-Couette flow. *J. Colloid Interface Sci.*, 285: 167, 2005.

X. Y. Woo, R. B. H. Tan, P. S. Chow, and R. D. Braatz. Simulation of mixing effects in antisolvent crystallization using a coupled CFD-PDF-PBE approach. *Cristal Growth & Design*, 6:1291, 2006.

X. Y. Woo, B. H. R. Tan, and R. D. Braatz. Modelling and computational fluid dynamics-population balance equation-micromixing simulation of impinging jet crystallizers. *Cristal Growth & Design*, 9:156, 2009.

D. L. Jr Wright. Numerical advection of moments of the particle size distribution in Eulerian models. *Journal of Aeresol Science*, 38:353, 2007.

C. Wu, T.F. Jim, Z. Gan, Y. Zhao, and S. Wang. A heterogeneous catalytic kinetics for enzymatic biodegradation of poly(ε-caprolactone) nanoparticles in aqueous solution. *Polymer*, 41:3593, 2000.